



## THESIS APPROVAL

### GRADUATE SCHOOL, KASETSART UNIVERSITY

Master of Science (Earth Science and Technology)

**DEGREE**

Earth Science and Technology

Earth Science

**FIELD**

**DEPARTMENT**

**TITLE:** Application of Geoarchaeological and Archaeometrical Techniques to  
Archaeometallurgical Evidence from Northeast Thailand

**NAME:** Miss Theeraporn Chuenpee

**THIS THESIS HAS BEEN ACCEPTED BY**

**THESIS ADVISOR**

( Mr. Krit Won-in, Ph.D. )

**DEPARTMENT HEAD**

( Mr. Passakorn Pananon, Ph.D. )

**APPROVED BY THE GRADUATE SCHOOL ON** \_\_\_\_\_

**DEAN**

( Associate Professor Gunjana Theeragool, D.Agr. )

THESIS

APPLICATION OF GEOARCHAEOLOGICAL AND ARCHAOMETRICAL  
TECHNIQUES TO ARCHAOMETALLURGICAL EVIDENCE FROM  
NORTHEAST THAILAND



THEERAPORN CHUENPEE

A Thesis Submitted in Partial Fulfillment of  
the Requirements for the Degree of  
Master of Science (Earth Science and Technology)  
Graduate School, Kasetsart University  
2014

Theeraporn Chuenpee 2014: Application of Geoarchaeological and Archaeometrical Techniques to Archaeometallurgical Evidence from Northeast Thailand. Master of Science (Earth Science and Technology), Major Field: Earth Science and Technology, Department of Earth Science. Thesis Advisor: Mr. Krit Won-in, Ph.D. 182 pages.

When a metallurgical history in some region in Southeast Asia, especially in Thailand, is written, the main substance on copper and iron seem likely to concentrate on three topics. One of these has already aroused lively interest of production technology that could provide clues to the metal working technology and process in the past. The other one is equally puzzling and interesting: the question of the date when copper and iron came into use. Lastly one is the relationship between metallurgical site and geomorphological feature. Unfortunately, in the past several decades, they were still unknown in almost part of the mentioned regions. This study essays a preliminary treatment of these three topics. In this study, archaeometallurgical evidences concerning with copper and iron, namely metallurgical slags, smelting furnace fragment, their associated finds (potsherds and baked sediment), and also the geomorphological features of each study area, were investigated by geoarchaeological and archaeometrical techniques. Four interesting study areas are located in northeast Thailand. The results indicated that, the smelting activity occurred in four study area during the Ancient Time. In addition, four sites tend to be located in floodplain or terrace close to water space. The Ancient Time Non Nong Hor copper process may be used the oxidic copper ores with sulphidic copper ores or a dead-roasting of ore charge before smelting, the smelting process was at high enough temperature to afford good liquation of the metal through the slag. Whist, the iron production at Krok Kroy, Ban Saitho 7 and Ban Khao Din Tai slag evidence is entirely consistent with the expect waste product of the bloomery iron-making process or direct smelting process).

---

Student's signature

---

Thesis Advisor's signature

## ACKNOWLEDGEMENTS

I wish to thank to my advisor, Dr. Krit Won-in for his suggestion of thesis. I am also deeply grateful to Assoc. Prof. Surapol Natapintu, Dr. Prayath Nantasin and Dr. Kannaree Chuangcham, for their advice and helping me on this thesis. I also wish to thank Dr. Somrudee Satitkun, the thesis defense chairman. I am most indebted, respect and thank Prof. Dr. Isao Takashima, for giving me a great opportunity to do the thesis works in Japan and providing us all support and guidance which made me complete the project on time.

I would like to thank the members of Faculty of Engineering and Resource Science, Akita University, Japan for their support and assistance on XRD, ED-XRF and SEM-EDS, sample preparation and analysis. I also wish to express my gratitude to the members of Scientific Equipment Center, Faculty of Science, Kasetsart University for the support on XRD analysis. I would like to thank Department of Geology, Faculty of Science, Chulalongkorn University for their support on optical microscope and SEM-EDS sample preparation. I also wish to thank Mr. Arak Wititeeranon, Mrs. Sumalee Nilpruk and staffs at Office of Atoms for Peace, for their assistance on TL sample irradiation. I am sincerely grateful to all staffs of Department of Earth Science, Faculty of Science, Kasetsart University for all supports and making this research possible. I would like to extend my acknowledgements to the Graduate School, Kasetsart University for providing The Graduate Study Research Scholarship for International Publications.

I also wish to gratefully thank Ms. Rapeeporn Sakunee, Ms. Yuratikan Chantaravikon and my friends for their help in various ways during this thesis work. Finally, I would like to express my deeply appreciation to my family, especially my mother, for their love, care and kindness.

Theeraporn Chuenpee

August 2013

## TABLE OF CONTENTS

|   | <b>Page</b> |
|---|-------------|
| TABLE OF CONTENTS   | i           |
| LIST OF TABLES  | iii         |
| LIST OF FIGURES   | vi          |
| LIST OF ABBREVIATIONS   | xiv         |
| INTRODUCTION  | 1           |
| OBJECTIVES  | 3           |
| LITERATURE REVIEW   | 4           |
| MATERIALS AND METHODS   | 24          |
| Materials   | 24          |
| Methods   | 26          |
| RESULTS AND DISCUSSION  | 37          |
| Results   | 37          |
| Discussion  | 80          |
| CONCLUSION  | 96          |
| LITERATURE CITED  | 98          |
| APPENDICES  | 106         |
| Appendix A Slag sample and TL sample, catalogues and images   | 107         |
| Appendix B Aerial photography   | 116         |
| Appendix C X-ray fluorescence spectrometry (XRF) and ED-XRF<br>data of the bulk chemical composition of the slags | 120         |
| Appendix D X-ray diffraction and XRD data of the phase composition<br>of the slags                                | 130         |

**TABLE OF CONTENTS (Continued)**

|  | <b>Page</b> |
|--|-------------|
| Appendix E Scanning electron microscopy with energy dispersive x-ray fluorescence spectrometry (SEM-EDS), reflected light microscopy and the results of microscopic analysis of slag | 135         |
| Appendix F SEM-EDS data of the phase composition of the slags  | 165         |
| Appendix G Thermoluminescence dating (TL) and the results of thermoluminescence dating   | 175         |
| CIRRICULUM VITAE   | 182         |

## LIST OF TABLES

| <b>Table</b> |  | <b>Page</b> |
|--------------|--|-------------|
| 1            | Bulk chemical composition (in wt%) of slag samples from Non Nong Hor archaeological site (determined by ED-XRF method)   | 42          |
| 2            | Phase compositions (in wt%) of slag samples from Non Nong Hor archaeological site obtained by XRD analysis (%wt), optical microscope and scanning electron microscope                              | 43          |
| 3            | The results of elemental content (U,Th, K <sub>2</sub> O), annual dose, palaeodose and TL age with error of five furnace fragment samples from Non Nong Hor archaeological site                    | 48          |
| 4            | Bulk chemical composition (in wt%) of slags from Khok Kroy archaeological site (determined by ED-XRF method)   | 53          |
| 5            | Phases in Khok Kroy slag samples obtained by XRD analysis (%wt), optical microscope and scanning electron microscope   | 54          |
| 6            | The results of elemental contents (U,Th, K <sub>2</sub> O), annual dose, palaeodose and TL age with error of four furnace fragment and baked sediment samples from Khok Kroy archaeological site   | 59          |
| 7            | Bulk chemical composition (in wt%) of slags from Ban Saitho 7 archaeological site (determined by ED-XRF method)  | 64          |
| 8            | Phases in Ban Saitho 7 archaeological site slag samples obtained by XRD analysis (%wt), optical microscope and scanning electron microscope  | 65          |
| 9            | The results of elemental contents (U,Th, K <sub>2</sub> O), annual dose, palaeodose and TL age with error of five furnace fragment and two potsherds samples from Ban Saitho 7 archaeological site | 69          |

## LIST OF TABLES (Continued)

| <b>Table</b>          |   | <b>Page</b> |
|-----------------------|---|-------------|
| 10                    | Bulk chemical composition (in wt%) of slags from Ban Khao Din Tai archaeological site (determined by ED-XRF method)   | 74          |
| 11                    | Phases in Ban Khao Din Tai archaeological site slag samples obtained by XRD analysis (%wt), optical microscope and scanning electron microscope                                     | 75          |
| 12                    | The results of elemental contents (U,Th, K <sub>2</sub> O), annual dose, palaeodose and TL age with error of six furnace fragment samples from Ban Khao Din Tai archaeological site | 79          |
| 13                    | Bulk chemical analyses of copper slags from Non Nong Hor (NNH) and Non Pa Wai (NPW) archaeological site (determined by XRF method, concentration in wt%).                           | 88          |
| 14                    | Bulk chemical analyses of iron slags from Khok Kroy (BKT), Ban Saitho 7 (STH) and Ban Khao Din Tai (KDT) archaeological site. (determined by ED-XRF method, concentration in wt%).  | 93          |
| <b>Appendix Table</b> |   |             |
| A1                    | Slag sample catalogue   | 108         |
| A2                    | TL sample catalogue (Smelting furnace fragment, potsherds and baked sediment)   | 112         |
| C1                    | ED-XRF data of the bulk chemical composition of the slags (wt.%).   | 128         |
| D1                    | XRD data of the phase composition of the slags (wt.%)   | 134         |
| F1                    | SEM-EDS data of the phase composition of the slags from Non Nong Hor Archaeological Site (wt.%)   | 167         |

**LIST OF TABLES (Continued)**

| <b>Appendix Table</b> |   | <b>Page</b> |
|-----------------------|---|-------------|
| F2                    | SEM-EDS data of the phase composition of the slags from Khok Kroy Archaeological Site (wt.%)                | 169         |
| F3                    | SEM-EDS data of the phase composition of the slags from Ban Saitho 7 Archaeological Site (wt.%)             | 171         |
| F4                    | SEM-EDS data of the phase composition of the slags from Ban Khao Din Tai Archaeological Site (wt.%)         | 174         |
| G1                    | The results of thermoluminescence dating of Smelting furnace fragment, potsherds and baked sediment samples | 181         |

## LIST OF FIGURES

| <b>Figure</b> |  | <b>Page</b> |
|---------------|--|-------------|
| 1             | Digital Elevation Model (DEM) showing four investigated sites where located in the northeastern region of Thailand   | 8           |
| 2             | Topographic map of Non Nong Hor archaeological site, Tambon Na Udom, Amphoe Nikhom Kham Soi, Mukdahan Province (red triangle: study area)  | 10          |
| 3             | Topographic map of Khok Kroy archaeological site, Tambon Na Bua, Amphoe Mueang Surin, Surin Province (red triangle: study area)  | 12          |
| 4             | Topographic map of Ban Saitho 7 Ban Saitho 7 archaeological site, Tambon Chanthop Phet, Amphoe Ban Kruat, Buri Ram Province (red triangle: study area)   | 14          |
| 5             | Topographic map of Ban Khao Din Tai archaeological site, Tambon Ban Kruat, Amphoe Ban Kruat, Buri Ram Province (red triangle: study area)  | 16          |
| 6             | Simplified flow chart illustrating investigation procedures for the study  | 27          |
| 7             | Aerial photograph of Non Nong Hor archaeological site, Tambon Na Udom, Amphoe Nikhom Kham Soi, Mukdahan Province (red triangle: study area)  | 38          |
| 8             | Interpreted morphological landforms of Non Nong Hor archaeological site, Tambon Na Udom, Amphoe Nikhom Kham Soi, Mukdahan Province   | 39          |
| 9             | (A) Macroscopic of sample A0573 (B) green spots (marked with a red circle) on the surface of sample A0572 (C) Sectioned of sample A0573, showing homogeneous texture with a small amounts of pores (D) Sand inclusions inside sample A0574 | 41          |

## LIST OF FIGURES (Continued)

| <b>Figure</b> |  | <b>Page</b> |
|---------------|--|-------------|
| 10            | Reflected light microscope image (A) Sample A0581, showing skeletal fayalite laths, fine-dendritic magnetite crystals with bright spots of copper prill (B) Copper sulphide among the clusters of magnetites, euhedral magnetites crystals, copper prills and skeletal fayalite laths of sample A0572; Scanning electron microscope image (C) Sample A0574, showing skeletal fayalite laths, euhedral magnetites crystals with quartz inclusions (D) Euhedral magnetite crystals with skeletal fayalite laths in glassy matrix of sample A0581; fa-fayalite, ma-magnetite, Qt-quartz, m-metal (copper), cs-copper sulphide, gl-glassy matrix | 45          |
| 11            | FeO-CaO-SiO <sub>2</sub> ternary diagrams presenting the distribution of studied slags of Non Nong Hor archaeological site   | 46          |
| 12            | Aerial photograph of Khok Kroy archaeological site, Tambon Na Bua, Amphoe Mueang Surin, Surin Province (red triangle: study area)  | 50          |
| 13            | Interpreted morphological landforms of Khok Kroy archaeological site, Tambon Na Bua, Amphoe Mueang Surin, Surin Province   | 51          |
| 14            | (A) Macroscopic of lumpy shape of sample A0595 (B) Macroscopic of flattened shape of sample A0586  | 52          |

1943

## LIST OF FIGURES (Continued)

| <b>Figure</b> |   | <b>Page</b> |
|---------------|---|-------------|
| 15            | Reflected light microscope image (A) Image of sample A0586, showing residual quartz inclusions (B) Image of sample A0595, showing skeletal fayalite laths and residual quartz inclusions in a glassy matrix.; Scanning electron microscope image (C) Skeletal fayalite laths, coarse-dendritic hercynite with bright large spots of iron prill in the glassy matrix of sample A0588 (D) Euhedral hercynite with skeletal fayalite laths with bright small spots of iron prill in glassy matrix of sample A0590; fa-fayalite, he-hercynite, Qt-Quartz, m-metal, gl-glassy matrix | 57          |
| 16            | FeO-SiO <sub>2</sub> -Al <sub>2</sub> O <sub>3</sub> ternary diagrams, presenting the distribution of studied slags of Khok Kroy archaeological site  | 58          |
| 17            | Aerial photographs of Ban Saitho 7 archaeological site, Tambon Chanthop Phet, Amphoe Ban Kruat, Buri Ram Province (red triangle: study area)  | 61          |
| 18            | Interpreted morphological landforms of Ban Saitho 7 archaeological site, Tambon Chanthop Phet, Amphoe Ban Kruat, Buri Ram Province  | 62          |
| 19            | (A) Macroscopic of sample A0273 (B) Sectioned of sample A0546, showing glassy texture with a large number of charcoals and pores  | 63          |

## LIST OF FIGURES (Continued)

| <b>Figure</b> |  | <b>Page</b> |
|---------------|--|-------------|
| 20            | Reflected light microscope image (A) Euhedral fayalite crystals in glassy matrix (sample A0547) (B) Fayalite and quartz with cracks of sample; Scanning electron microscope image (C) A0278 Polished thin-sections of sample A0273, showing elongate skeletal fayalite laths, euhedral hercynite and iron prill (at center) in a glassy matrix (D) Coarse-dendritic hercynite and fayalite laths in glassy matrix of sample A0281, fa-fayalite, he-hercynite, Qt-Quartz, m-metal, gl-glassy matrix | 67          |
| 21            | FeO-SiO <sub>2</sub> -Al <sub>2</sub> O <sub>3</sub> ternary diagrams, presenting the distribution of studied slags of Ban Saitho 7 archaeological site  | 68          |
| 22            | Aerial photograph of Ban Khao Din Tai archaeological site, Tambon Ban Kruat, Amphoe Ban Kruat, Buri Ram Province (red triangle: study area)  | 71          |
| 23            | Interpreted morphological landforms of Ban Khao Din Tai archaeological site, Tambon Ban Kruat, Amphoe Ban Kruat, Buri Ram Province   | 72          |
| 24            | (A) Macroscopic of block to lump slag (sample A0538). (B) Macroscopic of flattened shape slag (sample A0539)   | 73          |
| 25            | Reflected light microscope image (A) Skeletal fayalite laths in glassy matrix (sample A0540) (B) Iron prill in sample A0541; Scanning electron microscope image (C) Corroded iron in sample A0540 (D) Euhedral hercynite and fayalite laths in glassy matrix of sample A0538, fa-fayalite, he-hercynite, Qt-Quartz, m-metal, gl-glassy matrix  | 77          |

## LIST OF FIGURES (Continued)

| <b>Figure</b>              |  | <b>Page</b> |
|----------------------------|--|-------------|
| 26                         | FeO- SiO <sub>2</sub> -Al <sub>2</sub> O <sub>3</sub> ternary diagrams, presenting the distribution of studied slags of Ban Khao Din Tai archaeological site   | 78          |
| 27                         | Bivariate compositional scatter plots of CuO-FeO and CuO-SO <sub>3</sub> of copper slags from Non Nong Hor and Non Pa Wai archaeological site. (Oxides are shown in wt%.)  | 90          |
| 28                         | FeO-CaO-SiO <sub>2</sub> ternary diagrams presenting the distribution of studied slags from Non Nong Hor (red circle) and Non Pa Wai archaeological site (green circle)  | 91          |
| 29                         | Bivariate compositional scatter plots of FeO-SiO <sub>2</sub> , FeO-CaO and FeO-Al <sub>2</sub> O <sub>3</sub> of iron slags from Khok Kroy, Ban Saitho 7 and Ban Khao Din Tai archaeological site. (Oxides are shown in wt%.)       | 94          |
| 30                         | FeO-SiO <sub>2</sub> -Al <sub>2</sub> O <sub>3</sub> ternary diagram, presenting the distribution of studied slags from Krok Kroy (red circle), Ban Saitho 7 (green circle) and Ban Khao Din Tai (yellow circle) archaeological site | 95          |
| <br><b>Appendix Figure</b> |  |             |
| A1                         | Images of slag samples   | 110         |
| A2                         | Images of TL samples (Smelting furnace fragment, potsherds and baked sediment samples)   | 114         |
| B1                         | Stylized view of flight path of airplane for vertical aerial photos that can be used for stereoscopic viewing in three dimensions  | 118         |
| C1                         | Continuous and characteristic radiation for copper   | 123         |
| C2                         | The measurement of ED-XRF  | 126         |

## LIST OF FIGURES (Continued)

| <b>Appendix Figure</b>  | <b>Page</b> |
|---|-------------|
| D1 Diffraction of X-rays by planes of atoms (A-A' and B-B')   | 132         |
| D2 Schematic diagram of an x-ray diffractometer; T = x-ray source, S = specimen, C = detector, and O = the axis around which the specimen and detector rotate | 133         |
| E1 Photon and charged particle emissions from an electron-bombarded surface   | 137         |
| E2 Schematic drawing of SEM   | 141         |
| E3 Light path in the Reflected light microscope   | 144         |
| E4 The results of microscopic analysis of slag (A0572) from Noen Nong Ho Archaeological Site  | 145         |
| E5 The results of microscopic analysis of slag (A0573) from Noen Nong Ho Archaeological Site  | 146         |
| E6 The results of microscopic analysis of slag (A0574) from Noen Nong Ho Archaeological Site  | 147         |
| E7 The results of microscopic analysis of slag (A0577) from Noen Nong Ho Archaeological Site  | 148         |
| E8 The results of microscopic analysis of slag (A0581) from Noen Nong Ho Archaeological Site  | 149         |
| E9 The results of microscopic analysis of slag (A0586) from Khok Kroy Archaeological Site   | 150         |
| E10 The results of microscopic analysis of slag (A0588) from Khok Kroy Archaeological Site  | 151         |
| E11 The results of microscopic analysis of slag (A0590) from Khok Kroy Archaeological Site  | 152         |

## LIST OF FIGURES (Continued)

| <b>Appendix Figure</b>   | <b>Page</b> |
|--|-------------|
| E12    The results of microscopic analysis of slag (A0594) from Khok Kroy Archaeological Site        | 153         |
| E13    The results of microscopic analysis of slag (A0595) from Khok Kroy Archaeological Site        | 154         |
| E14    The results of microscopic analysis of slag (A0273) from Ban Saitho 7 Archaeological Site     | 155         |
| E15    The results of microscopic analysis of slag (A0278) from Ban Saitho 7 Archaeological Site     | 156         |
| E16    The results of microscopic analysis of slag (A0281) from Ban Saitho 7 Archaeological Site     | 157         |
| E17    The results of microscopic analysis of slag (A0546) from Ban Saitho 7 Archaeological Site     | 158         |
| E18    The results of microscopic analysis of slag (A0547) from Ban Saitho 7 Archaeological Site     | 159         |
| E19    The results of microscopic analysis of slag (A0538) from Ban Khao Din Tai Archaeological Site | 160         |
| E20    The results of microscopic analysis of slag (A0539) from Ban Khao Din Tai Archaeological Site | 161         |
| E21    The results of microscopic analysis of slag (A0540) from Ban Khao Din Tai Archaeological Site | 162         |
| E22    The results of microscopic analysis of slag (A0541) from Ban Khao Din Tai Archaeological Site | 163         |
| E23    The results of microscopic analysis of slag (A0542) from Ban Khao Din Tai Archaeological Site | 164         |
| F1     SEM-EDS data of the phase composition of the slags from Non Nong Hor Archaeological Site      | 166         |

## LIST OF FIGURES (Continued)

| <b>Appendix Figure</b>  | <b>Page</b> |
|---|-------------|
| F2 SEM-EDS data of the phase composition of the slags from Khok Kroy Archaeological Site  | 168         |
| F3 SEM-EDS data of the phase composition of the slags from Ban Saitho 7 Archaeological Site   | 170         |
| F4 SEM-EDS data of the phase composition of the slags from Ban Khao Din Tai Archaeological Site   | 172         |
| G1 A simple types of defect in the lattice structure of an ionic crystal: A negative-ion vacancy on the left, A negative-ion interstitial at the center, and substitution impurity center on the bottom right   | 177         |
| G2 Thermoluminescence-process diagram showing energy–level related to three processes; (i) irradiation process, caused by crystal exposed to nuclear radiation, ionized electrons are trapped at hole (T); (ii) Storage stage in which electrons have been trapped, need hole deep enough for electrons (E) during geological time period of sample; and (iii) Heating process, at optimum level of temperature, electrons are released and re-combined at luminescence center (L), and then light (TL) is released | 178         |
| G3 Diagram of thermoluminescence instrument   | 179         |
| G4 (A) A TL glow curve (temperature versus TL signal intensity); (B) A TL growth curve  | 180         |

## LIST OF ABBREVIATIONS

|           |   |   |
|-----------|---|---|
| AD        | = | Anno Domini or In the year of the Lord  |
| BC        | = | Before Christ   |
| BCE       | = | Before the Common Era   |
| DEM       | = | Digital Elevation Model   |
| SEM-EDS   | = | Scanning electron microscopy with energy dispersive x-ray fluorescence spectrometry |
| [P]ED-XRF | = | Polarising energy dispersive x-ray fluorescence spectrometry                        |
| ED-XRF    | = | Energy dispersive x-ray fluorescence spectrometry                                   |
| XRF       | = | X-ray fluorescence spectrometry   |
| XRD       | = | X-ray diffractometion   |
| WDS       | = | Wavelength dispersive spectrometer  |
| EDS       | = | Energy dispersive spectrometer  |
| BSE       | = | Backscattered electron  |
| SE        | = | Secondary electron  |
| CRT       | = | Cathode ray tube  |
| TL        | = | Thermoluminescence dating   |
| Z         | = | Atomic number   |
| g         | = | Gram  |
| m         | = | Meter   |
| mm        | = | Millimeter  |
| km        | = | Kilometer   |

**LIST OF ABBREVIATIONS (Continued)**

|                       |   |                   |
|-----------------------|---|-------------------|
| $\mu\text{m}$         | = | Micrometer        |
| nm                    | = | Nanometer         |
| m/s, $\text{ms}^{-1}$ | = | Meter per second  |
| $\text{cm}^2$         | = | Square centimeter |
| Å                     | = | Angstrom          |
| eV                    | = | Electronvolt      |
| keV                   | = | Kiloelectronvolt  |
| kV                    | = | Kilovolt          |
| °C                    | = | Degree celcius    |
| $c$                   | = | Velocity          |
| $\nu$                 | = | Frequency         |
| $\lambda$             | = | Wavelength        |
| $E$                   | = | Energy            |
| $h$                   | = | Planck constant   |
| $p$                   | = | Momentum          |
| $m$                   | = | Mass              |
| PD                    | = | Palaeodose        |
| AD                    | = | Annual dose       |

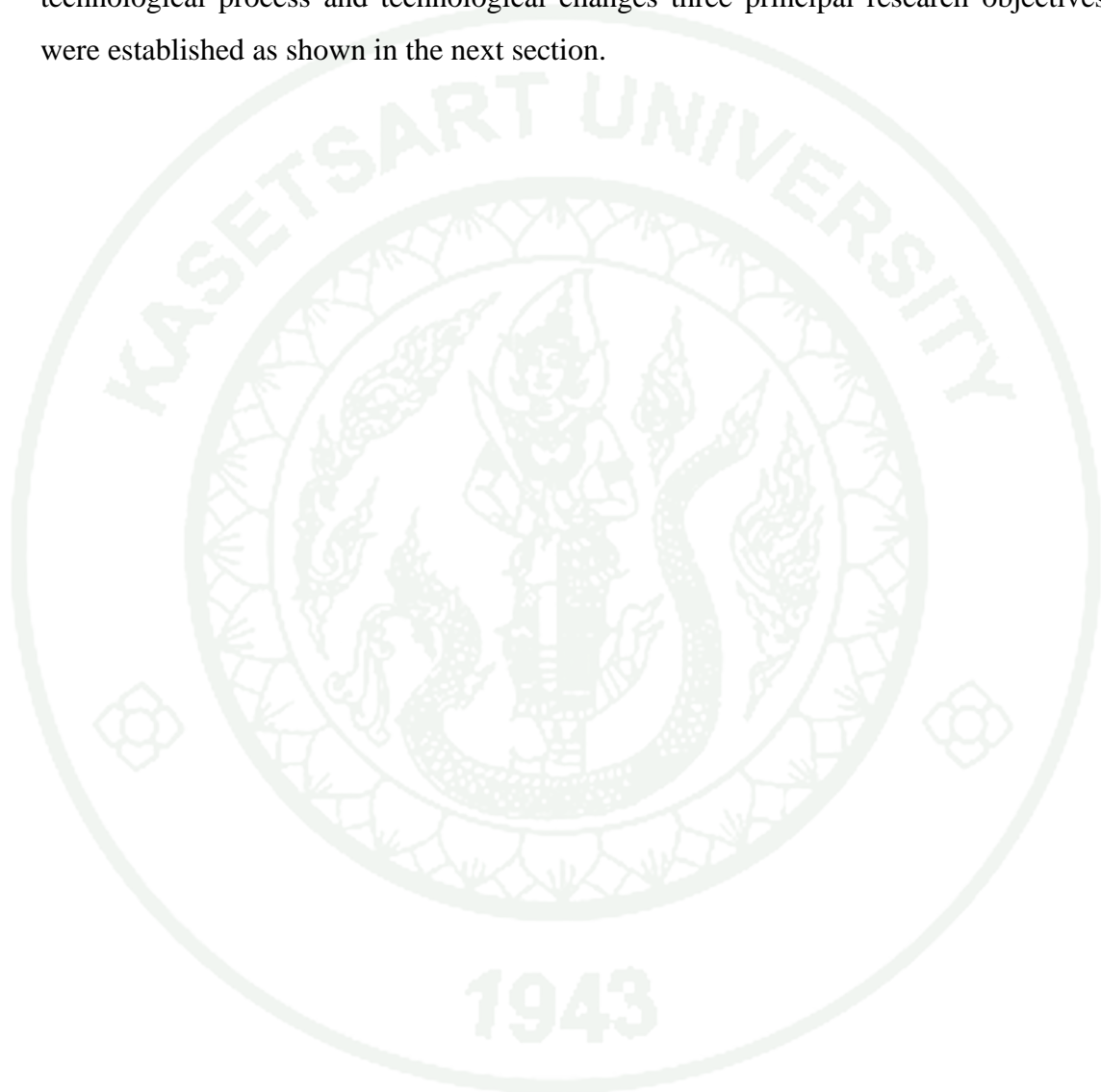
**APPLICATION OF GEOARCHAEOLOGICAL  
AND ARCHAOMETRICAL TECHNIQUES  
TO ARCHAEOLOGICAL EVIDENCE FROM  
NORTHEAST THAILAND**

**INTRODUCTION**

Archaeometallurgical research in mainland Southeast Asia, including Cambodia, Laos, Myanmar (Burma), Vietnam, Peninsular Malaysia and Thailand, is a relatively new field and there are huge gaps in our fundamental data and understanding. Nonetheless, in the several decades since the discovery that a discrete Bronze Age preceded the Iron Age in this region, much has been learned about the dating, technology, production, organization, and use of metallurgy in the region, particularly in prehistoric Thailand. Although independent invention of metal smelting in Southeast Asia has not been considered likely by most regional archaeologists since the 1980s, the source of metal technology and the mechanisms of adoption remain poorly understood (White and Hamilton, 2009: 357).

In northeast Thailand early metal using village communities display metal products in a variety of forms manufactured from the copper and iron. Nonetheless their technological precedents, chronologies and geomorphological features are not clear as the prehistory of Thailand continued to be unexplored. This thesis comprises an archaeometallurgical investigation of copper and iron smelting by using Geoarchaeological and Archaeometrical techniques, in a bronze production site: Non Nong Hor and three iron production sites: Khok Kroi, Ban Saitho 7 and Ban Khao Din Tai of northeast Thailand. The major research aim of the present study was to better understand the development of copper and iron smelting technologies over a period of production. The production techniques practiced by metalworker at these sites have left enormous quantities of metallurgical material culture namely, slag and smelting furnace fragment and an associated finds namely, potsherds and baked

sediment. The metallurgical assemblages and the structure of the archaeological deposits from Non Nong Hor, Khok Kroi, Ban Saitho 7 and Ban Khao Din Tai are quite dissimilar, suggesting that the extraction technologies employed at each site may have changed over the course of the production period. In order to comprehend these technological process and technological changes three principal research objectives were established as shown in the next section.



## OBJECTIVES

1. To study the relationship between Geomorphological features and metal production site in Non Nong Hor, Khok Kroi, Ban Saitho 7 and Ban Khao Din Tai archaeological site (northeast Thailand) by using Geoarchaeological technique.

2. To generate detailed technological reconstructions of the copper and iron smelting activities evidenced at Non Nong Hor, Khok Kroi, Ban Saitho 7 and Ban Khao Din Tai archaeological site (northeast Thailand) based upon the available archaeometallurgical evidence by using Archaeometrical techniques.

3. To date the copper and iron smelting activities at Non Nong Hor, Khok Kroi, Ban Saitho 7 and Ban Khao Din Tai archaeological site (northeast Thailand) based upon the available archaeometallurgical evidence and their associated finds by using archaeometrical techniques.

## LITERATURE REVIEW

### 1. Early copper and iron smelting technology

The ancient world passed from the Stone Age through the Bronze Age and Iron Age to our modern developed society. Formerly, six metals were used by prehistoric man: gold, silver, copper, tin, lead, and iron. Gold and silver were too soft to be useful for much except decoration. Copper could be hardened by hammering or forging and was, therefore, useful as a tool, but had little value as a weapon. Bronze, developed by alloying copper with tin, had useful strengths, could be hardened by forging, and could be casting to shape. The discovery of bronze significantly altered the development of civilization. Lead was soft, easily worked, and could be made into vessels; later in history it was made into pipes such as those used to transport water in the early Roman Empire. Iron was so important to civilization that its discovery led to the Iron Age and a transition from the Bronze Age (Reardon, 2011: 73).

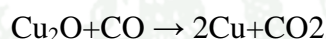
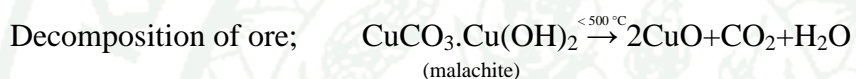
In Thailand, with the current available evidence it is reasonable to suggest that metal appeared in northeast of the country at some times between 4,500-4,000 years BP, and bronze was the first type of metal used in this area. Later in the period around 2,700-2,500 years BP, iron began to make its appearance and later became the major raw material for making the edged and agricultural implements and weapons (Fine Arts Department, 2007: 70). While the number of field walk and excavation provided insight into the ancient copper and iron metallurgy in Thailand, especially in the smelting technology as follows.

#### 1.1 Copper smelting

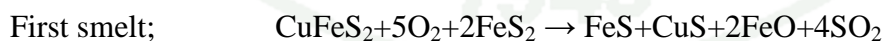
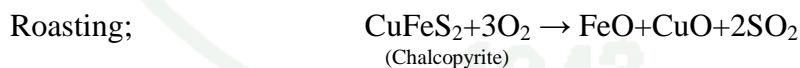
Before we consider the smelting operations, carried out on copper ores, it would be as well to discuss the principles of the process. As we have seen, copper ores may be oxidized, i.e. sulphates, carbonates or pure oxide, or sulphides, i.e. chalcocite ( $\text{Cu}_2\text{S}$ ). The oxidized ores are found at the top of the surface of an ore deposit and are the result of atmospheric oxidation or weathering of the sulphides. Naturally, early copper smelter would discover the oxidized ores and smelt them with

relatively little trouble, and later, start to work on the sulphide ores. Otherwise it is very difficult to give a date of this transition.

Due to the high melting point of pure copper (1,083 °C), copper was usually smelted into ingots formed within the smelting furnace. The liquid copper could not be run out far, as its temperature was very little above the melting point. Early smelting furnaces undoubtedly consisted of a small hollow in a depression in the ground above which was placed the fire containing charcoal and oxidized ore, assisted with bellows. Metallurgically, no difficulty would be experienced with this operation, copper and slag being readily reduced according to the reaction below (Tylecote, 1962),



While sulphide ores were either roasted to oxide according to the reaction, or first smelted to give copper sulphide and slag, and the resulting sulphide oxidized to copper according to,



## 1.2 Iron smelting

Iron came late in the history of Thailand metallurgy and also other country because the technique required for smelt was more difficult than that required for the more common non-ferrous metals—any metal, include alloys that does not contain iron in appreciable amounts. Although pure iron has a much higher melting point than any one of common non-ferrous metals, this is not the main reason for the difficulty in smelt it. Iron is a fourth most abundant element in the earth's crust, of which it constitutes about 5% by weight, and is believed to be the major component of the earth's core. Iron is found distributed in the soil in low concentrations and is found dissolved in ground-waters and the ocean to a limited extent. It is rarely found uncombined in nature except in meteorites, but iron ores and minerals are abundant and widely distributed. The principal ores of iron are hematite and limonite. Other ores include siderite, taconite and magnetite, which often occur as white sand. Iron pyrite is a crystalline gold-colored mineral known as fool's gold. Chromite is a chromium ore that contains iron. Lodestone is a form of magnetite that exhibits natural magnetic properties. Mostly, iron occurs in ores as an oxide, but compared with tin, iron is more difficult to reduce, i.e. to separate from oxygen. It requires much more strongly reducing conditions.

Some metals may be produced by smelting below their melting point or others above. Fortunately iron may be reduced from pure iron oxide at about 800 °C, considerably below its melting point of 1,540 °C. However, iron ores do not consist only of iron oxide, commonly they are mixtures of these and gangue or unwanted minerals. Since it is not practicable to remove all the gangue by washing, a substantial number must be separated by slagging in the smelting process. The slags consist mostly of a compound formed of silica and iron, i.e. Fayalite ( $\text{Fe}_2\text{SiO}_4$ ). As much as possible these slags has to be removed from the iron by liquation, and therefore the smelting process must take place at or above the temperature at which the slags become sufficiently fluid to drain away from the solid iron. This temperature is about 1,150-1,200 °C, well above the minimum temperature at which iron oxide can be reduced to iron, but substantially below the melting point of the metals. Thus, iron is

produced in the solid state as a sponge or raw bloom from which the slag partly drains away, this known as the direct process, as illustrated by the relation below (Humphris, 2010:45-46). The rest is removed by hammering while the bloom is still hot and slag still in a fluid state.

$3\text{Fe}_2\text{O}_3 + \text{CO} \rightarrow 2\text{Fe}_3\text{O}_4 + \text{CO}_2$ ..... Iron oxides in the ore react with CO to produce decreasing iron to oxygen ratios: haematite reducing to magnetite

$\text{Fe}_3\text{O}_4 + \text{CO} \rightarrow 3\text{FeO} + \text{CO}_2$ ..... Magnetite reducing to wüstite

$\text{FeO} + \text{CO} \rightarrow \text{Fe} + \text{CO}_2$ ..... Finally, wüstite reducing to iron metal

Slag formation;  $\text{SiO}_2 + 2\text{FeO} \rightarrow 2\text{FeO} \cdot \text{SiO}_2$

While *in* 1992, Suchitta suggests that the indirect process of iron smelting involves heating a mixture of iron ore and fuel (either charcoal or coal) in larger and taller furnace than that used for bloomer. The temperature inside the furnace is usually high enough to liquefy the iron. At this stage the iron will concentrate at the bottom of the furnace as a molten pool that solidifies into a piece of a brittle cast iron with a very high carbon content. The liquefied iron may also be tapped off the furnace and poured into some kind of container or mould. Owing to the presence of a high carbon content that makes the iron brittle, and unsuitable for making objects or tools such as swords, which need to be resistant to shock, it is necessary to put this high carbon cast iron through a second process in another furnace. However, this type of iron smelting process did not become popular in Thailand until around the seventeenth or eighteenth century.

## 2. Study areas

This section commences with a discussion of the archaeological and geographic information of study areas, of a bronze production site: Non Nong Hor and three iron production sites: Khok Kroi, Ban Khao Din Tai, and Ban Saitho 7, the four significant sites focused in this study (figure 1).

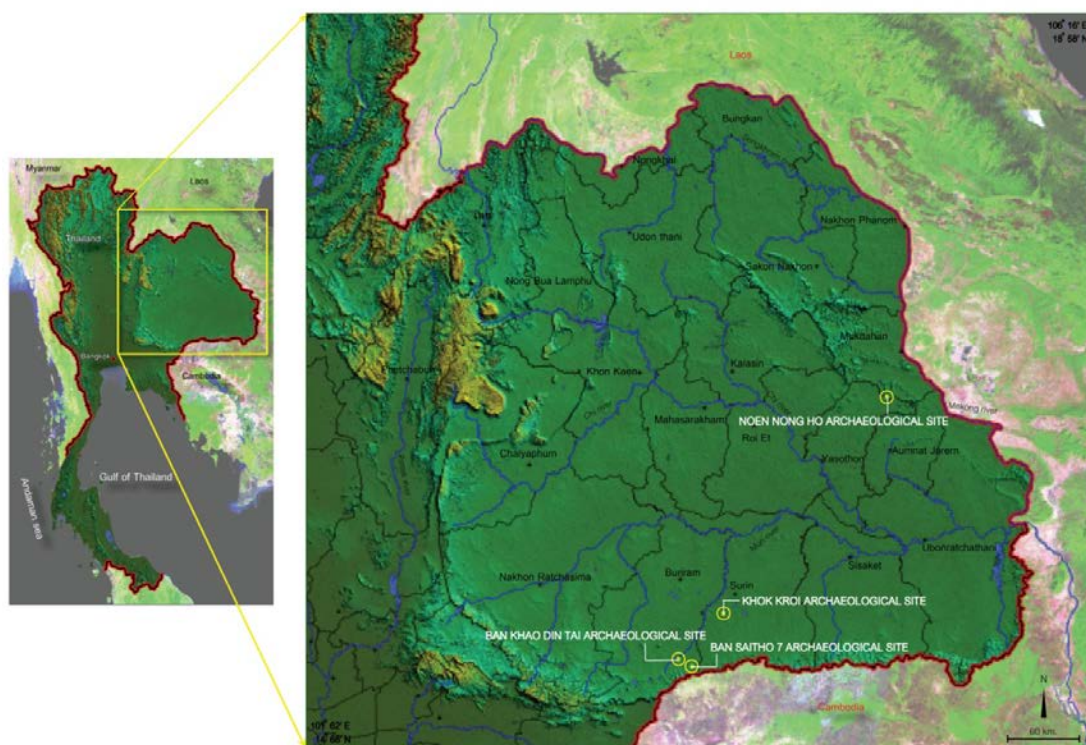


**Figure 1** Digital Elevation Model (DEM) showing four study sites where located in northeast Thailand.

**Source:** Thin Than Thai Institute (2012)

## 2.1 Non Nong Hor Archaeological site

Non Nong Hor archaeological site is centered on 16°24' N, 104°62' E. It is situated about 40 km west of Mekong River, near small village in Tambon Na Udom, Amphoe Nikhom Kham Soi, Mukdahan Province. Neighboring province are Amnat Charoen, Yasothon, Roi Et, Kalasin, Sakon Nakhon and Nakhon Phanom. The site is located near small stream and surrounded by agricultural fields (rice and sugar cane field). The site of Non Nong Hor was originally excavated in 2000, by the 11<sup>th</sup> Regional Office of Fine Arts, Ubon Ratchathani. From the excavation, archaeological evidence relate to bronze/copper metallurgy found on site include copper ingots, crucible fragments and various kinds of mould.

The excavation took place again on May 2000, as part of the project entitled “The study on the relationship of the ancient through present culture for the development of cultural and civilization database for GMS and Malay Peninsula regions” (the extension of Living Angkor Road project). As the latter excavation, the archaeological evidence discovered on site include copper smelting slags, charcoal, smelting furnace fragments, potsherds, mould, bronze artifacts and animal bones (Natapintu, 2011). A sample of charcoal relating to the bronze/copper production also collected for radiocarbon dating at the Radiocarbon Dating Laboratory, The University of Waitago. The result indicates that the age of charcoal sample is 2,105±25 years BP (Hogg, 2013).

1943

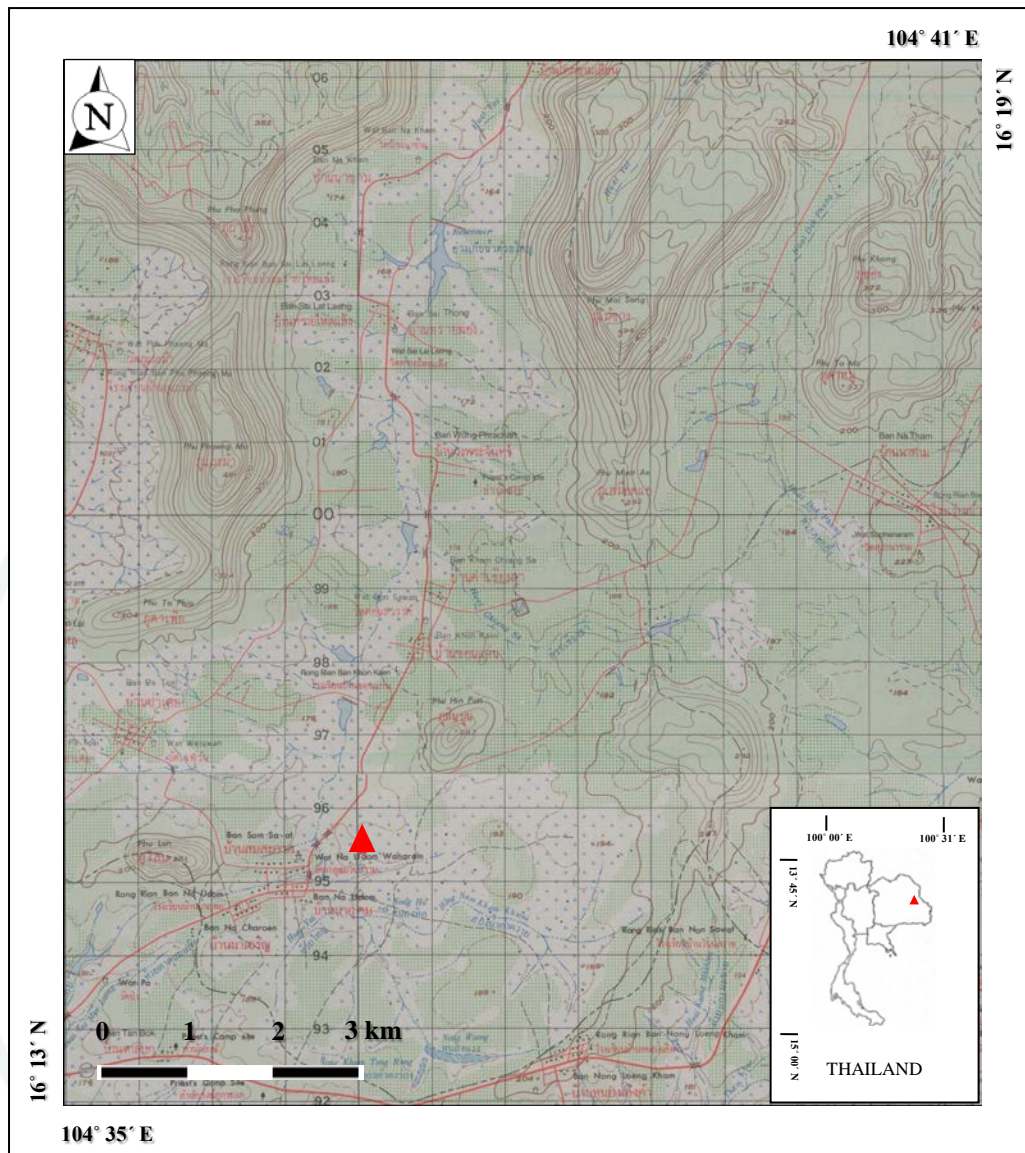


**Figure 2** Topographic map of Non Nong Hor archaeological site, Tambon Na Udom, Amphoe Nikhom Kham Soi, Mukdahan Province (red triangle: study area).

**Source:** Royal Thai Survey Department (n.d.)

## 2.2 Khok Kroy Archaeological site

The excavation of Khok Kroy archaeological site took place between January-February 2011. As part of the project entitled “The study on the relationship of the ancient through present culture for the development of cultural and civilization database for GMS and Malay Peninsula regions” (the extension of Living Angkor Road project), this site was chosen because initial examination of probably ancient iron slags and their associated finds exposed at the eroding part of the mound. The modern village of the site (latitude: 14°76′ N, longitude: 103°42′ E), in Tambon Na Bua, Amphoe Mueang Surin, Surin Province, located near small stream which is called Huai Na Bua and surrounded by agricultural fields. One pit were excavated on the mound, in order to understand the site information, the pit has an orientation from north-south, covered an area of 3 by 5 meters, and was divided into 15 grids for an ease of excavation and recording. The cultural sequence being divisible into three layers. The top most comprised an iron smelting slags and small potsherds. The second layer comprised much iron smelting slags, smelting furnace wall, tuyère and a small amount of potsherds. The third layer comprised much potsherds and a small amount of iron smelting slags. As summarized, the archaeological evidence discovered on site include probably iron smelting slags, tuyère, smelting furnace walls, potsherds, baked sediment, clay roundles. The project yielded relative dates of topology of potsherds, which give a range of ages from 2,300 years BP at the earliest to 1,500 years BP at the lastest (Natapintu, 2011).

1943

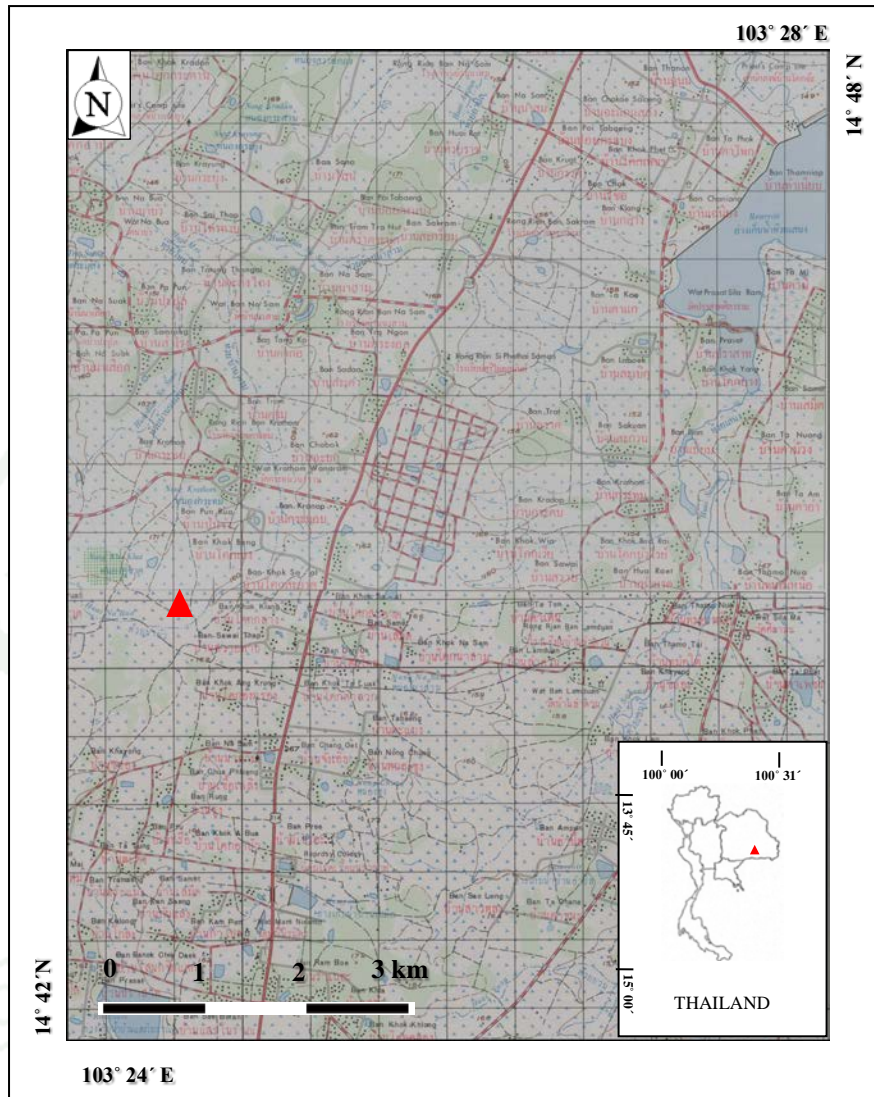


**Figure 3** Topographic map of Khok Kroy archaeological site, Tambon Na Bua, Amphoe Mueang Surin, Surin Province (red triangle: study area).

**Source:** Royal Thai Survey Department (n.d.)

### 2.3 Ban Saitho 7 Archaeological site

Ban Saitho 7 archaeological site is one of the ancient rural sites in the region of Buriram Province, northeast Thailand. It is located at 14°38' N latitude and 103°18' E longitude, situated near small stream which is called Huai Tako and approximately 5 km north of the Thai-Cambodian border. The site was originally surveyed by the project entitled "The study on the relationship of the ancient through present culture for the development of cultural and civilization database for GMS and Malay Peninsula regions" (the extension of Living Angkor Road project) in 2008, while the excavations there were undertaken in February-March 2009. The excavation was divided into three pits. The pit number one has an orientation from east-west, covering an area of two by five meters. The last two pits have an orientation from north-south, the pit number two is located relatively 31 meters north of the pit number one, covering an area of two by three meters. The test pit is situated at the eastern edge of the mound, near the pit number one, covering an area 2 by 2 meters. From the excavation, archaeological evidence relating to probably iron metallurgy, include smelting slags, tuyère, smelting furnace walls, potsherds, baked sediment, iron artifacts, shells, animal bones and human remains. The chronological study of the archaeometallurgical evidence associated with Ban Saitho 7 by the same project as mentioned in Khok Kroy, yielded relative dates of agate beads, which give a range of older ages from 2,000 years BP at the earliest to 1,800 years BP at the latest (LARP, 2010).

1943

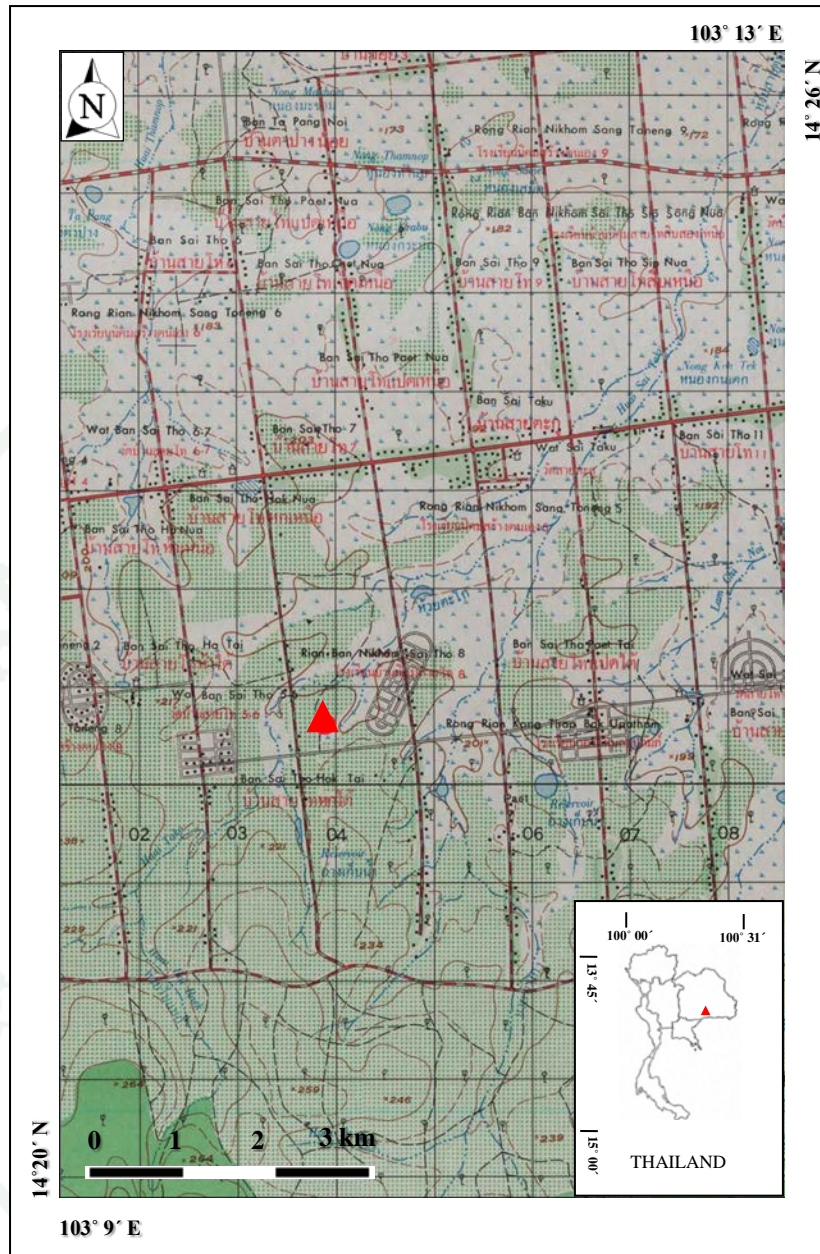


**Figure 4** Topographic map of Ban Saitho 7 archaeological site, Tambon Chanthop Phet, Amphoe Ban Kruat, Buri Ram Province (red triangle: study area).

**Source:** Royal Thai Survey Department (n.d.)

#### 2.4 Ban Khao Din Tai Archaeological site

Ban Khao Din Tai archaeological site is one of the ancient rural sites in the region of Buriram Province, northeast Thailand. It is located at 14°44' N latitude and 103°08' E longitude, situated near small stream which is called Huai Ta Sek, approximately 10 km north of the Thai-Cambodian border. The site was originally surveyed by the Fine Arts Department in 1987, the project found numerous slag heaps on the surface of the mound. *In* 1989 to 1992, a joint project entitled “An archaeological study of the iron-smelting and salt-making industries in the northeast of Thailand” was repeatedly surveyed at the site by Prof. Eiji Nitta and his colleagues. Until 2005, a team of Living Angkor Road Project was repeatedly surveyed. Though a previous archaeological survey before 2007 confirmed the metallurgical evidence in the vicinity of present Ban Ban Khao Din Tai, there was no excavation ever conducted to research intensively on metallurgy in this area. While the excavation was undertaken in 2007, by the team of Living Angkor Road Project as mentioned above. This excavation was divided into two pits that is, the first pit on the center of the mound and the second on the west slope of mound. From the excavation, archaeological evidence relating to probably iron metallurgy, include smelting slags, tuyère, smelting furnace fragments, potsherds, baked sediment and charcoal (Yoopom, 2010). The scientific dates of pieces of ceramics (found on site) dated to 13<sup>rd</sup> century AD or around 800 years BP (Venunan, 2011).

1943

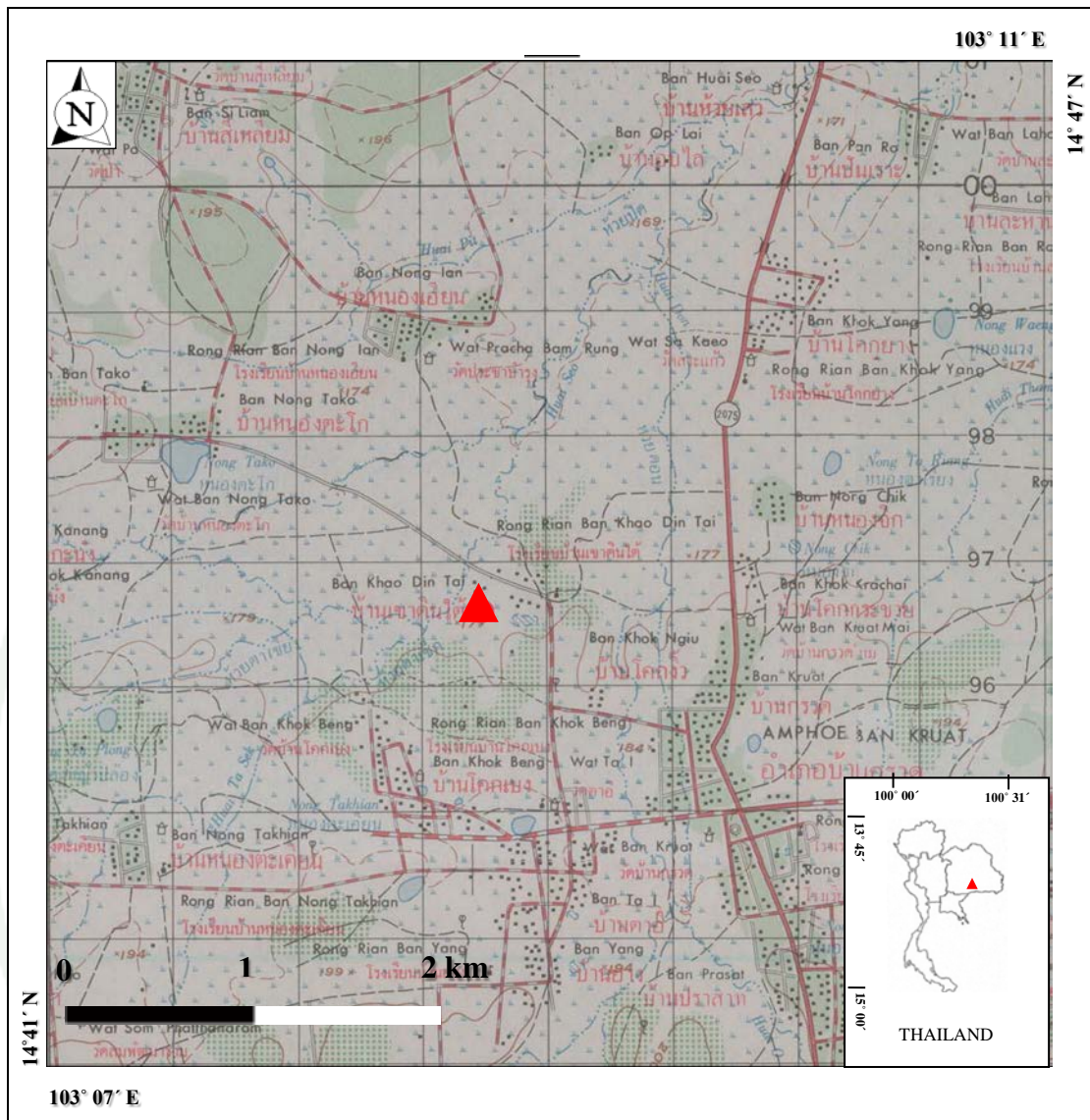


**Figure 5** Topographic map of Ban Khao Din Tai archaeological site, Tambon Ban Kruat, Amphoe Ban Kruat, Buri Ram Province. (red triangle: study area).

**Source:** Royal Thai Survey Department (n.d.)

### **3. Geoarchaeological and Archaeometrical Techniques.**

Geoarchaeology is critical to understanding the archaeological record and the human past. Indeed, the earth science played a pivotal role in interpreting evidence of the human past in terms of both concepts and techniques. The antecedents for using an earth science approach in evaluating the archaeological record lie in the history of the disciplines, beginning with the concern in the eighteenth and nineteenth centuries for an appreciation of prehistoric time and the development of basic principles, moving into the twentieth century with the collaboration between natural scientists and archaeologists, and arriving at the present with the convergence of the two disciplines in a number of areas. Throughout the history of this interaction, ideas and methods originating with the earth sciences have been used to study the processes involved in the formation of the sedimentary archaeological record, to infer the palaeoenvironmental settings associated with archaeological sites, etc.

The term geoarchaeology has been used with increasing frequency since the 1970s to designate a variety of types of research that use geosciences techniques in the evaluation of the archaeological record. The labeling of research as an aspect or a subsidiary of geoarchaeology depends in part on whether the term is used to designate a narrower, more focused set of concepts and methods or a broader, more inclusive set. There are many viewpoints concerning what can appropriately be called geoarchaeology. Konigsson (1992) describes geoarchaeology as a study in which the geologist tries to determine the cultural development of an area; geologists are not in direct collaboration with archaeologists and rely exclusively on geologic materials and methods. Ferring (1995) is definition of geoarchaeology emphasizes the changes in archaeological perspective since the advent of Lewis Binford's New Archaeology. As practiced, Ferring sees geoarchaeology as a grossly empirical approach to archaeological problems. In perhaps its broadest sense and the way the term is used in this study geoarchaeology refer to the application of any earth science concept, technique or knowledge base to the study of artifacts and the processes involved in the creation of the archaeological record. When viewed from the broad definition, geoarchaeology would include many aspects of environmental archaeology, physical geography, geocology, especially in archaeometry. Broader connections between the

earth sciences and archaeology such as dating techniques, provenance of artifacts, site location, and the like have been assigned by some practitioners to the realm of archaeometry. In the broader geoarchaeological approach that the author advocated, such aspects of archaeometry as dating, provenance, and site location become part of geoarchaeology when they represent the application of earth science methods to archaeological problems (Rapp and Hill, 2006).

Archaeometrical techniques are the application of scientific techniques and procedures to the analysis of archaeological works. It is a collaboration of archaeology between sciences such as, physics, chemistry, biology, biochemistry, material science, mathematics, and so on. This technique observes and identifies artifacts in terms of dating, artifact studies, man and his environment, mathematical methods, and conservation concerns. The term Archaeometry has been in common use since 1958, when the first volume of the journal *Archaeometry* was published by the Research Laboratory for Archaeology at Oxford. The contents of this journal were and have remained technical expositions of physical and chemical methods applicable to dating and materials identification in archaeology. Other periodicals publishing substantial contributions to archaeometry include the *Journal of Archaeological Science* since 1974 and *Revue d' Archéométrie* since 1977. A broader array of relevant techniques and applications has been presented in the Brothwell and Higgs compendium *Science in Archaeology* in 1970, first edition 1963 and by Brill in 1971. Despite some overlap with Geoarchaeological research but the input of physical and chemical methodologies to archaeology continues to be distinctive. These efforts are labeled as Archaeometry (Butzer, 1982).

At present, there are several researches using Geoarchaeological and Archaeometrical Techniques to investigate archaeological evidence from several archaeological sites. In order to gain more information about the ancient technology, that is,

Hunt (1950) had established aerial photography as an archaeological tool for the unstudied area of Northeast Thailand. He identified the abundant irregular earthwork site of the Mae Nam Mun Valley as important prehistoric archaeological

site. He noted potentially significant site structural regularity and geographic patterning worthy of subsequent archaeological study. Significant though this contribution was, perhaps William-Hunt's most important contribution lay in what may have been a subconscious comment. Having carefully described the site as earthworks sites, towards the close his paper he refer to ramparts and, importantly, moats; the site have become known as moated site, with all the implications that such a structure embodies.

Publication of the research by Boyd (2004), with paper being published under a series title "The geoarchaeology of the prehistoric ditched sites of the Upper Mae Nam Mun valley, Thailand". Commencing with a detailed regional mapping programme, largely based on aerial photograph interpretation, Boyd constructed palaeogeographical model for the study area, demonstrating, in particular, that the fluvial conditions of the floodplain have changed in the past, and that the archaeological sites are intimately and geographically associated with a former river system. This model thus provided a basis for hypotheses regarding the role of environmental, and possibly climatic, change in the history of the Iron Age presence. In particular, the model identified a close relationship between the channel surrounding the sites, and the former fluvial system.

Dillmann and Balasubramaniam (2001) analyzed an ancient 1,600 year old Indian iron by using microprobe techniques (EDS,  $\mu$ XRD and  $\mu$ PIXE), in order to obtain compositional and structural information. Several different local locations in the iron matrix and in the entrapped slag inclusions were analyzed. The P content of the metallic iron matrix was very heterogeneous. Lower P contents were observed in the regions near slag inclusions. This was correlated to the de-phosphorization capacity of the slag. The crystallized phases identified in the slag inclusions were wüstite and fayalite and the compositions of the slag inclusions were relatively homogeneous.

Gimeno-Adelantado *et al.* (2003) analyzed different types of materials used in iron production in the Iberian Period (6<sup>th</sup> - 2<sup>nd</sup> century BC). The materials were recovered in several archaeological digs (which makes it possible to date the

archaeological remains) on different sites in the Levante area of the Iberian Peninsula. The samples selected for this study belong to different materials used in the ancient iron production process such as ores, slags, finished objects, etc. The use of scanning electron microscopy (SEM) is proposed to observe surface images of the samples to determine their morphological, microstructural and topographic characteristics to obtain valuable information on the materials studied. The study also proposes chemical analysis of the elements in the sample by X-ray microanalysis (SEM-EDS) which provides both qualitative and quantitative information. The archaeometric study suggests that the iron obtained was very good quality, but the process was not economically efficient when viewed from today's perspective. Furthermore, the slag produced in the furnace can be related with the slag or impurities contained in the iron. It has also been possible to relate the ores and slag, some furnace conditions, the use of fluxes and also to differentiate types of slag.

Haustein *et al.* (2003) dated seven archaeometallurgical slags from different sites in central Europe and the Mediterranean. The TL measurements were carried out on these samples. They founded that, in most cases, the TL ages determined show good agreement with reference data.

Godfrey-Smith and Casey (2003) present luminescence dates which demonstrate a full-blown smelting technology in Northern Ghana, West Africa, during the Early Iron Age. Their chronology is based on thermoluminescence (TL) dating of quartz grains extracted from the walls of three iron smelters located at the Birimi site in the Northern Region of Ghana. Two of the smelters yielded statistically indistinguishable ages of  $1080 \pm 70$  and  $1090 \pm 60$  years, while the third yielded a higher age of  $1600 \pm 100$  years. All are significantly older than the sole direct radiocarbon date of  $550 \pm 330$  cal BP ( $460 \pm 90$  BP) obtained on a furnace in the Northern Region. The TL ages indicate that iron smelting was well established in the Northern Region before the middle of the first millennium AD, and corroborate the validity of a number of similarly early radiocarbon dates associated with Early Iron Age ceramics but not directly associated with smelting activity, from other sites in northern Ghana.

Pryce (2008) analyzed the mineral, technical ceramic and slag from Non Pa Wai and Nil Kham Haeng, Lopburi Province, Thailand by using reflected-light microscopy, scanning electron microscopy with energy dispersive x-ray fluorescence spectrometry (SEM-EDS) and polarizing energy dispersive x-ray fluorescence spectrometry ([P]ED-XRF). The results indicate a long term improvement in the technical proficiency of Valley metalworkers, accompanied by an increase in the human effort of copper production. This shift in local metallurgical ethos is interpreted as a response to rising regional demand for copper in late prehistory.

Chiarantini *et al.* (2009) studied copper production at Baratti (Populonia, southern Tuscany). Slag samples were analyzed by optical microscopy, x-ray powder diffraction and wavelength dispersive x-ray fluorescence spectrometry. In addition, charcoal fragments that founded associated with the slag samples were dated by radiocarbon date. They concluded that charcoal fragments dated to the 9<sup>th</sup> - 8<sup>th</sup> centuries BC. While the overall features of copper slags indicate a single-step smelting process of copper-rich ores containing variable amounts of Zn and Pb. Chemical and textural features of copper slags indicate an optimized, high-efficiency metallurgical process.

Ettler *et al.* (2009) studied the mineralogy of primary phases of historical and recent slags from smelters in the Tsumeb district (Namibia) by using x-ray diffraction analysis (XRD), scanning electron microscopy (SEM) and electron microprobe (EPMA) techniques. They concluded that the 100-year old slags (slag I) are mainly composed of Pb-bearing feldspars, Cu-rich spinels, delafossite-like phases and complex Ca-Pb arsenates. In contrast, 30-40 year old and recent granulated slags (slags II and III) are mainly composed of high-temperature phases: Ca-Fe aluminosilicates (olivines, melilite), Pb- and Zn-bearing silicate glass, spinel oxides and small metallic/sulphide inclusions trapped within the silicate glass. The differences in the mineralogical composition of the slags are related to the initial composition and the cooling regime of the melt. The slag I melts were probably low in alkalis, Ca and Si and strongly enriched in Cu, Pb and as and were cooled very slowly. In addition, the presence of Cu<sup>1+</sup>- bearing phases (delafossite CuFeO<sub>2</sub> and mcconnelite CuCrO<sub>2</sub>) in these slags indicates highly variable redox conditions in the historical shaft

furnaces. Furthermore, the Ca-Pb arsenates found in the matrix indicate that these slags have undergone an alteration process in the dumping environments. In contrast, more recent granulated slags (II and III) were cooled very rapidly (presence of silicate glass) and the slag melt was poorer in Cu and enriched in alkalis, Ca and Zn.

Muralha *et al.* (2010) studied the iron slag from Northern Zimbabwe by using Raman microscopy (RM) and electron beam analysis (EBA). They concluded that the phases identified in a slag found at an iron making site not only reflect the chemical composition of the slag but can also provide crucial information regarding the reconstruction and interpretation of the metallurgical operations, such as the prevailing redox conditions in a furnace at the time of cooling. Free iron oxides, such as haematite, magnetite and wüstite, are important indicators of these redox conditions. However, while classical techniques of phase identification can be used to identify the different iron oxides, they cannot distinguish between dissimilar oxidation states due to their non-stoichiometric nature, and also the effect of substituting elements in iron oxides. RM proved invaluable in both respects. By combining the results provided by RM and EBA, it was possible to identify (1) the free iron oxides, haematite and magnetite in the original ore, and magnetite and wüstite in the slag, (2) oxidised magnetite and wüstite, characterized by a shift to higher wavenumbers of their intense characteristic Raman bands and (3) Al<sup>3+</sup>-substituted magnetite and a solid solution between magnetite and hercynite (FeAl<sub>2</sub>O<sub>4</sub>). This pilot study aims to develop a model that enables close identification of the redox conditions by analyzing the free iron oxides from a variety of smelting processes. It is hoped that this will provide an independent and quantifiable criterion to distinguish smithing slags (more oxidizing) from smelting slags (more reducing), and to understand better the actual smelting process that transforms highly oxidized iron ore to fully reduced iron metal.

Bani-Hani *et al.* (2012) studied the slag lumps and iron artifacts collecting from the archaeological site of Barsinia, Northern Jordan. For the analytical and metallurgical study, x-ray diffraction was used to identify the mineralogical composition of samples. Inductively coupled plasma-optical emission spectrometer, energy dispersive x-ray and x-ray fluorescence spectrometer were used to determine the accurate elemental composition of these finds. Furthermore examinations by using

metallographic, polarizing microscope and scanning electron microscopy were employed to diagnose the characteristic morphology and environmental effects of these archaeometallurgical finds. Microstructural investigations emphasized that iron production processes were performed locally at the archaeological site of Barsinia even if the iron ores were imported from other mining location in Jordan. Direct or bloomery was the main method used for smelting iron ores followed by smithing methods to locally produce iron artifacts. This, most probably, was the state of technology from the Bronze Age to the Byzantine period.

In this study, Geoarchaeological and Archaeometrical techniques were used to enlighten specific questions from Archaeometallurgical works—the study of metallurgical production in the past. Archaeometallurgical evidence namely, copper and iron slags, smelting furnaces, potsherds and baked sediments that found accompany with these archaeometallurgical evidence, were analyzed by Geoarchaeological and Archaeometrical techniques as shown in appendices B to G.

## MATERIALS AND METHODS

### Materials

#### 1. Raw materials

- Aerial photographs
- Slag samples
- Smelting furnace fragment, potsherds and baked sediment samples

#### 2. Equipments

- Rubber hammer
- Petri dish
- Plastic pipe
- Permanent pen
- Sample holder
- Cover slide
- Mould
- Epoxy and hardener
- Tungsten carbide grits
- Aluminum oxide pastes
- A black bag
- Aluminium foil
- Iron mortar and pestle
- Sieve
- Beaker
- Magnet

### 3. Reagents

- Hydrochloric Acid 35%
- Hydrofluoric acid 24%

### 4. Instruments

- Edwards CC-40F carbon coater
- Mirror stereoscope
- JEOL JSM-5900 microscope with Oxford energy dispersive X-ray spectroscopy
- Seiko SEA-2010 energy dispersive X-ray fluorescence spectrometer
- Press machine
- Zepper electric balance
- Binder FP 53 laboratory drying oven
- Electric agate pestle and mortar
- Slab saw
- Rigaku miniflex 2 X-ray diffractometer
- Transsonic 460/H ultrasonic bath
- Struers RotoPol-35 grinding-polishing machine
- Struers DP U4 polishing machine
- Olympus BX-41 microscope with Nikon digital camera.
- Gamma-ray spectrometer

## Methods

The methods of the study are divided into five steps namely, planning and preparation of a significant data, aerial photograph interpretation, laboratory analysis, analyses of the results and discussion and finally conclusion. A flowchart depicting the general procedure for this study is shown in figure 6. This chapter introduces Geoarchaeological and Archaeometrical techniques employed in three iron production sites: Khok Kroi, Ban Khao Din Tai, and Ban Saitho 7 and a bronze/copper production site: Non Nong Hor. Geomorphological feature of each study area was interpreted by aerial photograph interpretation. Archaeometallurgical evidence and their associated finds from each investigation site namely, metal slag, smelting furnace fragment, potsherds and baked sediment samples were collected for evaluation. Slag samples were evaluated by bulk chemical analysis (energy dispersive x-ray fluorescence spectrometry), micro-structural analysis (reflected-light microscopy and scanning electron microscopy), phase composition analysis (x-ray diffraction, scanning electron microscopy with energy dispersive x-ray spectrometry). Only the combined results of bulk chemical, micro-structural and phase composition analysis will give the necessary background for the evaluation and reconstruction of ancient metallurgical processes. Otherwise, the other archaeometallurgical evidence and their associated finds, namely smelting furnace fragment, potsherds and baked sediment samples were evaluated by absolute dating (thermoluminescence dating), to obtain the information about the age of smelting activities of each site. Each analytical technique employed has a sequential discussion of its purpose, preparation, and measurement as shown in the next section.

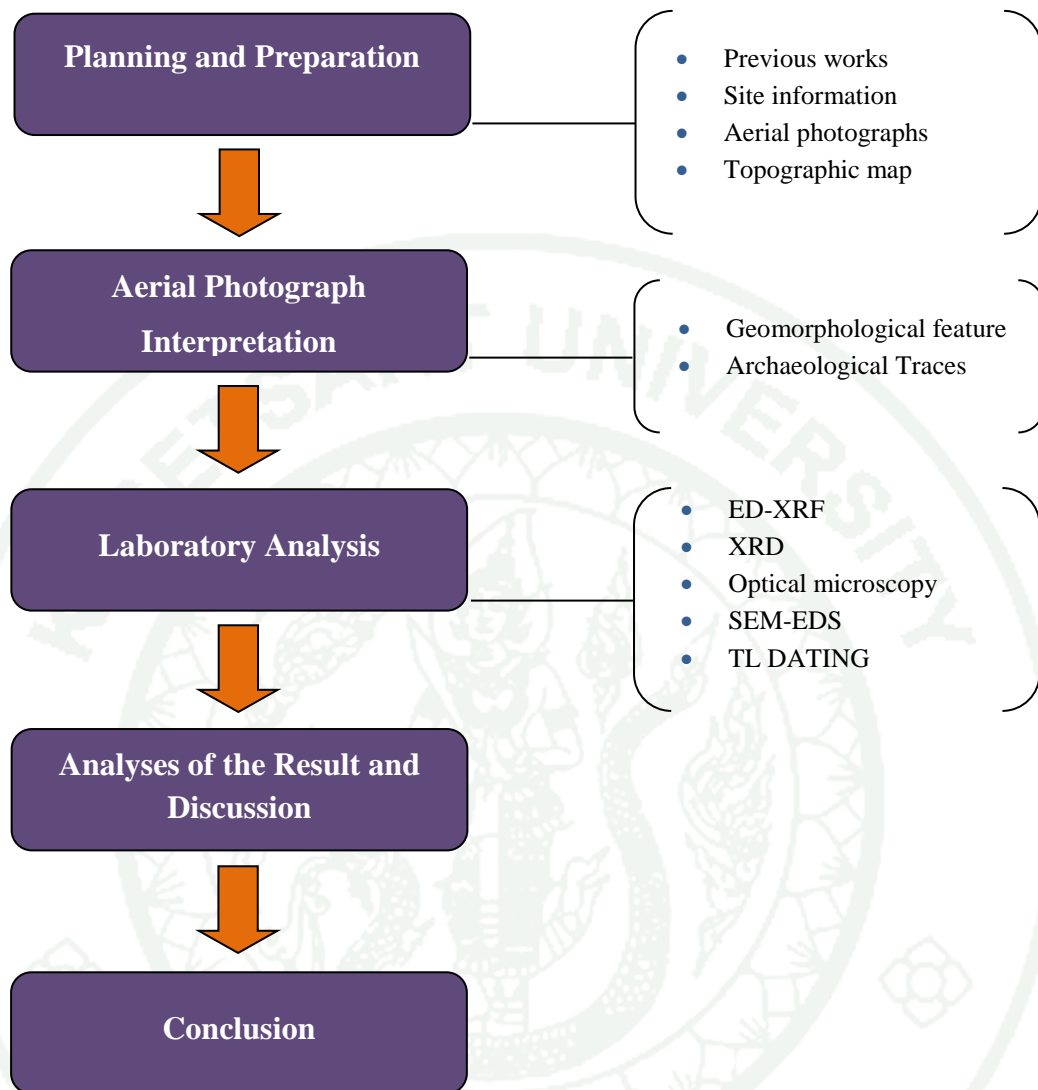


**Figure 6** Simplified flowchart illustrating investigation procedures for the study.

## **1. Aerial photograph interpretation**

In archaeology, geomorphological principles and analysis are helpful in site interpretation because only ground level analysis may not be clearly to view entire site, its archaeological traces, and especially recognize geomorphological features that resulted from geologic processes (e.g. landform, etc.). Aerial photographs are often the first choice of imagery datasets available to help interpret their characteristics. Success in interpretation of aerial photograph is related to experience. It is as simple as that. Successful interpreters have spent a lot of time with photos and, in particular, a lot of time on the ground correlating the imagery to the actual ground conditions.

### **1.1 Measurement**

In this study, all aerial photographs are examined and any archaeological traces and landforms are identified. The author used a Sokkia MS-27 Mirror Stereoscope to do this. Pairs of photographs are taken with an overlap in which a point on the ground is visible on both images, each taken a small distance apart. When the pair of photographs is looked at stereoscopically, a three-dimensional image can be seen and interpreted.

## **2. Energy dispersive x-ray fluorescence spectroscopy (ED-XRF)**

The second step in this study of slag is bulk chemical analysis. After slag has been tentatively interpreted and allocated to various parts of a production process according to its external appearance, its bulk composition is the first tool to confirm or deny these interpretations. Identical looking pieces of slag may have very different chemical compositions, possibly indicating different origins or processes. For example, the difference between copper and iron smelting slag can often only be determined by measuring its minute copper content. Other chemical elements, or ratios between elements, can help determining the nature of the production process. The ratio between iron and lime, for example, can indicate whether a slag derives from a bloomery or a blast furnace, or may indicate the accidental or intentional use of fluxes (Veldhuijzen, 2003).

## 2.1 Sample preparation

The first stage of ED-XRF preparation was to removing all weathered or previously exposed surfaces of slag sample. The sample was washed, first under a running tap water to remove heavy dirt, and drying with a laboratory drying oven. Thereafter, the sample was then crushed by rubber hammer, into a small size of 1-2 mm. For ED-XRF analysis of pressed pellets it is necessary to have a maximum grain size of around 50  $\mu\text{m}$  to minimize the effects of x-ray diffraction and refraction by the crystalline matrix of the material. The sample powders were pulverized to 50 $\mu\text{m}$  in an electric agate pestle and mortar. The analytical powders were decanted into petri-dish and placed in the laboratory drying oven to eliminate any moisture that would prevent the pellets from forming correctly.

The dried powder sample was weighed in a fine balance, to give a total of 8-10 gram of thoroughly powder. This dried powder sample was placed into a plastic pipe (1 inch in diameter) before forming into a pellet using a press machine applying 15 Torr of pressure for 30 seconds. Pellets were labelled, and stored in a low-moisture environment to prevent rehydration until they were used.

## 2.2 Measurement

For this study, the XRF measurements are carried out on a Seiko SEA-2010 energy dispersive x-ray fluorescence spectrometer (SiLi detector / LN<sub>2</sub>; 50KV; 3 mm beam; Rel. Std. Dev. 0.13% Au 1-sigma; FP calibration / one standard). It offers some minor elements and trace elements which are below the detecting limitation of SEM-EDS.

## 3. Reflected light microscopy

The third step of archaeometallurgical analysis is optical microscopy by using reflected light microscopy which is used in order to determine the sample's crystalline phases, color, homogeneity, porosity, and inclusions of interest, in explaining the formation and composition of the sample. Micro-structural study is used to explain chemical groupings in terms of phases present: e.g. slags generally contain a large amount of iron oxide, but bulk analyses were unable to tell us whether this iron was

chemically bonded to silica in the slag (e.g.  $\text{Fe}_2\text{SiO}_4$ ), or was present in its original mineral form, or has precipitated from the slag as primary iron oxides, or even as secondary oxidation, although this should have been cut away during preparation. Phase analysis can also provide information on the physicochemical (e.g. furnace temperature and redox atmosphere) conditions that were present when the material was formed, and thus aid the technological reconstruction of the process (Pryce, 2008).

### 3.1 Sample preparation

The preparation of the specimen is most important. Although in the past few decades, there has been increasing automation of the grinding, polishing and finishing of the sample, there still is considerable skill and experience needed in selecting the procedures that are best suited for particular sample types. Polished sections are very convenient because they can be used for both reflected light microscopy and scanning electron microscopy with energy dispersive x-ray fluorescence analysis. More details of polished section preparation are present below.

#### 3.1.1 Cutting and moulding

After removing all weathered or previously exposed surfaces, of metal slag sample. Each sample was cut to a size of around  $1 \text{ cm}^2$  that would fit comfortably in the 25 mm diameter resin moulds (put two or three samples per mould). Resin was prepared by carefully mixing epoxy and hardener in a ratio of around 3:1, although this depends on the volume and porosity of the material being mounted. Once poured into the moulds, the resin cured at room temperature for 24 hours.

#### 3.1.2 Grinding and Polishing

The analytical surface was then cleansed of any excess resin by grinding with 200, 320, 800, and 1,000 tungsten carbide grits, respectively. Then, the sample was cleaned in an ultrasonic bath. Thereafter, the sample was polished with 3 and  $1 \mu\text{m}$  aluminum oxide paste, respectively. The purpose of polishing the sample is to remove the final deformation induced by the grinding process and yield a surface

that is essentially damage-free. Due to this is the last procedure in the preparation sequence, any deformation still remaining at the specimen surface will be visible when the specimen is observed with the microscope. Finally, the sample was cleaned in an ultrasonic bath again and dried with a laboratory drying oven, and then kept in a low-moisture environment to avoid oxidation.

### 3.2 Measurement

For this study, samples were examined at magnifications between 4, 10, 40 and 100 times in Olympus BX41 microscope with 6V-30 watt power supply, Kohler Illumination light paths for transmitted light path. Phase identifications were achieved with standard mineralogy textbooks, but with an understanding of the anthropogenic phases produced rapidly at high temperatures during metallurgical processes.

## 4. X-ray diffraction (XRD)

X-ray diffraction analysis can tell us the identity and distribution of minerals in metal slags. Minerals present in metal slags are often good indicators of gas atmosphere in furnace, cooling rate of slag and homogeneity of slag. If there is un-decomposed charge trapped in slag, more information about ore and flux can be learnt.

### 4.1 Sample preparation

XRD analysis was performed on the same samples as were studied by ED-XRF analysis. The only difference was not forming the powder sample into a pellet. On the other hand, the powder sample was mounted in the sample holder.

### 4.2 Measurement

Crystalline phase was identified by powder x-ray diffraction. The XRD experiments were performed on a Bruker D8-advance diffractometer. The x-ray source is a 2.2 kW Cu-anode long fine focus ceramic X-ray tube. The running conditions for the x-ray tube are 40 kV and 40 mA, the power supply controls these with a stability of better than 0.01% for the high voltage and 10% of the variation of

the supply for the current. X-ray powder diffraction patterns were recorded in the range between 10 and 70 degree.

## **5. Scanning electron microscopy with energy dispersive x-ray spectroscopy (SEM-EDS)**

The SEM-EDS was principally applied to this study for multiple purposes, namely the identification of phases, the chemical compositional spot analysis of each phase. The significant efficiency, which is allows the mentioned tasks to be achieved is that SEM-EDS is a qualitatively and quantitatively chemical analyzer and the analyst can control a sharp focused beam to analyze very specific area or spot inside a sample in contrast to XRF which provides only the chemical composition of the whole sample. Thus, it benefits in terms of providing an identification or confirmation of phases or inclusions using a spot analysis together with a back scattered electron imaging. An area analysis can provide a bulk chemical composition in which it is very good for the complicated sample, especially ones with many areas or phases.

### 5.1 Sample preparation

SEM-EDS analysis was performed on the same samples as were studied by reflected light microscopy (see below). The only difference was the addition of a layer of carbon, applied by a sputter coater. This carbon layer touches the metal skeleton of the SEM and allows the analytical surface to conduct electrons whilst being analyzed, and grounds the sample so it does not become charged.

### 5.2 Measurement

Morphology and elemental compositions of all slag samples were determined by JEOL JSM-5900 microscope with Oxford energy dispersive x-ray fluorescence spectroscopy, with Probe current up to  $\mu\text{A}$ , optimized resolution  $\sim 5$  nm, vacuum  $\sim 1$  Pa, beam energy up to 30 keV.

## 6. Thermoluminescence dating

TL dating is a tool frequently used for age determination of Quaternary materials such as archaeological evidence, volcanic deposits and a variety of sediments from different environmental settings. In this study, TL dating was adopted for smelting furnace fragment, potsherds and baked sediment samples instead of metal slag samples. Whereas, direct dating of slag through thermoluminescence dating could not be a good method because of the complex composition of slag always affect the quality of TL measurement. This method is useful for the sample containing the quartz once burned in high temperature (about 800-1200 °C) as furnaces, potsherds and baked sediment. In this section, gives details of procedures from sampling to age calculation.

### 6.1 Sample collection

During collected the smelting furnace fragment, potsherds and baked sediment samples, a black cloth must use to shield the samples from light because the samples were collected during the daylight hour. Thereafter, wrapped it in aluminium foil, a black bag and tape tightly to prevent water content and protect the samples from light. The weight of each sample must be 350 grams, at least. TL laboratory procedure in this research is mainly followed Takashima and Honda (1989) and the main objective of procedure is purification of quartz mineral. Upon arrival in the laboratory, all samples were dried by 40-50 °C for 24 hours, except for the samples for water content calculation because it necessary to dried by 105 °C for 24 hours.

### 6.2 Water content calculation

Water content was also measured for all samples being dated because it is the one significant parameter for annual dose determination. The equation for calculating percent water content is present below.

$$W = \frac{W_w \times 100}{W_d} \quad (1)$$

Where:  $W$  is percent water content

$W_w$  is weight of water

$W_d$  is weight of dry matter

### 6.3 Palaeodose evaluation

#### 6.3.1 Chemical treatment

After getting dried from the previous process, sample was crushed and sieved. Samples which grain size 74-250  $\mu\text{m}$  were collected for palaeodose evaluation. Samples were washing by distilled water ten times or more for removing some organic materials and clay particles. Treated with 35% HCl for 1 Hour and washed several times with distilled water. Thereafter, etching samples in 24% HF for 15-30 minutes and re-washed it several times with distilled water. Samples were re-treated with 35% HCl for 30 minutes again. Finally, re-washed it several times with distilled water and dried by 40-50  $^{\circ}\text{C}$ . Finally, remain iron minerals were removed by using a magnet. All procedures were performed in dim red light.

#### 6.3.2 Sample preparation for palaeodose measurement

In this study, palaeodose was obtained by the regeneration method (Takashima and Honda, 1989). All except the natural aliquots were zeroed by heating 320  $^{\circ}\text{C}$  for 5 hours and then given artificial gamma-ray irradiation by using  $^{60}\text{Co}$  source. After irradiation, the unstable signals must be reduced by heating 130  $^{\circ}\text{C}$  for 24 hours.

#### 6.3.3 Palaeodose measurement

The emission of TL signals (glow curve) were measured by using TL instruments which consisting C1230 photon counter (Hamamatsu Photonics), KP 1,000 temperature controller (Chino Co.), blue and red filter in  $\text{N}_2$  condition. The palaeodose by regeneration method was obtained from the resulting of growth curves, in other words a direct comparison was made of the natural TL with the TL resulting from artificial irradiation.

#### 6.4 Annual dose evaluation

After getting dried, crushed, and sieved. Samples which grain size < 841  $\mu\text{m}$  were collected for 290 g, for annual dose evaluation by using gamma-ray spectrometer. The annual dose is calculated from the concentrations of Uranium, Thorium, Potassium, and Cosmic ray by the method of Bell (1979) and Aitken (1985), as shown below.

$$\begin{aligned}
 AD &= D_{\alpha} + D_{\beta} + D_{\gamma} + D_c \\
 &= (0.15(2.783U + 0.783Th) / (1+1.50(W/100))) + \\
 &\quad ((0.1148BU + 0.0514BTh + 0.2492BK) / (1+1.14(W/100))) + \\
 &\quad ((0.1462U + 0.0286Th + 0.8303K)K / (1+1.25(W/100))) + \\
 &\quad 0.15
 \end{aligned} \tag{2}$$

Where: AD is Annual dose (mGy/year)

$D_{\alpha}$  is alpha radiation dose

$D_{\beta}$  is beta radiation dose

$D_{\gamma}$  is gamma radiation dose

$D_c$  is cosmic radiation dose

$U$  is concentration of uranium in ppm

$Th$  is concentration of thorium in ppm

$K$  is concentration of potassium oxide in percent

$B$  is beta coefficient in quartz grains

$W$  is water content in percent

#### 6.5 TL age and error calculations

TL is a function of the absorbed radiation dose. Hence, TL dating is mainly to measure two parameters as shown in section 6.3 and 6.4: the palaeodose (PD) and the annual dose (AD). PD is the accumulated natural irradiation absorbed dose of minerals from ancient time to present day. AD is the irradiation absorbed dose by minerals in one year. The TL age is equal to the palaeodose divided by the annual dose. In this way, can obtain the date or the age of the smelting furnace fragment and potsherds samples by equation as follow,

$$\text{TL age} = \frac{\text{PD}}{\text{AD}} \quad (3)$$

Whilst TL age error result derives mainly from sample preparation and TL measuring apparatus, as well as standard deviation (SD) from measured values of ratio  $H+\gamma / N$  on growth curve. So equation for dating errors is described as

$$\text{TL age error} = \text{Absolute} [(SD_{\text{PD}}^2) + (SD_{\text{AD}}^2)] \times \text{age} \quad (4)$$

Where:  $SD_{\text{PD}} = \text{Absolute} \left[ \frac{(\bar{X} - \bar{X})^2}{N} \right]$

$$SD_{\text{AD}} = 5 \%$$

## RESULTS AND DISCUSSION

### Results

This chapter presents the Geoarchaeological and Archaeometrical analyzes and interpretation of metallurgical activities at Non Nong Hor, Khok Kroy, Ban Saitho 7 and Ban Khao Din Tai Archaeological Site. According to the methodology detailed in the previous chapter, aerial photographs were prepared for geomorphological interpretation, the samples of slag were prepared for bulk chemical compositional, microstructural and phase composition analysis. The samples of furnace fragment, potsherds and baked sediment were prepared for age determination. All sample catalogues, the principle of each instruments and complete analytical data are presented in appendices A to G.

#### 1. Non Nong Hor Archaeological Site

##### 1.1 Aerial photograph interpretation

Aerial photographs of Non Nong Hor archaeological site in 1991 (roll 94-112, run 09, image number 105-106 by Department of Lands, figure 7), were interpreted using a Sokkia MS-27 Mirror Stereoscope. Geomorphologically, the area can be divided into three-main landforms (figure 8), namely flood plain, terrace and hill with a dendritic stream networks—an extensively branched or tree-like pattern which have an orientation from north-south (the main streams), northeast-southwest and northwest-southeast. Flood plains are observed along major streams that have gentle slopes. This landform is the most distinctive class on the photographs because the streams are, more or less, parallel to the margins on both sides. The width of the flood plains ranges from about 500 m to several km. Terraces are observed between hills and flood plains and commonly founded at the southern part of the site. In some cases, terraces can-

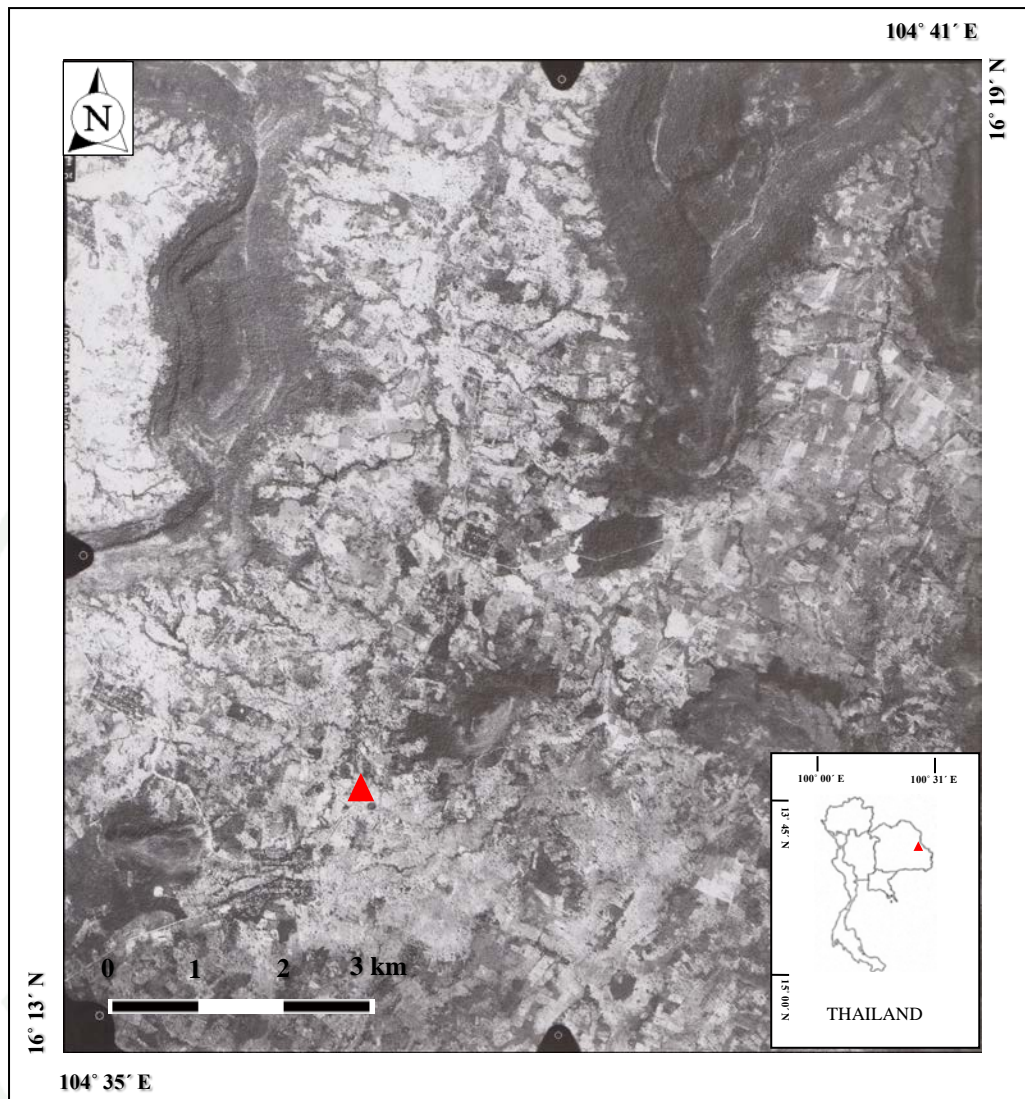


**Figure 7** Aerial photograph of Non Nong Hor archaeological site, Tambon Na Udom, Amphoe Nikhom Kham Soi, Mukdahan Province (red triangle: study area).

**Source:** Department of Lands (1991)

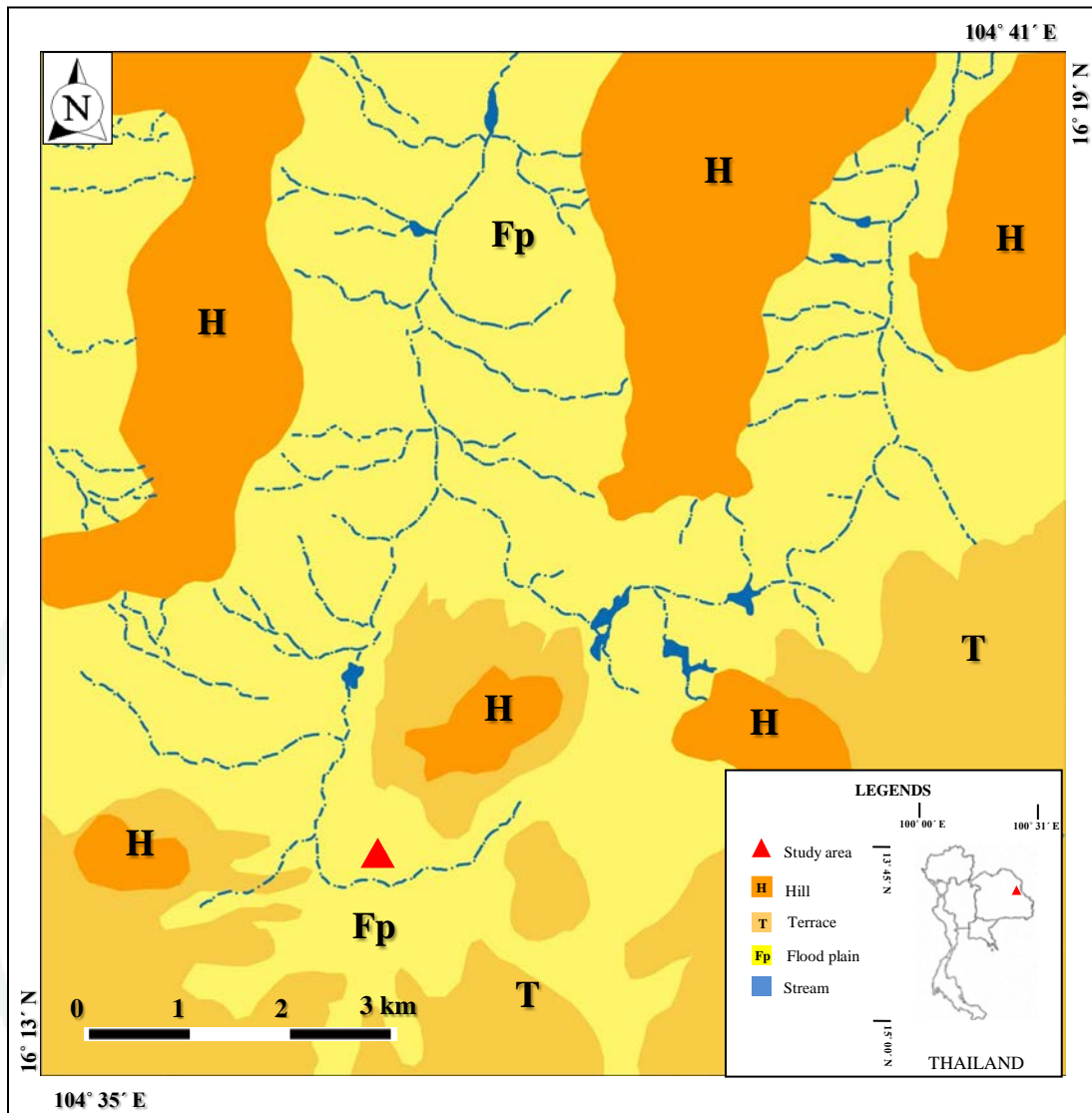


**Figure 8** Interpreted morphological landforms of Non Nong Hor archaeological site, Tambon Na Udom, Amphoe Nikhom Kham Soi, Mukdahan Province.

be observed between two streams without hill (at the southeast part). The hills are mostly situated at the northern part of the site. They are easily identified on the aerial photographs because of their distinct summit. Elevation of the hill ranges between about 240 to 490 m above mean sea level.

## 1.2 Bulk chemical compositional and Microscopic analysis

Macroscopically, five slag samples (A0572, A0573, A0574, A0577 and A0581, see appendix A) seem to have been broken unintentionally into small pieces of a size from 4 to 4.5 cm (figure 9 A). Their total weight is about 20 to 35 g. The samples are roughly plano-convex in shape, like they were formed in a mould of some sort. On the surfaces of sample A0572, a distinct green spot are visible (figure 9 B), which provide a first hint about the presence of copper. In sectioned, all five samples are relatively homogeneous with a low proportion of pores (figure 9 C), which vary substantially in size. Inclusions of sand or quartz are also visible (figure 9 D). No charcoals are observed.

The bulk chemical compositions of the slag samples are reported in table 1. All samples analyzed were dominated by relatively high iron oxides (71.00-92.85%), as typical for slag, as well as oxides of Cu (2.020-6.567%) and Si (0.637-21.72%) with trace amounts (< 3 wt.%) of Mn, Ca, K, Zn (except sample A0572), Cr (in sample A0577), Zr (in sample A0572), Ba (in sample A0574) and Pb (in sample A0574). Potentially more interesting, they showed traces of SO<sub>3</sub> in sample A0572 and A0573.

Microscopically, the mineralogy of the samples obtained by x-ray diffraction, optical microscope and scanning electron microscope analyses is given in table 2 and appendix d and e. The samples contain fayalite, magnetite, quartz, metallic phase with relatively rare copper sulphide phase in a glassy matrix. Fayalite (Fe<sub>2</sub>SiO<sub>4</sub>)—the iron-rich end-member of the olivine solid solution series—is a major phase in all samples,-

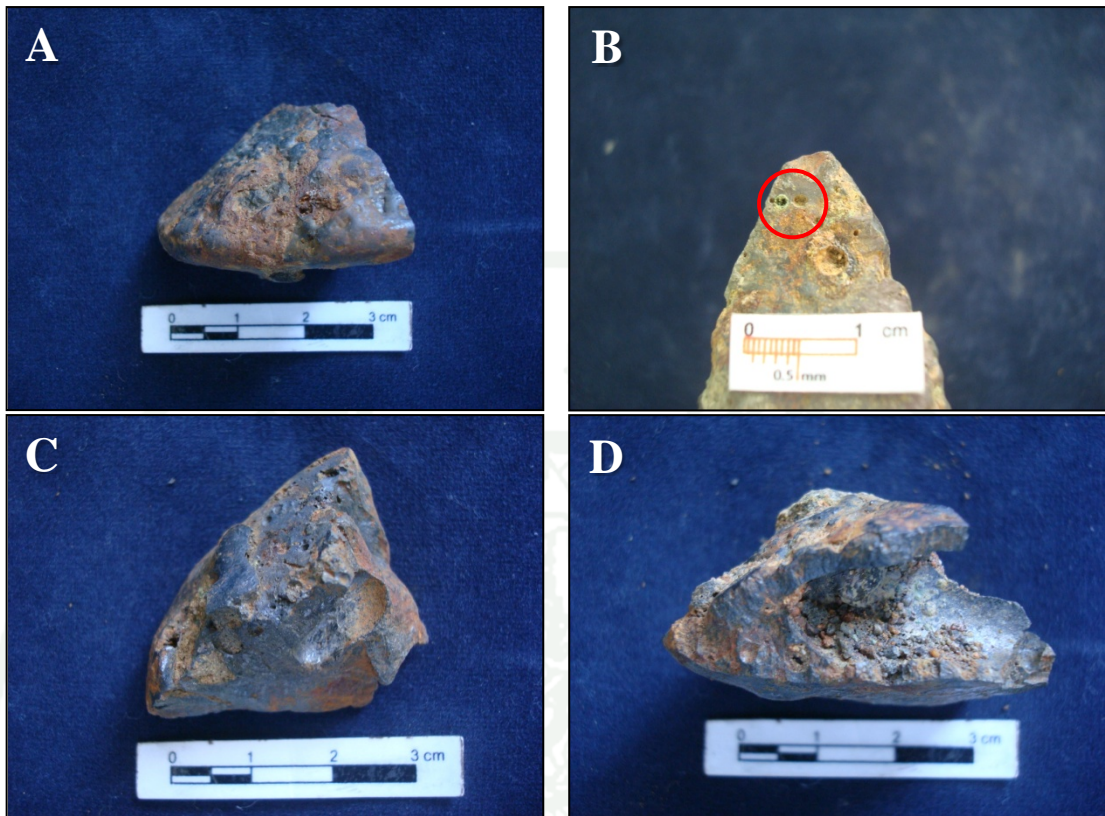


**Figure 9** (A) Macroscopic of sample A0573 (B) green spots (marked with a red circle) on the surface of sample A0572 (C) Sectioned of sample A0573, showing homogeneous texture with a small amounts of pores (D) Sand inclusions inside sample A0574.

1943

**Table 1** Bulk chemical composition (in wt%) of slag samples from Non Nong Hor archaeological site (determined by ED-XRF method).

| LAB ID | SO <sub>3</sub> | SiO <sub>2</sub> | K <sub>2</sub> O | CaO   | Cr <sub>2</sub> O <sub>3</sub> | MnO   | FeO   | CuO   | ZnO   | ZrO <sub>2</sub> | BaO   | PbO   |
|--------|-----------------|------------------|------------------|-------|--------------------------------|-------|-------|-------|-------|------------------|-------|-------|
| A0572  | 0.069           | 0.908            | 0.306            | 0.279 | -                              | 1.269 | 81.43 | 6.567 | -     | 0.103            | -     | -     |
| A0573  | 0.309           | 21.72            | 0.445            | 0.030 | -                              | 0.95  | 63.88 | 3.312 | 2.239 | -                | -     | -     |
| A0574  | -               | 0.679            | 0.429            | 0.028 | -                              | 1.242 | 75.10 | 4.429 | 0.673 | -                | 8.210 | 0.789 |
| A0577  | -               | 0.637            | 0.271            | 0.927 | 0.113                          | 2.937 | 83.54 | 2.020 | 0.247 | -                | -     | -     |
| A0581  | -               | 0.918            | 0.350            | 0.090 | -                              | 1.187 | 82.73 | 4.949 | 0.504 | -                | -     | -     |
| Mean   | n/a             | 4.972            | 0.360            | 0.271 | n/a                            | 1.517 | 77.33 | 4.255 | 0.733 | n/a              | n/a   | n/a   |

Symbols used: -, not detected; n/a, not available

**Table 2** Phase compositions of slag samples from Non Nong Hor archaeological site obtained by XRD analysis (%wt), optical microscope and scanning electron microscope.

| LAB ID.   |                 |                                  | A0572 | A0573 | A0574 | A0577 | A0581 |
|-----------|-----------------|----------------------------------|-------|-------|-------|-------|-------|
| Group     | Name            | Ideal/range composition          |       |       |       |       |       |
| Silicates | Fayalite        | Fe <sub>2</sub> SiO <sub>4</sub> | 75.02 | 89.89 | 72.97 | 91.93 | 92.03 |
|           | Quartz low      | SiO <sub>2</sub>                 | -     | 4.440 | 20.01 | -     | 1.270 |
| Oxides    | Magnetite       | Fe <sub>3</sub> O <sub>4</sub>   | 24.98 | 5.660 | 7.020 | 8.070 | 6.700 |
| Metal     | Pure metal      | Cu                               | *     | *     | *     | *     | *     |
|           | Intermetallic   | Cu, Fe                           | *     | *     | -     | -     | -     |
| Glass     |                 |                                  | *     | *     | *     | *     | *     |
| Others    | Copper sulphide | CuS                              | *     | -     | *     | *     | -     |

Symbols used: -, not detected; \*, detected by optical microscope and scanning electron microscope

their compositions (by EDS spot analyses, see appendix f) contain O (54.62-56.16 wt.%), Fe (22.48-28.94 wt.%) and Si (16.44-17.30 wt.%) with minor amounts of Mg (1.49-1.65 wt.%) and Mn (2.48 wt.%). Regarding the shapes of the fayalites, they show a skeletal lath crystals (figure 10).

Magnetite ( $\text{Fe}_3\text{O}_4$ ) is commonly intergrown with fayalites. Its shape varies from fine-dendritic or euhedral crystals (figure 10). In addition, abundant metallic prills with range in diameter between a few  $\mu\text{m}$  to 80  $\mu\text{m}$ , maximum 200  $\mu\text{m}$  (figure 10 A, B, C) identified are composed almost of pure copper with low iron impurities (less than 7.5 wt% by SEM/EDS analyses, see appendix f). Copper sulphide phase rarely embedded within other minerals in sample A0572, A0574 and A0587 with range in diameter between a few  $\mu\text{m}$  up to 50  $\mu\text{m}$  (figure 10 B). Residual quartz (rarely present) is usually anhedral and found as unmelted or as partially melted inclusions (figure 10 C). Glassy matrix rarely occurs primarily as interstitial pools between crystals of fayalite. The glass appears opaque in plain and polarized light, despite its transparency, so it is best viewed in reflected light.

According to recently summarized by Chiarantini *et.al.* (2008), the chemical compositions of ancient copper smelting slags, in Baratti, Southern Tuscany, are composed by iron oxide, silica and calcia. They can therefore be plotted in ternary phase equilibrium diagrams, which typically show slag compositions and allows them to estimate the operating temperatures in the past. The Non Nong Hor slag samples, also does themselves for this type of model. When plotted in the  $\text{FeO-SiO}_2\text{-CaO}$  ternary diagrams, all samples fall into two different regions (figure 11): the olivine region (sample A0573) which indicating operating temperature of about 1,200 °C; the wüstite region (A0572, A0574, A0577 and A0581) which indicating higher operating temperature of about 1,360-1,369 °C.

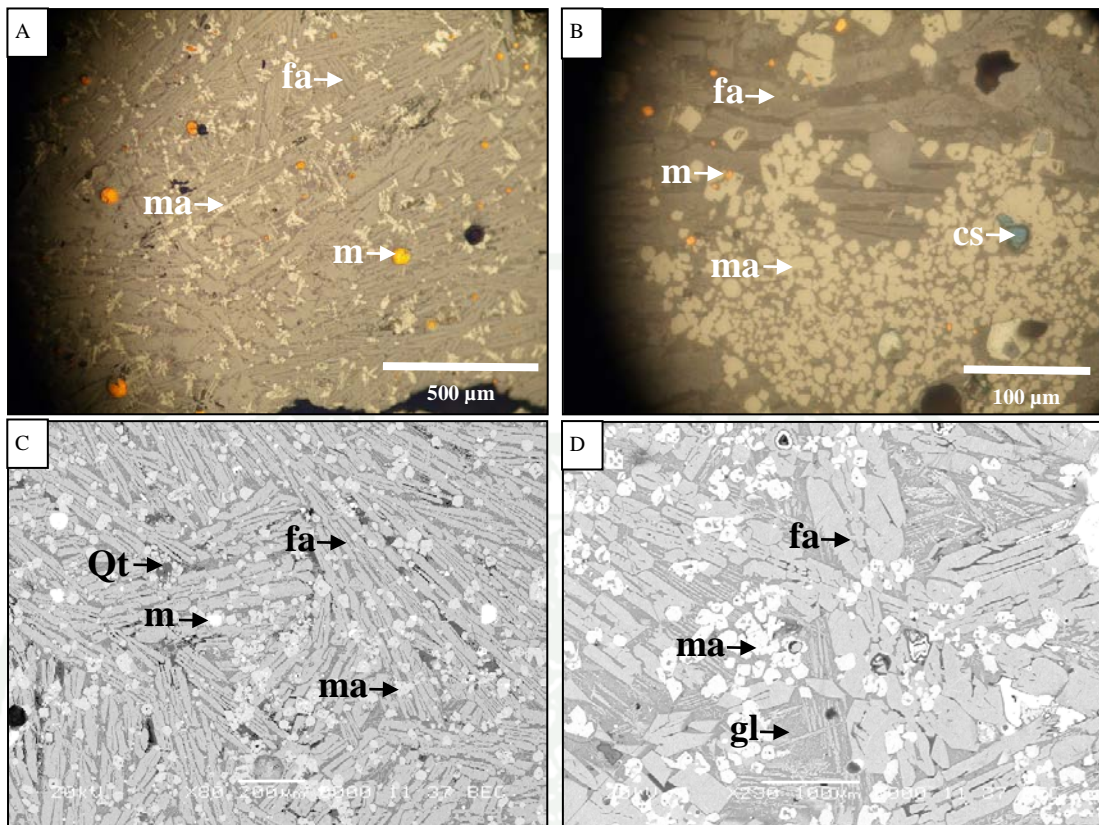


**Figure 10** Reflected light microscope image (A) Sample A0581, showing skeletal fayalite laths, fine-dendritic magnetite crystals with bright spots of copper prill (B) Copper sulphide among the clusters of magnetites, euhedral magnetites crystals, copper prills and skeletal fayalite laths of sample A0572; Scanning electron microscope image (C) Sample A0574, showing skeletal fayalite laths, euhedral magnetites crystals with quartz inclusions (D) Euhedral magnetite crystals with skeletal fayalite laths in glassy matrix of sample A0581; fa-fayalite, ma-magnetite, Qt-quartz, m-metal (copper), cs-copper sulphide, gl-glassy matrix.

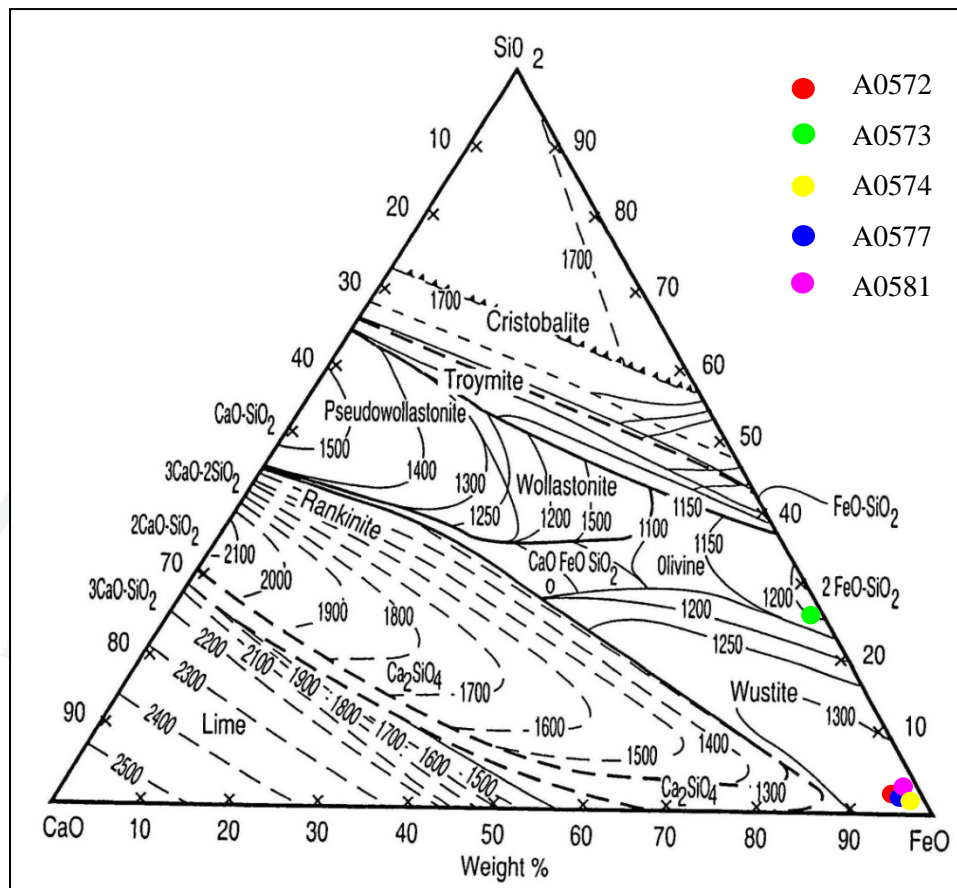


**Figure 11** FeO-CaO-SiO<sub>2</sub> ternary diagrams presenting the distribution of studied slags of Non Nong Hor archaeological site.

**Source:** Chiarantini *et al.* (2008)

1943

### 1.3 Age determination

Due to direct dating of slag through thermoluminescence dating could not be an appropriated technique as mentioned in the previous chapter. Therefore, five furnace fragment samples (A0548, A0549, A0550, A0551 and A0552) which found associated with the copper slag samples were taken to obtain the age of copper activity in Non Nong Hor archaeological site. The results of TL assessment are summarized in table 3. The uncertainties were calculated taking into account both the statistical errors and the uncertainty in the laboratory calibration. Thermoluminescence ages of five samples fall within a wide range from  $1,005\pm 80$  to  $1,439\pm 115$  years before present (BP). TL ages were converted to calendar ages of the 6<sup>th</sup> to 10<sup>th</sup> century AD.

**Table 3** The results of elemental content (U,Th, K<sub>2</sub>O), annual dose, palaeodose and TL age with error of five furnace fragment samples from Non Nong Hor archaeological site.

| LAB ID. | K <sub>2</sub> O (%) | U (ppm) | Th (ppm) | W.C. (%) | AD (mGy/a) | PD (Gy) | TL age (a) | Century (A.D.) |
|---------|----------------------|---------|----------|----------|------------|---------|------------|----------------|
| A0548   | 1.892                | 3.769   | 16.64    | 10.71    | 3.955      | 5.692   | 1,439±115  | 6              |
| A0549   | 4.642                | 6.022   | 21.28    | -        | 7.298      | 7.335   | 1,005±80   | 10             |
| A0550   | 2.588                | 5.256   | 17.17    | 9.524    | 4.978      | 6.063   | 1,218±97   | 8              |
| A0551   | 4.350                | 8.200   | 25.15    | -        | 7.863      | 9.940   | 1,264±100  | 8              |
| A0552   | 1.296                | 6.288   | 13.10    | -        | 3.778      | 4.723   | 1,250±100  | 8              |

Symbols used: -, not detected; %, weight in percent; ppm, weight in part per million; mGy/a, milligray per annual; a, annual; A.D., anno domini

## 2. Khok Kroy Archaeological Site

### 2.1 Aerial photograph interpretation

Aerial photographs of Khok Kroy Archaeological Site in 1988 (roll 302-327, run 11, image number 309-310 by Department of Lands, see figure 12), were interpreted using a Sokkia MS-27 Mirror Stereoscope. Geomorphologically, the area can be divided into three landforms (figure 13), namely flood plain, high-terrace and low-terrace with a dendritic stream network which have an orientation from north-south (the main streams), northeast-southwest and northwest-southeast. Flood plains are observed along major streams. Some can be observed between high-terrace and low-terrace, and high-terrace and high-terrace without streams (usually founded at the southern part). The width of the flood plains ranges from about a few m. to several km. Low-terraces in this site are abundant and also founded all over the site. They are observed between high-terrace and flood plains and high-terrace and high-terrace. In some cases, low-terraces can be observed between flood plain and flood plain. High-terraces are also situated all over the site by several characteristic features.

### 2.2 Bulk chemical compositional and Microscopic analysis

Macroscopically, five slag samples (A0586, A0588, A0590, A0594 and A0595, see appendix A) were categorized into two groups, according to their general morphology. Firstly, the four slag samples (A0588, A0590, A0594 and A0595) are lumpy in shape (figure 14 A) with range in diameter from 5 to 12 cm. When sectioned, the colors of the samples mostly range from dark gray to black. The macroscopic luster of four samples is variable and ranges from vitreous to dull, textures include glassy and vesicular. The samples are extremely porous and the voids have irregular shapes with a diameter from a fraction of mm to few mm.

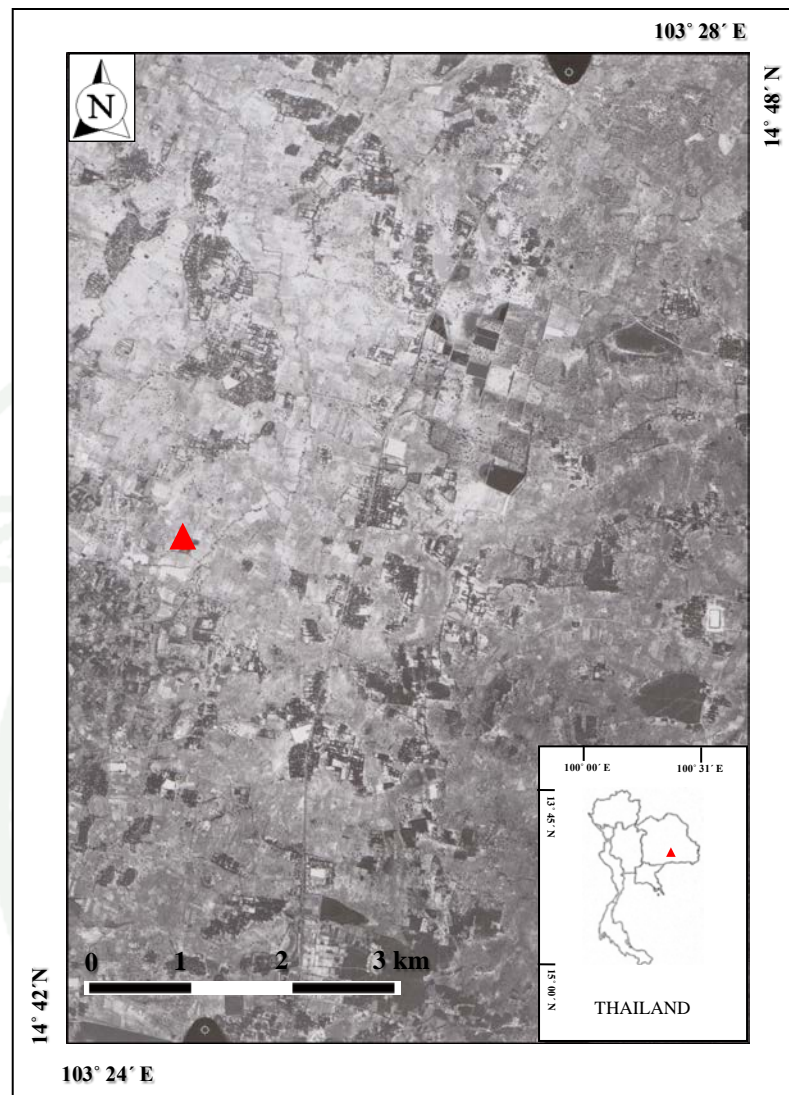


**Figure 12** Aerial photograph of Khok Kroy archaeological site, Tambon Na Bua, Amphoe Mueang Surin, Surin Province (red triangle: study area).

**Source:** Department of Lands (1988)

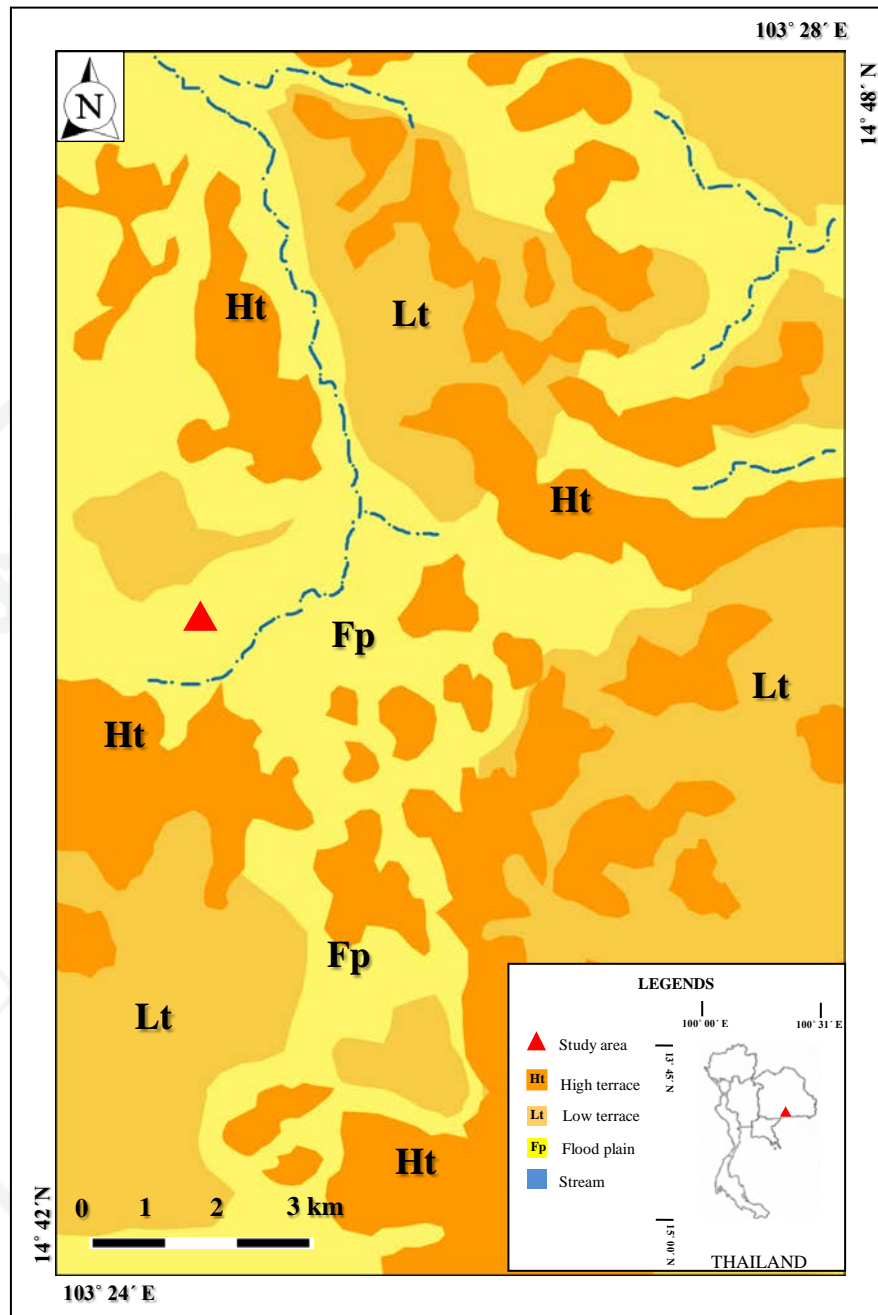


**Figure 13** Interpreted morphological landforms of Khok Kroy archaeological site, Tambon Na Bua, Amphoe Mueang Surin, Surin Province.

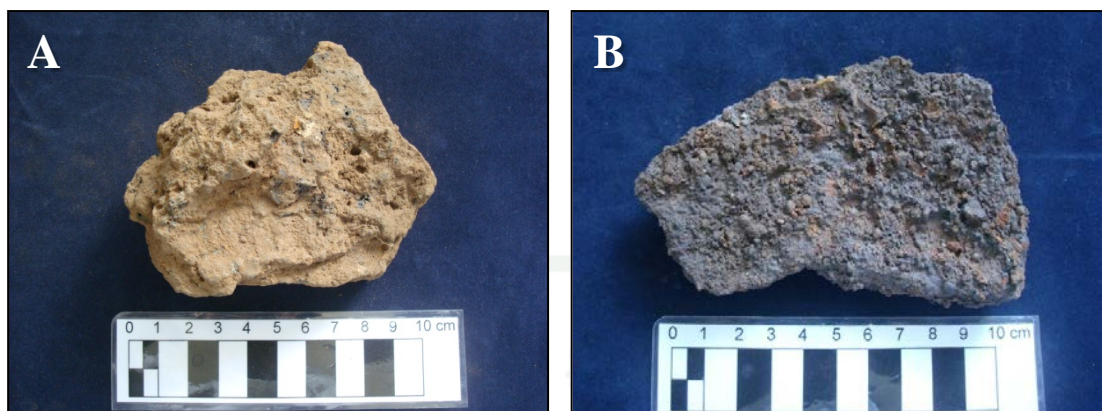


**Figure 14** (A) Macroscopic of lumpy shape of sample A0595 (B) Macroscopic of flattened shape of sample A0586.

Secondly, the slag (A0586) has a flattened shape (figure 14 B) with minor amounts of porosity. The size of the sample is about 9x13 cm with the thickness ranges from approximately 1 to 2 cm. There was not a piece of slag displaying flow structures. However, no smithing features, such as a plano-convex shape or hammer scales in the slag fabric, were also observed.

The bulk chemical compositions of slag samples are given in table 4. All samples analyzed were dominated by FeO (50.47-85.60 wt.%) and other oxides of Si (0.807-27.82 wt.%), Al (11.21-12.28 wt.% in sample A0588 and A0590), Mn (1.130-6.581 wt.%), Ti (1.402-2.544 wt.%) with < 2wt.% of Ca, Cr, Zr, K (in sample A0586, A0588 and A0594), V (in sample A0586, A0588, A0590 and A0595), Sr (in sample A0586, A0590 and A0595) and Ba (in sample A0586, A0588 and A0594). In addition, there are differences between some of the compound levels that is, Alumina and silica oxide levels appear to be dominant in sample A0588 and A0590, whereas other samples have relatively low/ or invisible contents.

**Table 4** Bulk chemical composition (in wt%) of slags from Khok Kroy archaeological site (determined by ED-XRF method).

| LAB ID | Al <sub>2</sub> O <sub>3</sub> | SiO <sub>2</sub> | K <sub>2</sub> O | CaO   | TiO <sub>2</sub> | V <sub>2</sub> O <sub>5</sub> | Cr <sub>2</sub> O <sub>3</sub> | MnO   | FeO   | SrO   | ZrO <sub>2</sub> | BaO   |
|--------|--------------------------------|------------------|------------------|-------|------------------|-------------------------------|--------------------------------|-------|-------|-------|------------------|-------|
| A0586  | -.                             | 1.826            | 0.092            | 0.921 | 2.544            | 0.088                         | 0.158                          | 4.456 | 80.16 | 0.078 | 0.281            | 0.469 |
| A0588  | 12.28                          | 26.27            | 0.174            | 0.131 | 2.234            | 0.086                         | 0.160                          | 2.349 | 50.52 | -.    | 0.077            | 0.103 |
| A0590  | 11.21                          | 27.82            | -.               | 1.098 | 2.073            | 0.275                         | 0.211                          | 1.130 | 50.47 | 0.021 | 0.064            | -     |
| A0594  | -                              | 1.229            | 0.279            | 0.235 | 2.457            | -                             | 0.265                          | 6.581 | 78.78 | -     | 0.202            | 1.195 |
| A0595  | -                              | 0.807            | -                | 0.817 | 1.402            | 0.163                         | 0.116                          | 1.392 | 85.60 | 0.064 | 0.104            | -     |
| Mean   | n/a                            | 11.59            | n/a              | 0.640 | 2.142            | n/a                           | 0.182                          | 3.182 | 69.11 | n/a   | 0.146            | n/a   |

Symbols used: -, not detected; n/a, not available

**Table 5** Phases in Khok Kroy slag samples obtained by XRD analysis (%wt), optical microscope and scanning electron microscope.

| LAB ID.   |               | A0586                            | A0588 | A0590 | A0594 | A0595 |       |
|-----------|---------------|----------------------------------|-------|-------|-------|-------|-------|
| Group     | Name          | Ideal/range composition          |       |       |       |       |       |
| Silicates | Fayalite      | Fe <sub>2</sub> SiO <sub>4</sub> | -     | 55.62 | 46.76 | 49.69 | 73.10 |
|           | Quartz        | SiO <sub>2</sub>                 | -     | -     | -     | 7.480 | -     |
|           | Quartz low    | SiO <sub>2</sub>                 | 57.95 | 10.40 | 35.98 | 11.27 | 15.95 |
|           | Cristobalite  | SiO <sub>2</sub>                 | 17.38 | -     | -     | -     | -     |
| Oxides    | Hercynite     | FeAl <sub>2</sub> O <sub>4</sub> | 14.29 | 33.98 | 17.27 | 31.56 | 10.95 |
|           | Magnetite     | Fe <sub>3</sub> O <sub>4</sub>   | 10.38 | -     | -     | -     | -     |
|           | Iron oxide    | FeO                              | *     | *     | *     | *     | *     |
| Metal     | Pure metal    | Fe                               | *     | *     | *     | *     | *     |
|           | Intermetallic | Fe, Ni                           | -     | -     | -     | *     | -     |
| Glass     |               |                                  | *     | *     | *     | *     | *     |

Symbols used: -, not detected; \*, detected by optical microscope and scanning electron microscope

Microscopically, the peculiar chemical composition of the slag is reflected in the microstructures, the mineralogy of the samples obtained by x-ray diffraction, optical microscope and scanning electron microscope analyses is given in table 5, and appendix d and e. All samples consist of various phases including fayalite, hercynite, iron oxide, quartz, cristobalite and metallic phase in a glassy matrix. Fayalites are the major phase in all samples (figure 15 B, C, D), they were founded as skeletal lath as poor crystallized crystals. EDS spot analyses (see appendix f) confirmed that the crystals can be identified as fayalite because their compositions are O (52.83-56.69 wt.%), Fe (17.79-28.36 wt.%) and Si (16.68-18.16 wt.%) with minor amounts of Al (4.310 wt.%) in sample A0594, Mn (3.050 and 3.330 wt.%) in sample A0588 Ni (3.05-3.33 wt.%) in sample A0588 and A0594 and A0594 and Br (0.940 wt.%) in sample A0595.

Hercynite is spare, forms of the crystals varies from euhedral to coarse-dendrite and often founded interpenetrate with fayalite crystals in all samples (figure 15 C, D). It might be indicated that, they formed prior to/or at the same time as the fayalites. The identification has confirmed by EDS spot analyses (see appendix f), the compositions of hercynite are O (51.10-54.82 wt.%), Al (27.95-31.58 wt.%) and Fe (13.74-15.95 wt.%) with less than 2.5 wt.% of Mg in sample A0594, Si in sample A0586 and sample A0595, Ti in sample A0588, A0590 and A0594, V in sample A0586, A0590, A0594 and A0595 and Cr in sample A0588 and A0594. Iron oxide phase also contain in the samples (except sample A0586) but only a few contain which is not enough to detect by XRD (Detection limit is dependent on each instrument). They have fine-dendritic crystals, rarely crystallized out of glasses interstitial to the fayalite crystals.

Metallic iron occurs as prill to irregular in shape, up to around 50  $\mu\text{m}$  in diameter, most are only a few  $\mu\text{m}$  in diameter, interspersed in all of the samples (figure 15 C, D). By EDS spot analyses (see appendix f), the composition of all metal is Fe (100 wt.%), Only sample A0594 contains a mixture of Fe (98.05 wt.%) and Ni (1.950 wt.%) in a grain 50  $\mu\text{m}$  in diameter. Quartz is rarely present as microscopic to microscopic anhedral fractured grains of unmelted or partially melted inclusions in sample A0586, A0590 and A0595 (figure 15 A, B). Cristobalite was identified by

XRD in only sample A0586. Glass occurs primarily as interstitial pools between crystals of fayalite and iron oxide, displaying crypto-crystallinity in the form of feathery dendrites at high magnifications.

According to recently summarized by Rehren *et al.* (2007), the chemical compositions of the vast majority of bloomery iron smelting slags, in Africa and elsewhere, are dominated by iron oxide, silica and alumina. They can therefore be plotted in ternary phase equilibrium diagrams, which typically show slag compositions clustering around the two eutectic or optima, i.e. those areas where the slag composition approaches the lowest possible melting temperature, facilitating the metal-slag separation. Although there is room for human choice and cultural variation, the system is largely driven by the thermo-chemical behavior of these three compounds. This allows researchers to compare smelting slags from different sites, and also to plot the compositions of ores, technical ceramics and fluxes to model their behavior and relative contributions to the slag formation, as well as the operating temperatures. The Khok Kroy, Ban Saitho 7 and Ban Khao Din Tai slag samples, also do themselves for this type of model.

When plotted in the FeO-SiO<sub>2</sub>-Al<sub>2</sub>O<sub>3</sub> ternary diagrams to estimate the operating temperature as mentioned previously, all samples fall into two different regions, indicated that they were from the operation of different smelting system (figure 16): the hercynite region (sample A0588 and A0590), indicating operating temperature of about 1,180-1,220 °C; the wüstite region, the iron rich corner of the system (A0586, A0594 and A0595) which indicating higher operating temperature of about 1,350-1,369 °C.

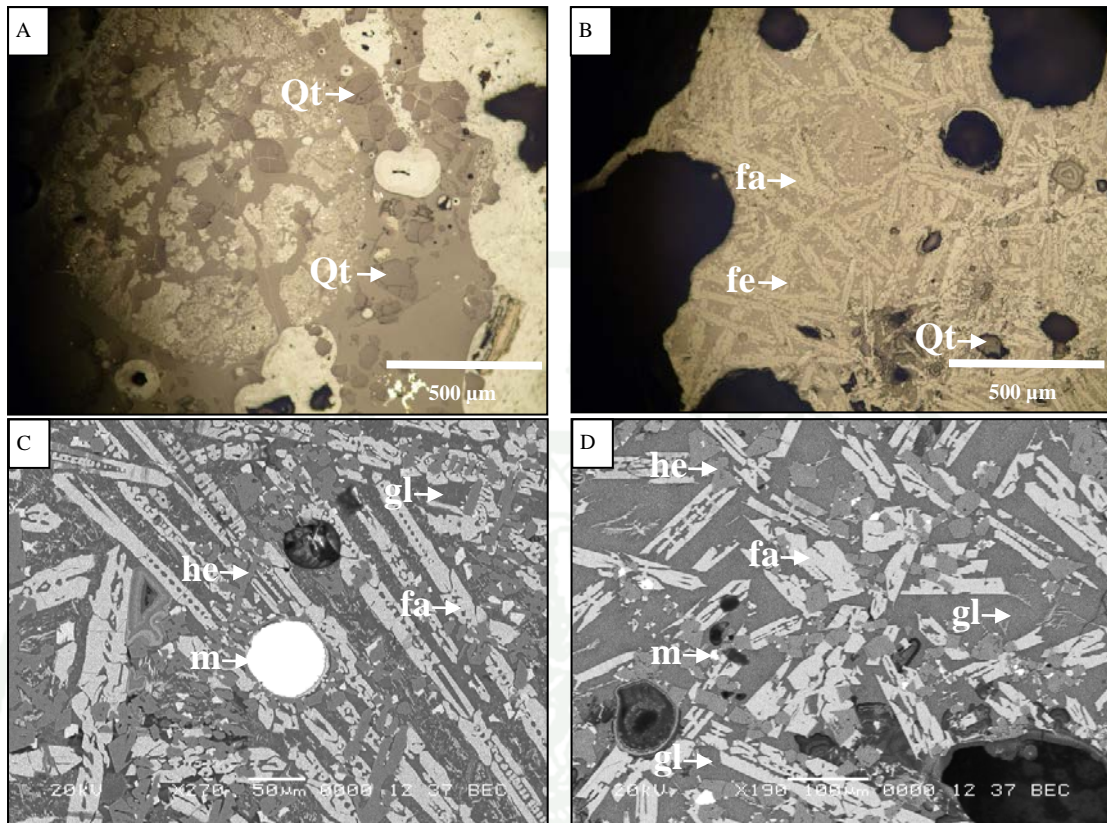


**Figure 15** Reflected light microscope image (A) Image of sample A0586, showing residual quartz inclusions (B) Image of sample A0595, showing skeletal fayalite laths and residual quartz inclusions in a glassy matrix.; Scanning electron microscope image (C) Skeletal fayalite laths, coarse-dendritic hercynite with bright large spots of iron prill in the glassy matrix of sample A0588 (D) Euhedral hercynite with skeletal fayalite laths with bright small spots of iron prill in glassy matrix of sample A0590; fa-fayalite, he-hercynite, Qt-Quartz, m-metal, Fe- iron oxide, gl-glassy matrix.

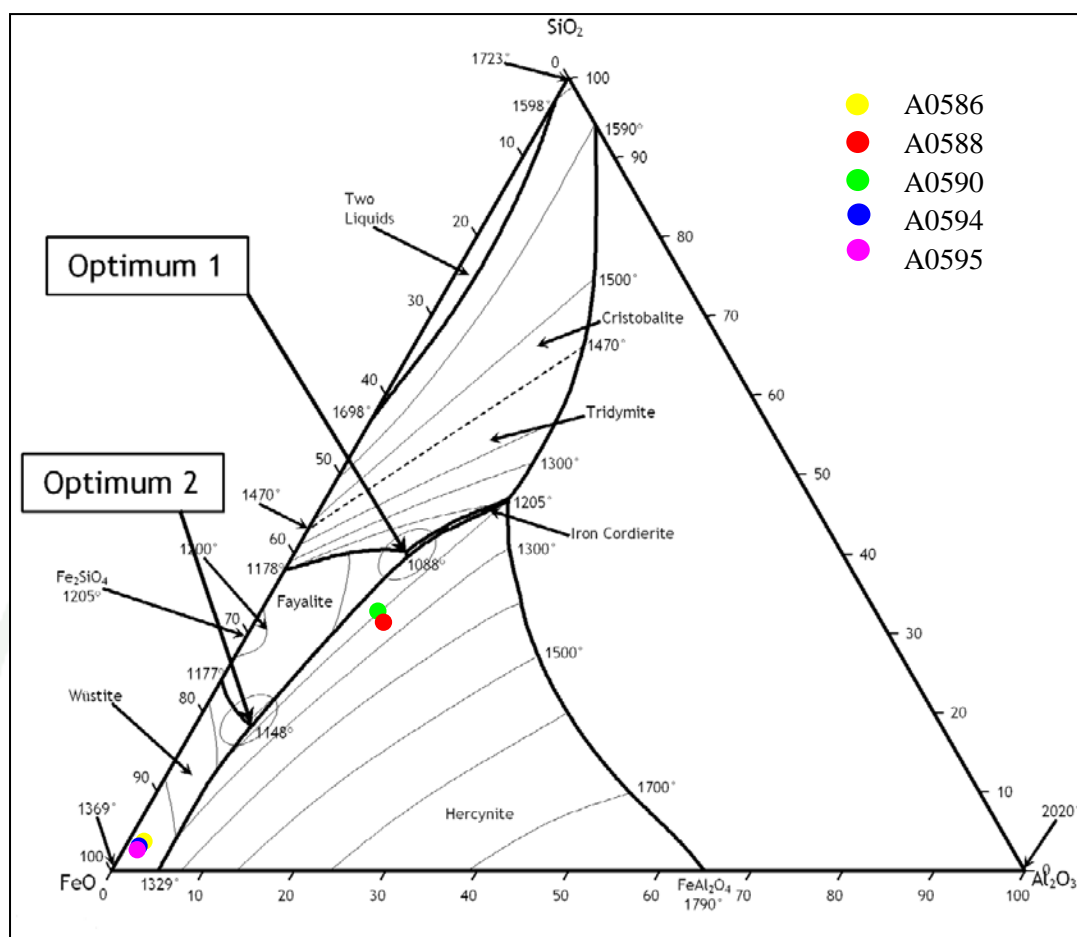


**Figure 16** FeO-SiO<sub>2</sub>-Al<sub>2</sub>O<sub>3</sub> ternary diagrams, presenting the distribution of studied slags of Khok Kroy archaeological site.

**Source:** Rehren *et al.* (2007)

### 2.3 Age determination

In Khok Kroy archaeological site, four furnace fragment (A0555, A0556, A0557 and A0558) and baked sediment samples (A0554), which found associated with the iron slag samples were taken to obtain the age of iron activity at the site. The results of TL assessment are summarized in table 6. Thermoluminescence ages of five samples fall within a relatively narrow range from  $620 \pm 50$  to  $686 \pm 55$  years before present (BP). TL ages were converted to calendar ages of the 14<sup>th</sup> century AD.

**Table 6** The results of elemental contents (U,Th, K<sub>2</sub>O), annual dose, palaeodose and TL age with error of four furnace fragment and baked sediment samples from Khok Kroy archaeological site.

| LAB ID. | K <sub>2</sub> O (%) | U (ppm) | Th (ppm) | Water content (%) | AD (mGy/a) | PD (Gy) | TL age (a) | Century (A.D.) |
|---------|----------------------|---------|----------|-------------------|------------|---------|------------|----------------|
| A0554   | 0.248                | 2.913   | 5.537    | -                 | 1.451      | 0.900   | 620±50     | 14             |
| A0555   | 3.992                | 5.081   | 14.14    | 1.042             | 5.953      | 3.923   | 659±53     | 14             |
| A0556   | 8.292                | 10.14   | 21.40    | -                 | 11.55      | 7.770   | 672±54     | 14             |
| A0557   | 9.200                | 10.63   | 25.45    | -                 | 12.67      | 8.050   | 635±51     | 14             |
| A0558   | 1.928                | 4.504   | 10.06    | -                 | 3.672      | 2.519   | 686±55     | 14             |

Symbols used: -, not detected; %, weight in percent; ppm, weight in part per million; mGy/a, milligray per annual; a, annual; A.D., anno domini

### 3. Ban Saitho 7 Archaeological Site

#### 3.1 Aerial photograph interpretation

Aerial photographs of Ban Saitho 7 archaeological site in 1996 (roll 5/40 (1), image number 206-207 by the Royal Thai Survey Department, see figure 17), were interpreted using a Sokkia MS-27 Mirror Stereoscope. Geomorphologically, the area can be divided into three landforms (figure 18), namely flood plain, high-terrace and low-terrace with a dendritic stream network which mainly flows from southwest-northeast and some can be observed from south-north. Flood plain commonly situated beside the streams with elevation ranges from about 180 to 190 m above mean sea level. The width of the flood plains ranges from about a few m. to three km. Low-terraces located above the flood plains with an altitude of 190 to 200 m above mean sea level. High-terraces are distinctively situated in the south of the site. An area occupied nearly 50 percent of the site with an altitude of 210 to 230 m above mean sea level.

#### 3.2 Bulk chemical compositional and Microscopic analysis

Macroscopically, all five slags (A0273, A0278, A0281, A0546 and A0547, see appendix A) are lumpy in shape with range in diameter from 5 to 14 cm (figure 19 A). Luster of the samples ranges from glassy to matte and textures include frothy, glassy, smooth and vesicular. Vesicles from microscopic to several cm in diameter are common in most samples and formed from trapped volatiles. The impressions of charcoal fragments are visible in sample A0546 with about 1 to 2 cm in size (figure 19 B). No flow textures are evident in all samples. All samples have no smelting feature same as the slag samples from Khok Kroy archaeological site, such as flowing structure which is typically associated with a smelting process carried out in a furnace rather than in crucible. However, no smithing features, such as a plano-convex shape or hammer scales in the slag fabric, were also observed. At this stage of investigation, again it might be preliminary assumed that the samples were conducted from the smelting process.

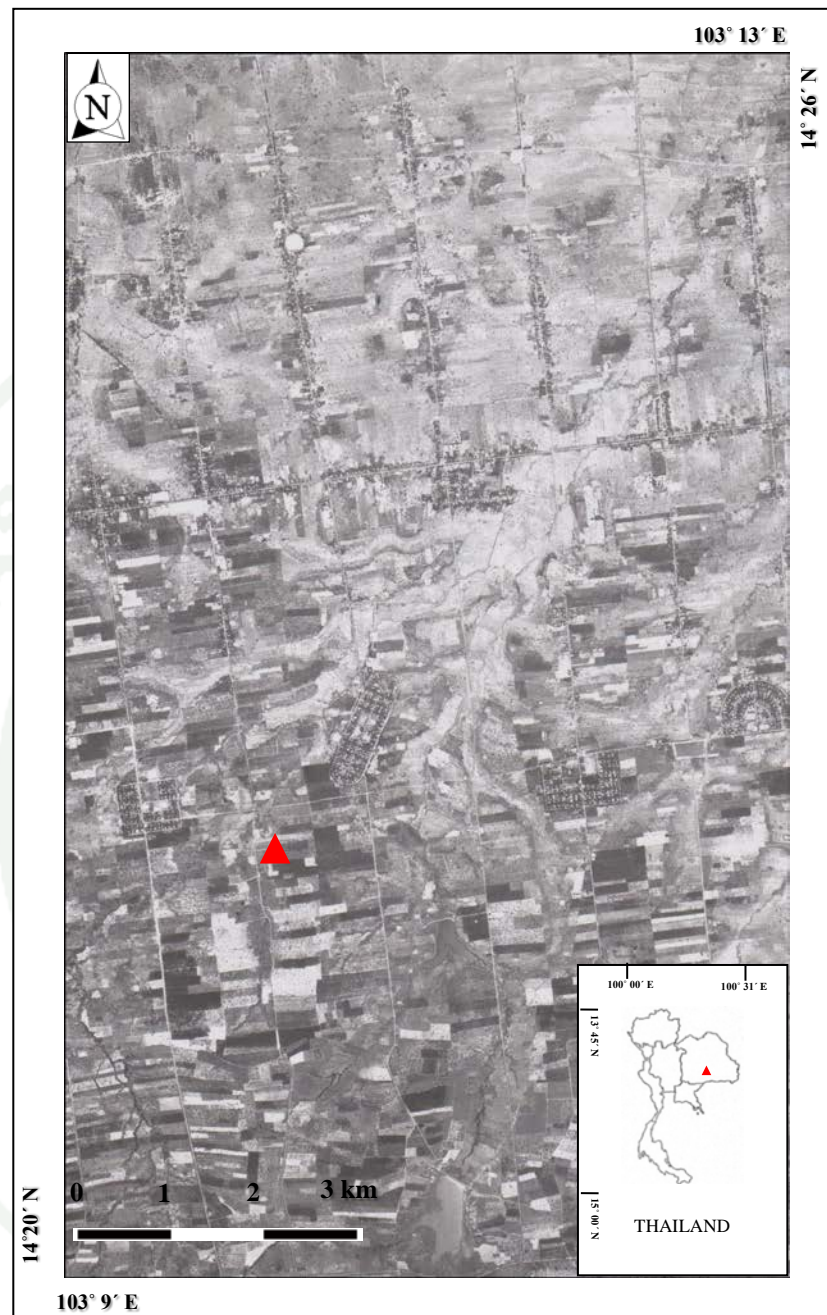


**Figure 17** Aerial photographs of Ban Saitho 7 archaeological site, Tambon Chanthop Phet, Amphoe Ban Kruat, Buri Ram Province (red triangle: study area).

**Source:** Department of Lands (1991)

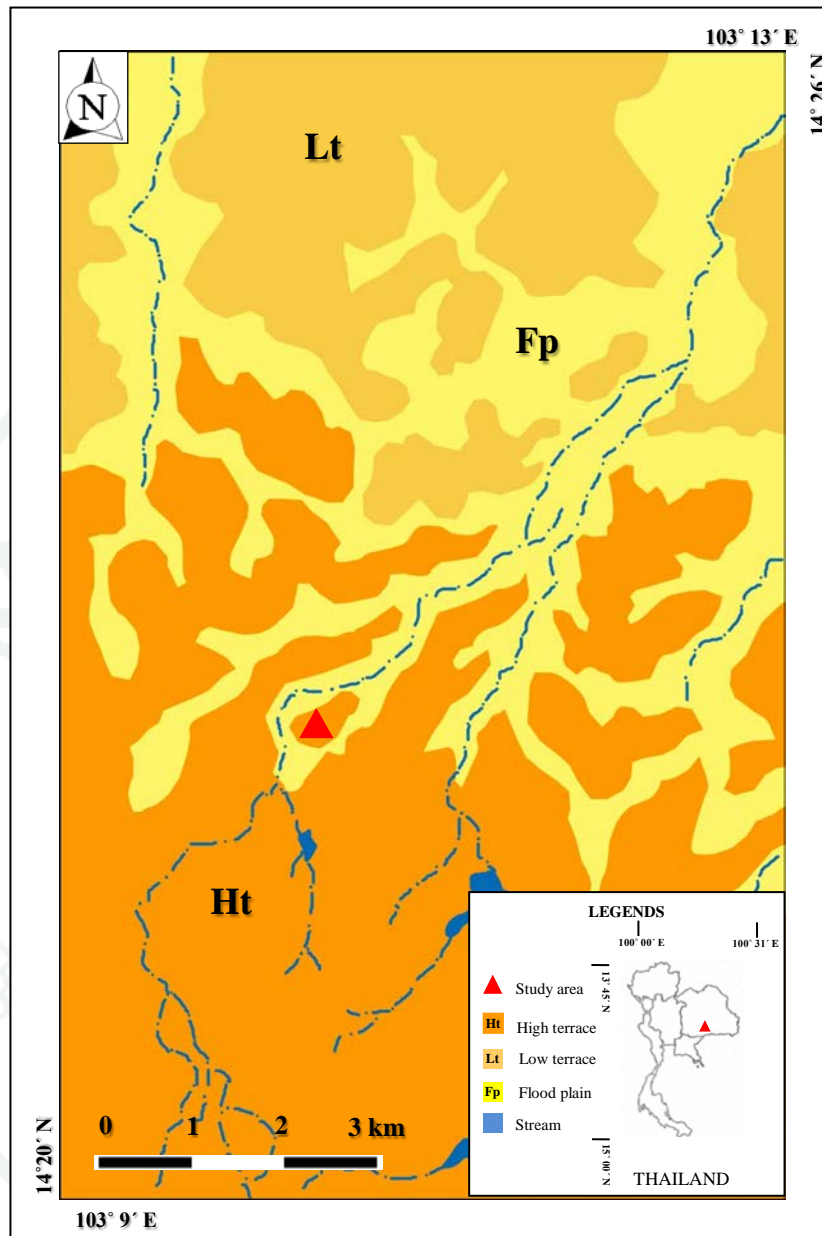


**Figure 18** Interpreted morphological landforms of Ban Saitho 7 archaeological site, Tambon Chanthop Phet, Amphoe Ban Kruat, Buri Ram Province.

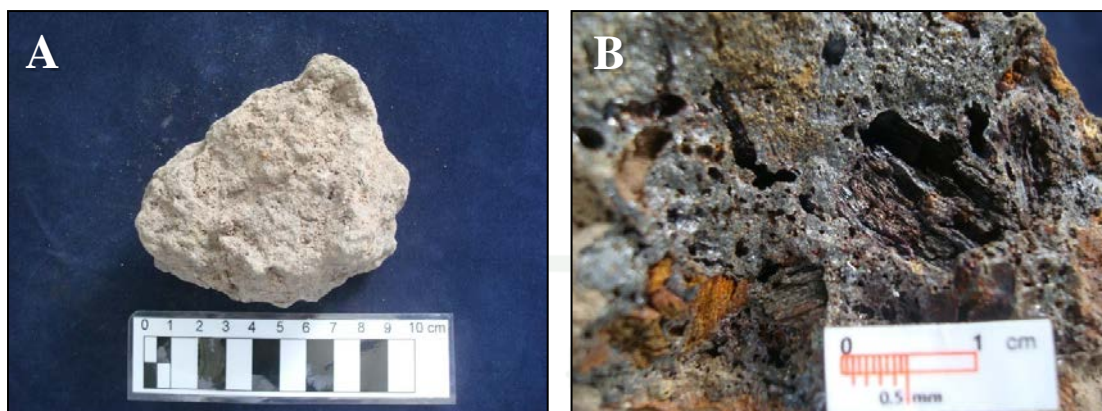


**Figure 19** (A) Macroscopic of sample A0273 (B) Sectioned of sample A0546, showing glassy texture with a large number of charcoals and pores.

The bulk chemical compositions of all samples are given in table 7. The samples generally contain the highest concentrations of FeO (44.37-87.61 wt.%) whilst the concentrations of the other major elements are variable, having SiO<sub>2</sub> (0.876-35.09 wt.%), Al<sub>2</sub>O<sub>3</sub> (12.36-13.41 wt.%) in sample A0273 and A0278, K<sub>2</sub>O (0.230-1.117 wt.%), CaO (0.466-4.006 wt.%), TiO<sub>2</sub> (0.271-3.096 wt.%) ,except sample A0546, V<sub>2</sub>O<sub>5</sub> (0.070-0.313 wt.%), Cr<sub>2</sub>O<sub>3</sub> (0.101-0.206 wt.%), except sample A0546, MnO (0.327-1.716 wt.%), SrO (0.033-0.123 wt.%) in sample A0281 and A0547 respectively, Zr<sub>2</sub>O (0.044-0.241 wt.%) except sample A0547 and CdO (0.117 wt.%) in sample A0281 only.

Microscopically, the mineralogy of the samples obtained by x-ray diffraction, optical microscope and scanning electron microscope analyses is given in table 8 and appendix d and e. The phases present in the samples including fayalite, hercynite, quartz, wüstite and metallic phase in a glassy matrix. Fayalites, a major component of the samples in Ban Saitho 7 (figure 20), commonly form either/both fine-skeletal laths to-

**Table 7** Bulk chemical composition (in wt%) of slags from Ban Saitho 7 archaeological site (determined by ED-XRF method).

| LAB ID | Al <sub>2</sub> O <sub>3</sub> | SiO <sub>2</sub> | K <sub>2</sub> O | CaO   | TiO <sub>2</sub> | V <sub>2</sub> O <sub>5</sub> | Cr <sub>2</sub> O <sub>3</sub> | MnO   | FeO   | SrO   | ZrO <sub>2</sub> | CdO   |
|--------|--------------------------------|------------------|------------------|-------|------------------|-------------------------------|--------------------------------|-------|-------|-------|------------------|-------|
| A0273  | 12.36                          | 32.27            | 0.230            | 0.466 | 0.381            | 0.216                         | 0.101                          | 0.327 | 48.24 | -     | 0.044            | -     |
| A0278  | 13.41                          | 35.09            | 0.350            | 0.705 | 0.441            | 0.185                         | 0.111                          | 0.336 | 44.37 | -     | 0.051            | -     |
| A0281  | -                              | 1.389            | 0.572            | 4.006 | 3.096            | 0.313                         | 0.206                          | 1.716 | 79.38 | 0.123 | 0.241            | 0.117 |
| A0546  | -                              | 0.876            | 0.350            | 0.468 | -                | 0.117                         | -                              | 0.768 | 87.61 | -     | 0.056            | -     |
| A0547  | -                              | 0.982            | 1.117            | 1.457 | 0.271            | 0.070                         | 0.125                          | 0.639 | 85.75 | 0.033 | -                | -     |
| Mean   | n/a                            | 14.12            | 0.52             | 1.42  | n/a              | 0.18                          | n/a                            | 0.76  | 69.07 | n/a   | n/a              | n/a   |

Symbols used: -, not detected; n/a, not available

**Table 8** Phases in Ban Saitho 7 archaeological site slag samples obtained by XRD analysis (%wt), optical microscope and scanning electron microscope.

| LAB ID.   |            |                           | A0273 | A0278 | A0281 | A0546 | A0547 |
|-----------|------------|---------------------------|-------|-------|-------|-------|-------|
| Group     | Name       | Ideal/range composition   |       |       |       |       |       |
| Silicates | Fayalite   | $\text{Fe}_2\text{SiO}_4$ | 69.69 | 62.33 | 44.56 | 90.53 | 97.4  |
|           | Quartz     | $\text{SiO}_2$            | -     | 23.33 | -     | -     | -     |
|           | Quartz low | $\text{SiO}_2$            | 10.82 | -     | 33.91 | 2.64  | 2.6   |
| Oxides    | Hercynite  | $\text{FeAl}_2\text{O}_4$ | 19.49 | 14.35 | 21.53 | 6.83  | -     |
|           | Wüstite    |                           | -     | -     | -     | *     | -     |
| Metal     | Pure metal | Fe                        | *     | *     | *     | *     | *     |
| Glass     |            |                           | *     | *     | *     | *     | *     |

Symbols used: -, not detected; \*, detected by optical microscope and scanning electron microscope

ehedral crystals, In sample A0546 exhibit a more developed crystal structure, indicative of a slower cooling rate (when the furnace would be hottest), compared to the other samples (see appendix e), where fayalite shows a more skeletal growth. However, no other significant differences are noticeable. The laths of fayalite up to several millimeters in length are abundant. Their compositions (by EDS spot analyses, see appendix f) contain O (53.94-56.74 wt.%), Fe (27.21-28.97 wt.%) and Si (16.05-17.61 wt.%).

Hercynites are very rare in all samples, they present as euhedral to coarse-dendritic crystals with contain (see appendix f) O (51.55-54 wt.%), Al (27.32-31.35 wt.%), Fe (15.30-17.37 wt.%) and traces of V (0.560-1.610 wt.%) and Ti (0.520-1.130 wt.%). Residual quartz present as anhedral to subhedral grains with cracks, ranging from a few to several  $\mu\text{m}$  in diameter in sample A0278 and A0546. Metallic phases are present in all samples and generally occur as prills ranging from  $<1$  to  $150 \mu\text{m}$  in diameter, some occur as irregular in shape. By EDS spot analysis (see appendix f) indicated that, they are 100 wt.% Fe. The matrix of all samples is glass and occurs abundant as interstitial pools between crystals of fayalite, accept sample A0547.

When plot in the  $\text{FeO-SiO}_2\text{-Al}_2\text{O}_3$  ternary diagrams as the Khok Kroy slags, to estimate the operating temperature, the samples fall into two different regions (figure 21): the first, hercynite region (A0273 and A0278), indicating operating temperature at about  $1,188\text{-}1,200 \text{ }^\circ\text{C}$ .; the second, wüstite region (A0281, A0546 and A0547), indicating operating temperature at about  $1,350\text{-}1,369 \text{ }^\circ\text{C}$ . More interesting, sample A0273 and A0278 cluster on the low temperature trough, around the low iron eutectic.

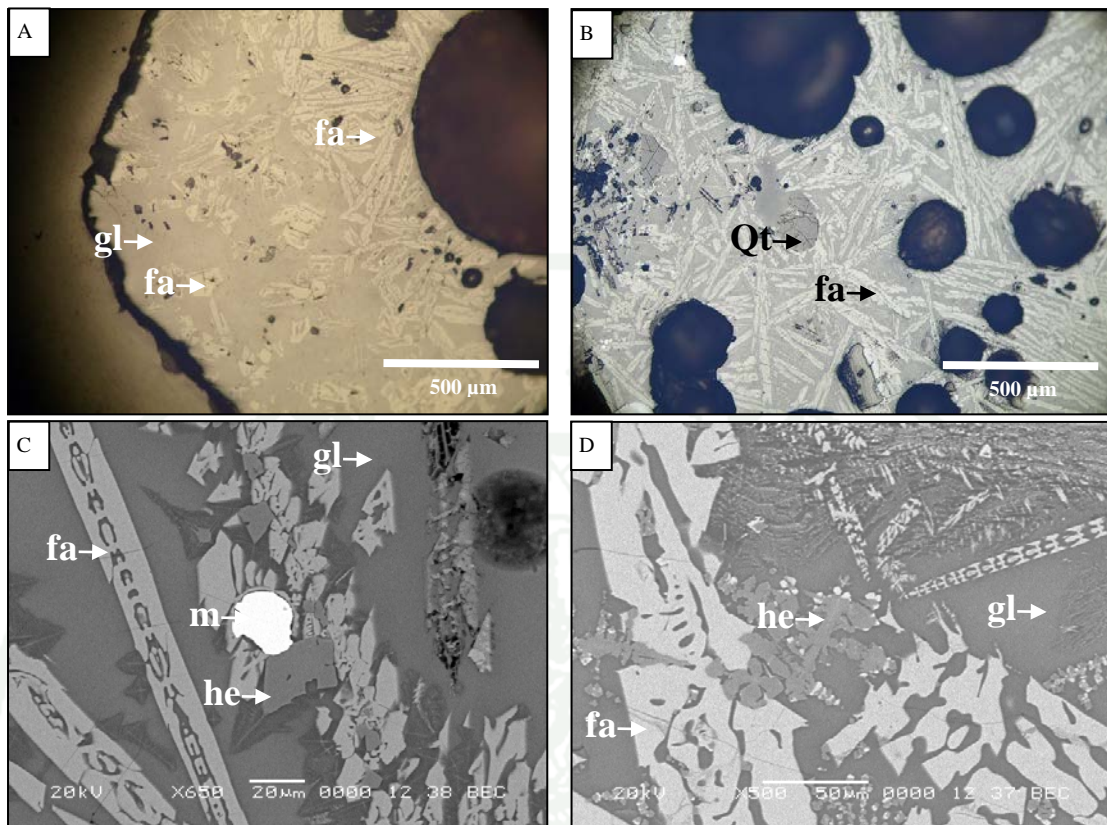


**Figure 20** Reflected light microscope image (A) Euhedral fayalite crystals in glassy matrix (sample A0547) (B) Fayalite and quartz with cracks; Scanning electron microscope image (C) Polished sections of sample A0273, showing elongate skeletal fayalite laths, euhedral hercynite and iron prill (at center) in a glassy matrix (D) Coarsened dendritic hercynite and fayalite laths in glassy matrix of sample A0281, fa-fayalite, he-hercynite, Qt-Quartz, m-metal, gl-glassy matrix.

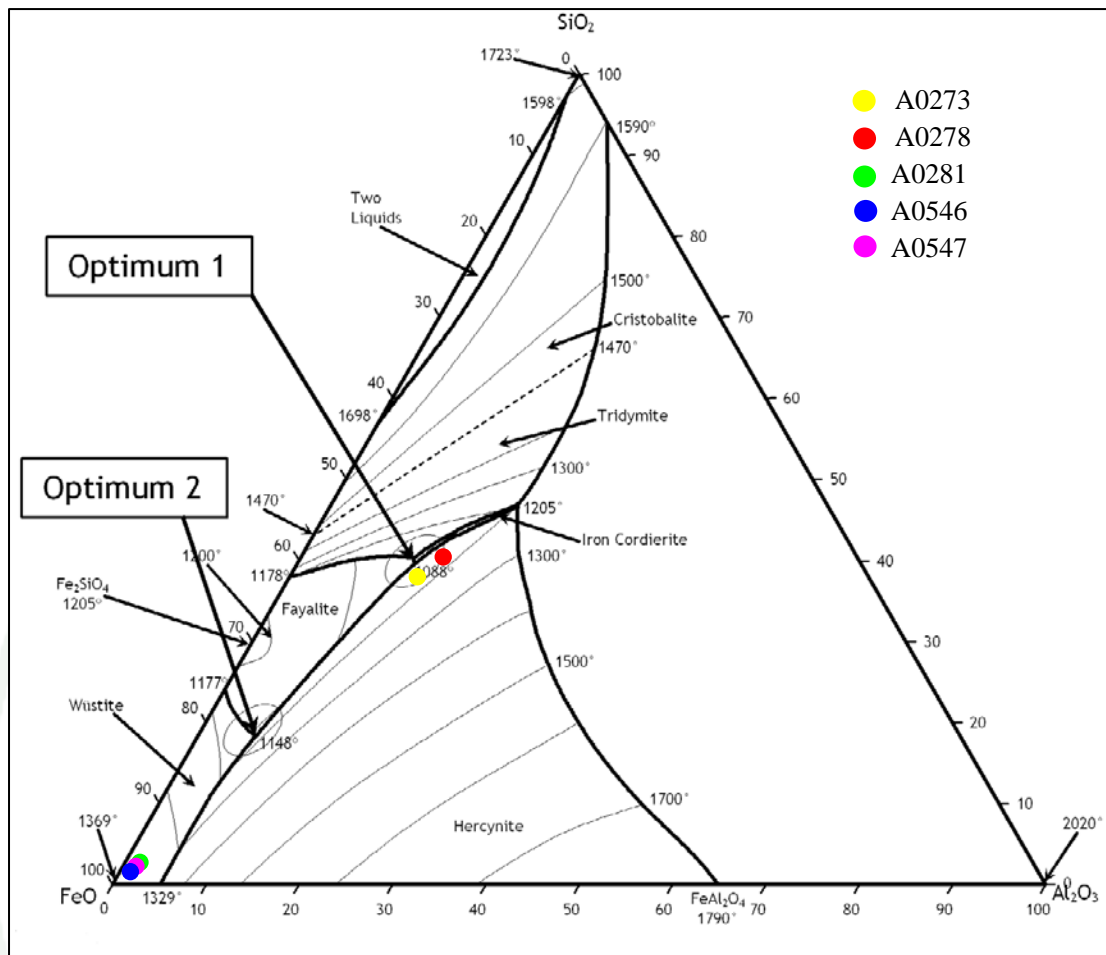


**Figure 21** FeO-SiO<sub>2</sub>-Al<sub>2</sub>O<sub>3</sub> ternary diagrams, presenting the distribution of studied slags of Ban Saitho 7 archaeological site.

**Source:** Rehren *et al.* (2007)

### 1.3 Age determination

Five furnace fragment (A0338, A0339, A0340, A0341 and A0282) and two potsherds samples (A0272 and A0277), which found associated with the iron slag samples were taken to obtain the age of iron activity in Ban Saitho 7 archaeological site. The results of TL assessment are summarized in table 9. Thermoluminescence ages of five samples fall within a range from 1,058±85 to 1,202±180 years before present (BP). TL ages were converted to calendar ages of range from the 9<sup>th</sup> to 10<sup>th</sup> century AD.

**Table 9** The results of elemental contents (U,Th, K<sub>2</sub>O), annual dose, palaeodose and TL age with error of five furnace fragment and two potsherds samples from Ban Saitho 7 archaeological site.

| LAB ID. | K <sub>2</sub> O (%) | U (ppm) | Th (ppm) | Water content (%) | AD (mGy/a) | PD (Gy) | TL age (a) | Century (A.D.) |
|---------|----------------------|---------|----------|-------------------|------------|---------|------------|----------------|
| A0338   | -                    | -       | 9.046    | 2.994             | 0.777      | 0.916   | 1,179±71   | 9              |
| A0339   | -                    | -       | 7.878    | 2.536             | 0.690      | 0.819   | 1,186±142  | 9              |
| A0340   | -                    | 4.509   | 7.243    | 1.480             | 1.740      | 2.045   | 1,176±202  | 9              |
| A0341   | -                    | -       | 6.530    | 0.370             | 0.589      | 0.708   | 1,202±180  | 9              |
| A0272   | 5.003                | 6.075   | 27.71    | 2.890             | 8.045      | 9.557   | 1,188±110  | 9              |
| A0277   | 4.636                | 4.968   | 23.99    | 3.623             | 7.175      | 8.075   | 1,126±135  | 9              |
| A0282   | -                    | 0.774   | 6.490    | 1.010             | 0.774      | 0.819   | 1,058±85   | 10             |

Symbols used: -, not detected; %, weight in percent; ppm, weight in part per million; mGy/a, milligray per annual; a, annual; A.D., anno domini

## 4. Ban Khao Din Tai Archaeological Site

### 4.1 Aerial photograph interpretation

Aerial photographs of Ban Khao Din Tai Archaeological Site in 1987 (roll 48, run 71, image number 358-360 by Department of Lands, see figure 22), were interpreted using a Sokkia MS-27 Mirror Stereoscope. Geomorphologically, the area can be divided into two landforms (figure 23), namely flood plain and terrace with a dendritic stream network which flows from south-north (the main streams) and southwest-northeast. Flood plains are observed along major streams that have gentle slopes. This landform is the most distinctive class on the site. The width of the flood plains ranges from a few m to several km. Terraces are observed above flood plains and located between two streams. Elevation of the terrace ranges between about 190 to 197 m above mean sea level.

### 4.2 Bulk chemical compositional and Microscopic analysis

Macroscopically, five slag samples (A0538, A0539, A0540, A0541 and A0542, see appendix A) obviously different in their inner and outer morphologies. Two major types of slag were identified and labeled as either lumpy or flattened shape. Firstly, lumpy slag samples (figure 24 A) appear the partially dense and porous, except for sample A0541, it consists of a large number of porosities. The size of samples ranging from 5 to 8 cm. Luster of the samples ranges from glassy to matte and textures include frothy, glassy, smooth and vesicular. Secondly, flattened shape slag samples (figure 24 B) are usually flat. The thickness ranges from approximately 1 to 1.5 cm. They contain minor amounts of porosity and signs of flow on one or more surfaces typical of tapped slags, which is typically associated with a smelting process.

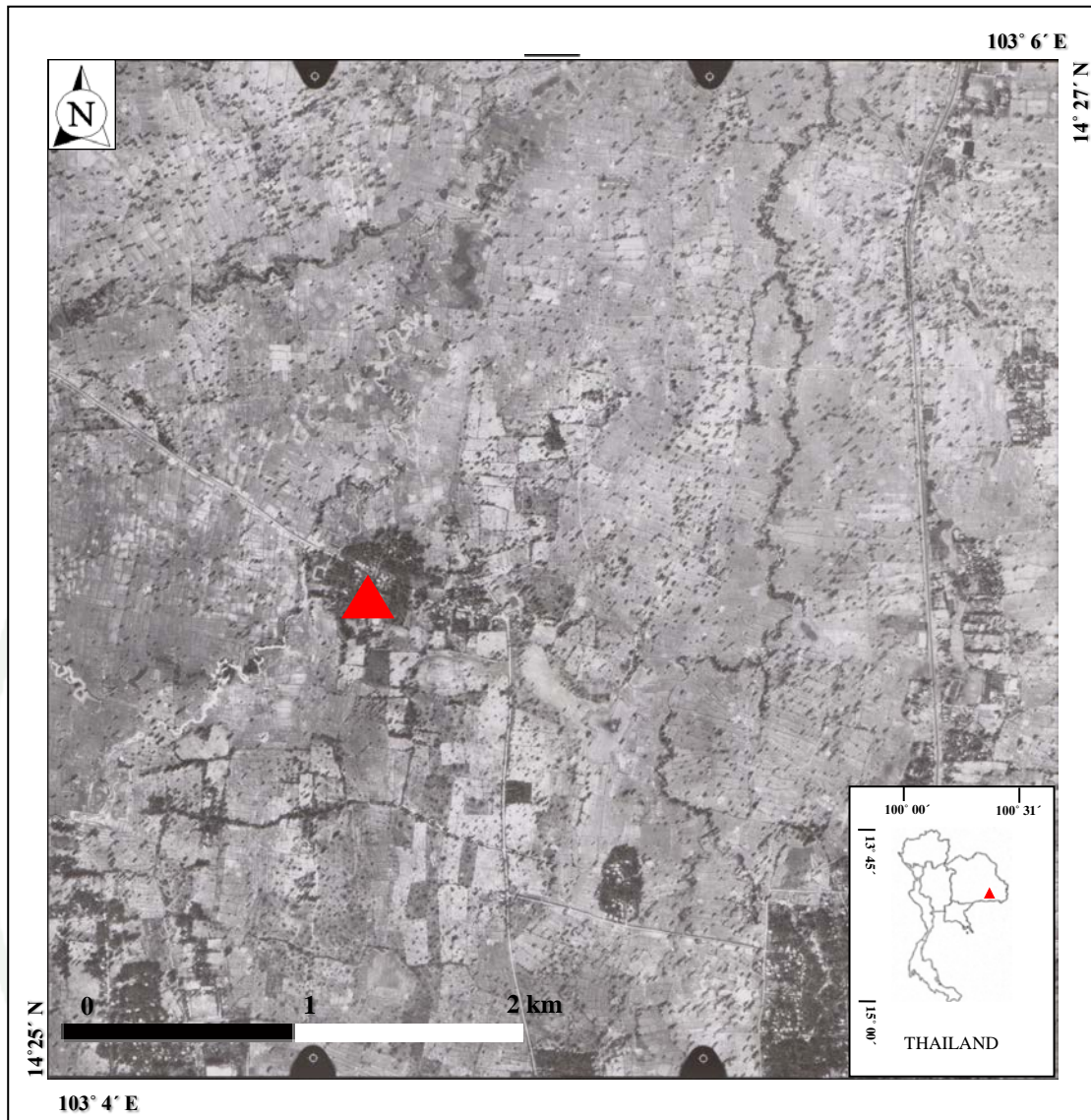


**Figure 22** Aerial photograph of Ban Khao Din Tai archaeological site, Tambon Ban Kruat, Amphoe Ban Kruat, Buri Ram Province (red triangle: study area).

**Source:** Department of Lands (1987)

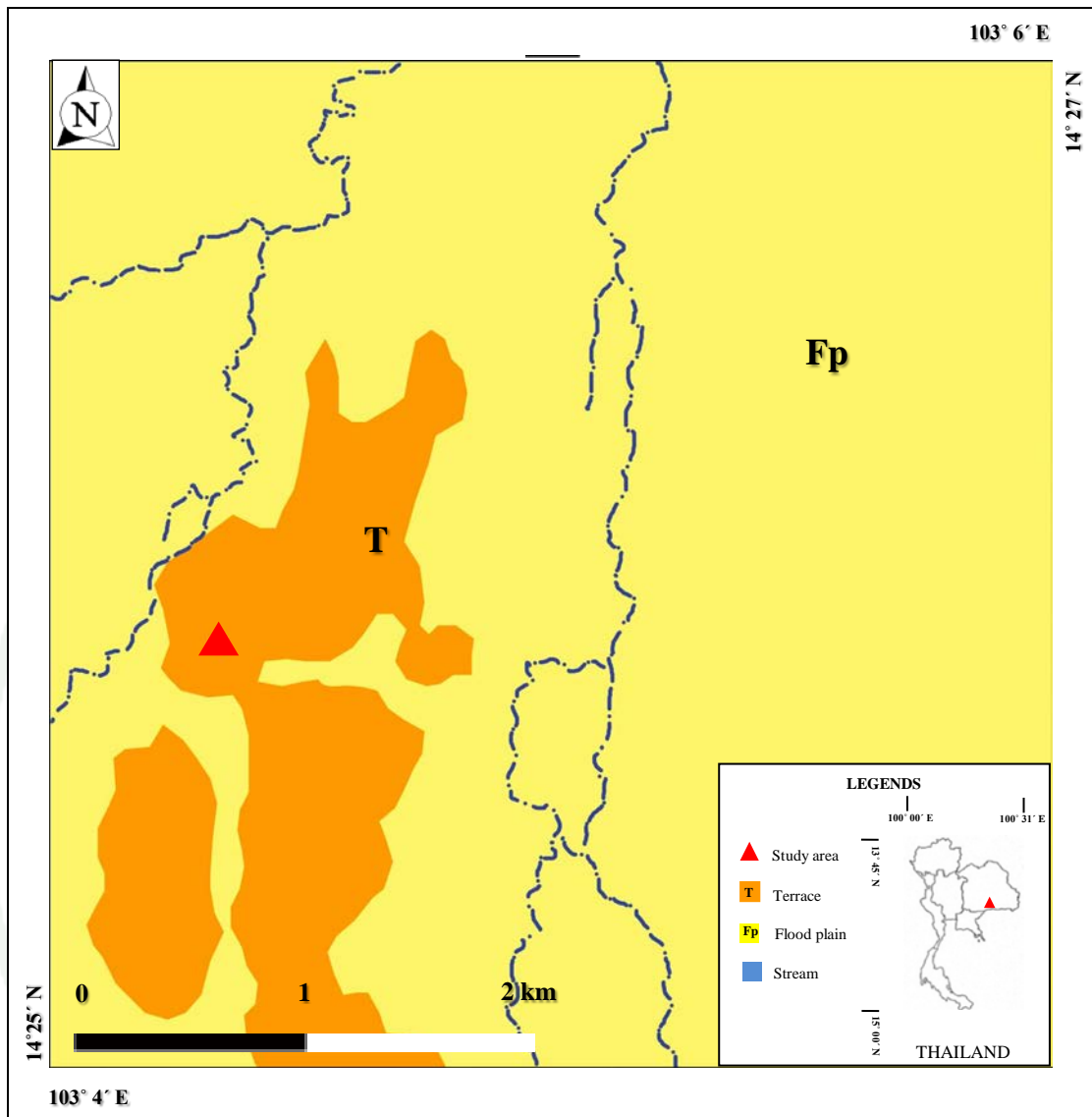


**Figure 23** Interpreted morphological landforms of Ban Khao Din Tai archaeological site, Tambon Ban Kruat, Amphoe Ban Kruat, Buri Ram Province.

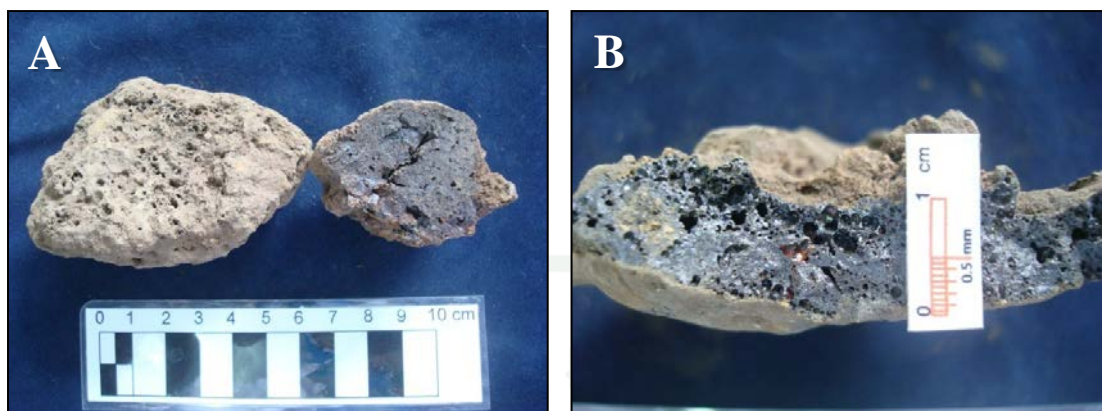


**Figure 24** (A) Macroscopic of block to lumpy slag (sample A0538). (B) Macroscopic of flattened shape slag (sample A0539).

The bulk chemistry for five samples is given in table 10. The samples relatively contain the highest FeO (45.10-52.25 wt.%), SiO<sub>2</sub> (26.23-33.97 wt.%) and Al<sub>2</sub>O<sub>3</sub> (11.58-12.70 wt.%) concentrations with lesser amounts (<2 wt.%) of K<sub>2</sub>O, CaO, TiO<sub>2</sub>, V<sub>2</sub>O<sub>5</sub>, Cr<sub>2</sub>O<sub>3</sub>, MnO, ZrO<sub>2</sub>, SrO in sample A0540 and CdO in sample A0539. Due to the relative high content of Al<sub>2</sub>O<sub>3</sub> related with abundant hercynites being seen in all slags (Muralha *et.al*, 2010).

Microscopically, the mineralogy of the samples obtained by x-ray diffraction, optical microscope and scanning electron microscope analyses is given in table 11, and appendix d and e. Slag samples from Ban Khao Din Tai consist of various phases including fayalite, hercynite, quartz, metallic phase in a glassy matrix. Fayalites were commonly found as very fine- to fine-skeletal laths crystals (figure 25 A). The laths up to several millimeters in length are very abundant. The following ranges in elements of fayalite were found (by EDS spot analyses, see appendix f): 52.46-58.83 wt.% O, 23.19-29.82 wt.% Fe, 16.21-17.84 wt.% Si with a trace of 1.760 wt.% Al in sample A0542. Regarding the shapes of the fayalites in slags, that can be informative in terms-

**Table 10** Bulk chemical composition (in wt%) of slags from Ban Khao Din Tai archaeological site (determined by ED-XRF method).

| LAB ID | Al <sub>2</sub> O <sub>3</sub> | SiO <sub>2</sub> | K <sub>2</sub> O | CaO   | TiO <sub>2</sub> | V <sub>2</sub> O <sub>5</sub> | Cr <sub>2</sub> O <sub>3</sub> | MnO   | FeO   | SrO   | ZrO <sub>2</sub> | CdO   |
|--------|--------------------------------|------------------|------------------|-------|------------------|-------------------------------|--------------------------------|-------|-------|-------|------------------|-------|
| A0538  | 12.15                          | 26.23            | 0.344            | 0.466 | 1.898            | 0.182                         | 0.138                          | 0.456 | 52.25 | -     | 0.064            | -     |
| A0539  | 11.58                          | 27.91            | 0.192            | 0.289 | 1.621            | 0.155                         | 0.118                          | 0.443 | 51.84 | -     | 0.054            | 0.028 |
| A0540  | 11.63                          | 33.97            | 0.298            | 0.910 | 1.792            | 0.153                         | 0.125                          | 0.925 | 45.10 | 0.014 | 0.057            | -     |
| A0541  | 12.20                          | 28.07            | 0.317            | 0.754 | 1.997            | 0.080                         | 0.068                          | 0.445 | 50.39 | -     | 0.061            | -     |
| A0542  | 12.70                          | 29.76            | 0.331            | 0.307 | 1.257            | 0.133                         | 0.068                          | 0.572 | 49.31 | -     | 0.069            | -     |
| Mean   | 12.06                          | 29.19            | 0.296            | 0.545 | 1.713            | 0.140                         | 0.103                          | 0.568 | 49.78 | n/a   | 0.061            | n/a   |

Symbols used: -, not detected; n/a, not available

**Table 11** Phases in Ban Khao Din Tai archaeological site slag samples obtained by XRD analysis (%wt), optical microscope and scanning electron microscope.

| LAB ID.   |            | A0538                     | A0539 | A0540 | A0541 | A0542 |       |
|-----------|------------|---------------------------|-------|-------|-------|-------|-------|
| Group     | Name       | Ideal/range composition   |       |       |       |       |       |
| Silicates | Fayalite   | $\text{Fe}_2\text{SiO}_4$ | 81.31 | 74.45 | 71.00 | 74.91 | 72.91 |
|           | Quartz low | $\text{SiO}_2$            | -     | 4.200 | 15.85 | 6.760 | 7.650 |
| Oxides    | Hercynite  | $\text{FeAl}_2\text{O}_4$ | 18.69 | 21.34 | 13.15 | 18.32 | 19.44 |
| Metal     | Pure metal | Fe                        | *     | *     | *     | *     | *     |
| Glass     |            |                           | *     | *     | *     | *     | *     |

Symbols used: -, not detected; \*, detected by optical microscope and scanning electron microscope

of the smelting process, and exists in all samples, they show the very fine- to fine-skeletal laths crystals. It is assumed that they could have been produced by either being tapping out of furnace or dripped down into a cold slag pit.

All samples also contain coarse-dendritic to euhedral hercynite crystals with large amounts of O (49.19-55.41 wt.%), Al (29.37-31.55 wt.%), Fe (14.48-17.36 wt.%) and minor amounts (<1.5 wt.%) of V, Cr in sample A0539 and Ti in sample A0538. Metallic iron commonly occurs as rounded blebs or prills up to 250  $\mu\text{m}$  in diameter, some metallic iron occurs as irregular in shape. By EDS spot analyses (see appendix f), the chemical component of metallic iron is 100 wt.% Fe. Quartz is rarely present as macroscopic to microscopic anhedral fractured grains with cracks of unmelted inclusions. The matrix of most samples is abundant glass, some areas of sample A0541 is only clear glass with iron prills (figure 25 B).

When plotted in the  $\text{FeO-SiO}_2\text{-Al}_2\text{O}_3$  ternary diagrams to provides insight into the evolution of the melt as phases crystallize as well as required smelting temperatures, as Khok Kroy and Ban Saitho 7 slags. All slag samples fall into hercynite region close to the optimum 1, indicating operating temperature at about 1,088-1,250  $^\circ\text{C}$  (figure 26), although sample A0540 plots within the little more  $\text{SiO}_2$  region, characterized by lower operating temperature and approaching the optimum 1.

1943

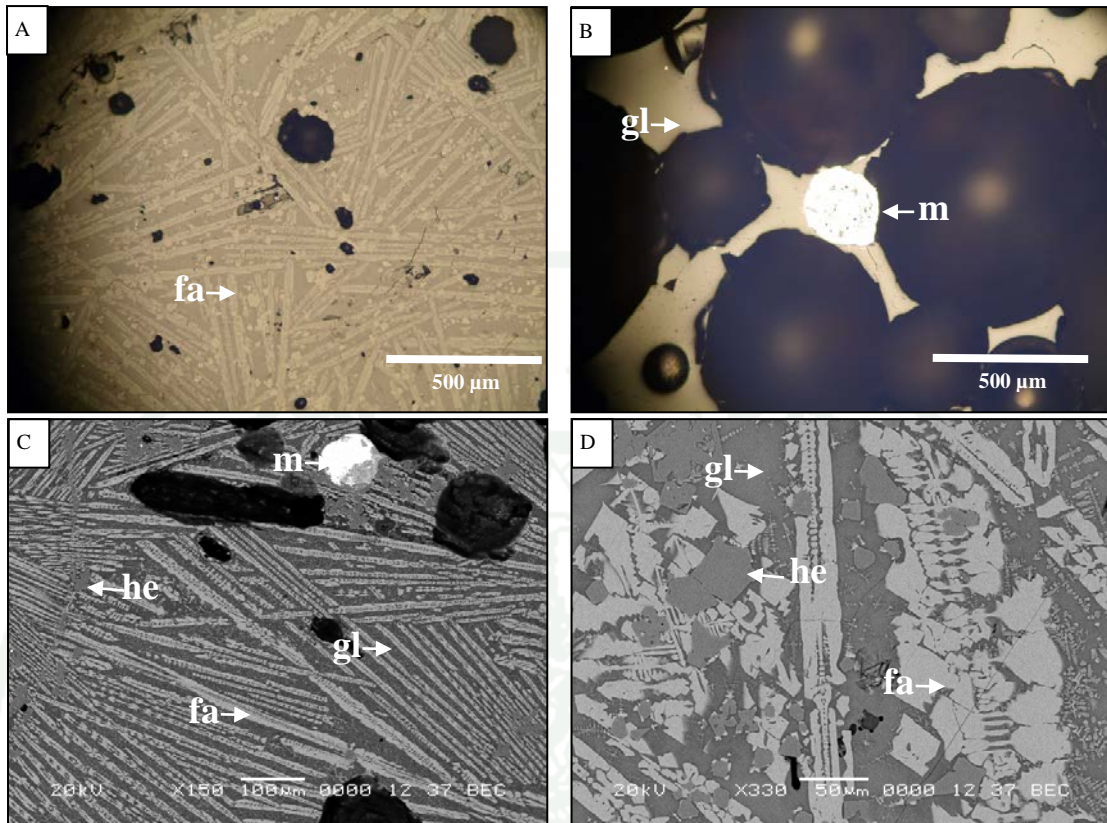


**Figure 25** Reflected light microscope image (A) Skeletal fayalite laths in glassy matrix (sample A0540) (B) Clear glass with iron prill in sample A0541; Scanning electron microscope image (C) Corroded iron prill in sample A0540 (D) Euhedral hercynite and fayalite laths in glassy matrix of sample A0538, fa-fayalite, he-hercynite, Qt-Quartz, m-metal, gl-glassy matrix.

1943

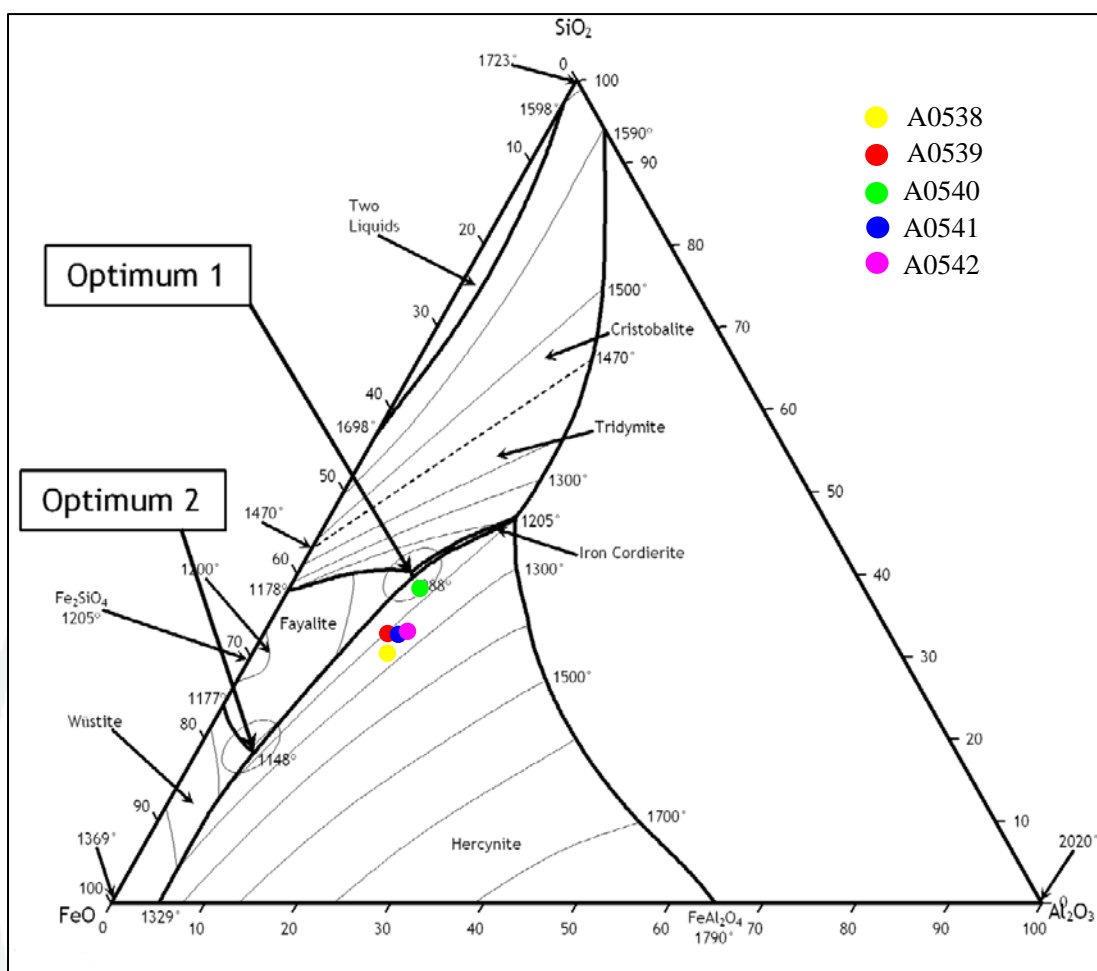


**Figure 26** FeO- SiO<sub>2</sub>-Al<sub>2</sub>O<sub>3</sub> ternary diagrams, presenting the distribution of studied slags of Ban Khao Din Tai archaeological site.

**Source:** Rehren *et al.* (2007)

#### 4.3 Age determination

Six furnace fragment samples (A0535, A0536, A0537, A0605, A0606 and A0607) which found associated with the iron slag samples were taken to obtain the age of iron activity in Khao Din Tai archaeological site. The results of TL assessment are summarized in table 12. Thermoluminescence ages of six samples fall within a narrow range from 1,099±88 to 1,232±99 years before present (BP). TL ages were converted to calendar ages of the 8<sup>th</sup> to 10<sup>th</sup> century AD.

**Table 12** The results of elemental contents (U,Th, K<sub>2</sub>O), annual dose, palaeodose and TL age with error of six furnace fragment samples from Ban Khao Din Tai archaeological site.

| LAB ID. | K <sub>2</sub> O (%) | U (ppm) | Th (ppm) | Water content (%) | AD (mGy/a) | PD (Gy) | TL age (a) | Century (A.D.) |
|---------|----------------------|---------|----------|-------------------|------------|---------|------------|----------------|
| A0335   | -                    | 0.167   | 8.568    | 2.564             | 0.782      | 0.886   | 1,133±168  | 9              |
| A0336   | -                    | 0.256   | 7.948    | 0.935             | 0.757      | 0.860   | 1,135±76   | 9              |
| A0337   | -                    | 0.311   | 6.801    | 2.830             | 0.685      | 0.761   | 1,111±192  | 10             |
| A0607   | 1.989                | 4.459   | 12.90    | -                 | 3.929      | 4.320   | 1,099±88   | 10             |
| A0605   | 0.686                | 2.725   | 7.933    | -                 | 1.974      | 2.300   | 1,165±93   | 9              |
| A0606   | 0.565                | 11.49   | 51.44    | -                 | 7.287      | 8.980   | 1,232±99   | 8              |

Symbols used: -, not detected; %, weight in percent; ppm, weight in part per million; mGy/a, milligray per annual; a, annual; A.D., anno domini

## Discussion

### 1. Non Nong Hor Archaeological Site

The landforms around the study area comprised hill, terrace and floodplain whereas the study area lies in the middle of the floodplain. Five TL-dating samples have been obtained from furnace fragments at the site, these TL determinations provided evidence that the smelting activity occurred at this site from 1,400 to 1,000 years before present (BP).

The Non Nong Hor slag evidence is entirely consistent with the expect waste product of a copper smelting operation according to their macroscopic, chemical compositional, microscopic information. Analysis of slag samples showed that all samples have relatively different chemical compositions. Table 1 showed bulk chemical compositions obtained from five slag samples. The samples contain in fact high amount of iron oxide (FeO) (63.88 to 83.54 wt.%), which was preferentially partitioned in silicate phase (fayalite). The presence of copper oxide which range in five samples between 2.020 to 6.567 wt.%, unambiguously characterize the slag as copper smelting slag. In addition, the relatively low S content presented in sample A0572 and A0573 (0.028 to 0.124 wt% by converting from SO<sub>3</sub>) and the rarely present of sulphidic copper phase in three other samples, could be either due to the use of copper ores with variable sulphur content and/or to deep roasting of the ore charge. The formation of slags with relatively low S contents after smelting of oxide-rich ores with minor amounts of sulphides is well documented in the scientific literature (e.g. Bartelheim *et al.*, 2003; Hauptmann, 2003; Rostoker *et al.*, 1989; Rovira, 2003; Sáez *et al.*, 2003; Schreiner *et al.*, 2003)

The microstructural and compositional features of copper slags indicated that copper production at Non Nong Hor were able to optimize the slagging process and obtain high copper yields. This is demonstrated by the relatively low amounts of Cu in the slags (on average 4.255 wt%, see table 2), mainly as small metal prills (a few to 80 µm in diameter, maximum 200 mm). Almost slag samples consistently show abundant skeletal laths crystals of fayalite, indicating that they were all produced by a

rapid cooling process, such as slag tapping or dropping into a slag pit, probably full of a cooler air. In addition, it seems like the copper smelting in Non Nong Hor using sand as flux during the smelting process.

Estimates of operating temperature based on the bulk chemistry in the simplified FeO-SiO<sub>2</sub>-CaO ternary diagrams in figure 14, all slag samples apparently were formed under different condition, all slag samples fall into two different regions: the olivine region (sample A0573) which indicating operating temperature of about 1,200 °C; the wüstite region (A0572, A0574, A0577 and A0581) which indicating higher operating temperature of about 1,360 to 1,369 °C. It is indicates that the smelting process was at high enough temperature to afford good liquation of the metal through the slag.

## **2. Khok Kroy Archaeological Site**

The landforms around the study area comprise high-terrace, low-terrace and floodplain whereas the study area lies in the floodplain. Five TL-dating samples have been obtained from furnace fragments and baked sediment (the associated finds) at the site, these determinations provided evidence that the smelting activity occurred at this site during 700 to 600 years BP. Anyways, there was the project of “The study on the relationship of the ancient through present culture for the development of cultural and civilization database for GMS and Malay Peninsula regions” to report the age of this site was 2,300 to 1,500 years BP by relative dates of topology of potsherds. Based on these result, it is suggested that the methods are chosen for chronological investigations of the smelting activity in the future should focus more on materials directly associated with this smelting process and also more on other dating methods. Lastly, it seems likely that the bloomery smelting process (direct smelting process) was practiced continually in this area without interference from indirect smelting process from China or other smelting process.

From the results, it is clear that this is a slag related to iron production. The macroscopic, chemical compositional and microscopic information are characteristic of bloomery iron smelting slag. Analysis of slag samples showed that all samples have relatively different chemical compositions. Table 4 shows bulk chemical compositions obtained from five slag samples. Two samples (A0588 and A0590) are dominated by  $\text{Al}_2\text{O}_3$  and  $\text{SiO}_2$  while the three others have higher concentration of FeO. It suggests that these two groups of the samples were produced in different manner in terms of the methodological approach to the technology and the ingredients used. In addition, the iron oxide content is relatively high in all samples (average content is 69.11 wt. %) which is typical of slags produced during the smelting of iron. The concentration of iron oxide in the slag depends on atmosphere inside the furnace and the iron ore used. In this site, no content of wüstite (FeO) in all samples points to a more efficient reduction process (Hani et.al, 2011). However, the relatively low content of CaO (0.131 to 1.098 wt.%) in all samples, suggests that no flux was used in this operation but the process could benefit from the self-fluxing of used material ore (Tylecote, 1987)

The microstructure and phase composition result indicated that the essential phase of the samples is fayalite, generally the crystal structures are skeletal lath, occurs as poor crystallized crystals, indicating a fast cool. Cristobalite was identified in only sample A0586. Regarding sample A0586, was totally different to other slags in terms of the macroscopic, microstructure and chemical compositions. It was supposedly formed by materials rich in cristobalite and quartz and it was likely to be technical ceramics adhering by relatively rare slag on the upper surface. Metallic iron occurs as prill, interspersed in all of the samples. Schmidt (1997) documented similar features in the slag produced by the Haya smelters of Tanzania, and interpreted them as the result of the locally reducing conditions created by the charred grass filling the furnace slag pit, which promoted further iron reduction. An alternative explanation may be that the slag was exposed to reducing furnace gases after being deposited in the bowl, with the consequent reduction of a top layer of the slag to metallic iron before the next slag layer dripped on top of it. Either way, this presence of metallic iron in this case does not seem indicative of a high viscosity preventing the separation

between metal and slag, rather this metal probably formed after the slag had separated from the bloom. However, the present of metallic iron is firmly confirmed that they were conducted from the smelting process and also the atmosphere was obviously a reducing condition (Piatak and Seal, 2011:641) and the presence of magnetite in sample A0586 also indicating rather reducing condition (Biswas and Davenport, 1976).

Estimates of operating temperature based on the bulk chemistry in the simplified FeO-SiO<sub>2</sub>-Al<sub>2</sub>O<sub>3</sub> ternary diagrams in figure 16, all slag samples fall into two different regions: the hercynite region (sample A0588 and A0590), denoting a technology producing sufficient quantities of iron, with relatively low slag melting temperatures between 1,180 to 1,220 °C; the wüstite region, the iron rich corner of the system (A0586, A0594 and A0595) which indicating higher operating temperature of about 1,350 to 1,369 °C. This is indicated that all slag samples apparently were formed under different condition. In addition, the sample A0586 likely to be technical ceramic, contains cristobalite—a high temperature poly morph of quartz that forms above 1,470 °C—that can occur as a metastable phase at lower temperature, however its presence likely reflects the high furnace temperature.

### **3. Ban Saitho 7 Archaeological Site**

The landforms around the study area comprise high-terrace, low-terrace and floodplain whereas the study area lies in the low-terrace. Seven TL-dating samples have been obtained from furnace fragments and potsherds (the associated finds) at the site, these determinations provide evidence that the smelting activity occurred at this site during 1,200 to 1,000 years BP. While the chronological study of the archaeometallurgical evidence associated with Ban Saitho 7 by the same project as mentioned in Khok Kroy, yielded relative dates of agate beads, which give a range of older ages from 2,000 years BP at the earliest to 1,800 years BP at the latest. Based on these results, it is suggests that the methods are chosen for chronological investigations of the smelting activity in the future should focus more on materials directly associated with this smelting process such as smelting slag, tuyère, etc., and

also more on other dating methods such as radiocarbon dating, optically stimulated luminescence dating, fission track dating, etc.

The bulk chemical compositions of slags from Ban Saitho 7 are given in table 7. Slag contains many proportions of many different elements. This is due to the fact that it contains the reduction residue. Bulk chemical analyses of all slag samples revealed that iron oxide (calculated here as FeO) content is relatively high in most samples (44.37 to 87.61 wt.%) which is typical of slags produced during the smelting of iron. The concentration of SiO<sub>2</sub> in sample A0273 and sample A0278 ranging between 32.27 to 35.09 wt.% which lead to a higher amount of fayalite. Analysis of slag samples showed that all samples have relatively different chemical compositions. Two samples (A0273 and A0278) are dominated by Al<sub>2</sub>O<sub>3</sub> and SiO<sub>2</sub> while the three others have higher concentration of FeO. It suggests that these two groups of the samples were produced in different manner in terms of the methodological approach to the technology and the ingredients used. The another important component in the slag is calcium oxide (CaO) which range in five samples between 0.466 to 4.006 wt.%. This value is relatively low (the most suitable for iron smelting slag is about 3 to 6 wt.% (Hani *et.al.*, 2011)). However, it suggests that no flux was used in this operation but the process could benefit from the self-fluxing of used material ore (Tylecote, 1987).

The microstructure and phase composition show that fayalite is dominant component of iron slag. They commonly formed either/both fine-skeletal laths crystals, indicating a fast cooling (Humphris, 2010). In sample A0546 exhibits a more developed crystal structure (euhedral crystal), indicative of a slower cooling rate (when the furnace would be hottest), compared to the other samples. On the other hand, fast cooling was also revealed by the high glass content in almost samples. In addition, the present of metallic iron is firmly confirmed that they were conducted from the smelting process and also the atmosphere was obviously a reducing condition (Piatak and Seal, 2011:641). It is interesting to note that, the presence of wüstite in only sample A0546 (observed by reflected light microscopy) points to a less efficient reduction process in this sample (Hani *et.al.*, 2011: 320).

Estimates of operating temperature based on the bulk chemistry in the simplified FeO-SiO<sub>2</sub>-Al<sub>2</sub>O<sub>3</sub> ternary diagrams in figure 21, all slag samples apparently were formed under different condition because these samples fall into two different regions: the hercynite region (sample A0588 and A0590), denoting a technology producing sufficient quantities of iron, with relatively low slag melting temperatures between 1,188 to 1,200 °C; the wüstite region, the iron rich corner of the system (A0586, A0594 and A0595) which indicating higher operating temperature of about 1,350 to 1,369 °C. However, the slag compositions of sample A0588 and A0590 plot within the optimum 1 zone which is explained by Charlton (2006) and Rehren *et.al* (2007) that slag of this composition is indicative of two potential scenario: either 1) an especially reducing smelting atmosphere, with more iron oxides being reduced to metal and proportionally less iron end up in the slag, or 2) a system with a substantial contribution of silica (through deliberate fluxing or the melting of technical ceramics and/or gangue), which in turn dilutes the bulk iron oxide content in the slag. In this case, due to the presence of iron metal (mainly as iron prills) in all samples as mentioned previously, it is strongly suggests that the atmosphere was obviously a reducing condition (Piatak and Seal, 2011: 641; Schmidt, 1997: 119-124; Humphris, 2010).

#### **4. Ban Khao Din Tai Archaeological Site**

The landforms around the study area comprise terrace and floodplain whereas the study area lies in the terrace. Six TL-dating samples have been obtained from furnace fragments at the site, these determinations provide evidence that the smelting activity occurred at this site from 1,232±99 years before present (BP) and continued throughout 1,099±88 years BP. This is older than the scientific dates of pieces of ceramics at the same site, that dated to 13<sup>th</sup> century AD or around 800 years BP.

The Ban Khao Din Tai slag evidence is entirely consistent with the expect waste product of the bloomery iron-making process according to their macroscopic, chemical compositional and microscopic information. The chemistry of the slag melt as well as the condition within the smelter determined which phase will ultimately

form in the slag. Therefore, the phase as well as their chemical composition and microstructure all provide insight into the smelting condition in their furnaces.

Regarding the bulk chemical composition, all samples have very similar chemical compositions, suggests that these samples were produced in a very similar manner in terms of the methodological approach to the technology and the ingredients used. This similarity in chemical composition between the slag samples is illustrated in table 10 as mentioned above. In addition, Alumina, silica and iron oxide are the main compounds in most iron smelting slags, together they make up over 90% of the bulk weight of the samples. This indicates that all of samples are metallurgical slags produced during the bloomery iron-making process. However, low content of CaO in all samples (0.289 to 0.910 wt.%), suggests that no flux was used in this operation but the process could benefit from the self-fluxing of used material ore (Tylecote, 1987).

The microstructure and phase composition show that fayalite and hercynite are dominant component of all samples. As mentioned in the bulk chemical compositions, all samples have relatively low CaO content which is in good agreement with the presence of fayalite. In contrast, if the system contains relatively high CaO content, the crystal may become Kirschsteinite ( $\text{CaFeSiO}_2$ ). Regarding the shapes of the fayalites in the samples, which can be informative in terms of the smelting process, and exists in all samples, they show the very fine- to fine-skeletal laths crystals. Technically, this very fine- to fine-skeletal laths crystals is formed when their solidification is speeded up by exposure to cooler air. This fast cooling may be due to many reasons during the processes. However, for the studied slags, it is assumed that they could have been produced by either being tapping out of furnace or dripped down into a cold slag pit (Venunan, 2011) and the presence of fayalite might be preliminarily indicate a relatively high operating temperature of exceed 1,100 °C (Maldonado, 2006). In addition, the relative high content of  $\text{Al}_2\text{O}_3$  related with abundant hercynites being seen in all slags (Muralha *et.al*, 2010).

All slag samples likely formed under similar condition, based on the FeO- $\text{SiO}_2$ - $\text{Al}_2\text{O}_3$  ternary diagrams in figure 26, all slag samples fall into hercynite region, denoting a technology producing sufficient quantities of iron, with relatively low slag

melting temperatures between 1,088 to 1,250 °C. In addition, the overall alumina to silica ratio within the slags at this site is relatively high at about 1:2, in the FeO-SiO<sub>2</sub>-Al<sub>2</sub>O<sub>3</sub> ternary diagrams the high alumina within the sample is apparent, in accordance with the generally dominant hercynite phase. However, the slag compositions of sample A0540 plot within the optimum 1 zone as mentioned in Ban Saitho 7 previously, this is strongly suggests that the atmosphere was obviously a reducing condition (Piatak and Seal, 2011: 641; Schmidt, 1997: 119-124; Humphris, 2010).

In summary, the four locations investigated within this study have provided a substantial amount of information concerning past copper and iron metallurgy in northeast Thailand, which complement and refine what we knew about this topic in a number of ways. Based upon the analyses, it appears that all four studied sites were occupied during the Ancient Time of Thailand. In addition, it is found that the geomorphological features and the distance to water source influenced the selection of the smelting site location in the Ancient Times. Four sites tend to be located in floodplain or terrace close to water space. This is probably because the distance to water source was the most important factor in selecting sites.

The Non Nong Hor slag evidence is entirely consistent with the expected waste product of an ancient copper smelting, probably utilising oxidic and sulphidic copper minerals or a dead-roasting of ore charge before smelting. The slag characteristics consistently indicate the metalworkers were different skilled smelters if compare to Non Pa Wai site in central Thailand (dated to Early Iron Age) (see more on Pryce, 2008). The principal sign of this technological change is the relatively different homogeneity of the slag, as evidenced by bulk chemical and smelting temperature. This technical could result from relatively different chemical composition (Table 13, figure 27) and operating temperatures at 1,200 to 1,369 °C, while the smelting temperature at Non Pa Wai is 1,100 to 1,300 °C (figure 28) as shown below.

**Table 13** Bulk chemical analyses of copper slags from Non Nong Hor (NNH) and Non Pa Wai (NPW) archaeological site (determined by XRF method, concentration in wt%).

| Element | Na <sub>2</sub> O | MgO   | Al <sub>2</sub> O <sub>3</sub> | SiO <sub>2</sub> | P <sub>2</sub> O <sub>5</sub> | SO <sub>3</sub> | K <sub>2</sub> O | CaO   | Cr <sub>2</sub> O <sub>3</sub> |
|---------|-------------------|-------|--------------------------------|------------------|-------------------------------|-----------------|------------------|-------|--------------------------------|
| Site    | Wt%               |       |                                |                  |                               |                 |                  |       |                                |
| NNH     | 0.000             | 0.000 | 0.000                          | 0.908            | 0.000                         | 0.069           | 0.306            | 0.279 | 0.000                          |
| NNH     | 0.000             | 0.000 | 0.000                          | 21.72            | 0.000                         | 0.309           | 0.445            | 0.030 | 0.000                          |
| NNH     | 0.000             | 0.000 | 0.000                          | 0.679            | 0.000                         | 11.30           | 0.429            | 0.028 | 0.000                          |
| NNH     | 0.000             | 0.000 | 0.000                          | 0.637            | 0.000                         | 4.800           | 0.271            | 0.927 | 0.113                          |
| NNH     | 0.000             | 0.000 | 0.000                          | 0.918            | 0.000                         | 0.000           | 0.350            | 0.090 | 0.000                          |
| NPW     | 0.700             | 0.300 | 1.400                          | 24.00            | 0.000                         | 2.600           | 0.000            | 10.50 | 0.000                          |
| NPW     | 0.500             | 0.300 | 3.200                          | 34.70            | 0.000                         | 0.900           | 0.100            | 11.30 | 0.000                          |
| NPW     | 0.500             | 0.500 | 3.800                          | 24.90            | 0.400                         | 1.500           | 0.200            | 4.800 | 0.000                          |
| NPW     | 0.500             | 0.700 | 2.700                          | 20.60            | 0.000                         | 6.000           | 0.100            | 8.400 | 0.000                          |
| NPW     | 0.300             | 0.500 | 4.800                          | 36.70            | 0.100                         | 0.700           | 0.200            | 9.000 | 0.000                          |
| NPW     | 0.400             | 0.200 | 1.900                          | 13.90            | 0.000                         | 3.000           | 0.100            | 4.800 | 0.000                          |
| NPW     | 0.200             | 0.000 | 3.800                          | 31.10            | 0.100                         | 12.40           | 0.100            | 10.10 | 0.000                          |
| NPW     | 0.600             | 0.100 | 1.700                          | 20.70            | 0.000                         | 0.900           | 0.000            | 5.000 | 0.000                          |
| NPW     | 0.400             | 1.100 | 4.500                          | 30.30            | 0.200                         | 1.600           | 0.200            | 9.800 | 0.000                          |
| NPW     | 0.500             | 1.200 | 6.400                          | 25.90            | 0.600                         | 0.800           | 0.300            | 13.30 | 0.000                          |
| NPW     | 0.900             | 0.400 | 4.800                          | 25.90            | 0.100                         | 0.900           | 0.100            | 6.000 | 0.000                          |
| NPW     | 0.800             | 0.200 | 1.300                          | 19.40            | 0.100                         | 0.400           | 0.100            | 6.400 | 0.000                          |
| NPW     | 0.400             | 0.100 | 3.400                          | 35.10            | 0.000                         | 1.300           | 0.100            | 13.90 | 0.000                          |
| NPW     | 0.600             | 0.400 | 2.800                          | 22.80            | 0.100                         | 3.000           | 0.100            | 6.400 | 0.000                          |
| NPW     | 0.400             | 0.200 | 2.200                          | 26.70            | 0.700                         | 2.000           | 0.100            | 4.900 | 0.000                          |
| NPW     | 0.700             | 0.300 | 2.200                          | 25.60            | 0.200                         | 5.800           | 0.100            | 4.800 | 0.000                          |
| NPW     | 0.400             | 1.400 | 3.000                          | 40.70            | 0.300                         | 0.700           | 0.100            | 18.00 | 0.000                          |
| NPW     | 0.800             | 0.100 | 1.700                          | 24.20            | 0.100                         | 1.300           | 0.200            | 3.100 | 0.000                          |
| NPW     | 0.500             | 0.900 | 5.300                          | 32.10            | 0.000                         | 1.400           | 0.300            | 15.60 | 0.000                          |

**Table 13** (Continued).

| Element | TiO <sub>2</sub> | MnO   | FeO   | CuO    | ZnO   | ZrO <sub>2</sub> | BaO   | PbO   |
|---------|------------------|-------|-------|--------|-------|------------------|-------|-------|
| Site    | Wt%              |       |       |        |       |                  |       |       |
| NNH     | 0.000            | 1.269 | 81.43 | 6.567  | 0.000 | 0.103            | 0.000 | 0.000 |
| NNH     | 0.000            | 0.950 | 63.88 | 3.312  | 2.239 | 0.000            | 0.000 | 0.000 |
| NNH     | 0.000            | 1.242 | 75.10 | 4.429  | 0.673 | 0.000            | 8.210 | 0.789 |
| NNH     | 0.000            | 2.937 | 83.54 | 2.020  | 0.247 | 0.000            | 0.000 | 0.000 |
| NNH     | 0.000            | 1.187 | 82.73 | 4.949  | 0.504 | 0.000            | 0.000 | 0.000 |
| NPW     | 0.100            | 0.100 | 54.00 | 6.100  | 0.000 | 0.000            | 0.000 | 0.000 |
| NPW     | 0.100            | 0.200 | 46.60 | 2.000  | 0.000 | 0.000            | 0.000 | 0.000 |
| NPW     | 0.100            | 0.300 | 62.00 | 0.900  | 0.000 | 0.000            | 0.000 | 0.000 |
| NPW     | 0.100            | 0.200 | 58.00 | 2.600  | 0.000 | 0.000            | 0.000 | 0.000 |
| NPW     | 0.100            | 0.400 | 45.30 | 1.600  | 0.000 | 0.000            | 0.000 | 0.000 |
| NPW     | 0.000            | 0.100 | 71.00 | 4.400  | 0.000 | 0.000            | 0.000 | 0.000 |
| NPW     | 0.100            | 0.500 | 32.20 | 3.500  | 0.000 | 0.000            | 0.000 | 0.000 |
| NPW     | 0.000            | 0.100 | 66.00 | 4.600  | 0.000 | 0.000            | 0.000 | 0.000 |
| NPW     | 0.100            | 0.200 | 50.60 | 0.700  | 0.000 | 0.000            | 0.000 | 0.000 |
| NPW     | 0.100            | 0.600 | 48.10 | 2.000  | 0.000 | 0.000            | 0.000 | 0.000 |
| NPW     | 0.100            | 0.400 | 53.30 | 7.000  | 0.000 | 0.000            | 0.000 | 0.000 |
| NPW     | 0.000            | 0.600 | 59.40 | 11.10  | 0.000 | 0.000            | 0.000 | 0.000 |
| NPW     | 0.100            | 0.300 | 44.20 | 0.900  | 0.000 | 0.000            | 0.000 | 0.000 |
| NPW     | 0.100            | 0.300 | 59.10 | 4.300  | 0.000 | 0.000            | 0.000 | 0.000 |
| NPW     | 0.100            | 0.200 | 61.30 | 1.200  | 0.000 | 0.000            | 0.000 | 0.000 |
| NPW     | 0.000            | 0.200 | 44.20 | 15.700 | 0.000 | 0.000            | 0.000 | 0.000 |
| NPW     | 0.000            | 0.600 | 32.80 | 1.900  | 0.000 | 0.000            | 0.000 | 0.000 |
| NPW     | 0.000            | 0.100 | 59.90 | 8.200  | 0.000 | 0.000            | 0.000 | 0.000 |
| NPW     | 0.100            | 0.300 | 41.80 | 1.500  | 0.000 | 0.000            | 0.000 | 0.000 |



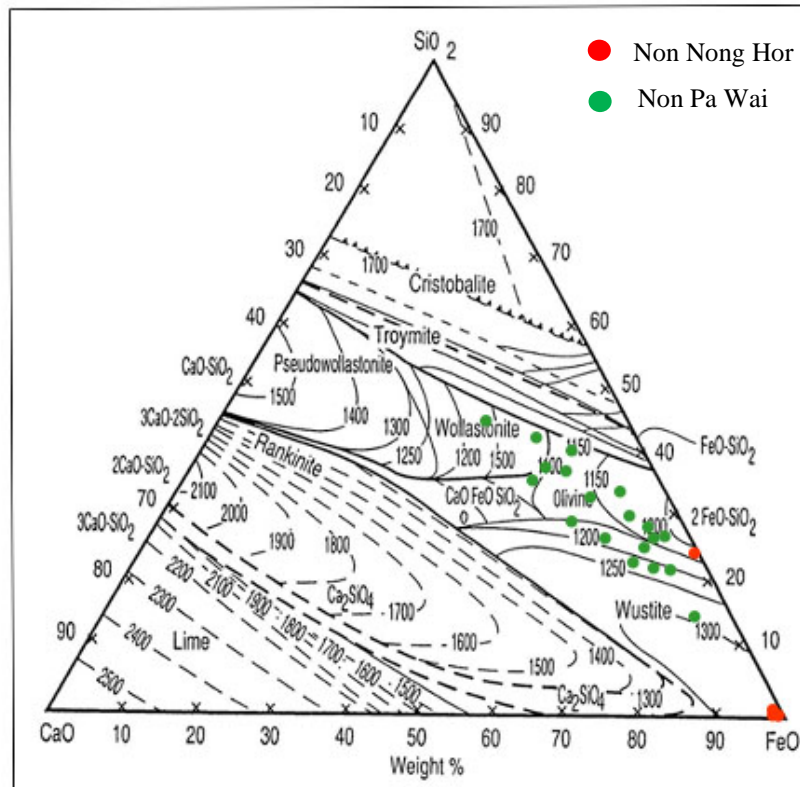


**Figure 28** FeO-CaO-SiO<sub>2</sub> ternary diagrams presenting the distribution of studied slags from Non Nong Hor (red circle) and Non Pa Wai archaeological site (green circle).

**Source:** Chiarantini *et al.* (2008)

Regarding the analyses of the iron slag samples, some significant differences emerge regarding the organization of iron production at Krok Kroy, Ban Saitho 7 and Ban Khao Din Tai, in spite of their relative geographic proximity and comparable chronology (especially, in case of Ban Saitho 7 and Ban Khao Din Tai). On the other hand, at Ban Khao Din Tai, it is found a standardized and relatively high efficient technology (comparing to Krok Kroy and Ban Saitho 7). While at Krok Kroy and Ban Saitho 7, the picture is that of both, relatively high efficient technology and a somewhat more haphazard and less efficient technology. The above analyses have shown that similar internal technological processes were undertaken at the site of Ban Khao Din Tai, a fair chemical uniformity of slags intimates that these slags were produced from the same efficient operation, the relatively similar set of raw materials

were also employed. On the other hand, they have shown that different internal technological processes were undertaken at the site of Krok Kroy and Ban Saitho 7 that is, the smelting system at these site produced both slag compositions closer to/ approaching the so-called optimum 1, whereas other portions plot closer to the iron rich corner. This is reflects different engineering solution (Charlton, 2006; Rehren, 2007) that, in turn, may speak of different iron making behaviors. By tweaking the ore to charcoal ratio, the air input and the flux employed, the smelter could have used the different set of raw materials and their production methods were also difference (table 14, figure 29, 30).

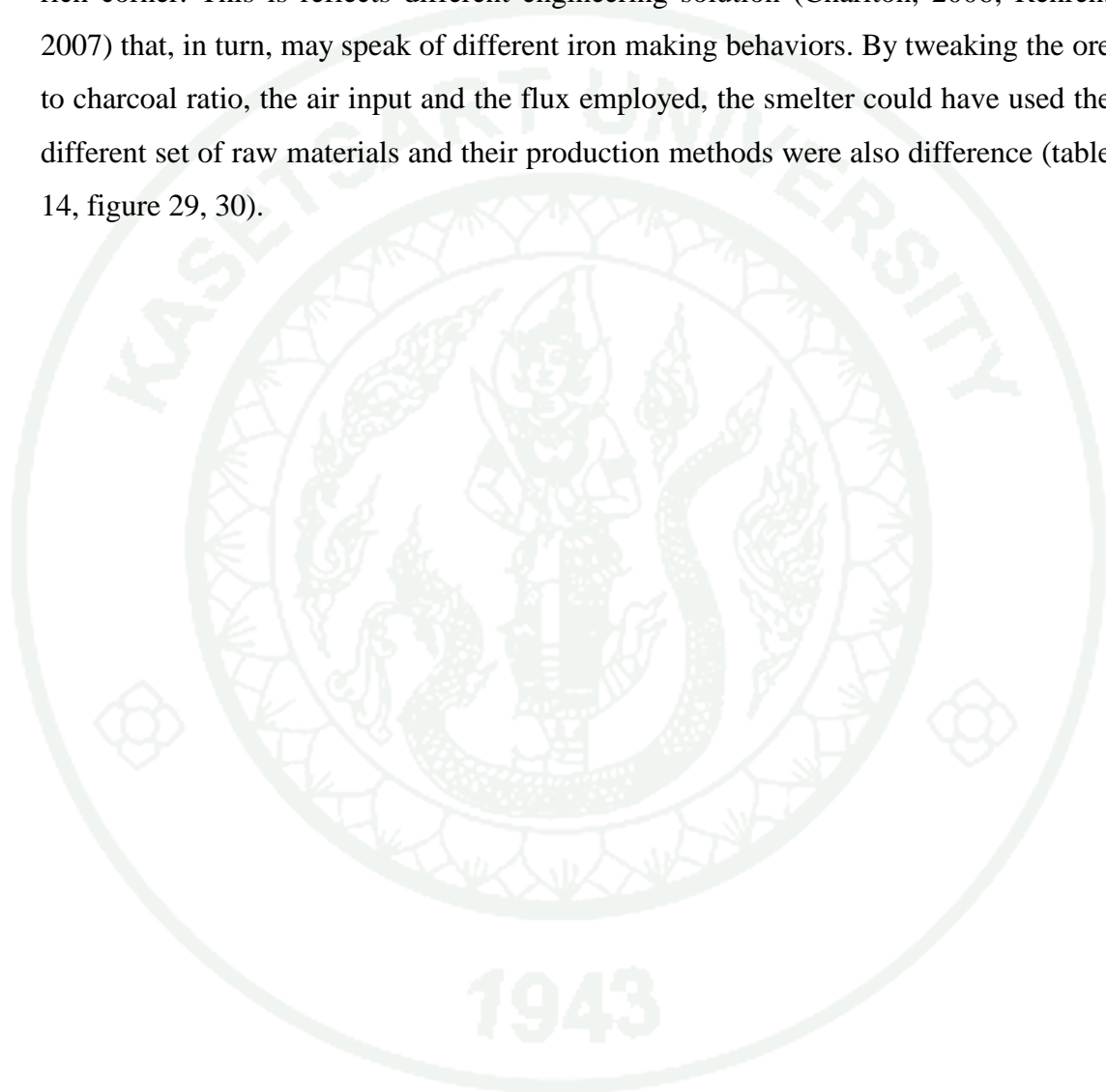


**Table 14** Bulk chemical analyses of iron slags from Khok Kroy (BKT), Ban Saitho 7 (STH) and Ban Khao Din Tai (KDT) archaeological site. (determined by ED-XRF method, concentration in wt%).

| Element | Al <sub>2</sub> O <sub>3</sub> | SiO <sub>2</sub> | K <sub>2</sub> O | CaO   | TiO <sub>2</sub> | V <sub>2</sub> O <sub>5</sub> | Cr <sub>2</sub> O <sub>3</sub> | MnO   | FeO   | SrO   | ZrO <sub>2</sub> | CdO   | BaO   |
|---------|--------------------------------|------------------|------------------|-------|------------------|-------------------------------|--------------------------------|-------|-------|-------|------------------|-------|-------|
| Site    | Wt%                            |                  |                  |       |                  |                               |                                |       |       |       |                  |       |       |
| BKT     | 0.000                          | 1.826            | 0.092            | 0.921 | 2.544            | 0.088                         | 0.158                          | 4.456 | 80.16 | 0.078 | 0.281            | 0.000 | 0.469 |
| BKT     | 12.28                          | 26.27            | 0.174            | 0.131 | 2.234            | 0.086                         | 0.16                           | 2.349 | 50.52 | 0.000 | 0.077            | 0.000 | 0.103 |
| BKT     | 11.21                          | 27.82            | 0.000            | 1.098 | 2.073            | 0.275                         | 0.211                          | 1.130 | 50.47 | 0.021 | 0.064            | 0.000 | 0.000 |
| BKT     | 0.000                          | 1.229            | 0.279            | 0.235 | 2.457            | 0.000                         | 0.265                          | 6.581 | 78.78 | 0.000 | 0.202            | 0.000 | 1.195 |
| BKT     | 0.000                          | 0.807            | 0.000            | 0.817 | 1.402            | 0.163                         | 0.116                          | 1.392 | 85.60 | 0.064 | 0.104            | 0.000 | 0.000 |
| STH     | 12.36                          | 32.27            | 0.23             | 0.466 | 0.381            | 0.216                         | 0.101                          | 0.327 | 48.24 | 0.000 | 0.044            | 0.000 | 0.000 |
| STH     | 13.41                          | 35.09            | 0.35             | 0.705 | 0.441            | 0.185                         | 0.111                          | 0.336 | 44.37 | 0.000 | 0.051            | 0.000 | 0.000 |
| STH     | 0.000                          | 1.389            | 0.572            | 4.006 | 3.096            | 0.313                         | 0.206                          | 1.716 | 79.38 | 0.123 | 0.241            | 0.117 | 0.000 |
| STH     | 0.000                          | 0.876            | 0.350            | 0.468 | 0.000            | 0.117                         | 0.000                          | 0.768 | 87.61 | 0.000 | 0.056            | 0.000 | 0.000 |
| STH     | 0.000                          | 0.982            | 1.117            | 1.457 | 0.271            | 0.07                          | 0.125                          | 0.639 | 85.75 | 0.033 | 0.000            | 0.000 | 0.000 |
| KDT     | 12.15                          | 26.23            | 0.344            | 0.466 | 1.898            | 0.182                         | 0.138                          | 0.456 | 52.25 | 0.000 | 0.064            | 0.000 | 0.000 |
| KDT     | 11.58                          | 27.91            | 0.192            | 0.289 | 1.621            | 0.155                         | 0.118                          | 0.443 | 51.84 | 0.000 | 0.054            | 0.028 | 0.000 |
| KDT     | 11.63                          | 33.97            | 0.298            | 0.91  | 1.792            | 0.153                         | 0.125                          | 0.925 | 45.10 | 0.014 | 0.057            | 0.000 | 0.000 |
| KDT     | 12.20                          | 28.07            | 0.317            | 0.754 | 1.997            | 0.08                          | 0.068                          | 0.445 | 50.39 | 0.000 | 0.061            | 0.000 | 0.000 |
| KDT     | 12.70                          | 29.76            | 0.331            | 0.307 | 1.257            | 0.133                         | 0.068                          | 0.572 | 49.31 | 0.000 | 0.069            | 0.000 | 0.000 |

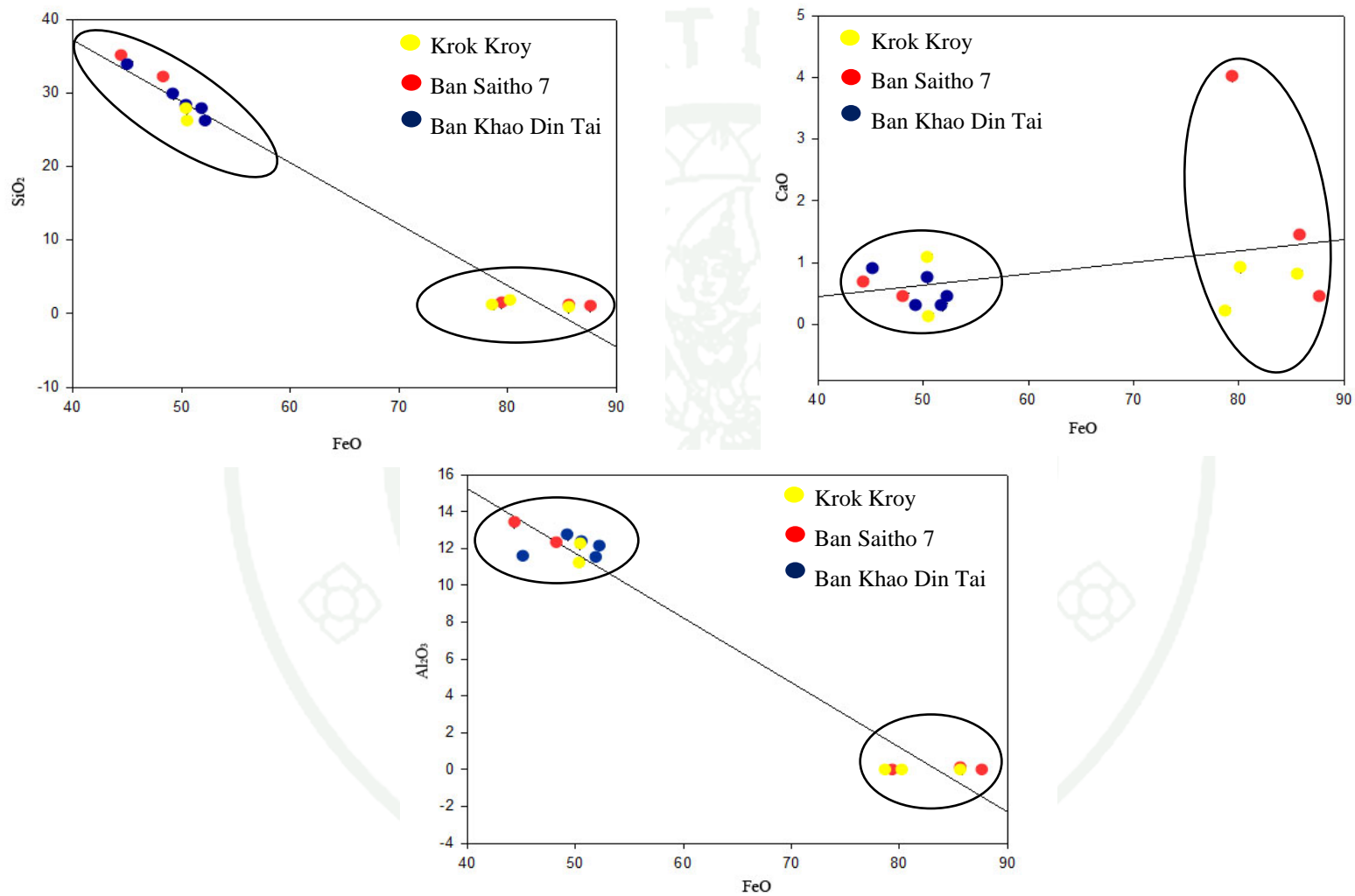


**Figure 29** Bivariate compositional scatter plots of FeO-SiO<sub>2</sub>, FeO-CaO and FeO-Al<sub>2</sub>O<sub>3</sub> of iron slags from Khok Kroy, Ban Saitho 7 and Ban Khao Din Tai archaeological site. (Oxides are shown in wt%.)

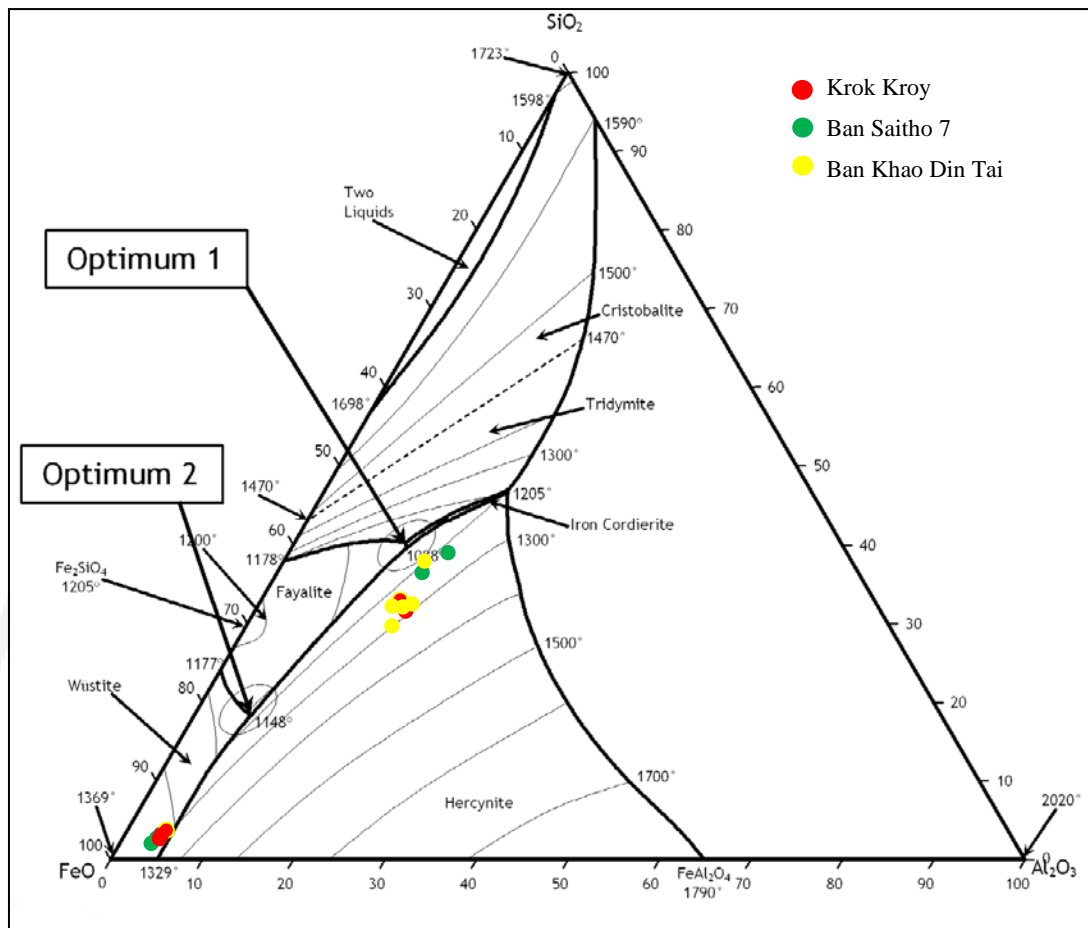


**Figure 30** FeO-SiO<sub>2</sub>-Al<sub>2</sub>O<sub>3</sub> ternary diagram, presenting the distribution of studied slags from Krok Kroy (red circle), Ban Saitho 7 (green circle) and Ban Khao Din Tai (yellow circle) archaeological site.

**Source:** Rehren *et al.* (2007)

## CONCLUSION

The aim of this study was to utilize an archaeometallurgical approach by using Geoarchaeological and Archaeometrical techniques to undertake an investigation of copper and iron smelting traditions in northeast Thailand. Non Nong Hor, Khok Kroi, Ban Saitho 7 and Ban Khao Din Tai was selected to provide a suitable study areas, as copper and iron production was already known to have been carried out for over several decades, but specific scientific reconstruction of the processes involved was lacking. This new fieldwork intensively focused on generating original archaeometallurgical data which was then interpreted and placed within the broader archaeological, linguistic, historical and ethnographic understandings of the region. This method has provided an enhanced insight into the complex role of copper and iron production in northeast Thailand's history, as well as a greater understanding of the manner in which technology was an active element influenced in the past.

It appears that the smelting activity occurred in four study area during the Ancient Time. In addition, four sites tend to be located in floodplain or terrace close to water space. This is probably because the distance to water source was the most important factor in selecting sites. The Ancient Time of Non Nong Hor copper process may be used the oxidic copper ores with sulphidic copper ores or a dead-roasting of ore charge before smelting, the smelting process was at high enough temperature to afford good liquation of the metal through the slag. Whist, the iron production at Krok Kroy, Ban Saitho 7 and Ban Khao Din Tai slag evidence is entirely consistent with the expect waste product of the bloomery iron-making process (direct process). At Ban Khao Din Tai, the author finds a standardised and relatively high efficient technology if compared to Krok Kroy and Ban Saitho sites. While, at Krok Kroy and Ban Saitho 7, the picture of each site is that of both, relatively high efficient technology and a somewhat more haphazard and less efficient technology, this is reflects different engineering solution and style of production. Finally, it is interesting to note that, the bloomery iron smelting process (direct smelting process) may practice continually in some area in northeast and/or other regions of Thailand

without interference from indirect smelting process from China or other smelting process.

It should be emphasized that the lack of an established baseline or measuring system to quantify standardization, is a problem to be future addressed in future work, in a way that is relevant from an anthropological viewpoint. Here the author has used simple numerical means to demonstrate difference between sites, and the author is confident that they represent two different pattern of human behavior. However, in other case, difference within or between site may be more subtle, and in those cases a question will remain as to whether the material difference are significant in human terms. The analytical study of smelting remain where relevant historical information attest to the scale and standardization of the production technologies may aid in establishing reference parameters for future comparison, but a degree of uncertainty will remain (Humphris *et.al*, 2008: 368-369).

Regarding the chronological study, it should be noted that, the methods chosen for chronological investigations of the smelting activity in the future should focus more on materials directly associated with this smelting process such as the smelting slag, charcoal, tuyère, etc. and also more on other dating methods such as radiocarbon dating, fission track dating and optically stimulated luminescence. However, the sampling of charcoal sample for radiocarbon dating has to be taken cautiously, if a charcoal sample in question has not come from an ancient hearth or the equivalent (Higham, 1983) so that the excavator can be absolutely certain that the carbon in the sample was not re-deposited from earlier levels.

## LITERATURE CITED

- Amzallag, N. 2009. From Metallurgy to Bronze Age Civilizations: The Synthetic Theory. **American Journal of Archaeology** 113: 497-519.
- Artoili, G. n.d. **Archaeometallurgy: the contribution of mineralogy**. n.p. (Unpublished manuscript)
- Azhar, S. 2007. **Synthesis of well defined hematite films and their use for sintering studies**. M.S. Thesis. Luleå University of Technology.
- Aitken, M.J. 1985. **Thermoluminescence Dating**. Academic Press, England.
- Blakelock, E., M. Martínón-Torres, H.A. Veldhuijzen and T. Young. 2009. Slag inclusions in iron objects and the quest for provenance: an experiment and a case study. **Journal of Archaeological Science** 36: 1745–1757.
- Bachmann, H.G. 1982. **The Identification of Slags from Archaeological Sites**. Left Coast Press, England.
- Bakraji, E.H. 2011. Study of Syrian archaeological pottery by the combined application of thermoluminescence (TL) dating, X-ray fluorescence analysis and statistical multivariate analysis. **Nuclear Instruments and Methods in Physics Research B** 269: 2052-2056.
- Bani-Hani, M., R. Abd-Allah and L. El-Khoury. 2012. Archeometallurgical finds from Barsinia, Northern Jordan: Microstructural characterization and conservation treatment. **Journal of Cultural Heritage** 13: 314-325.
- Ben-Yosef, E., L. Tauxe and T. E. Levy. 2010. Archaeomagnetic dating of copper smelting site f2 in the Timna valley (Israel) and its implications for the modeling of ancient technological developments. **Archaeometry** 52 (6): 1110-1121.

- Buchwald, V.F. and H. Wivel. 1998. Slag Analysis as a Method for the Characterization and Provenancing of Ancient Iron Objects. **Materials Characterization** 40: 73-96.
- Butzer, K.W. 1982. **Archaeology as human ecology**. Cambridge University Press, England.
- Charoenwongsa P. and Bronson B. 1988. **Prehistoric Studies: The Stone and Metal Ages in Thailand**. The Thai Antiquity Working Group, Thailand.
- Chiarantini, L., M. Benvenuti, P. Costagliola, M.E. Fedi, S. Guideri and A. Romualdi. 2009. Copper production at Baratti (Populonia, southern Tuscany) in the early Etruscan period (9<sup>th</sup> - 8<sup>th</sup> centuries BC). **Journal of Archaeological Science** 36: 626–1636.
- Chirikure, S., R.B. Heimann and D. Killick. 2010. The technology of tin smelting in the Rooiberg Valley, Limpopo Province, South Africa, ca. 1650-1850 CE. **Journal of Archaeological Science** 37: 1656–1669.
- Callister, W.D. and D.G. Rethwisch. 2012. **Fundamentals of Materials Science and Engineering: An Integrated Approach**. 4<sup>th</sup> ed. John Wiley and Sons, USA.
- Caterina, I., T. Maurizio and S. Giuseppe. 2008. Archaeometallurgy in Messina: Iron slag from a dig at block P, Laboratory analyses and Interpretation. **Mediterranean Archaeology and Archaeometry** 8 (1): 49-60.
- Connolly, J.R. 2012. **Introduction to X-Ray Powder Diffraction**. n.p.
- Darvill, T. 2010. **Concise Oxford Dictionary of Archaeology**. Oxford University Press, USA.
- Department of Lands. 1987. **NAKHON RATCHASIMA, roll 48, run 71, image number 358-360**.
- \_\_\_\_\_. 1988. **SURIN, roll 302-327, run 11, image number 309-310**.

Department of Lands. 1991. **UBON-YASD-MUKDAHAN, roll 94-112, run 09, image number 105-106.**

Dillmann, P. and R. Balasubramaniam. 2011. Characterization of ancient Indian iron and entrapped slag inclusions using electron, photon and nuclear microprobes. **Bull. Mater. Sci.** 24 (3): 317-322.

Doménech-Carbó, A., M.T. Doménech-Carbó and V. Costa. 2009. **Electrochemical Methods in Archaeometry, Conservation and Restoration.** Springer, Berlin.

Eliyahu-Behar, A., N. Yahalom-Mack, S. Shilstein, A. Zukerman, C. Shafer-Elliott, A.M. Maeir, E. Boaretto, I. Finkelstein and S. Weiner. 2012. Iron and bronze production in Iron Age IIA Philistia: new evidence from Tell es-Safi/Gath, Israel. **Journal of Archaeological Science** 39: 255-267.

Ettler, V., Z. Johan, B. Křibek, and H. Nolte. 2009. Mineralogy of primary phases in slags and mattes from the Tsumeb smelter (Namibia). **Communs geol. Surv. Namibia** 14: 3-14.

\_\_\_\_\_, \_\_\_\_\_, \_\_\_\_\_, O. Šebek, and M. Mihaljevič. 2009. Mineralogy and environmental stability of slags from the Tsumeb smelter, Namibia. **Applied Geochemistry** 24: 1-15.

Figueiredo, E., R.J.C. Silva, J.C. Senna-Martinez, M.F. Araújo, F.M.B. Fernandes and J.L.I. Vaz. 2010. Smelting and recycling evidence from the Late Bronze Age habitat site of Baiões (Viseu, Portugal). **Journal of Archaeological Science** 37: 1623–1634.

Fine Art Department. 2007. **Ban Chiang Heritage.** Dok Bia Publication, Bangkok.

Gautier, A. 2001. Luminescence dating of archaeometallurgical slag: use of the SAR technique for determination of the burial dose. **Quaternary Science Reviews** 20: 973-980.

- Gimeno Adelantado, J.V., M.A. Ferrer Eres, F.M. Valle Algarra, J. Peris Vicente and F. Bosch Reig. 2003. Analytical study by SEM/EDX and metallographic techniques of materials used in the iron production process during the iberian period. **Talanta** 60: 895-910.
- Godfrey-Smith, D.I. and J.L. Casey. 2003. Direct thermoluminescence chronology for Early Iron Age smelting technology on the Gambaga Escarpment, Ghana. **Journal of Archaeological Science** 30: 1037–1050.
- Goldberg, P. and R.I. Macphail. 2006. **Practical and Theoretical Geology**. Blackwell Publishing Company, England.
- Goldstein, I.J., D. Newbury, D. Joy, C. Lyman, P. Echlin, L. Sawyer and J. Michael. 2003. **Scanning Electron Microscopy and X-ray Microanalysis**. 3<sup>rd</sup> ed. Plenum Publishers, New York.
- Goodhew, P.J. and F.J. Humphreys. 1998. **Electron microscopy and Analysis**. 2<sup>nd</sup> ed. Alden Press, London.
- Gorai, B. and R.K. Jana. 2003. Characteristics and utilisation of copper slag-a review. **Resources, Conservation and Recycling** 39: 299-313.
- Hagihara, N., S. Miono, Z. Chengzhi, Y. Nakayama, K. Hanamoto and S. Manabe. 1999. The combined application of PIXE analysis and thermoluminescence (TL) dating for elucidating the origin of iron manufacturing in Japan. **Nuclear Instruments and Methods in Physics Research B** 150: 635-639.
- Higham, C., T. Higham, R. Ciarla, K. Douka, A. Kijngam and F. Rispoli. 2011. The Origins of the Bronze Age of Southeast Asia. **J World Prehist** 24: 227–274.
- Holl, A.F.C. 2009. Early West African Metallurgies: New Data and Old Orthodoxy. **J World Prehist** 22: 415-438.
- Humphris J.E. 2010. **An Archaeometallurgical Investigation of Iron Smelting Traditions in Southern Rwanda**. Ph.D. Thesis, University College London.

- Iles, L. and M. Martín-Torres. 2009. Pastoralist iron production on the Laikipia Plateau, Kenya: wider implications for archaeometallurgical studies. **Journal of Archaeological Science** 36: 2314-2326.
- Jenkins, R. 1999. **X-ray fluorescence spectrometry**. 2<sup>nd</sup> ed. A Wiley-interscience publication, New York.
- Jiménez-Sánchez, M., I. González-Álvarez, O. Requejo-Pagés and M.J. Domínguez-Cuesta. 2011. Enhancing rescue-archaeology using geomorphological approaches: Archaeological sites in Paredes (Asturias, NW Spain). **Geomorphology** 132: 99-110.
- Jones, A. 2004. Archaeometry and materiality: Materials-based analysis in theory and practice. **Archaeometry** 46 (3): 327-338.
- Khursheed, A. 2011. **Scanning Electron Microscope Optics and Spectrometers**. World Scientific Publishing, Singapore.
- Lawes, G. 1987. **Scanning Electron Microscopy and X-ray Microanalysis**. John Wiley and Sons, London.
- Lely, T.E., R.B. Adams, A. Hauptmann, M. Prange, S. Schmitt-Strecker and M. Najjar. 2002. Early Bronze Age metallurgy: a newly discovered copper manufactory in southern Jordan. **Antiquity** 76: 425-437.
- Manasse, A. and M. Mellini. 2002. Chemical and textural characterisation of medieval slags from the Massa Marittima smelting sites (Tuscany, Italy). **Journal of Cultural Heritage** 3: 187-198.
- Mihailova, I. and D. Mehandjiev. 2010. Characterization of fayalite from copper slags. **Journal of the University of Chemical Technology and Metallurgy** 45 (3): 317-326.
- Murillo-Barroso, M., T.O. Pryce, B. Bellina and M. Martín-Torres. 2010. Khao Sam Kaeo-an archaeometallurgical crossroads for trans-asiatic technological traditions. **Journal of Archaeological Science** 37: 1761-1772.

- Nakanishi, A. 2008. Mössbauer study of ancient iron smelting slag in Japan. **Hyperfine Interact** 186: 135–139.
- Ocean King India Company. 2009. **XRF: Brief Introduction**. Available Source: <http://www.goldtester.co/xrf.html>, January 23, 2013.
- Pryce, T.O. 2008. **Prehistoric Copper Production and Technological Reproduction in the Khao Wong Prachan Valley of central Thailand**. Ph.D. Thesis, University College London.
- \_\_\_\_\_ and S. Natapintu. 2010. Smelting Iron from Laterite: Technical Possibility or Ethnographic Aberration. **Asian Perspectives** 48 (2): 249-264.
- \_\_\_\_\_, C. Chiemsisouraj, V. Zeitoun and H. Forestier. 2011. An 8<sup>th</sup>-9<sup>th</sup> century AD iron smelting workshop near Saphim village, NW Lao PDR. **Historical Metallurgy** 45 (2): 81-89.
- \_\_\_\_\_, M. Brauns, N. Chang, E. Pernicka, A.M. Pollard, C. Ramsey, T. Rehren, V. Souksavatdy and T. Sayavongkhamdy. 2011. Isotopic and technological variation in prehistoric Southeast Asian primary copper production. **Journal of Archaeological Science** 38: 3309-3322.
- Prokop, P. and I. Suliga. 2013. Two thousand years of iron smelting in the Khasi Hills, Meghalaya, North East India. **Current Science** 104 (6): 761-768.
- Paine, D.P. and J.D. Kiser. 2012. **Aerial Photography and Image Interpretation**. 3<sup>rd</sup> ed. John Wiley & Sons, New Jersey.
- Park, J.S. and T. Rehren. 2011. Large-scale 2<sup>nd</sup> to 3<sup>rd</sup> century AD bloomery iron smelting in Korea. **Journal of Archaeological Science** 38: 1180-1190.
- Perkins, D. and K.R. Henke. 2004. **Minerals in Thin Section**. 2<sup>nd</sup> ed. Prentice Halls, New Jersey.

- Piatak, N.M. and R.R. Seal II. 2010. Mineralogy and the release of trace elements from slag from the Hegeler Zinc smelter, Illinois (USA). **Applied Geochemistry** 25: 302-320.
- \_\_\_\_\_ and \_\_\_\_\_. 2012. Mineralogy and environmental geochemistry of historical iron slag, Hopewell Furnace National Historic Site, Pennsylvania, USA. **Applied Geochemistry** 27: 623-643.
- Pigott, V.C. and R. Ciarla. n.d. **On the origins of metallurgy in prehistoric Southeast Asia: the view from Thailand**. n.p. (Unpublished manuscript)
- Rapp, G. 2009. **Archaeomineralogy (Natural Science in Archaeology)**. Springer, Berlin.
- Rapp, G.J. and C.L. Hill. 2006. **Geoarchaeology: The Earth Science Approach to Archaeological Interpretation**. 2<sup>nd</sup> ed. Yale University Press, London.
- Reardon, A.C. 2011. **Metallurgy for the Non-Metallurgist**. 2<sup>nd</sup> ed. ASM International, USA.
- Rehren, T. and E. Pernicka. 2008. Coins, Artifacts and Isotopes: Archaeometallurgy and Archaeometry. **Archaeometry** 50 (2): 232-248.
- \_\_\_\_\_, L. Boscher and E. Pernicka. 2012. Large scale smelting of speiss and arsenical copper at Early Bronze Age Arisman, Iran. **Journal of Archaeological Science** 39: 1717-1727.
- Reimer, L. 1998. **Scanning electron microscopy: physics of image formation and microanalysis**. Springer, Berlin.
- Royal Thai Survey Department. n.d. **3-RTSD, Series L7017, Sheet 5637-4**.
- \_\_\_\_\_. n.d. **3-RTSD, Series L7017, Sheet 5638-1**.
- \_\_\_\_\_. n.d. **3-RTSD, Series L7017, Sheet 5638-2**.

Royal Thai Survey Department. n.d. **6-RTSD, Series L7017, Sheet 5941-4.**

\_\_\_\_\_. n.d. **6-RTSD, Series L7017, Sheet 5941-4.**

\_\_\_\_\_. 1996. **R.T.S.D., roll 5/40 (1), image number 206-207.**

Sheikh, M.R., B.S. Acharya and R.K. Gartia. 2010. Characterization of iron slag of Kakching, Manipur by X-ray and optical spectroscopy. **Indian Journal of Pure and Applied Physics** 48: 632-634.

Selskienė, A. 2007. Examination of smelting and smithing slags formed in bloomery iron-making process. **Chemija** 18 (2): 22-28.

The University of Manchester. 2012. **Microscope.** Available Source: <http://www.microscopy.manchester.ac.uk/microscope>, January 31, 2013.

Thornton, C.P. and T. Rehren. 2009. A truly refractory crucible from fourth millennium Tepe Hissar, Northeast Iran. **Journal of Archaeological Science** 36: 2700-2712.

Tylecote, R.F. 1962. **Metallurgy in Archaeology: A Prehistory of Metallurgy in the British Isles.** Edward Arnold, London.

White, J.C. and E.G. Hamilton. 2009. The Transmission of Early Bronze Technology to Thailand: New Perspectives. **J World Prehist** 22: 357-397.

Watt, I.M. 1996. **The principles and practice of electron microscopy.** 2<sup>nd</sup> ed. University Press, Cambridge.

Yoopom, I. 2010. The study of Iron-smelting furnaces ay Ban Khao DinTai, Ban Kruad district, Buriram Province. Master thesis, Silpakorn University.

Zacharias, N., C. Michael, O. Philaniotou-Hadjianastasiou, A. Hein and Y. Bassiakos. 2006. Fine-grain TL dating of archaeometallurgical furnace walls. **Journal of Cultural Heritage** 7: 23-29.



**APPENDICES**



**Appendix A**

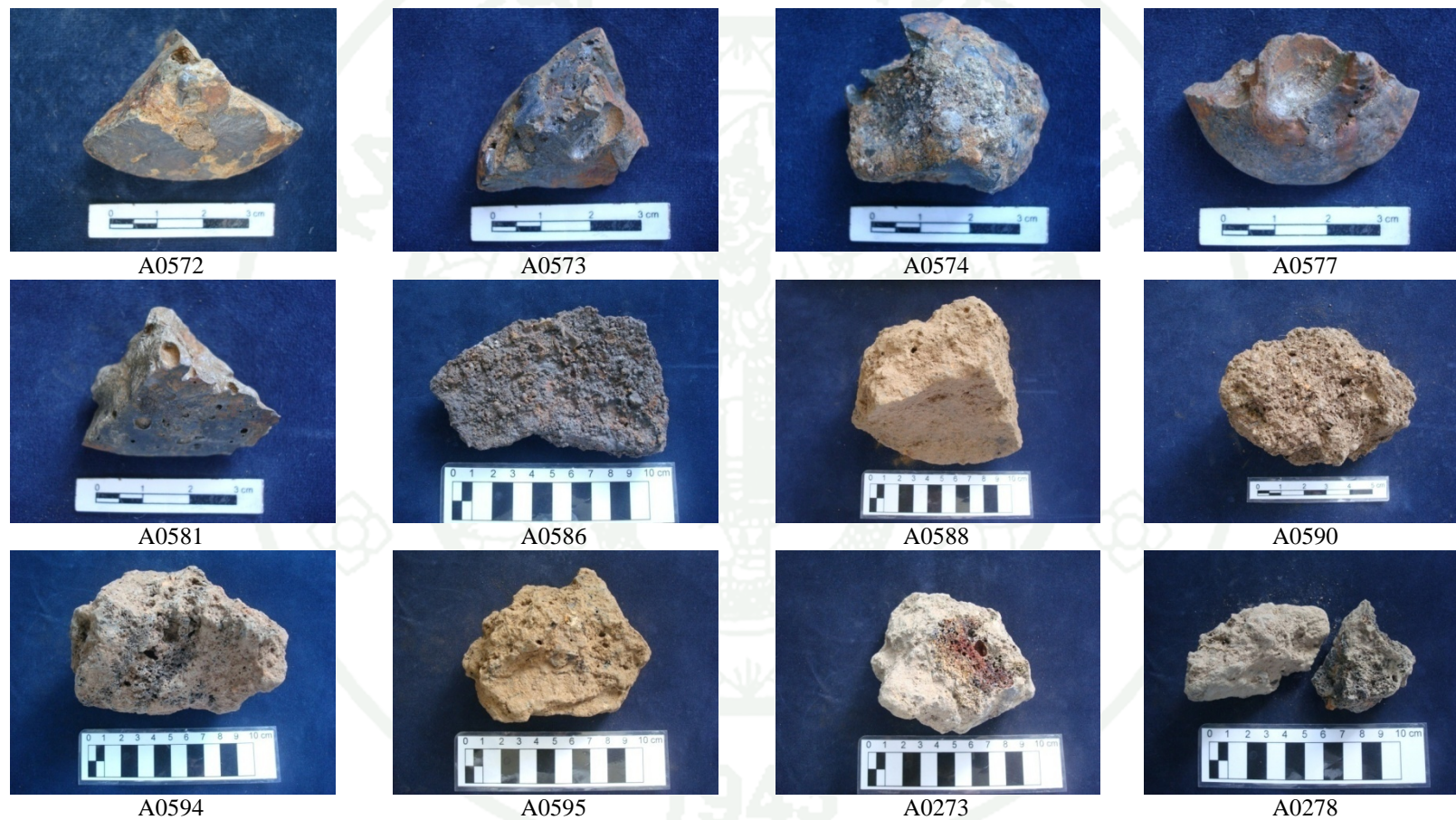
Slag sample and TL sample, catalogues and images

**Appendix Table A1** Slag sample catalogue.

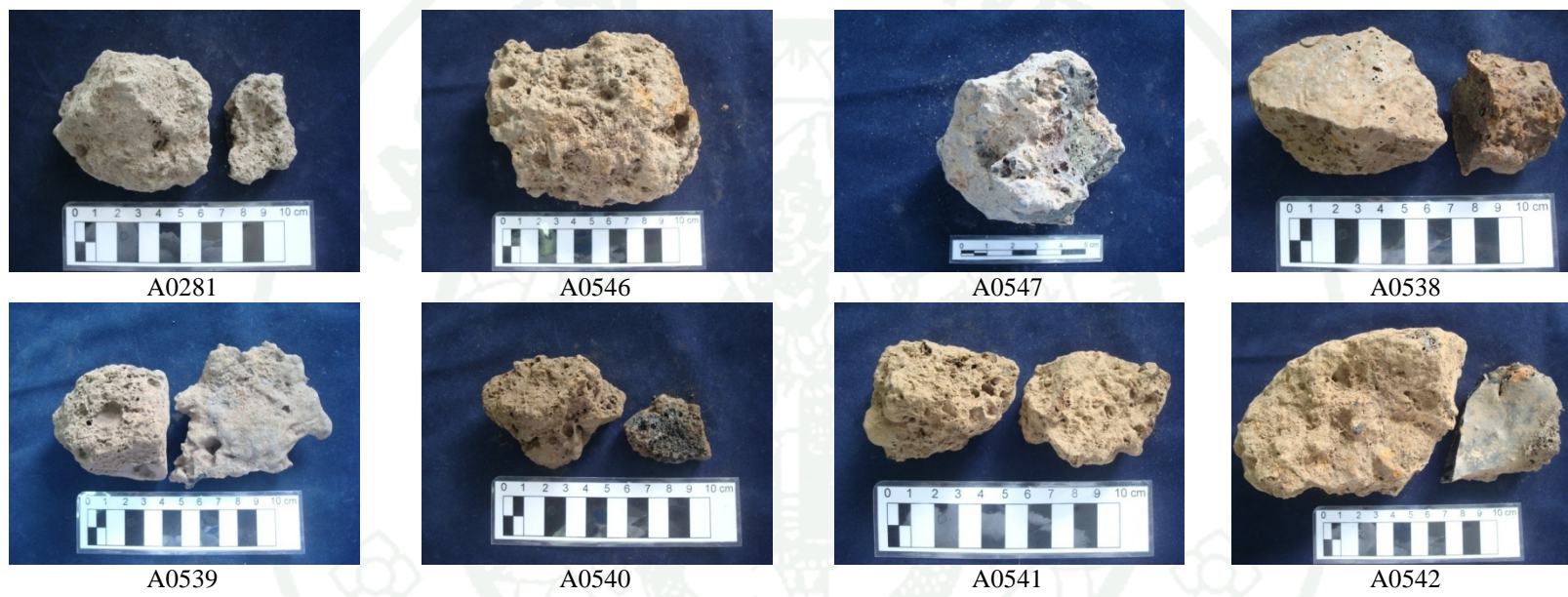
| No | Lab ID | Archaeological Site | Sample ID   |
|----|--------|---------------------|---|
| 1  | A0572  | Noen Nong Ho        | NNH 1   |
| 2  | A0573  | Noen Nong Ho        | NNH 2   |
| 3  | A0574  | Noen Nong Ho        | NNH 3   |
| 4  | A0577  | Noen Nong Ho        | NNH 4   |
| 5  | A0581  | Noen Nong Ho        | NNH 5   |
| 6  | A0586  | Khok Kroy           | BKT   |
| 7  | A0588  | Khok Kroy           | BKT'11#0659 (BKT'11 KK TP.1 G14 X 198 cm., Y 458 cm., Z 98 cm.DT  |
| 8  | A0590  | Khok Kroy           | BKT'11#0627 (BKT'11 KK TP.1 G7 X 17 cm., Y 259 cm., Z 105 cm.DT   |
| 9  | A0594  | Khok Kroy           | BKT'11#0637 (BKT'11 KK TP.1 G12 X 223 cm., Y 393 cm., Z 101 cm.DT |
| 10 | A0595  | Khok Kroy           | BKT'11#0460 (BKT'11 KK TP.1 G10 X 30 cm., Y 370 cm., Z 101 cm.DT  |
| 11 | A0273  | Ban Saitho 7        | STH 2 : 2009  |
| 12 | A0278  | Ban Saitho 7        | STH 7 : 2009  |
| 13 | A0281  | Ban Saitho 7        | STH 10 : 2009   |
| 14 | A0546  | Ban Saitho 7        | STH'10 T.1/W1/NEQ (6) 100-110 cm.dt (#086)                        |
| 15 | A0547  | Ban Saitho 7        | STH'2009 T.1/WQ (10) 140-150 cm.dt (#218)                         |

**Appendix Table A1** (continued).

| No. | Lab ID | Archaeological Site | Sample ID                            |
|-----|--------|---------------------|--------------------------------------|
| 16  | A0538  | Ban Khao Din Tai    | KDT'07 TP.1 NEQ Furnace#1 (#041/3)   |
| 17  | A0539  | Ban Khao Din Tai    | KDT'07 TP.1 NEQ Furnace#2 (#9136/3)  |
| 18  | A0540  | Ban Khao Din Tai    | KDT'07 TP.1 SEQ Furnace#3 (#108)     |
| 19  | A0541  | Ban Khao Din Tai    | KDT'07 TP.1 NWQ Furnace#4 (#0155/1)  |
| 20  | A0542  | Ban Khao Din Tai    | KDT'08 TP.1 NWQ 200-210 cm.dt (#109) |



**Appendix Figure A1** Images of slag samples.



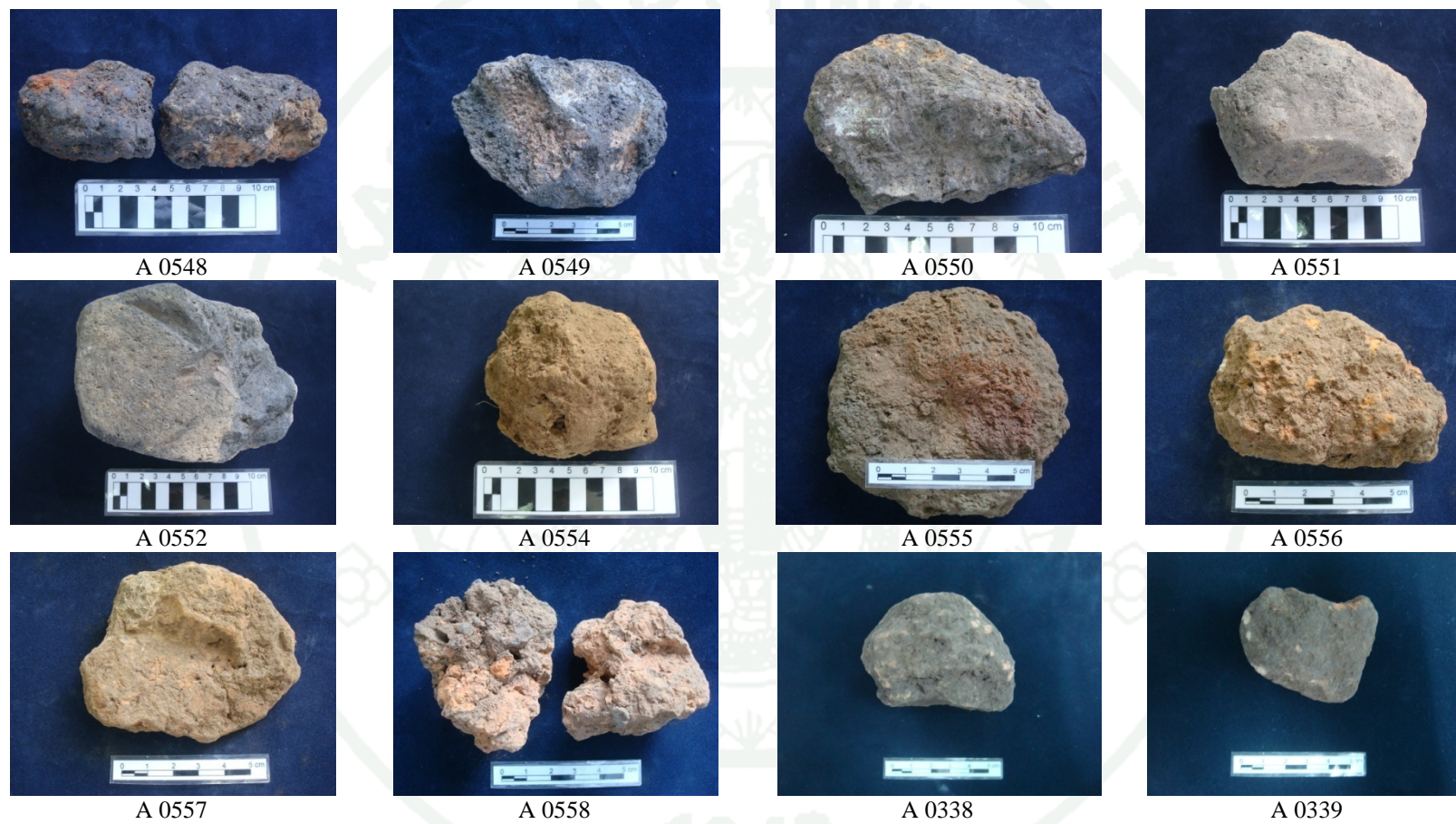
**Appendix Figure A1** (Continued).

**Appendix Table A2** TL sample catalogue (Smelting furnace fragment, potsherds and baked sediment).

| No. | Lab ID | Archaeological Site | Sample ID  | Object         |
|-----|--------|---------------------|--|----------------|
| 1   | A 0548 | Noen Nong Ho        | NNH 2011 TL sample #1  | Furnace        |
| 2   | A 0549 | Noen Nong Ho        | NNH 2011 TL sample #2  | Furnace        |
| 3   | A 0550 | Noen Nong Ho        | NNH 2011 TL sample #3  | Furnace        |
| 4   | A 0551 | Noen Nong Ho        | NNH 2011 TL sample #4  | Furnace        |
| 5   | A 0552 | Noen Nong Ho        | NNH 2011 TL sample #5  | Furnace        |
| 6   | A 0554 | Khok Kroy           | BKT'11#0520 (BKT'11 KK TP.1 G12 X 235 cm., Y 346 cm., Z 100 cm.dt. | baked sediment |
| 7   | A 0555 | Khok Kroy           | BKT'11#0668 (BKT'11 KK TP.1 G15 X 227 cm., Y 495 cm., Z 109 cm.dt. | Furnace        |
| 8   | A 0556 | Khok Kroy           | BKT'11#0515 (BKT'11 KK TP.1 G12 X 235 cm., Y 333 cm., Z 107 cm.dt. | Furnace        |
| 9   | A 0557 | Khok Kroy           | BKT'11#0535 (BKT'11 KK TP.1 G12 X 210 cm., Y 384 cm., Z 98 cm.dt.  | Furnace        |
| 10  | A 0558 | Khok Kroy           | BKT'11#0687 (BKT'11 KK TP.1 G14 X 134 cm., Y 497 cm., Z 99 cm.dt.  | Furnace        |
| 11  | A 0338 | Ban Saitho 7        | STH'09 L.1 60-70 cm.dt   | Furnace        |
| 12  | A 0339 | Ban Saitho 7        | STH'09 L.3 80-90 cm.dt   | Furnace        |
| 13  | A 0340 | Ban Saitho 7        | STH'09 L.4 90-100 cm.dt  | Furnace        |
| 14  | A 0341 | Ban Saitho 7        | STH'09 L.4 90-100 cm.dt  | Furnace        |

**Appendix Table A2 TL (Continued).**

| No. | Lab ID | Archaeological Site | Sample ID  | Object    |
|-----|--------|---------------------|--|-----------|
| 15  | A 0272 | Ban Saitho 7        | STH1   | Potsherds |
| 16  | A 0277 | Ban Saitho 7        | STH6   | Potsherds |
| 17  | A 0282 | Ban Saitho 7        | STH11  | Furnace   |
| 18  | A 0335 | Ban Khao Din Tai    | KDT'07 TP.1 NEQ S. 0 -100 cm.dt                          | Furnace   |
| 19  | A 0336 | Ban Khao Din Tai    | KDT'07 TP.1 SWQ L.11 170 -180 cm.dt                      | Furnace   |
| 20  | A 0337 | Ban Khao Din Tai    | KDT'07 TP.1 L.12-L.17 170-180 cm.dt                      | Furnace   |
| 21  | A 0607 | Ban Khao Din Tai    | KDT'08 TP.1 NEQ (FN#1,2) (2)-(3) (#152/001) 80-100 cm.dt | Furnace   |
| 22  | A 0605 | Ban Khao Din Tai    | KDT'08 TP.1 SWQ (16)-(18) (#008/001) 220-240 cm.dt       | Furnace   |
| 23  | A 0606 | Ban Khao Din Tai    | KDT'08 TP.1 NWQ (20) (#120/002) 260-270 cm.dt            | Furnace   |



**Appendix Figure A2** Images of TL samples (Smelting furnace fragment, potsherds and baked sediment samples).



A 0340



A 0341



A 0272



A 0277



A 0282



A 0335



A 0336



A 0337



A 0607

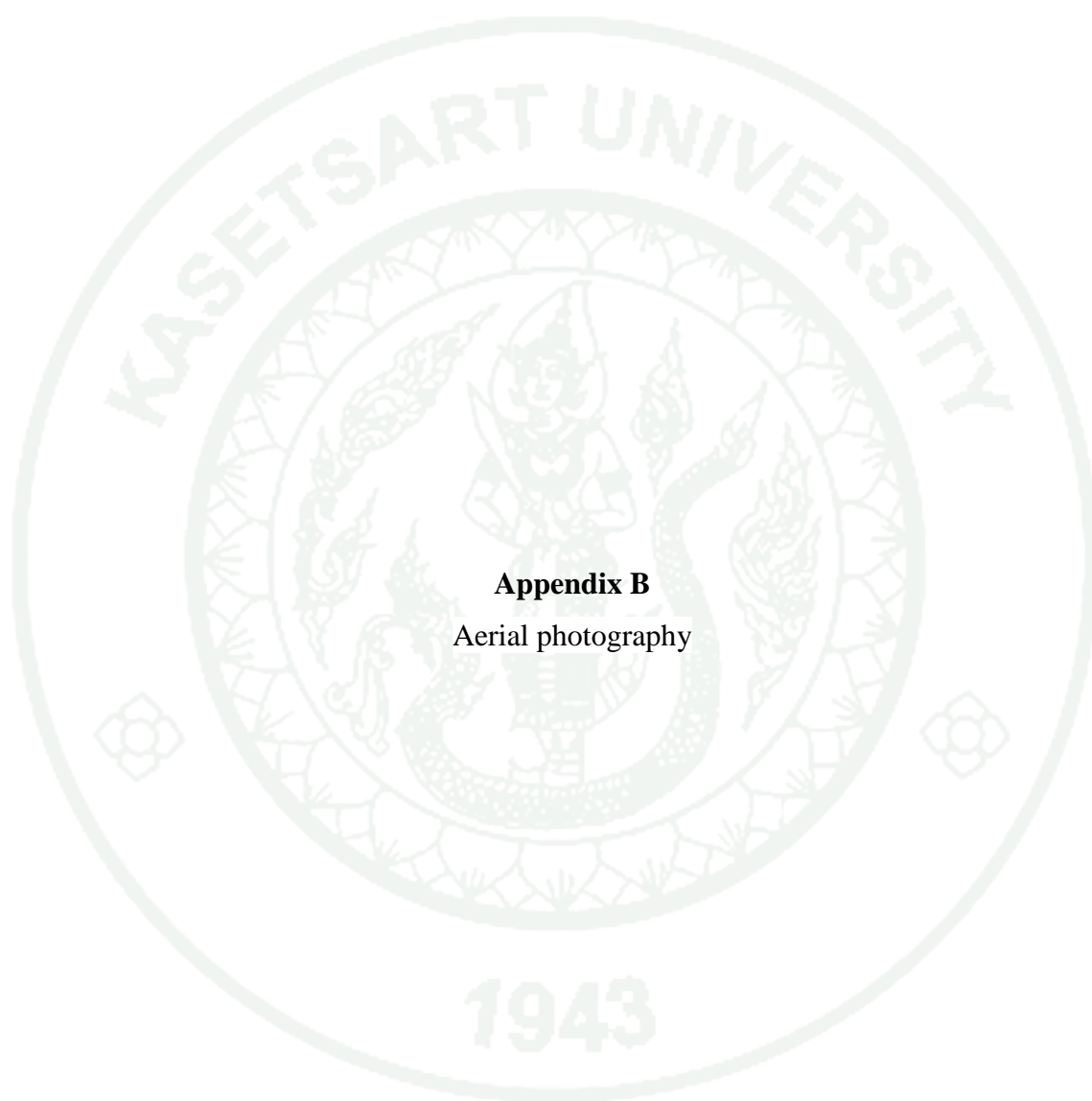


A 0605



A 0606

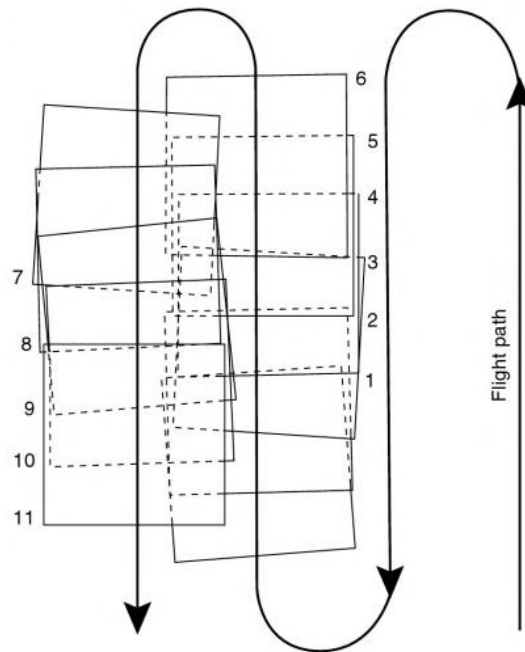
**Appendix Figure A2 (Continued).**



**Appendix B**  
Aerial photography

## Aerial photography

The study of aerial photography whether it be photogrammetry or photo interpretation, is a subset of a much larger discipline called remote sensing. Aerial photographs are taken at lower altitude, either from airplanes, from small balloons or photo towers constructed at the site. It has been used for over a century to depict landscapes and these early photographs have been valuable in documenting recent landscape modifications and their rates of change, even if they are over relatively short time spans. Aerial photographs may be further classified as vertical or oblique. The first type of aerial photo is oblique photographs, in which the axis of the photograph is purposely tilted between  $3^{\circ}$  and  $90^{\circ}$  from the vertical. If the horizon is not visible, the photo is a low oblique. If the horizon is visible, the photo is a high oblique. Terrestrial photos are usually obliques or horizontals where the axis of the camera is tilted about  $90^{\circ}$  from the vertical (Paine and Kiser, 2012: 28). It provides somewhat an artistic feeling for the landscape and relief and landscape features—both cultural and natural—are enhanced. The second type, vertical aerial photographs are more useful in archaeology and geology and thus it is used in this study. This is because the stereographic properties of overlapping vertical photographs can be used to view the ground surface in three dimensions. An airplane flying at a specific altitude will take a series of photographs so that there is about 60 percent overlap from one photograph to the next, and about 25 percent sidelap of photographs from successive adjacent flight paths (appendix figure B1). When two of the overlapping pairs are viewed with a stereoscope, a three dimensional image of the landscape can be seen. These stereo images provide a much clearer view of the landscape, including the vertical and spatial distribution of rocks and strata, vegetation, springs and other important features.



**Appendix Figure B1** Stylized view of flight path of airplane for vertical aerial photos that can be used for stereoscopic viewing in three dimensions.

**Source:** Goldberg and Macphail (2006)

Interpretation of aerial photographs translates the visual patterns on the photograph into information that becomes useable to the observer. The typical characteristics that are observed include the following.

- (1) Shape: morphology of objects, some are characteristic, some not.
- (2) Size: both absolute and relative, particularly with regard to the scale of the photograph.
- (3) Pattern: the spatial arrangement of individual entities, including repetition, layout and ordering.
- (4) Tone and hue: relative brightness or color of objects or materials; different types of soils will have different tones.

(5) Texture: frequency of change of tones and their arrangement on the photograph, typically by objects too small to be seen individually.

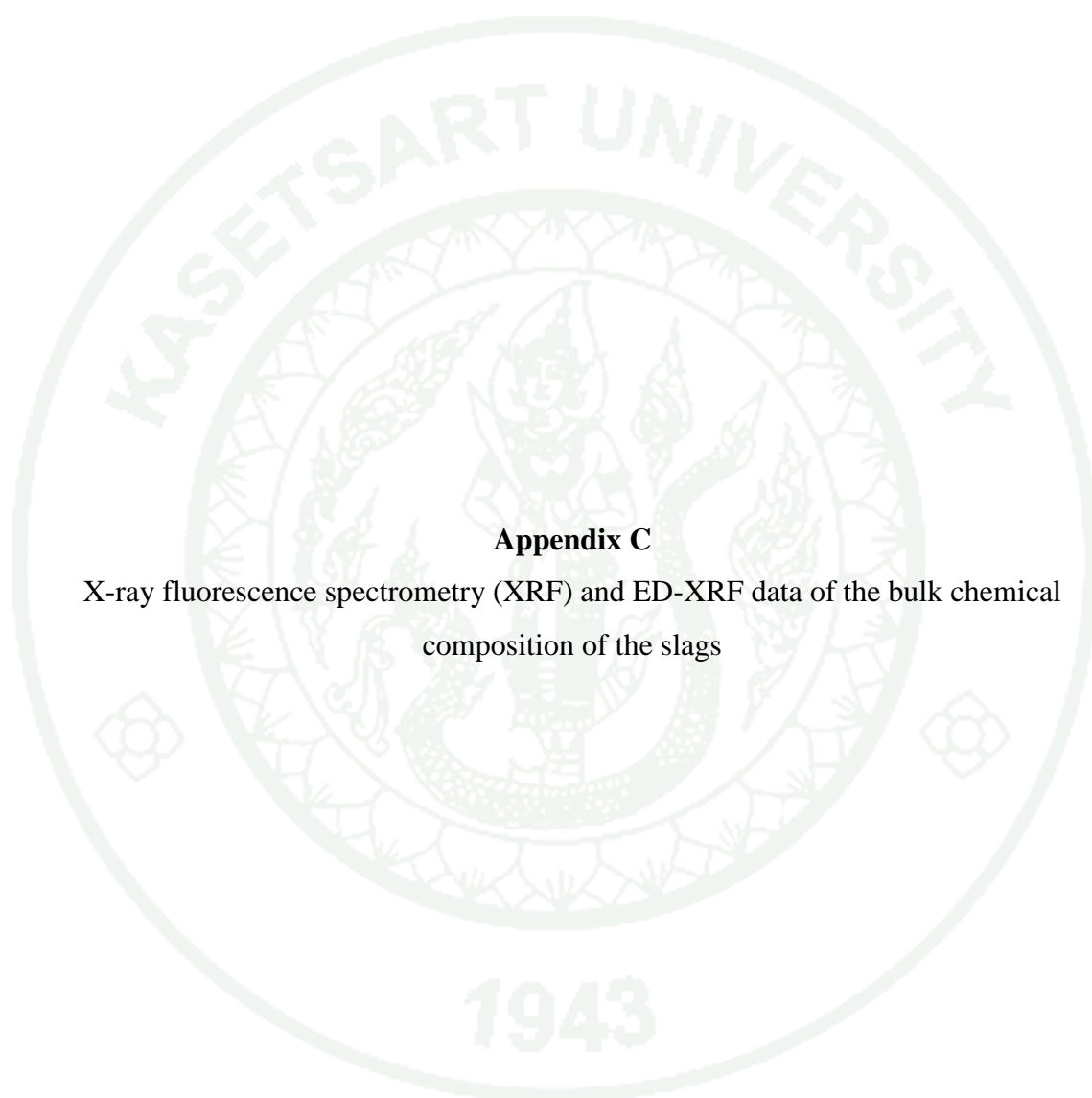
(6) Shadows: provide outline and relief, particularly if the photograph is taken at a low angle to the sun.

(7) Site: topographic or geographic location, reflecting.

Awareness, knowledge and experience with the above can be applied to geoarchaeological situations, with particular emphasis on geology and soils.

#### Aerial photographs in archaeology

Aerial photographs are often useful for seeing things that are simply invisible on the ground. Aerial photograph in archaeology has a long history, going back to photographs of the well-known site of Stonehenge in England, which was photographed from a military balloon in 1906. This tradition continued into the 1920s, and up to the present, with photographs of Bronze Age and Roman sites. A classical example of early work in archaeology is that Bradford and González (1960), mapped over 2,000 Etruscan graves at the site of Tarquinia in Italy. Most of these tombs were not visible at the surface, although some had been previously discovered centuries before. Aerial photographs can be used not only to discover sites—both on land and submerged—but also used for making measurements, constructing maps and three dimensional renditions of site and surroundings (Goldberg and Macphail, 2006: 302-306).



### **Appendix C**

X-ray fluorescence spectrometry (XRF) and ED-XRF data of the bulk chemical composition of the slags

## X-ray fluorescence spectrometry (XRF)

X-ray fluorescence spectrometry is a means of qualitatively and quantitatively determining elements by measurement of the wavelengths and intensities of characteristic emissions. This technique based upon the principle that individual atoms, when excited by an external energy source, the emission of x-ray photons of a characteristic energy (or wavelength) can be occurred. By counting the number of x-ray photons of energy that emitted from a sample, the elements present may be identified and quantitated. XRF is applicable to all but the very low atomic number elements, with sensitivities down to the low part per million levels. There are many different types of XRF instruments available, based on several different source and dispersion configurations. The most commonly employed instruments are based either on the energy dispersive method (ED-XRF) or wavelength dispersive method (WD-XRF). In ED-XRF, a solid-state detector is used to count the x-ray photons, simultaneously sorting them according to energy and storing the result in a multichannel memory. The result is the x-ray energy versus intensity spectrum.

In this study, the aim was to study the applicability of an ED-XRF to the multi-elemental analysis of ancient copper and slags from the archaeometallurgical site. For more details of WD-XRF, see x-ray fluorescence spectrometry by Ron Jenkins. Before we can use the x-rays for analytical purposes, we need to know the properties of x-rays as shown below.

### 1. The properties of X-ray

X-rays are short-wavelength electromagnetic radiation with energies ranging from about 100 eV to 10 MeV. It is different from the other electromagnetic radiation in wavelength and energy. X-rays show wave nature with wavelength ranging from about 10 to  $10^{-3}$  nm. According to the quantum theory, the electromagnetic wave can be treated as particles called photons or light quanta. The essential characteristics of photons are summarized as follows.

The propagation velocity ( $c$ ) of electromagnetic wave with frequency ( $\nu$ ) and wavelength ( $\lambda$ ) is given by the relation (1).

$$c = \nu\lambda \quad (1)$$

where:  $c$  is a velocity of photon in  $\text{ms}^{-1}$

The velocity of light in the vacuum is a universal constant given as  $c = 2.998 \times 10^8$  m/s. Each photon has energy ( $E$ ), which is proportional to its frequency,

$$E = h\nu = \frac{hc}{\lambda} \quad (2)$$

Where:  $E$  is an energy of photon in keV

$h$  is a Planck constant ( $6.6260 \times 10^{-34}$  J.s)

$\lambda$  is a wavelength of photon in nm, then the following relation is obtained,

$$E = \frac{1.240}{\lambda} \quad (3)$$

The momentum ( $p$ ) is given by  $mv$ , the product of the mass ( $m$ ), and its velocity ( $v$ ). The de Broglie relation for material wave relates wavelength to momentum.

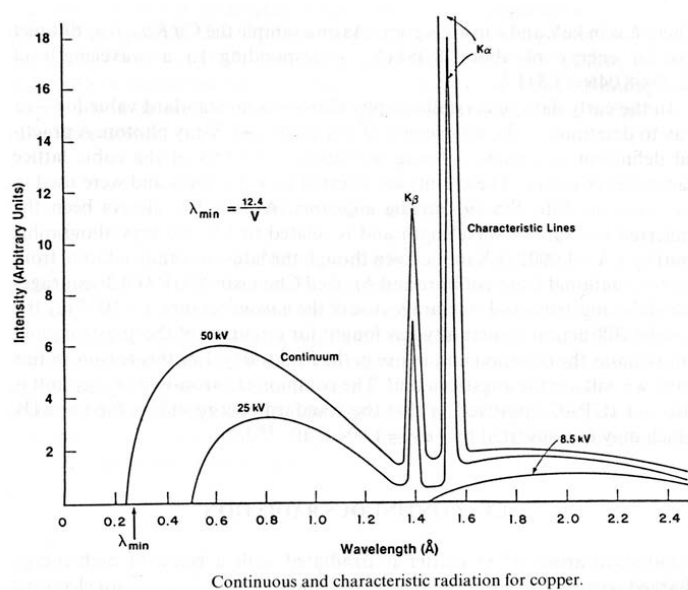
$$\lambda = \frac{h}{p} = \frac{h}{mv} \quad (4)$$

The velocity of light can be reduced when traveling through a material medium, but it does not become zero.

## 2. Production of X-rays

As we have known, when bombardment of a material with high energy particles will result in the emission of Characteristic x-ray, whose wavelengths depend on the nature of the atom in a specimen, together with Continuous radiation (Bremsstrahlung radiation) of all wavelengths down to a minimum corresponding to the incident electron energy. Both x-ray emissions are shown in appendix figure C1.

This continuous radiation is produced as the impinging high energy electrons are decelerated by the atomic electrons of the elements, the loss in electron energy  $\Delta E$  that occurs in such a deceleration event is emitted as a photon. The energy of this photon is  $\Delta E = h\nu$ , where  $h$  is Planck's constant and  $\nu$  is the frequency of the electromagnetic radiation as mentioned in The properties of x-ray. Because the interactions are random, the electron may lose any amount of energy in a single deceleration event. Therefore, the bremsstrahlung can take on any energy value from zero up to the original energy of the incident electron, forming a continuous electromagnetic spectrum.



**Appendix Figure C1** Continuous and characteristic radiation for copper.

**Source:** Connolly (2012)

The intensity of the continuous radiation is important in analytical x-ray fluorescence spectrometry because it forms a background under the characteristic peaks. Once a photon is created with a specific energy, it is impossible to determine whether it is a continuum or a characteristic x-ray. Thus, the background intensity due to the continuum process, occurring at the same energy as a characteristic x-ray, sets a limit to the minimum amount of an element that can be detected. The continuum is

therefore usually regarded as a nuisance to the analyst. (Goldstein *et al.*, 2003: 271-274).

If a high energy particle, strikes a bound atomic electron, and the energy  $E$  of the particle is greater than the binding energy ( $\phi$ ) of the atomic electron, it is possible that the atomic electron will be ejected from its atomic position, departing from the atom with a kinetic energy ( $E - \phi$ ), equivalent to the difference between that of the initial particle and the binding energy of the atomic electron. The ejected electron is called a photoelectron and the interaction is referred to as the photoelectric effect. While the fate of the ejected photoelectron has little consequence as far as the production and use of characteristic x-radiation (appendix figure C1) from an atom is concerned. As long as the vacancy in the shell exists, the atom is in an unstable state and there are two processes by which the atom can revert back to its original state. The first of these involves a rearrangement that does not result in the emission of x-ray photon, but in the emission of other photoelectrons from the atom. The effect is known as the Auger effect, and the emitted photoelectrons are called Auger electrons. The second process by which the excited atom can regain stability is by transference of an electron from one of the outer orbital to fill the vacancy. The energy difference between the initial and final states of the transferred electron may be given off in the form of an x-ray photon. Since all emitted x-ray photons have energies proportional to the difference in the energy states of atomic electrons, the line from a given element will be characteristic of that element (Jenkins, 1999: 5-6).

### 3. Interactions of X-rays with matter

XRF is concerned with several kinds of interactions of x-rays with matter. Absorption events occur when a photon incident on a sample interacts with electrons and gives up all its energy, disappearing in the process. It does so by causing transitions of electrons from lower atomic energy levels to higher levels. This leaves vacancies in the lower levels, which are filled a short time later by transitions of electrons from higher levels down to lower ones. The stored energy may be released radiatively, by emitting fluorescence radiation at a lower energy than the incident, or non-radiatively, by kicking off an electron in an Auger process. The cascade of de-

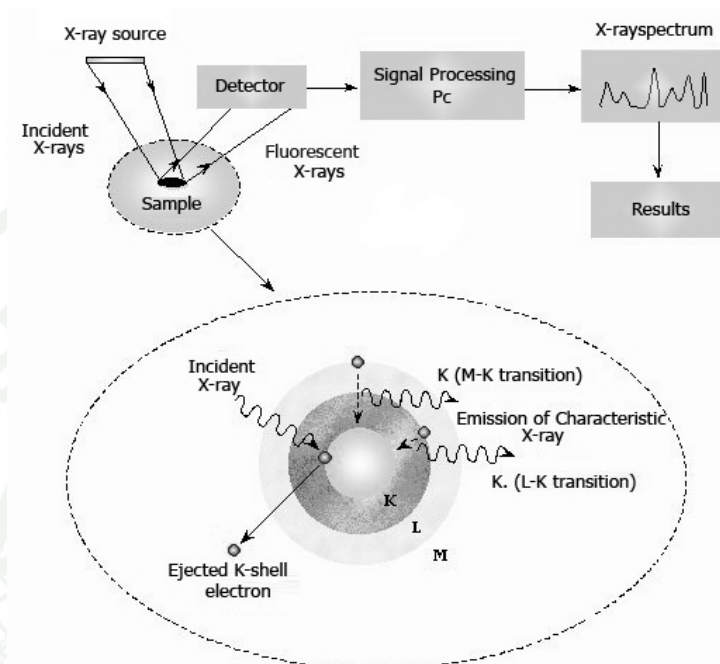
excitation following an absorption event can be complicated, because a sequence of many singles and multi-electron processes are possible. Photons generally are emitted at x-ray, UV-visible, and infrared wavelengths, electrons may be ejected from the atoms, and heat pulses are produced following the primary absorption event. These decay modes afford a number of possible detection methods, the most common of which are fluorescence and electron yield detection. Elastic scattering events occur when a photon impinges on a sample, interacts with the electrons, and a photon of the same frequency but different direction is emitted.

From a classical point of view, an incident electromagnetic wave causes the electrons bound to an atom to oscillate back and forth, and these accelerating electrons generate their own secondary wave field that has the same frequency as the incident wave. Elastic scattering takes place between photons and bound electrons and forms the basis of x-ray diffraction (see more details in x-ray diffraction spectrometry). Inelastic scattering events differ from elastic scattering events in that the frequency of the emitted photon is not the same as the incident photon; it is generally of lower frequency, i.e. lower energy. The energy difference between the scattered and incident photons is transferred to the sample by inducing electronic transitions in the same manner as absorption events. It will come as no surprise that Elastic Scattering, Inelastic Scattering, and Absorption events are closely related, and in fact can be viewed as different aspects of the same phenomena. Experimentally we tend to focus on one process or another, but they are intimately connected (Bunker, 2010).

#### 4. Energy dispersive x-ray fluorescence spectrometry

Energy dispersive x-ray fluorescence is an analytical technique used for the elemental analysis or chemical characterization of a sample. It is one of the variants of XRF. It relies on the investigation of a sample through interactions between incident x-rays and matter, x-ray photons emitted by the matter in response to being hit with charged particles. Its characterization capabilities are due in large part to the fundamental principle that each element has a unique atomic structure

allowing x-rays that are characteristic of an element's atomic structure to be identified uniquely from each other.



**Appendix Figure C2** The measurement of ED-XRF.

**Source:** Ocean King India company (2009)

To stimulate the emission of characteristic x-rays from a specimen, a high energy beam of incident x-rays, is focused into the sample being studied. At rest, an atom within the sample contains ground state electrons in discrete energy levels or electron shells bound to the nucleus. The incident beam may excite an electron in an inner shell, ejecting it from the shell while creating an electron hole where the electron was. An electron from an outer, higher-energy shell then fills the hole, and the difference in energy between the higher-energy shell and the lower energy shell may be released in the form of characteristic x-ray photons. The number and energy of the characteristic x-ray photons emitted from a specimen can be measured by an energy dispersive spectrometer. As the energy of the x-rays is characteristic of the difference in energy between the two shells, and of the atomic structure of the element

from which they were emitted, this allows the elemental composition of the specimen to be measured (appendix figure C2).

#### 5. Qualitative and Quantitative analysis in ED-XRF

Qualitative analysis is the process of identifying which elements are present in a sample. In its simplest form, qualitative analysis proceeds by determining the energies of peaks present in the spectrum and comparing them with a chart listing the known energies of x-ray emissions. Modern analyzers have automated this process to varying degrees, and most provide markers that can be called to the video display by atomic number or symbol. In highly automated versions, software routines detect the location of spectral peaks, compare them with tabulated energy values, check for inconsistencies, then print out a list of the elements present. In general, however, routines of this type are not intended to make sophisticated judgments, but rather to limit the number of judgments required of the user.

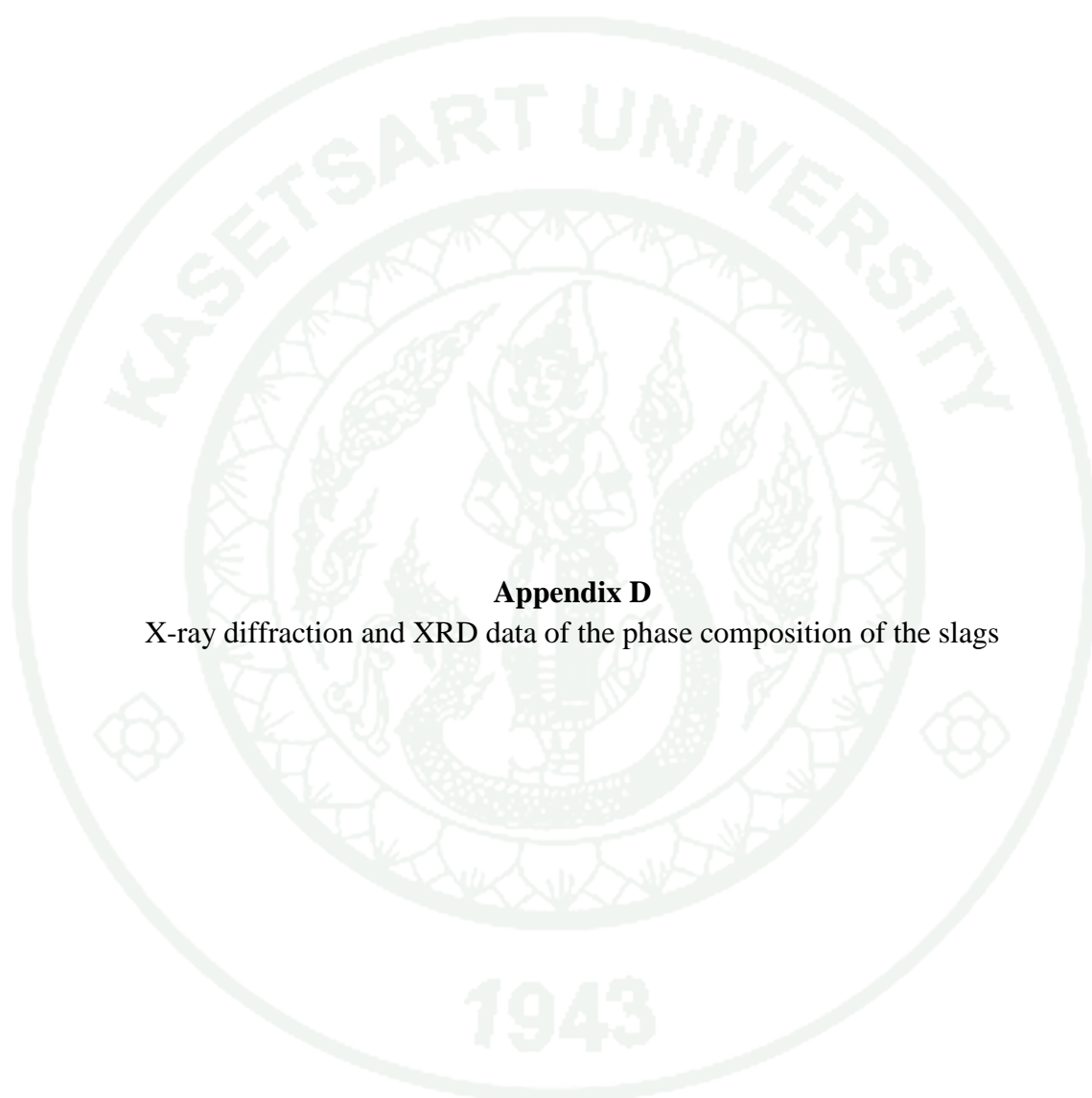
Quantitative analysis seeks to establish not only the identities of the elements present in a sample, but also their concentrations, together with an indication of the confidence that can be placed in the computed results. Assuming that a qualitative analysis has been concluded, the quantitative analysis must proceed through several phases: background removal, de-convolution of overlapped peaks, and calculation of elemental concentration.

**Appendix Table C1** ED-XRF data of the bulk chemical composition of the slags (wt.%).

|       | SO <sub>3</sub> | Al <sub>2</sub> O <sub>3</sub> | SiO <sub>2</sub> | K <sub>2</sub> O | CaO   | TiO <sub>2</sub> | V <sub>2</sub> O <sub>5</sub> | Cr <sub>2</sub> O <sub>3</sub> | MnO   | Fe <sub>2</sub> O <sub>3</sub> |
|-------|-----------------|--------------------------------|------------------|------------------|-------|------------------|-------------------------------|--------------------------------|-------|--------------------------------|
| A0572 | 0.069           | nil                            | 0.908            | 0.306            | 0.279 | nil              | nil                           | nil                            | 1.269 | 90.50                          |
| A0573 | 0.309           | nil                            | 21.72            | 0.445            | 0.030 | nil              | nil                           | nil                            | 0.950 | 71.00                          |
| A0574 | nil             | nil                            | 0.679            | 0.429            | 0.028 | nil              | nil                           | nil                            | 1.242 | 83.47                          |
| A0577 | nil             | nil                            | 0.637            | 0.271            | 0.927 | nil              | nil                           | 0.113                          | 2.937 | 92.85                          |
| A0581 | nil             | nil                            | 0.918            | 0.350            | 0.090 | nil              | nil                           | nil                            | 1.187 | 91.95                          |
| A0586 | nil             | nil                            | 1.826            | 0.092            | 0.921 | 2.544            | 0.088                         | 0.158                          | 4.456 | 89.09                          |
| A0588 | nil             | 12.28                          | 26.27            | 0.174            | 0.131 | 2.234            | 0.086                         | 0.160                          | 2.349 | 56.14                          |
| A0590 | nil             | 11.21                          | 27.82            | nil              | 1.098 | 2.073            | 0.275                         | 0.211                          | 1.130 | 56.10                          |
| A0594 | nil             | nil                            | 1.229            | 0.279            | 0.235 | 2.457            | nil                           | 0.265                          | 6.581 | 87.56                          |
| A0595 | nil             | nil                            | 0.807            | nil              | 0.817 | 1.402            | 0.163                         | 0.116                          | 1.392 | 95.13                          |
| A0273 | nil             | 12.36                          | 32.27            | 0.230            | 0.466 | 0.381            | 0.216                         | 0.101                          | 0.327 | 53.61                          |
| A0278 | nil             | 13.41                          | 35.09            | 0.350            | 0.705 | 0.441            | 0.185                         | 0.111                          | 0.336 | 49.32                          |
| A0281 | nil             | nil                            | 1.389            | 0.572            | 4.006 | 3.096            | 0.313                         | 0.206                          | 1.716 | 88.22                          |
| A0546 | nil             | nil                            | 0.876            | 0.350            | 0.468 | nil              | 0.117                         | nil                            | 0.768 | 97.37                          |
| A0547 | nil             | nil                            | 0.982            | 1.117            | 1.457 | 0.271            | 0.070                         | 0.125                          | 0.639 | 95.31                          |
| A0538 | nil             | 12.15                          | 26.23            | 0.344            | 0.466 | 1.898            | 0.182                         | 0.138                          | 0.456 | 58.07                          |
| A0539 | nil             | 11.58                          | 27.91            | 0.192            | 0.289 | 1.621            | 0.155                         | 0.118                          | 0.443 | 57.61                          |
| A0540 | nil             | 11.63                          | 33.97            | 0.298            | 0.910 | 1.792            | 0.153                         | 0.125                          | 0.925 | 50.12                          |
| A0541 | nil             | 12.20                          | 28.07            | 0.317            | 0.754 | 1.997            | 0.080                         | 0.068                          | 0.445 | 56.00                          |
| A0542 | nil             | 12.70                          | 29.76            | 0.331            | 0.307 | 1.257            | 0.133                         | 0.068                          | 0.572 | 54.80                          |

**Appendix Table C1 (Continued).**

|       | FeO   | CuO   | ZnO   | SrO   | ZrO <sub>2</sub> | CdO   | BaO   | PbO   | OsO <sub>4</sub> |
|-------|-------|-------|-------|-------|------------------|-------|-------|-------|------------------|
| A0572 | 81.43 | 6.567 | nil   | nil   | 0.103            | nil   | nil   | nil   | nil              |
| A0573 | 63.88 | 3.312 | 2.239 | nil   | nil              | nil   | nil   | nil   | nil              |
| A0574 | 75.10 | 4.429 | 0.673 | 0.049 | nil              | nil   | 8.210 | 0.789 | nil              |
| A0577 | 83.54 | 2.020 | 0.247 | nil   | nil              | nil   | nil   | nil   | nil              |
| A0581 | 82.73 | 4.949 | 0.504 | nil   | nil              | nil   | nil   | nil   | 0.053            |
| A0586 | 80.16 | nil   | nil   | 0.078 | 0.281            | nil   | 0.469 | nil   | nil              |
| A0588 | 50.52 | nil   | nil   | nil   | 0.077            | nil   | 0.103 | nil   | nil              |
| A0590 | 50.47 | nil   | nil   | 0.021 | 0.064            | nil   | nil   | nil   | nil              |
| A0594 | 78.78 | nil   | nil   | nil   | 0.202            | nil   | 1.195 | nil   | nil              |
| A0595 | 85.60 | nil   | nil   | 0.064 | 0.104            | nil   | nil   | nil   | nil              |
| A0273 | 48.24 | nil   | nil   | nil   | 0.044            | nil   | nil   | nil   | nil              |
| A0278 | 44.37 | nil   | nil   | nil   | 0.051            | nil   | nil   | nil   | nil              |
| A0281 | 79.38 | nil   | nil   | 0.123 | 0.241            | 0.117 | nil   | nil   | nil              |
| A0546 | 87.61 | nil   | nil   | nil   | 0.056            | nil   | nil   | nil   | nil              |
| A0547 | 85.75 | nil   | nil   | 0.033 | nil              | nil   | nil   | nil   | nil              |
| A0538 | 52.25 | nil   | nil   | nil   | 0.064            | nil   | nil   | nil   | nil              |
| A0539 | 51.84 | nil   | nil   | nil   | 0.054            | 0.028 | nil   | nil   | nil              |
| A0540 | 45.10 | nil   | nil   | 0.014 | 0.057            | nil   | nil   | nil   | nil              |
| A0541 | 50.39 | nil   | nil   | nil   | 0.061            | nil   | nil   | nil   | nil              |
| A0542 | 49.31 | nil   | nil   | 0.000 | 0.069            | nil   | nil   | nil   | nil              |



### **Appendix D**

X-ray diffraction and XRD data of the phase composition of the slags

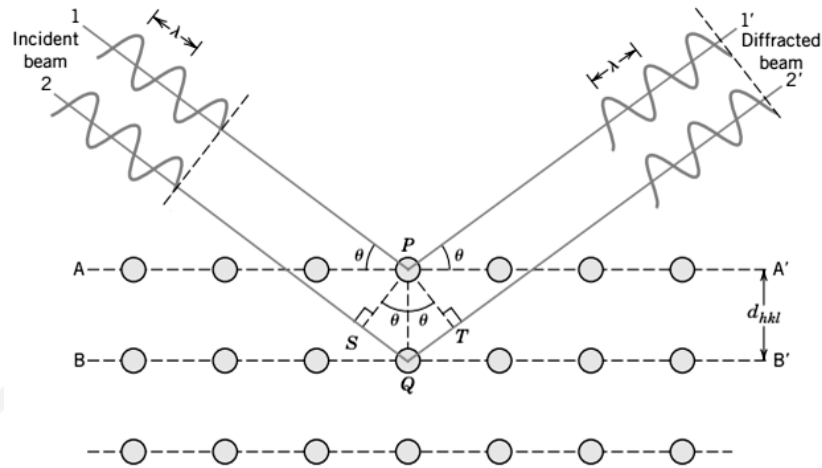
## X-ray diffractometry (XRD)

X-ray diffraction is an analytical technique for the study of crystal structures and mineral composition of natural and manufactured materials. It is based on constructive interference of incident x-rays and a crystalline sample. The interaction of incident x-rays with the sample produces constructive interference and a diffracted x-ray. These diffracted x-rays are then detected, processed and counted. Conversion of the diffraction peaks to d-spacings permits identification of the crystalline sample because each crystalline sample has a set of unique d-spacings. Typically, this is achieved by comparison of d-spacings with standard reference patterns.

In order to better convey an understanding of the fundamental principles and x-ray diffraction instruments, will look at Bragg's law behind these systems, as follows.

### 1. The Principle of X-rays Diffraction

X-rays are electromagnetic waves and high energy, wavelengths are considered to lie between  $0.1 \text{ \AA}$  to  $100 \text{ \AA}$ . When a beam of x-rays impinges on a solid material which consists of atom or molecules arranged in patterns, repeated regularly in three dimensions. A portion of this beam will be scattered in all directions by the electrons associated with each atom that lies within the beam's path as shown in appendix figure D1.



**Appendix Figure D1** Diffraction of X-rays by planes of atoms (A-A' and B-B').

**Source:** Callister and Rethwisch (2012)

Consider the two parallel planes of atoms A-A' and B-B' in appendix figure D1, which have the same  $h$ ,  $k$ , and  $l$  Miller indices and are separated by the interplanar spacing  $d_{hkl}$ . Now assume that a parallel, monochromatic, and coherent beam of X-rays of wavelength ( $\lambda$ ) is incident on these two planes at an angle  $\theta$ . Two rays in this beam, labeled 1 and 2, are scattered by atoms  $P$  and  $Q$ . Constructive interference of the scattered rays 1' and 2' occurs also at an angle  $\theta$  to the planes, if the path length difference between 1-P-1' and 2-Q-2' is equal to a whole number,  $n$ , of wavelengths. Then, the condition for diffraction is shown below,

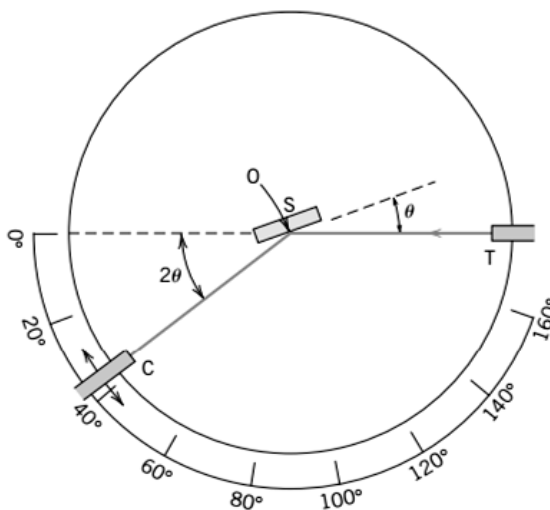
$$n\lambda = \overline{SQ} + \overline{QT} \quad (1)$$

$$= 2d_{hkl} \sin \theta \quad (2)$$

Equation 2 is known as Bragg's law;  $n$  is the order of reflection, which may be any integer (1, 2, 3, or more) consistent with  $\sin \theta$  not exceeding unity. Thus, we have a simple expression relating the x-ray wavelength and inter-atomic spacing to the angle of the diffracted beam.

## 2. The Powder Method and Operating Principles

There are several methods of x-rays diffraction analysis, a common one and also allowed in this work is powder diffraction method which employs a powdered or polycrystalline specimen consisting of many fine and randomly oriented particles that are exposed to monochromatic x-radiation. In x-ray powder diffractometry, x-rays are generated within vacuum condition. These x-rays are produced by accelerates electron to hit a target. The wavelength of these x-rays is characteristic of that target. These X-rays are collimated and directed onto the sample, which has been ground to a fine powder. A detector detects the x-ray signal, the signal is then processed either by a microprocessor or electronically, converting the signal to a count rate. Changing the angle between the x-ray source, the sample, and the detector at a controlled rate between preset limits is an x-ray scan (appendix figure D2).



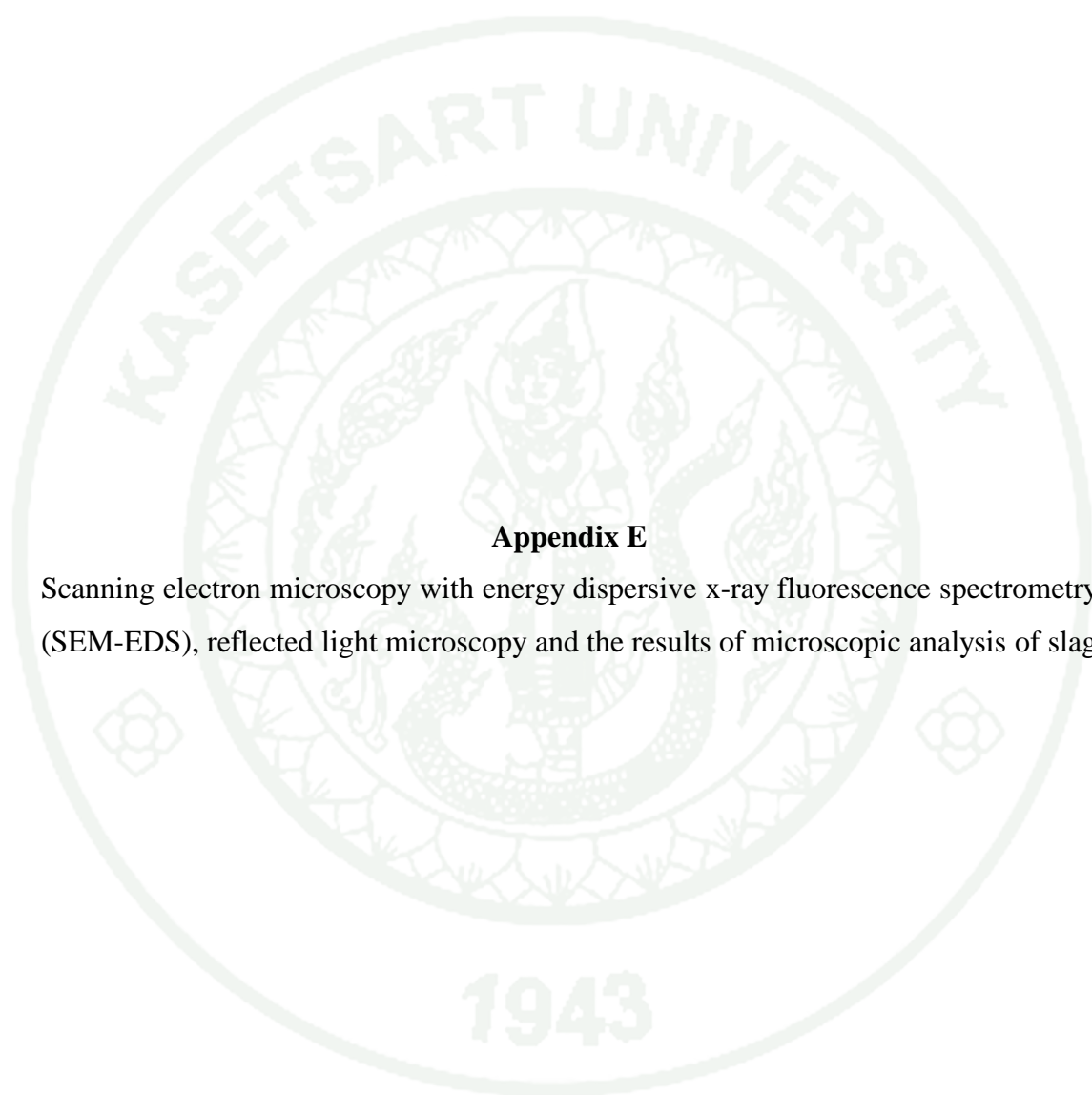
**Appendix Figure D2** Schematic diagram of an x-ray diffractometer; T = x-ray source, S = specimen, C = detector, and O = the axis around which the specimen and detector rotate.

**Source:** Callister and Rethwisch (2012)

When an x-ray beam hits a sample and diffracted, we can measure the distances between the planes of the atoms that constitute the sample by applying Bragg's Law as mentioned in section 1. Since we know wavelength ( $\lambda$ ) and we can measure the wavelength, we can calculate the  $d$ -spacings. The geometry of an XRD unit is designed to accommodate this measurement. The characteristic set of  $d$ -spacings generated in a typical x-ray scan provides a unique fingerprint of the mineral or minerals present in the sample. When properly interpreted, by comparison with standard reference patterns and measurements, this fingerprint allows for identification of the material.

**Appendix Table D1** XRD data of the phase composition of the slags (wt.%).

| Lab ID. | Fayalite | Hercynite | Quartz | Quartz Low | Cristobalite | Magnetite |
|---------|----------|-----------|--------|------------|--------------|-----------|
| A 0572  | 75.02    | -         | -      | -          | -            | 24.98     |
| A 0573  | 89.89    | -         | -      | 4.440      | -            | 5.660     |
| A 0574  | 72.97    | -         | -      | 20.01      | -            | 7.02      |
| A 0577  | 91.93    | -         | -      | -          | -            | 8.070     |
| A 0581  | 92.03    | -         | -      | 1.270      | -            | 6.700     |
| A 0586  | -        | 14.29     | -      | 57.95      | 17.38        | 10.38     |
| A 0588  | 55.62    | 33.98     | -      | 10.40      | -            | -         |
| A 0590  | 46.76    | 17.27     | -      | 35.98      | -            | -         |
| A 0594  | 49.69    | 31.56     | 7.480  | 11.27      | -            | -         |
| A 0595  | 73.10    | 10.95     | -      | 15.95      | -            | -         |
| A 0273  | 69.69    | 19.49     | -      | 10.82      | -            | -         |
| A 0278  | 62.33    | 14.35     | 23.33  | -          | -            | -         |
| A 0281  | 44.56    | 21.53     | -      | 33.91      | -            | -         |
| A 0546  | 90.53    | 6.830     | -      | 2.640      | -            | -         |
| A 0547  | 97.40    | -         | -      | 2.600      | -            | -         |
| A 0538  | 81.31    | 18.69     | -      | -          | -            | -         |
| A 0539  | 74.45    | 21.34     | -      | 4.200      | -            | -         |
| A 0540  | 71.00    | 13.15     | -      | 15.85      | -            | -         |
| A 0541  | 74.91    | 18.32     | -      | 6.76       | -            | -         |
| A 0542  | 72.91    | 19.44     | -      | 7.65       | -            | -         |



### **Appendix E**

Scanning electron microscopy with energy dispersive x-ray fluorescence spectrometry (SEM-EDS), reflected light microscopy and the results of microscopic analysis of slag

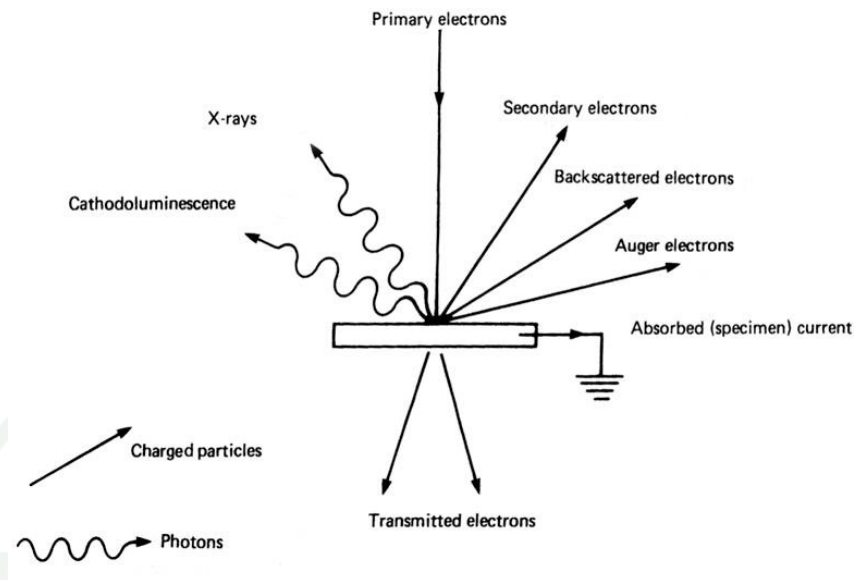
## 1. Scanning electron microscopy with energy dispersive x-ray fluorescence spectrometry (SEM-EDS)

Scanning electron microscopy with energy dispersive x-ray fluorescence spectrometry gives the morphological, topographical and elemental information of the solid surfaces that is necessary to understanding the behavior of the surfaces. In the SEM-EDS, the area to be examined is irradiated with a focused electron beam on the surface of the specimen to form images and chemical compositions. The types of signals produced from the interaction of the electron beam with the specimen include secondary electrons, backscattered electrons, characteristic x-rays, and other photons of various energies. These signals are obtained from specific emission volumes within the sample and can be used to examine many characteristics of the sample. The imaging signals of interest are the secondary and backscattered electrons because these vary primarily as a result of differences in surface topography. In the SEM, characteristic x-rays are also emitted as a result of electron bombardment. The analysis of the characteristic x-radiation emitted from samples can yield both qualitative identification and quantitative elemental information from regions of a specimen nominally 1  $\mu\text{m}$  in diameter and 1  $\mu\text{m}$  in depth under normal operating conditions. The more details of SEM-EDS are discussed in the next section.

### 1.1 The interaction between electrons and specimens

In the introduction, the author briefly described the SEM-EDS are the signals produced from electron beam-specimen interaction and operating principle, In this section, will look at more details interaction between electrons and specimens that necessary to be understood for how the signals produced by the electron beam-specimen interactions, are converted into images and/or spectra that convey useful information.

When a focused electron beam impinges on a specimen, it interacts with atoms within the surface in a pear-shaped volume and gives rise to several different types of signals (appendix figure E1) as follows (Lawes, 1987).



**Appendix Figure E1** Photon and charged particle emissions from an electron-bombarded surface.

**Source:** Watt (1996)

### 1.1.1 Elastically Scattered Electrons

A beam electron, which passes close to a positively charged atomic nucleus, may be attracted by its opposite charge. According to the result of its direction with hardly any loss of energy. The scatter angles, depends on how much energy it has, and how close it passes to the nucleus. It varies from almost from zero to  $180^\circ$ , so the electron may be affected at all, or may end up travelling back in the direction from which it came. In specimens of the same thickness, called elastic scattering, is more likely to occur in specimens of high atomic number ( $Z$ ). Elastically scattered electrons are commonly used in SEM image formation. Many of those which are deflected through very large angle (or more  $90^\circ$ ) re-emerge from the surface of the specimen with high energy. When collected as a signal for imaging, they are called backscattered electrons (BSE). The intensity of the BSE signal is dependent on the angle between the incident beam and specimen surface. It follows then, that if the specimen has a rough surface, the signal changes with surface detail.

### 1.1.2 Inelastic Scattering

Some of the incident primary electron will interact with the orbiting shell electrons and atomic nuclei, losing a large proportion of their kinetic energy. These events are very complex, and there are number of possible product, depending on how much energy is given up to the target atom.

### 1.1.3 Phonon Production

Phonons are collective oscillations of the atoms in a crystal lattice and can be initiated by an up-take of energy from the electron beam. If an incident electron hits onto an atom and transfers a part of its energy to it, this atom begins to vibrate. Since all atoms are linked together in a crystal, the vibration of an atom is felt by others that also start to vibrate. By this, the absorbed energy is distributed over a large volume. The collective vibrations are equivalent to heating up the specimen. Phonons can be generated as main or as by-product of any inelastic interaction.

### 1.1.4 Secondary Electron Emission

An inelastic collision can result in outermost electrons being detached from specimen atoms, leaving behind an ionized atom with positive charge. The dislodged electrons have a low kinetic energy, less than 50 eV, and are readily capture by nearby ionized atoms. Those electrons which are created nearer to the specimen surface than the electron escape distance  $R$ , can be emitted into the vacuum and form the secondary electron (SE) emission current from the surface. Secondary electrons are therefore abundant and are the most commonly used imaging signal in SEM.

### 1.1.5 Auger Electron Production

Auger electrons are generated by electronic transitions in atoms following excitation of bound electrons. Each different type of atom gives to characteristic auger emission energies that can be to identify the atom.

### 1.1.6 X-ray Production

When electrons are dislodged from specific orbits of an atom in the specimen, emission of Characteristic x-rays are generated together with white radiation (Bremsstrahlung radiation) of all wavelengths down to a minimum corresponding to the incident electron energy. Elemental information can be obtained in the x-ray mode, because the characteristic x-ray generated has a wavelength and energy characteristic of the elemental atom from which it originated. Problems arise when the x-rays hit other particles, they lose energy, this is changes the wavelength. As the number of hits increases, the x-rays will not have the appropriate energy to be classified as coming from the originating element and detection of these x-rays will be known as background. X-ray spectrometer detectors measure wavelength (Wavelength dispersive spectrometer or WDS) or energy level (Energy dispersive spectrometer or EDS). These are the two types of detectors used in x-ray fluorescence analysis.

### 1.1.7 Cathodoluminescence

Some specimens emitted long-wavelength photons, in the visible spectrum, when exposed to the incident electron beam. The light emitted can be put to use in the SEM, though it tends to be used to supplement information collected by other means rather than on its own.

Of these, secondary and backscattered electrons make up the two most common signals that are used to form the SEM image.

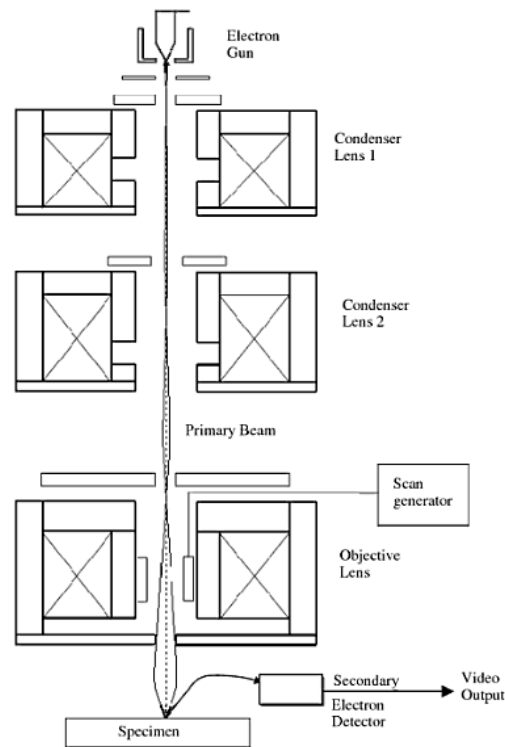
## 1.2 Operating Principles

The SEM column consists of an electron gun, two condenser lenses, an objective lens, an electron detection system, and a set of deflectors, all operating in a vacuum. Appendix Figure E2 show a schematic drawing of a typical SEM. The electron gun provides a source of electron and accelerates them to energies in the range of 1 to 30 keV. The smallest beam cross-section at the source, called the crossover, is subsequently de-magnified by the three-stage electron lens system, so that an electron probe of diameter 1 to 10 nm carrying a current of 1 to 100 pA is formed at the specimen surface. For higher currents, 1 to 10 nA, the electron probe diameter increases to 0.1 to 1  $\mu\text{m}$ . In most SEMs, the electron beam emerges from the final lens into the specimen chamber, where it interacts with the near-surface region of the specimen to a depth of approximately 1  $\mu\text{m}$  and generates signal electrons used to form an image.

A deflection system in front of the final lens scans the electron probe in a raster-like fashion across the specimen and operates in synchronism with a computer display monitor, or cathode-ray tube (CRT). Two pairs of magnetic deflection coils are usually used. The image magnification  $M_1$  of the specimen is defined to be the ratio of the linear size of the viewing screen to the linear size of the raster on the specimen. The magnification can be increased simply by decreasing the scan-coil current, keeping the image size on the CRT constant (Khursheed, 2011).

## 1.3 Energy dispersive x-ray fluorescence spectrometry on scanning electron microscope

Energy dispersive x-ray fluorescence spectrometry is standard attachment that can be fitted on most conventional SEMs. It is a powerful technique used to identify the elemental composition of material. EDS works by detecting x-rays that are produced by a sample placed in an electron beam. The electron beam excites the atoms in the sample that subsequently produce x-rays to discharge the excess energy. The energy of the x-rays is characteristic of the atoms that produced them, forming peaks in the spectrum.



**Appendix Figure E2** Schematic drawing of SEM.

**Source:** Khursheed (2011)

Although it is a powerful technique, widely used in SEMs, it has some notable limitations, such as the primary beam energy having to be typically between 10 to 20 keV, and the lateral resolution being relatively low, usually lying between 1 to 5  $\mu\text{m}$ . These limitations come from the fact that x-rays are generated deep within a comparatively large interaction volume. The standard EDS attachment therefore cannot operate at low primary beam voltages (less than 5 kV) and has considerably poorer spatial resolution than the SEM operating in its normal topographical mode. Another limitation of EDS is that it has considerably reduced sensitivity for lighter element. For this reason, EDS is limited to probe materials that have an atomic number of 4 and above (Khursheed, 2011).

## 2. Reflected light microscopy

In this study, a reflected-light microscopy was used to identify opaque minerals and translucent minerals in polished sections of copper and iron slags. Because opaque minerals (minerals with high density and a metallic luster) and translucent minerals can always be found in copper and iron slags, they don't transmit light even if they are thin-section thickness. They may be difficult or impossible to identify. Nevertheless, they present their colors in reflected light. These colors can be seen by shining a light on the top of polished section or a thin section surfaces and observing the reflected color, shape and other properties. This method normally serves to distinguish sulfides from oxides or graphite and perhaps to distinguish leucoxene or hematite. Telling the various sulfides apart, or distinguishing magnetite from ilmanite, can be impossible unless they are side by side. In addition, it is considerable technique for economic geologist who deals with metallic ores. For proper opaque mineral identification, it is normally necessary to use a reflecting light microscope and there are several properties that should be used to identifying the opaque minerals as follows.

### 2.1 Identification of Minerals

In this section, only briefly discuss the most common characteristic properties of opaque minerals that are used to distinguish them in reflected-light microscopy (Thalhammer and Mogessie, n.d.).

- Hardness: there are several ways to estimate the hardness in polished section surfaces. The relative hardness of minerals can sometimes be estimated by the depth and the width of existing scratches from the grinding and polish procedure. Another ways is can be made carefully observing grain boundaries of coexisting minerals. Kalb hardness can also be used for hardness estimation, at the junction soft and hard grain, there tends to be a slight departure from flatness. This effect can be observed by a white line.

- Texture: some opaque exhibit special texture of the polished surface. For example, intersecting orthogonal cleavage in galena give rise to prominent triangular pits.

- Reflectivity: the amount of light reflected back by a mineral. In a laboratory set up for quantitative work, monochromatic light sources are used and the light reflected from the mineral is measured by a photocell. It can be noted whether the reflectivity is strong, moderate, or weak.

- Reflectance color: the color of opaque minerals, which range from pure white to grey, are one of their most characteristic and beneficial properties.

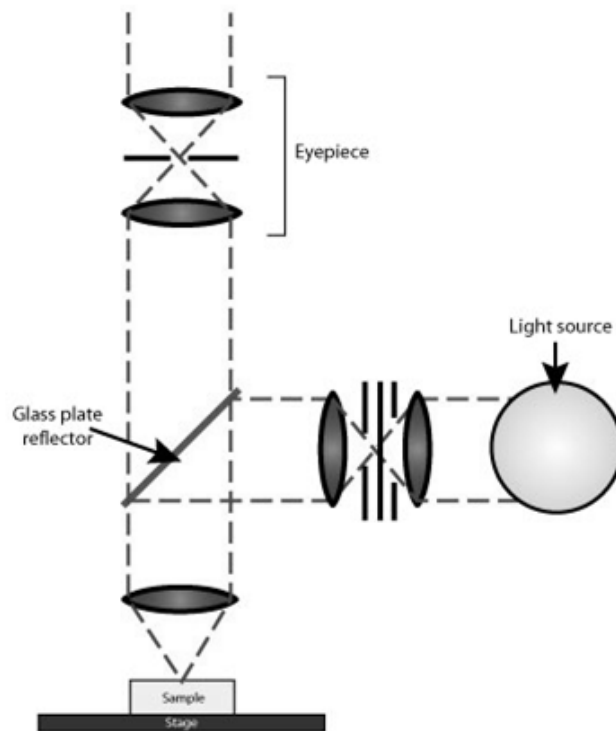
- Bireflectance and Reflection Pleochroism: some isometric opaque minerals remain unchanged in color and brightness as the stage of the microscope is turned. Contrarily, many minerals of other crystal systems show distinct changes in color, brightness with rotation of the stage, and grains of differing orientation side by side in a section differ in color or brightness. The effects are analogous in appearance to the pleochroism shown by transparent minerals in transmitted light.

- Anisotropy and Polarization colors: when the stage of the microscope is rotated with the polars crossed, it is noticeable that certain ore grains remain dark, these are referred to as uniradial section and are either isometric minerals or else basal sections of some uniaxial mineral. These basal sections can be recognized as such because different sections of the same mineral are bireflecting.

- Internal Reflections: many opaque minerals are translucent or transparent to admit incident light to substantial depths below the surface of the specimen. If the light is reflected back up through the tube of the microscopy by a cleavage crack, grain boundary, or some other subsurface feature, it will assume the color of mineral in transmitted light.

As mentioned in the introduction that it is necessary to use a reflected light microscopy for opaque and translucent mineral identification. In this section, briefly reviews of this scientific technique are necessary. Reflected light microscopy is often referred to as incident light, epi-illumination, or metallurgical microscopy, and is the method of choice for opaque objects as metal slags, most metals, ores, ceramics, and so on. If these objects are to be examined, the light is provided from a source. The light is reflected on to the specimen through the objective lens and passes

into the binocular head where it is directed either to the eyepieces or to a port for photomicrography (appendix figure E3).



**Appendix Figure E3** Light path in the Reflected light microscope.

**Source:** The University of Manchester (2012)



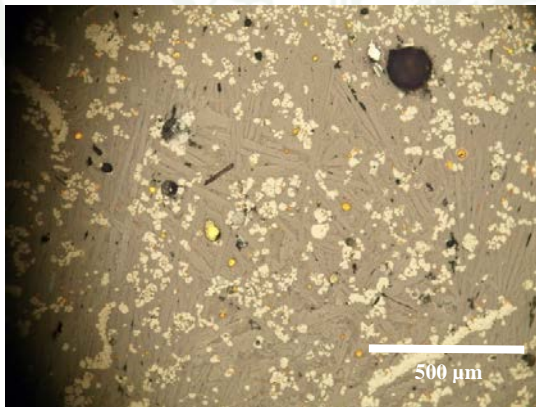
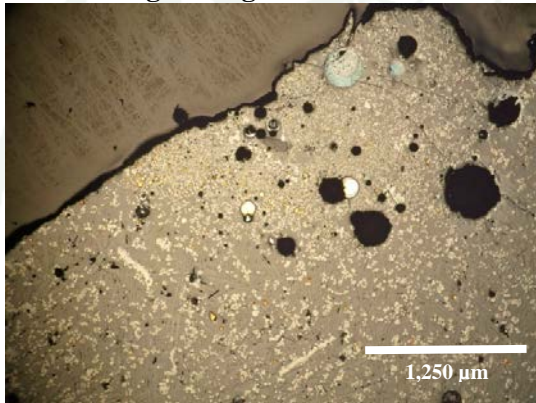
Site: Noen Nong Ho Archaeological Site,  
Tambon Na Udom, Amphoe Nikhom Kham  
Soi, Mukdahan.

Sample ID: NNH 1

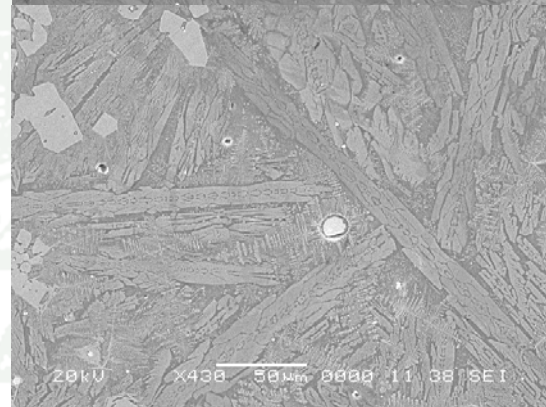
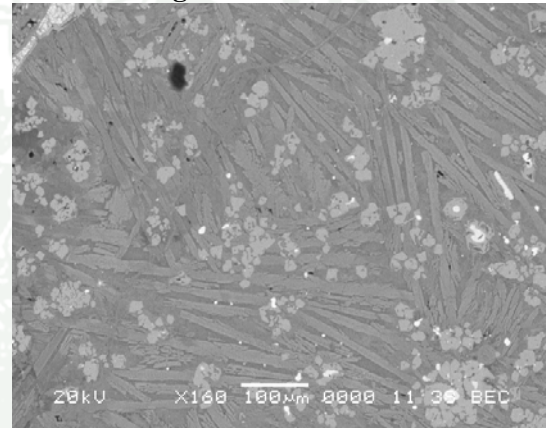
Lab ID: A0572

Object: Slag

**Reflected light images**



**Electron images**



**Appendix Figure E4** The results of microscopic analysis of slag (A0572) from Noen Nong Ho Archaeological Site.



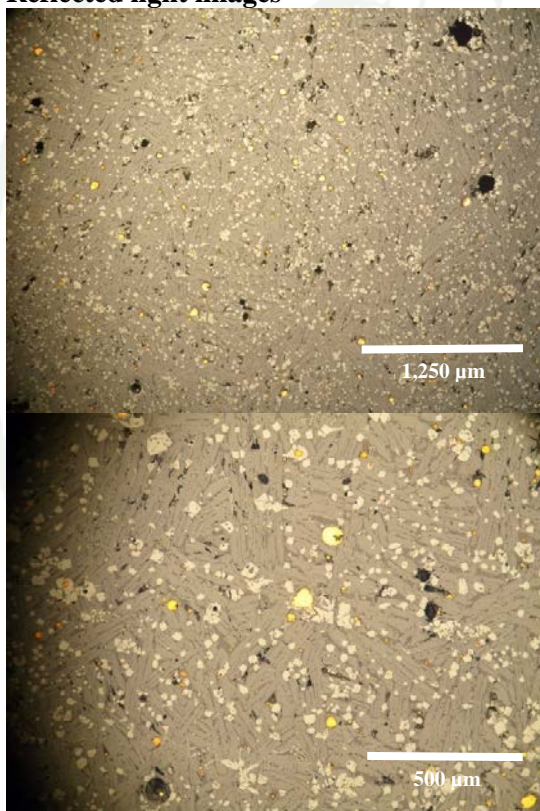
Site: Noen Nong Ho Archaeological Site,  
Tambon Na Udom, Amphoe Nikhom Kham  
Soi, Mukdahan.

Sample ID: NNH 2

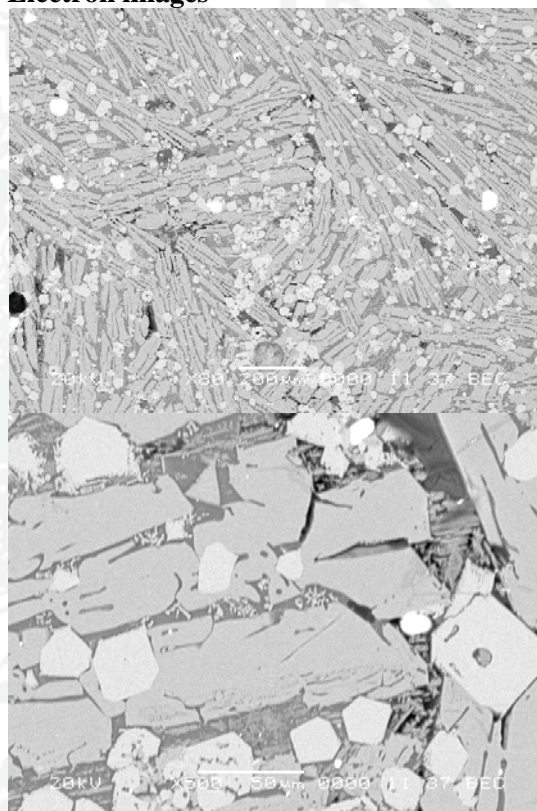
Lab ID: A0573

Object: Slag

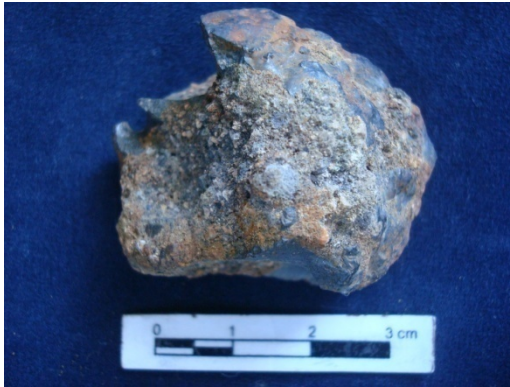
#### Reflected light images



#### Electron images



**Appendix Figure E5** The results of microscopic analysis of slag (A0573) from Noen Nong Ho Archaeological Site.



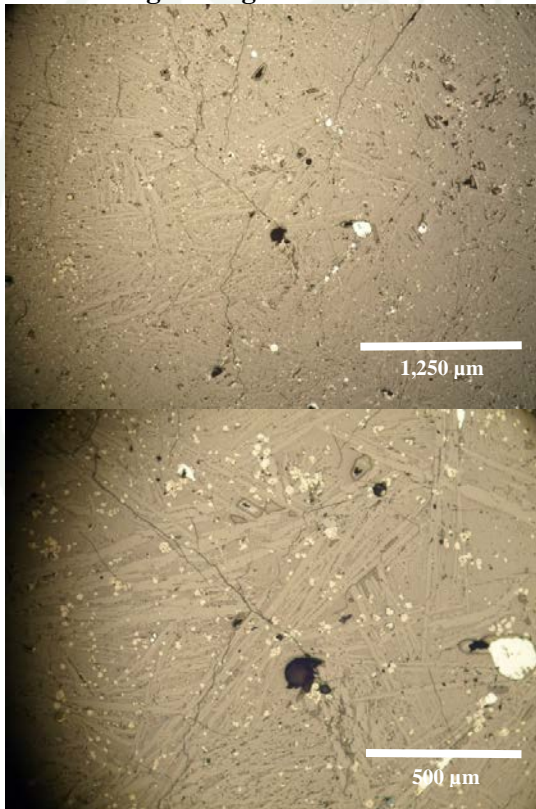
Site: Noen Nong Ho Archaeological Site,  
Tambon Na Udom, Amphoe Nikhom Kham  
Soi, Mukdahan.

Sample ID: NNH 3

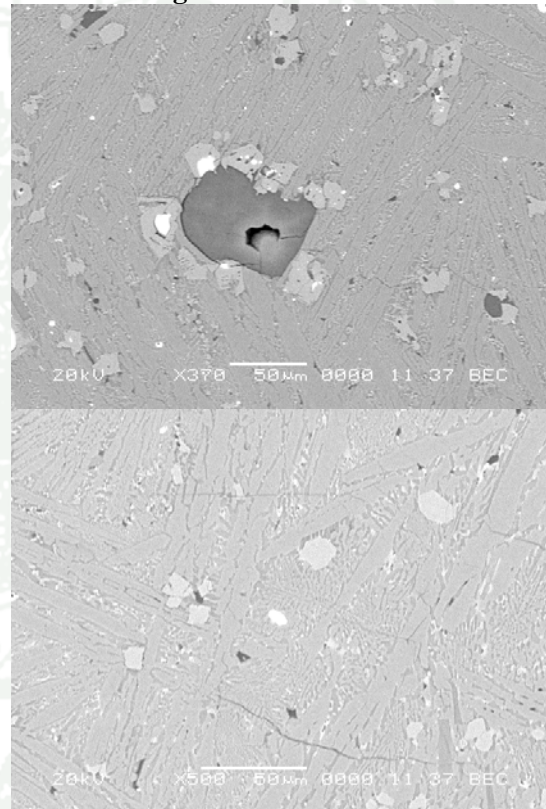
Lab ID: A0574

Object: Slag

**Reflected light images**



**Electron images**



**Appendix Figure E6** The results of microscopic analysis of slag (A0574) from Noen Nong Ho Archaeological Site.



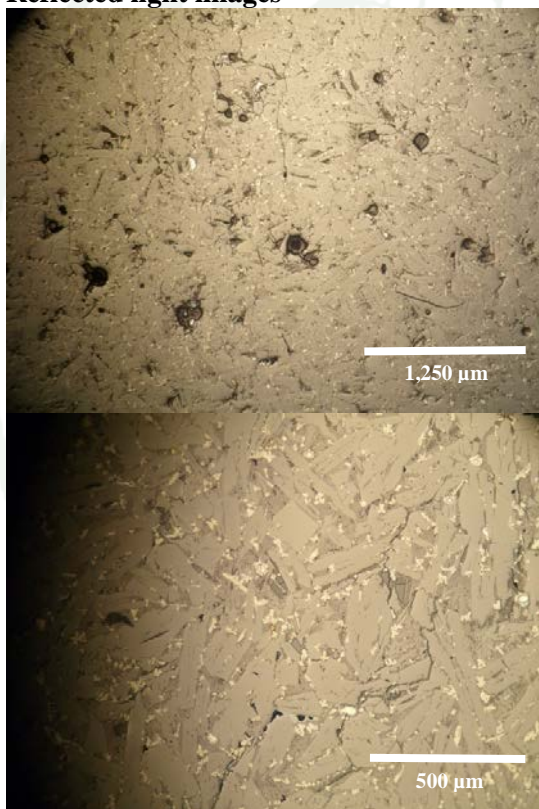
Site: Noen Nong Ho Archaeological Site,  
Tambon Na Udom, Amphoe Nikhom Kham  
Soi, Mukdahan.

Sample ID: NNH 4

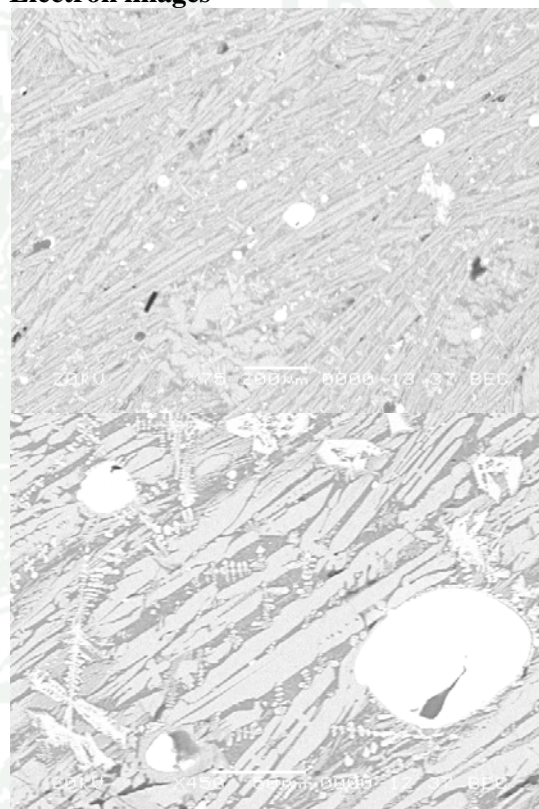
Lab ID: A0577

Object: Slag

**Reflected light images**



**Electron images**



**Appendix Figure E7** The results of microscopic analysis of slag (A0577) from Noen Nong Ho Archaeological Site.



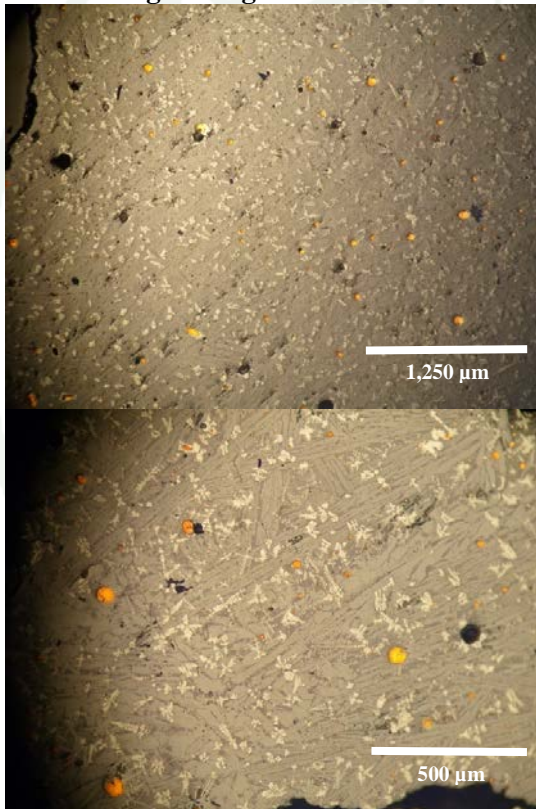
Site: Noen Nong Ho Archaeological Site,  
Tambon Na Udom, Amphoe Nikhom Kham  
Soi, Mukdahan.

Sample ID: NNH 5

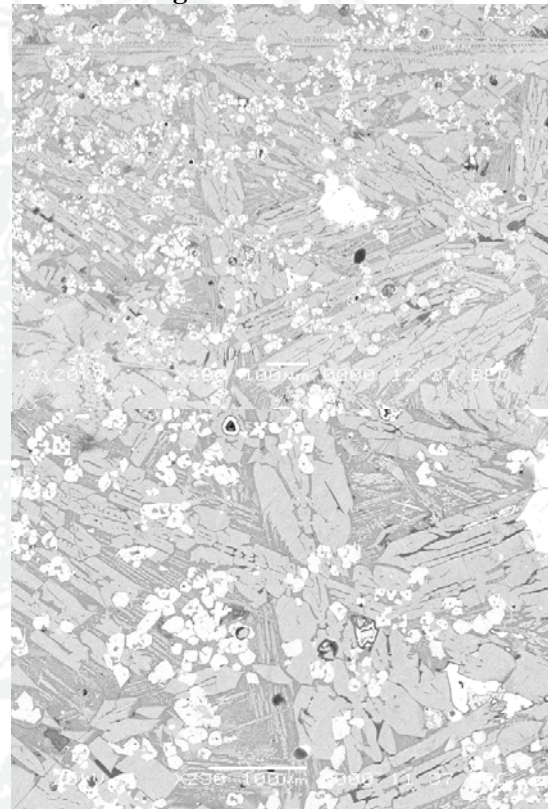
Lab ID: A0581

Object: Slag

**Reflected light images**



**Electron images**

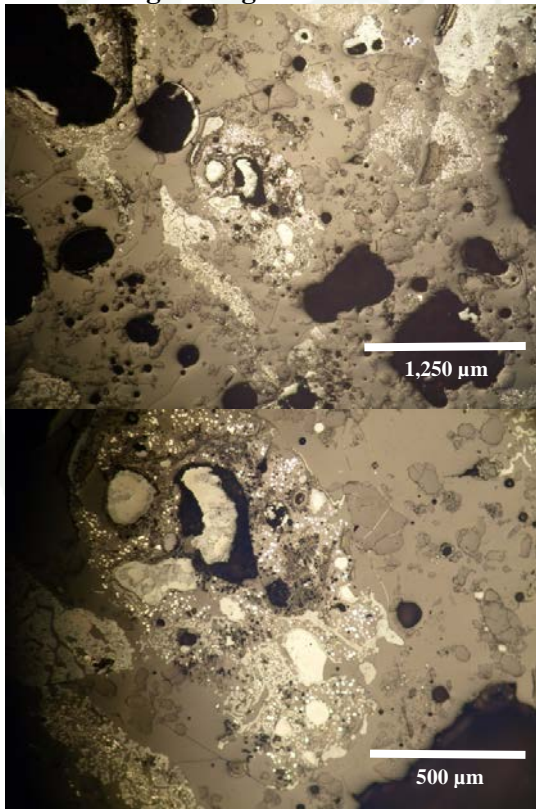


**Appendix Figure E8** The results of microscopic analysis of slag (A0581) from Noen Nong Ho Archaeological Site.

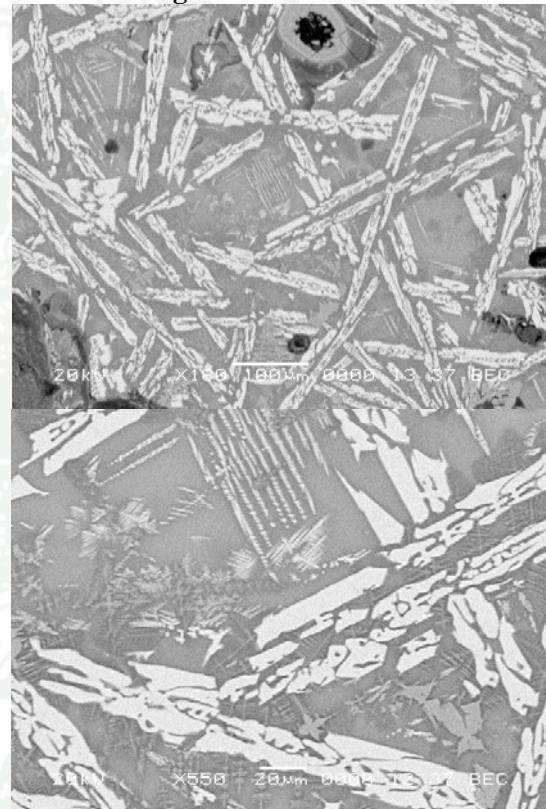


Site: Khok Kroy Archaeological Site,  
Tambon Na Bua, Amphoe Muang, Surin.  
Sample ID: BKT 1  
Lab ID: A0586  
Object: Slag

**Reflected light images**



**Electron images**

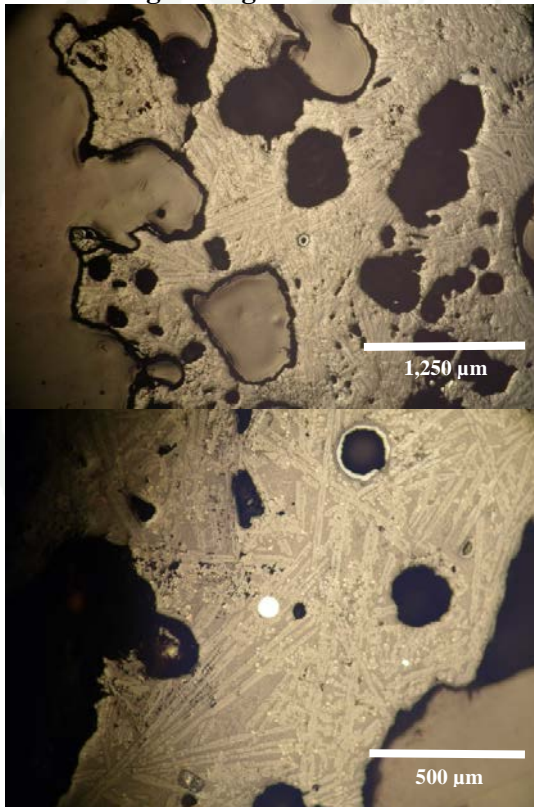


**Appendix Figure E9** The results of microscopic analysis of slag (A0586) from Khok Kroy Archaeological Site.

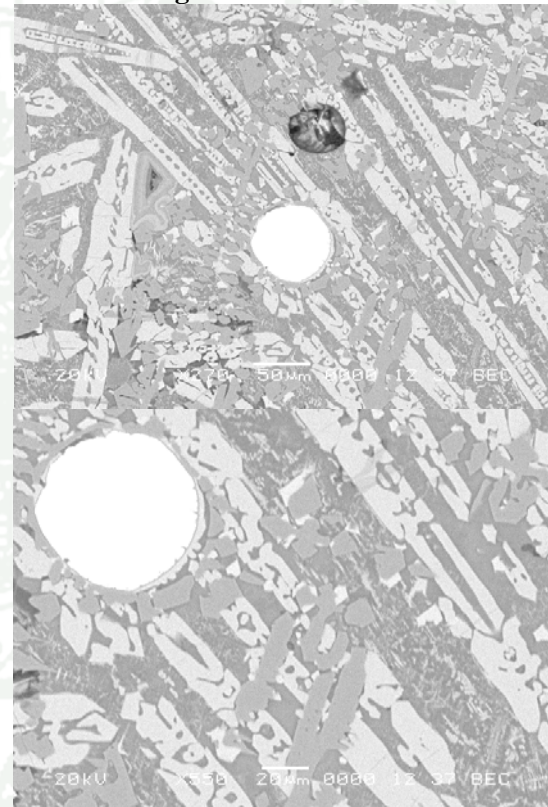


Site: Khok Kroy Archaeological Site,  
 Tambon Na Bua, Amphoe Muang, Surin.  
 Sample ID: BKT'11#0659  
 Lab ID: A0588  
 Object: Slag

**Reflected light images**



**Electron images**

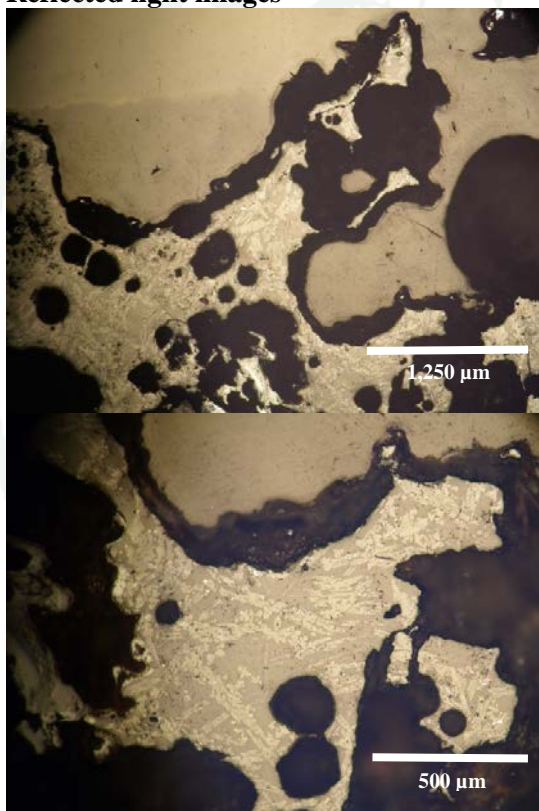


**Appendix Figure E10** The results of microscopic analysis of slag (A0588) from Khok Kroy Archaeological Site.

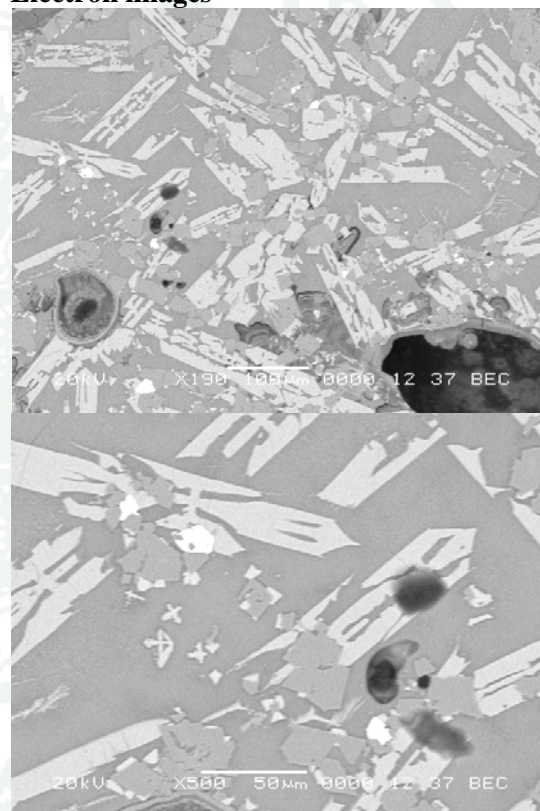


Site: Khok Kroy Archaeological Site,  
Tambon Na Bua, Amphoe Muang, Surin.  
Sample ID: BKT'11#0627  
Lab ID: A0590  
Object: Slag

**Reflected light images**



**Electron images**

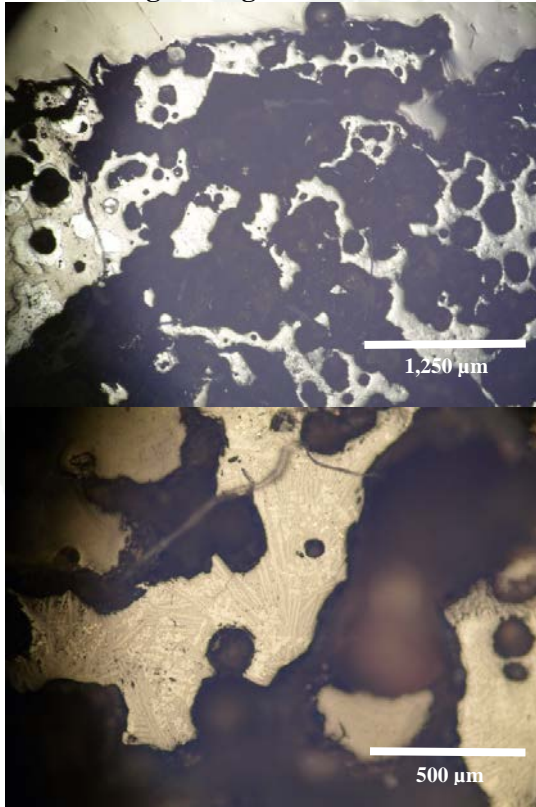


**Appendix Figure E11** The results of microscopic analysis of slag (A0590) from Khok Kroy Archaeological Site.

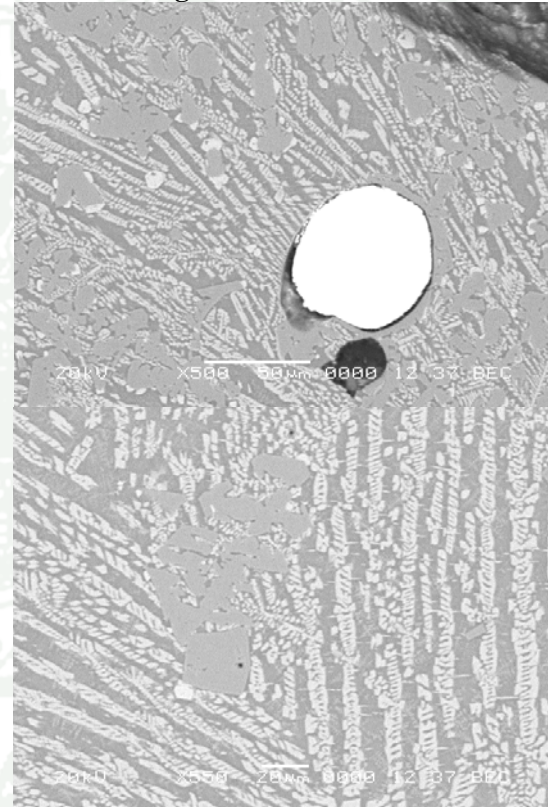


Site: Khok Kroy Archaeological Site,  
 Tambon Na Bua, Amphoe Muang, Surin.  
 Sample ID: BKT'11#0637  
 Lab ID: A0594  
 Object: Slag

**Reflected light images**



**Electron images**

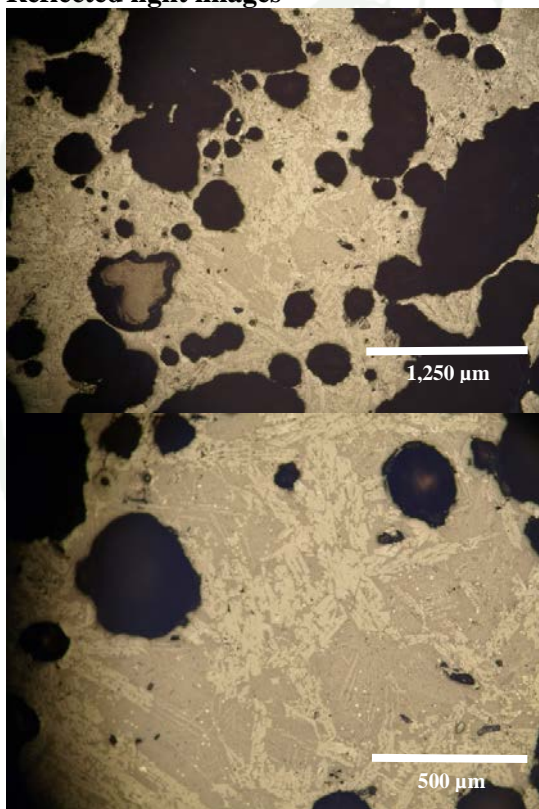


**Appendix Figure E12** The results of microscopic analysis of slag (A0594) from Khok Kroy Archaeological Site.



Site: Khok Kroy Archaeological Site,  
Tambon Na Bua, Amphoe Muang, Surin.  
Sample ID: BKT'11#0460  
Lab ID: A0595  
Object: Slag

**Reflected light images**



**Electron images**



**Appendix Figure E13** The results of microscopic analysis of slag (A0595) from Khok Kroy Archaeological Site.



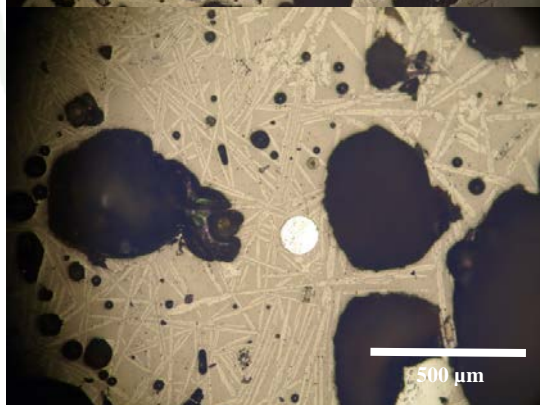
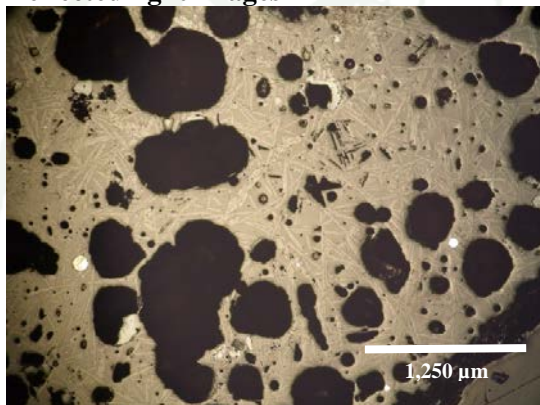
Site: Ban Saitho 7 Archaeological Site,  
Tambon Chanthop Phet, Amphoe Ban Kruat,  
Buriram.

Sample ID: STH 2 : 2009

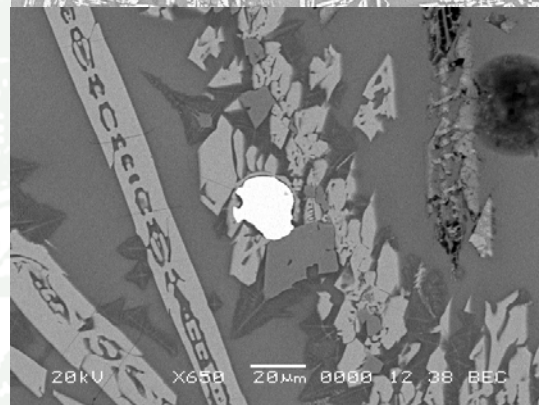
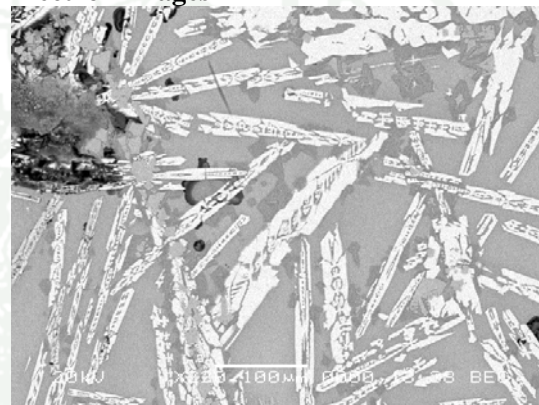
Lab ID: A0273

Object: Slag

#### Reflected light images



#### Electron images



**Appendix Figure E14** The results of microscopic analysis of slag (A0273) from Ban Saitho 7 Archaeological Site.



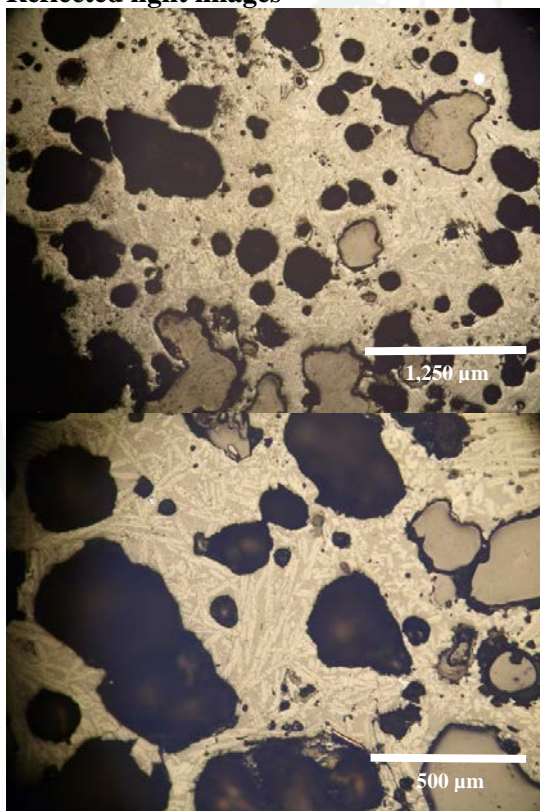
Site: Ban Saitho 7 Archaeological Site,  
Tambon Chanthop Phet, Amphoe Ban Kruat,  
Buriram.

Sample ID: STH 7 : 2009

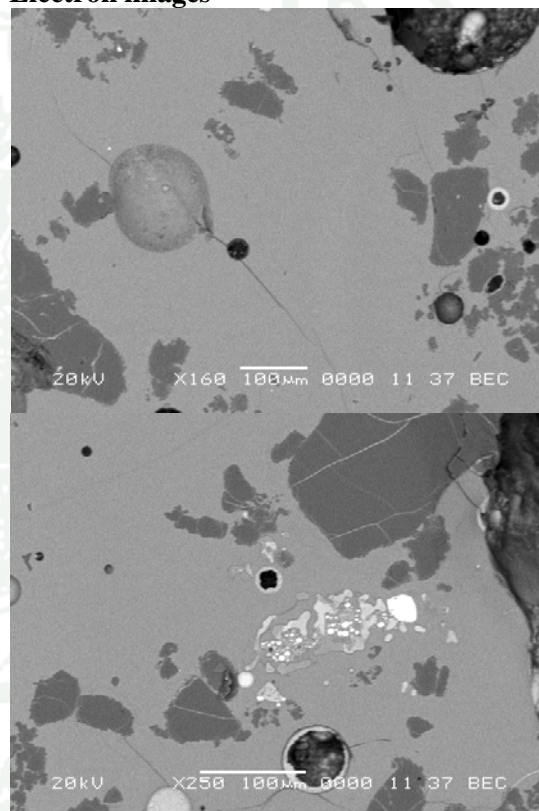
Lab ID: A0278

Object: Slag

#### Reflected light images



#### Electron images



**Appendix Figure E15** The results of microscopic analysis of slag (A0278) from Ban Saitho 7 Archaeological Site.



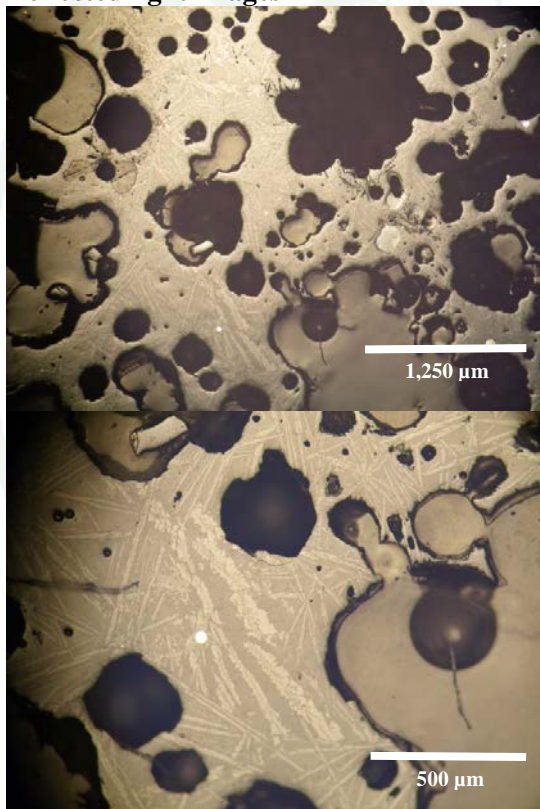
Site: Ban Saitho 7 Archaeological Site,  
Tambon Chanthop Phet, Amphoe Ban Kruat,  
Buriram.

Sample ID: STH 10 : 2009

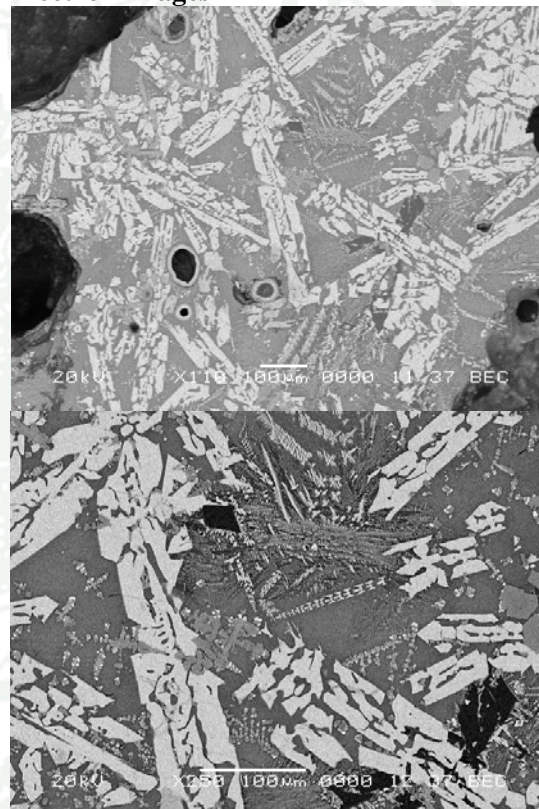
Lab ID: A0281

Object: Slag

**Reflected light images**



**Electron images**



**Appendix Figure E16** The results of microscopic analysis of slag (A0281) from Ban Saitho 7 Archaeological Site.



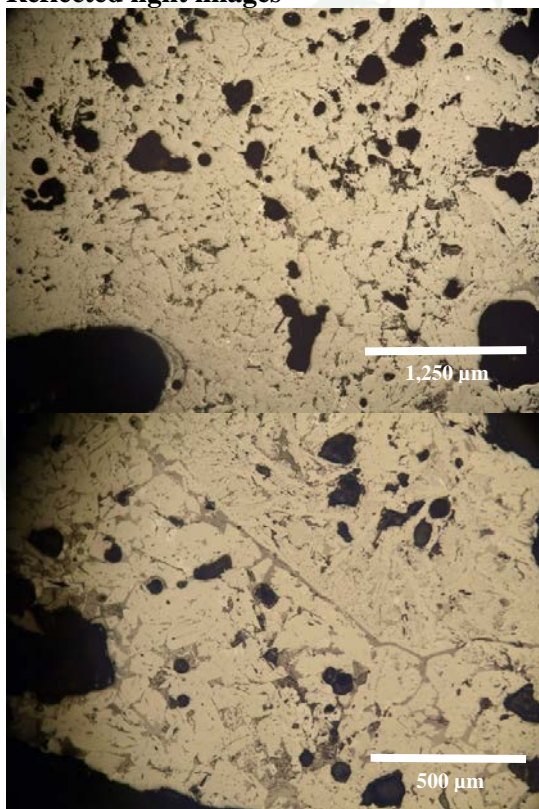
Site: Ban Saitho 7 Archaeological Site,  
Tambon Chanthop Phet, Amphoe Ban Kruat,  
Buriram.

Sample ID: STH'10 T.1/W1/NEQ (6) 100-  
110 cm.dt. (#086)

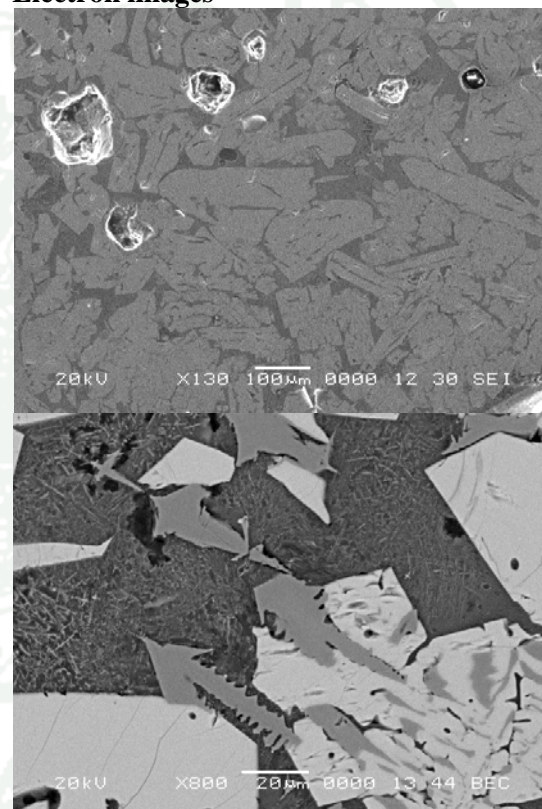
Lab ID: A0546

Object: Slag

#### Reflected light images



#### Electron images



**Appendix Figure E17** The results of microscopic analysis of slag (A0546) from Ban Saitho 7 Archaeological Site.



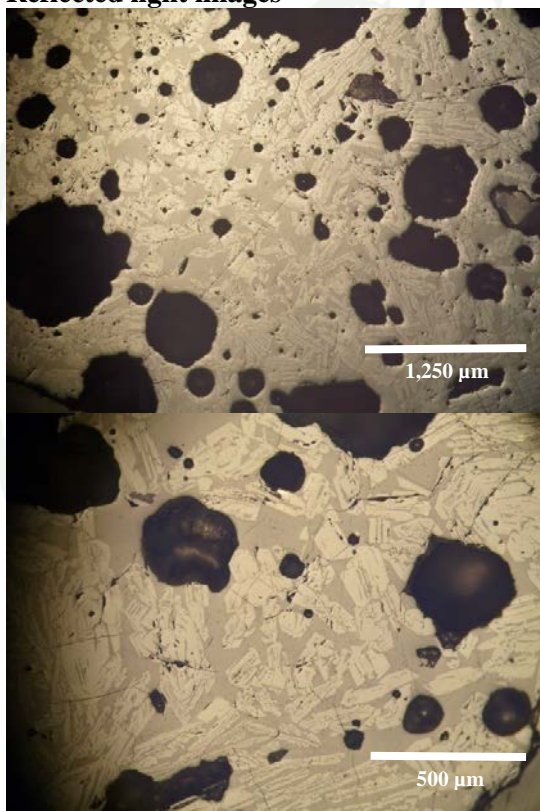
Site: Ban Saitho 7 Archaeological Site,  
Tambon Chanthop Phet, Amphoe Ban Kruat,  
Buriram.

Sample ID: STH'09 T.1/WQ (10) 140-150  
cm.dt. (#218)

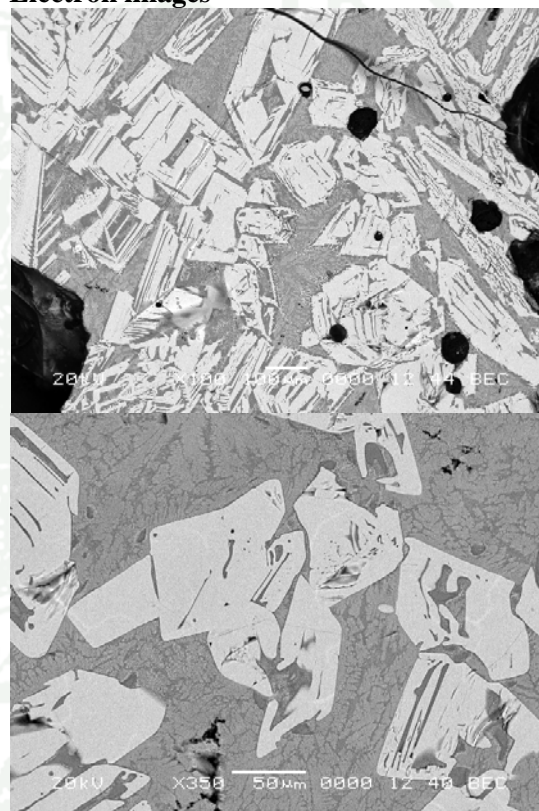
Lab ID: A0547

Object: Slag

#### Reflected light images



#### Electron images



**Appendix Figure E18** The results of microscopic analysis of slag (A0547) from Ban Saitho 7 Archaeological Site.



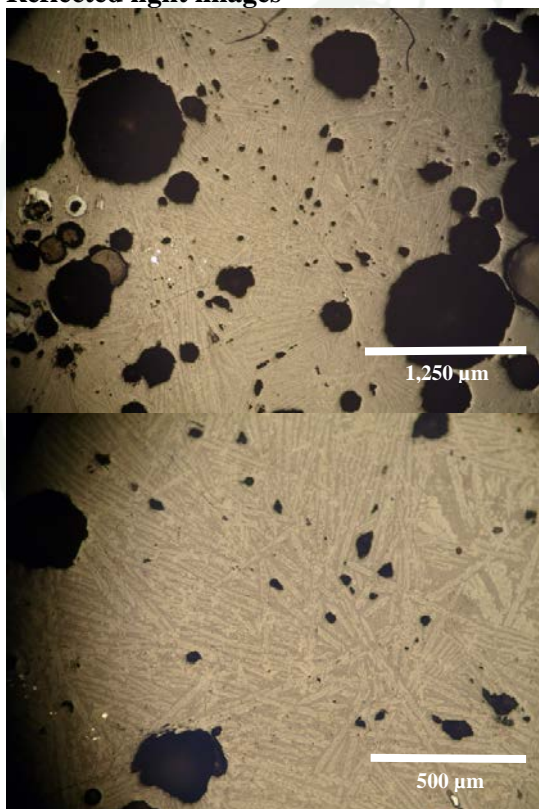
Site: Ban Khao Din Tai Archaeological Site,  
Tambon Ban Kruat, Amphoe Ban Kruat,  
Buriram.

Sample ID: KDT'07 TP.1 NEQ Furnace#1  
(#041/3)

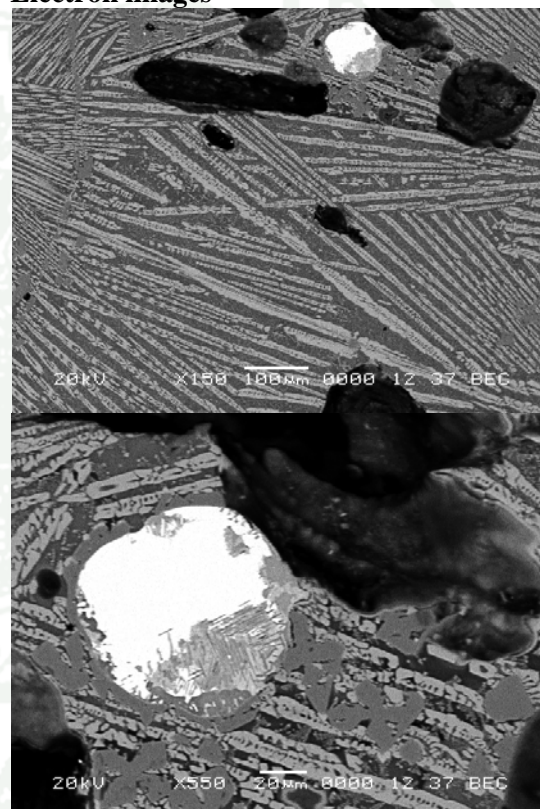
Lab ID: A0538

Object: Slag

#### Reflected light images



#### Electron images



**Appendix Figure E19** The results of microscopic analysis of slag (A0538) from Ban Khao Din Tai Archaeological Site.



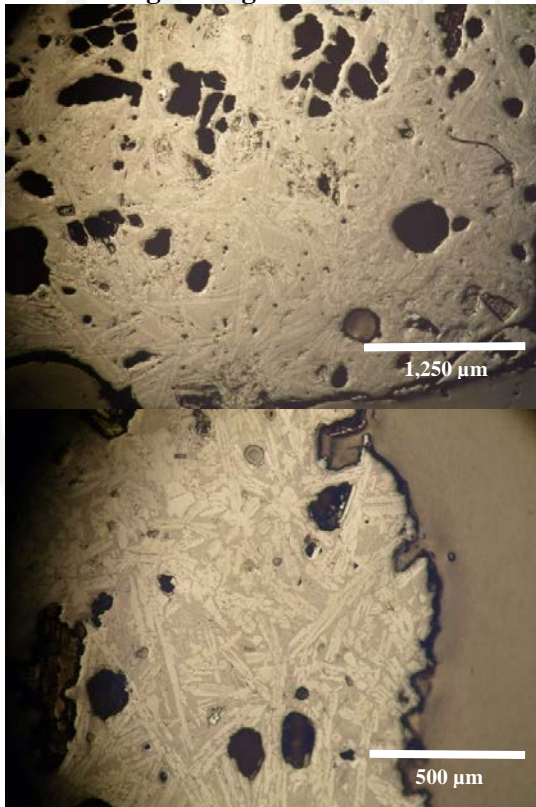
Site: Ban Khao Din Tai Archaeological Site,  
Tambon Ban Kruat, Amphoe Ban Kruat,  
Buriram.

Sample ID: KDT'07 TP.1 NEQ Furnace#2  
(#9136/3)

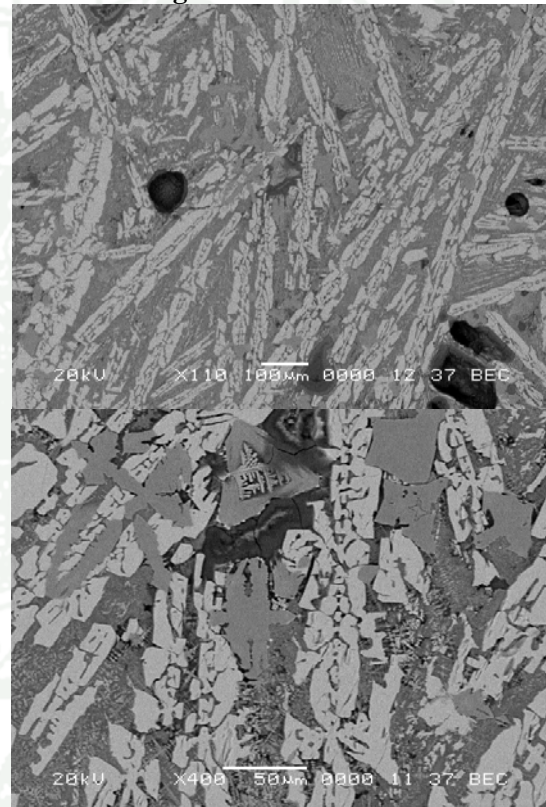
Lab ID: A0539

Object: Slag

**Reflected light images**



**Electron images**



**Appendix Figure E20** The results of microscopic analysis of slag (A0539) from Ban Khao Din Tai Archaeological Site.



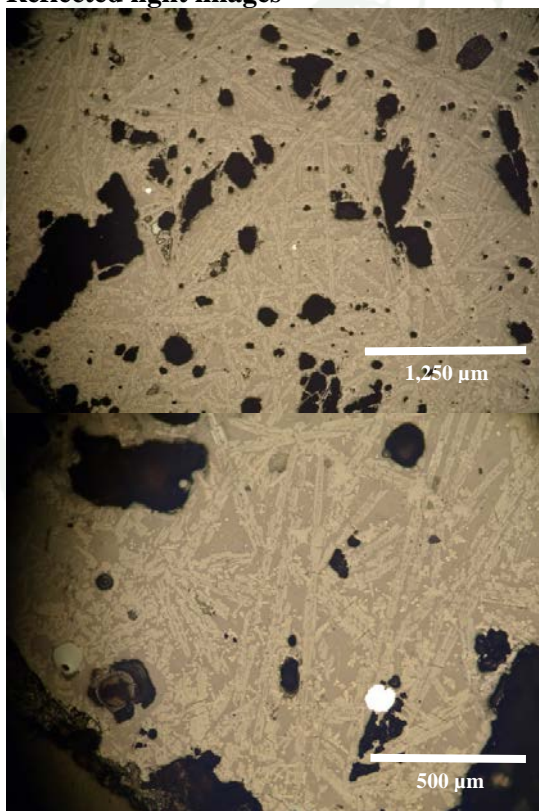
Site: Ban Khao Din Tai Archaeological Site,  
Tambon Ban Kruat, Amphoe Ban Kruat,  
Buriram.

Sample ID: KDT'07 TP.1 SEQ Furnace#3  
(#108)

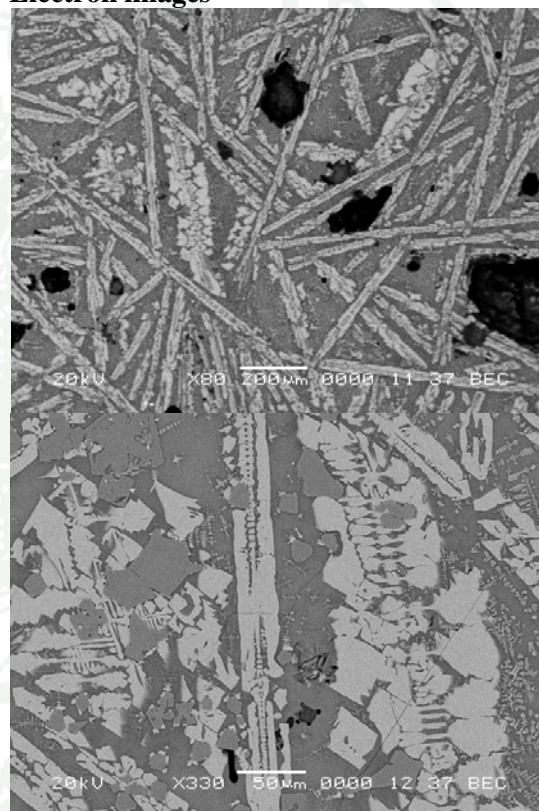
Lab ID: A0540

Object: Slag

#### Reflected light images



#### Electron images



**Appendix Figure E21** The results of microscopic analysis of slag (A0540) from Ban Khao Din Tai Archaeological Site.



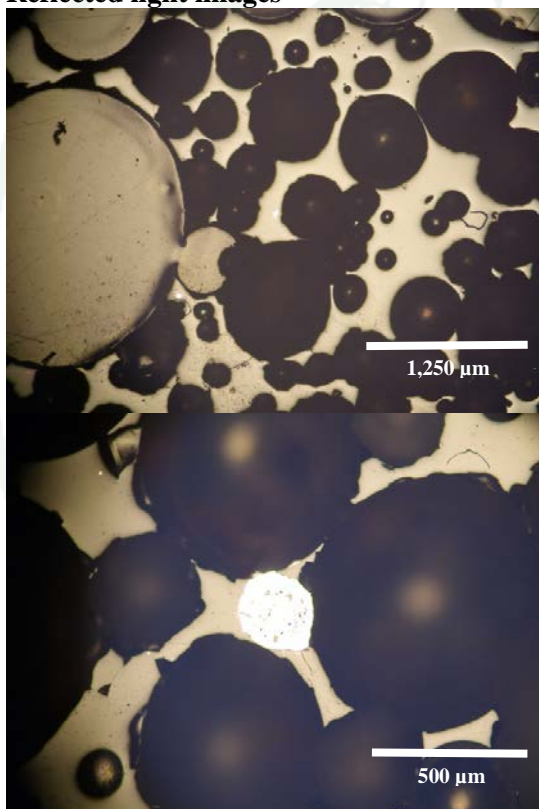
Site: Ban Khao Din Tai Archaeological Site,  
Tambon Ban Kruat, Amphoe Ban Kruat,  
Buriram.

Sample ID: KDT'07 TP.1 NWQ Furnace#4  
(#0155/1)

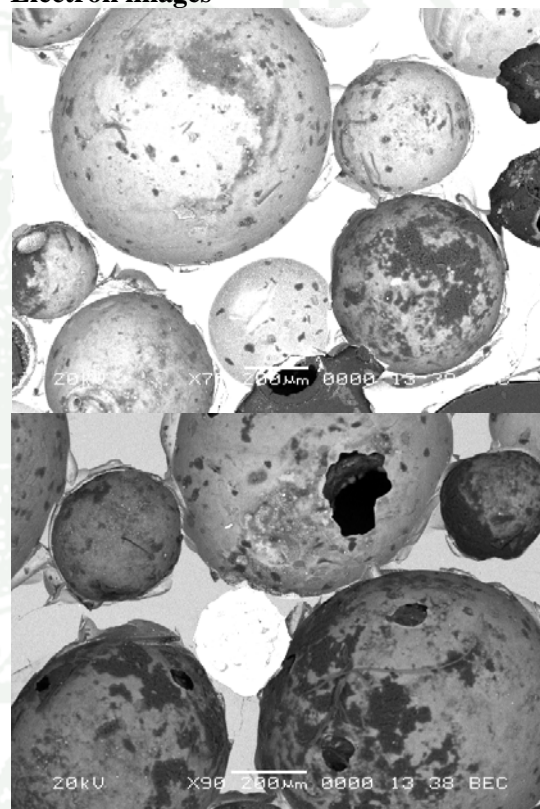
Lab ID: A0541

Object: Slag

**Reflected light images**



**Electron images**



**Appendix Figure E22** The results of microscopic analysis of slag (A0541) from Ban Khao Din Tai Archaeological Site.



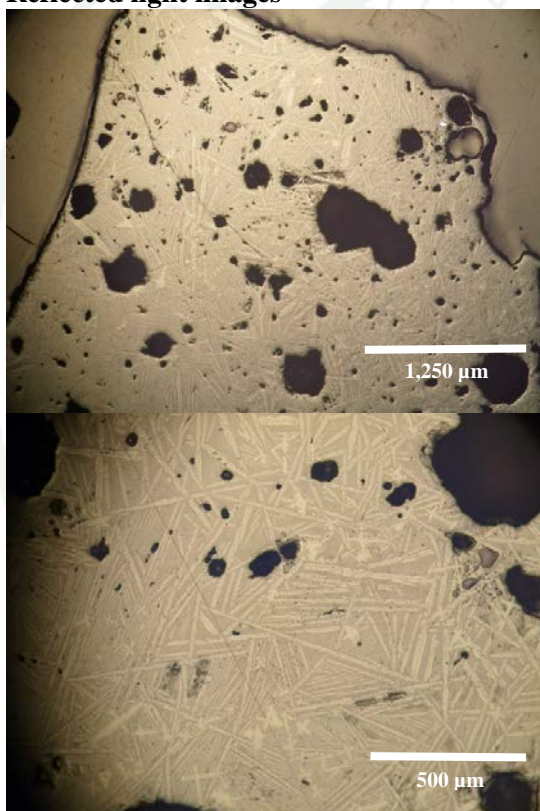
Site: Ban Khao Din Tai Archaeological Site,  
Tambon Ban Kruat, Amphoe Ban Kruat,  
Buriram.

Sample ID: KDT'08 TP.1 NWQ 200-210  
cm.dt (#109)

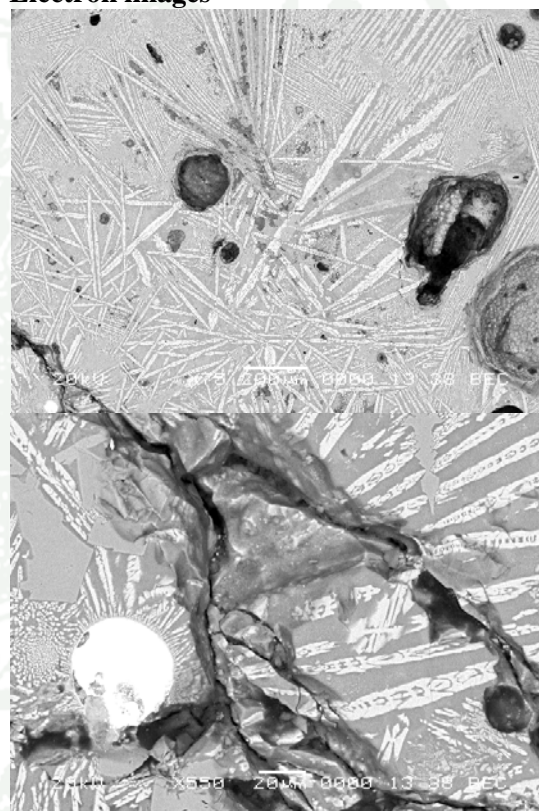
Lab ID: A0542

Object: Slag

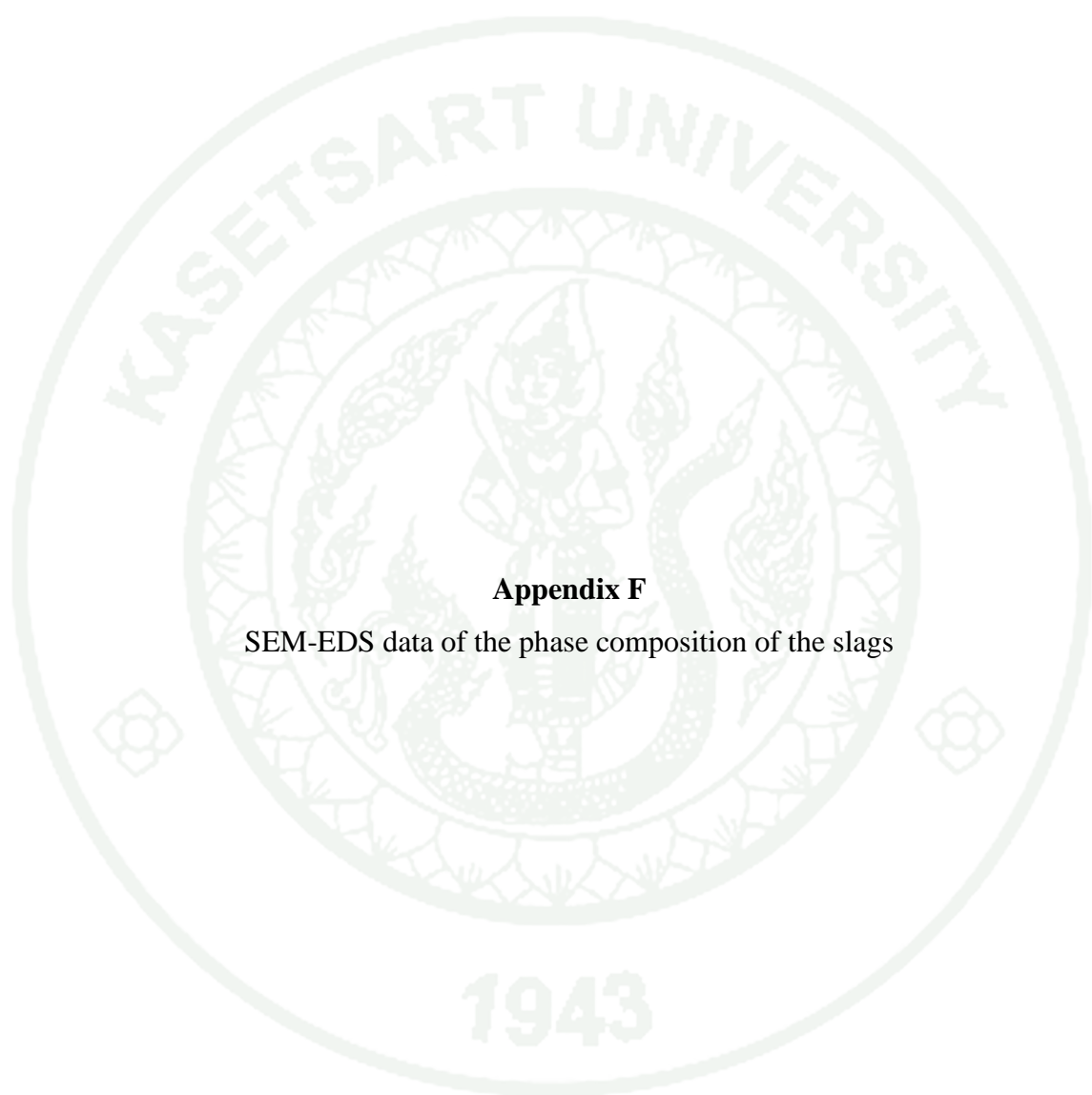
#### Reflected light images



#### Electron images

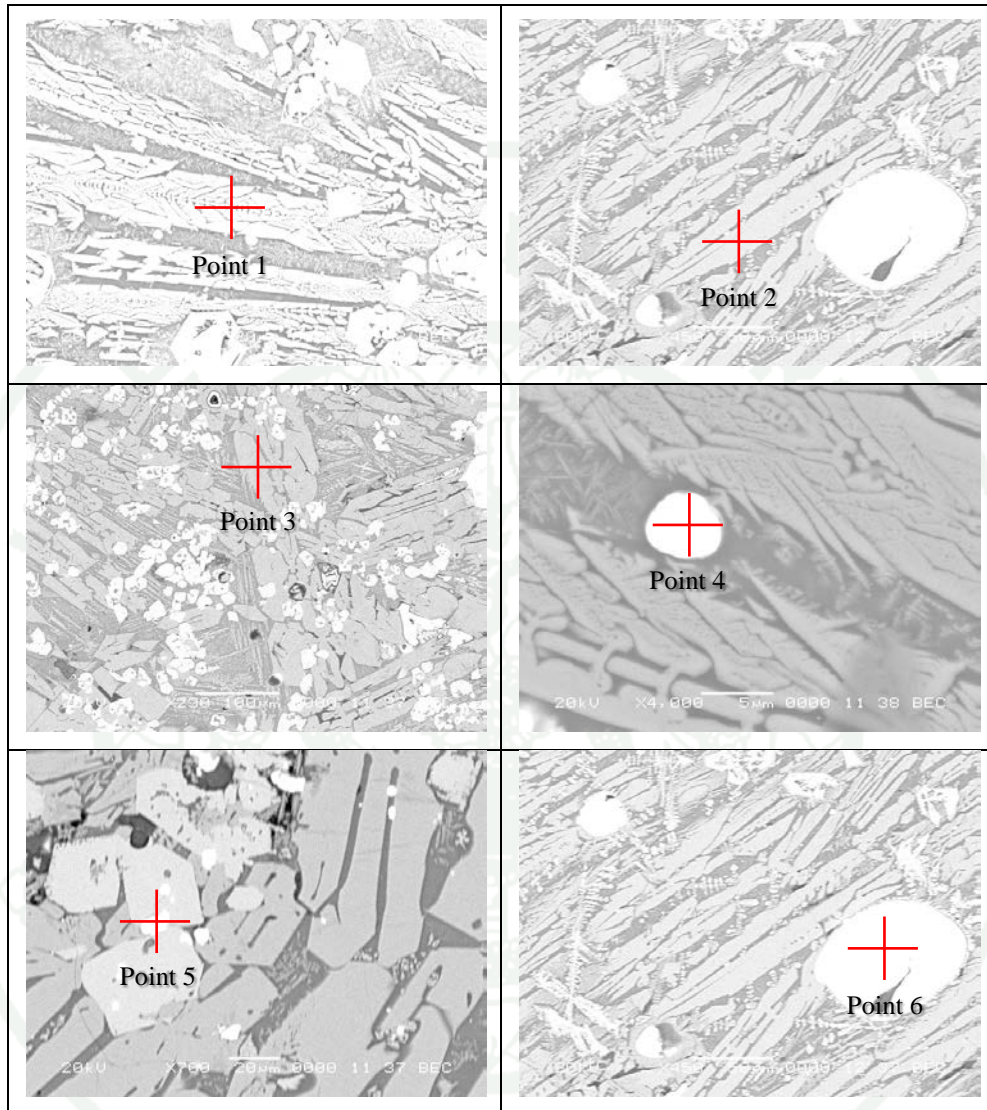


**Appendix Figure E23** The results of microscopic analysis of slag (A0542) from Ban Khao Din Tai Archaeological Site.



**Appendix F**

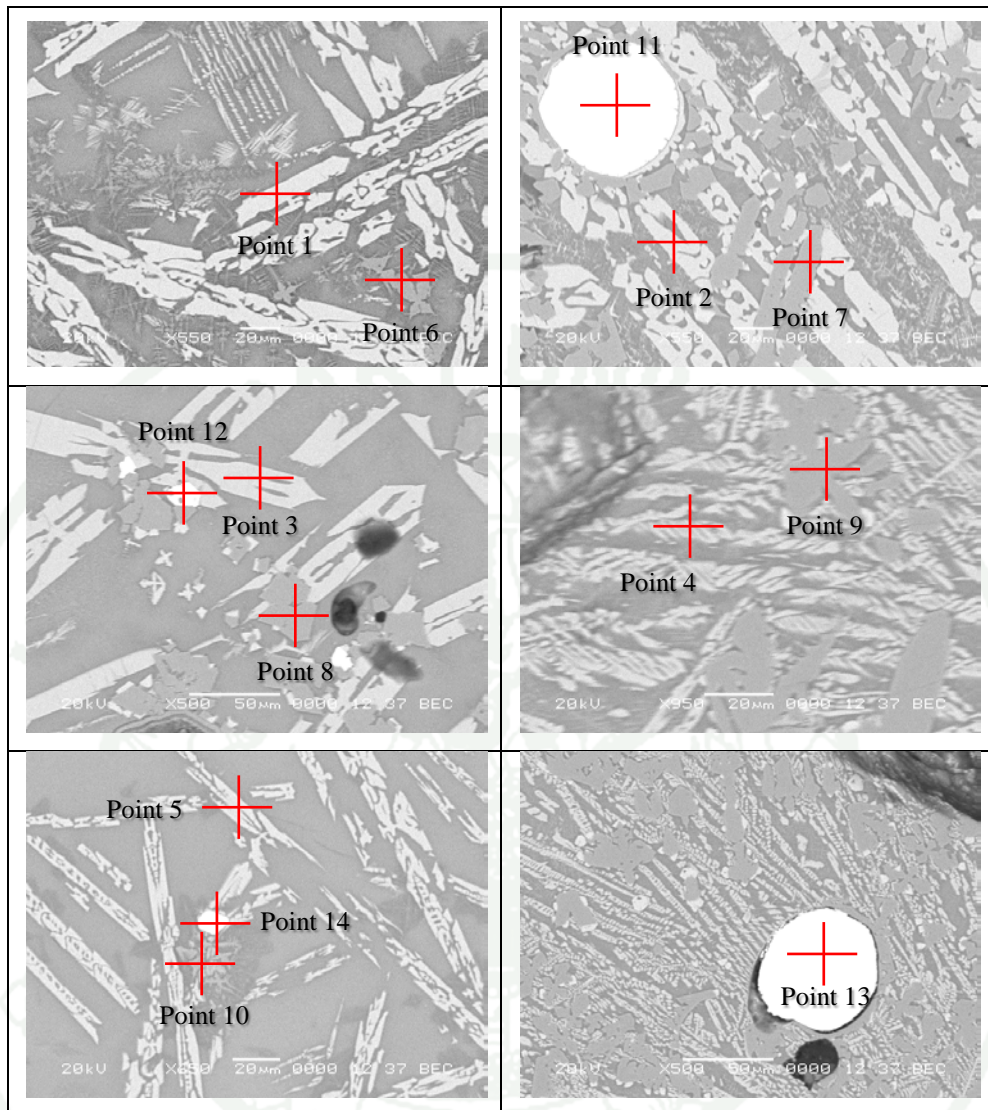
SEM-EDS data of the phase composition of the slags



**Appendix Figure F1** SEM-EDS data of the phase composition of the slags from Non Nong Hor Archaeological Site.

**Appendix Table F1** SEM-EDS data of the phase composition of the slags from Non Nong Hor Archaeological Site (wt.%).

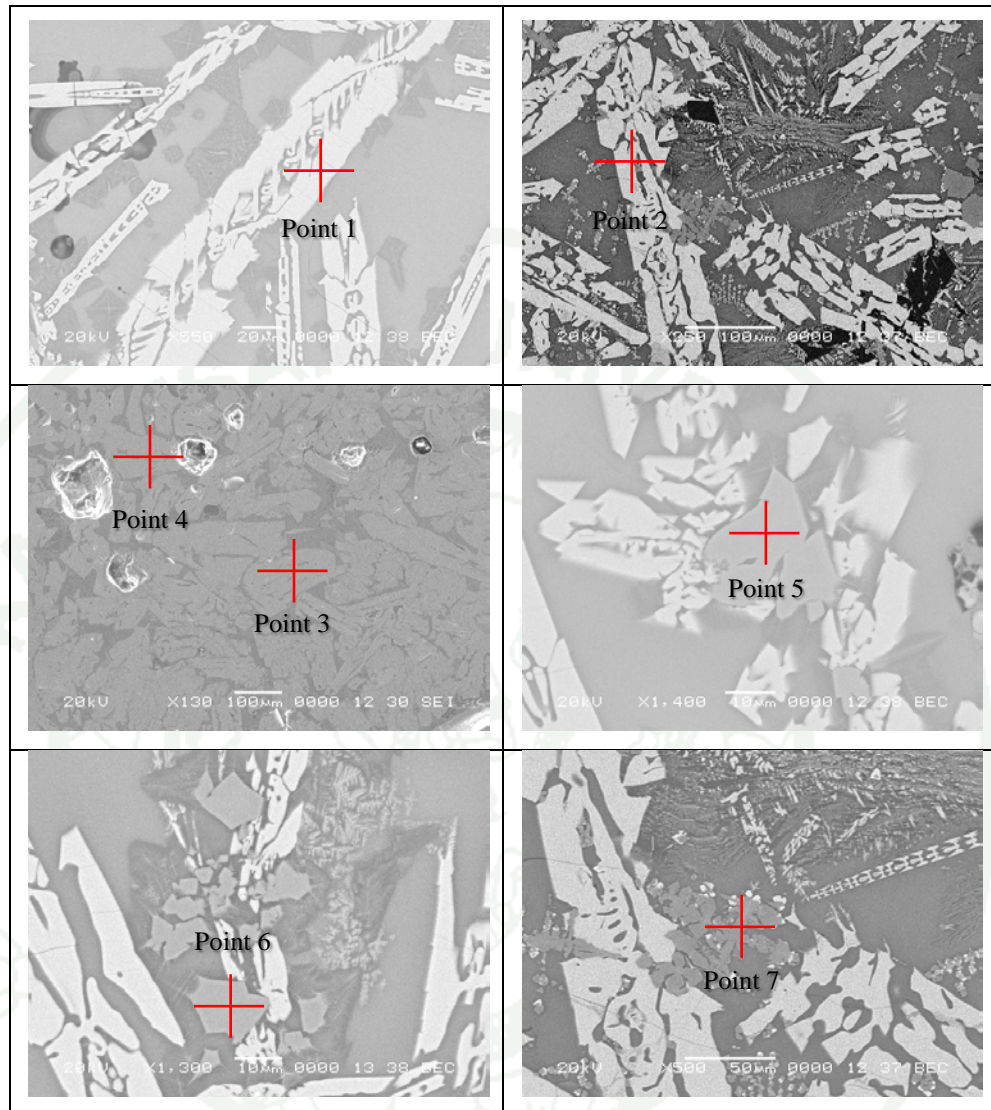
| Lab ID. | Point | Mineral/Metal | O     | Mg    | Si    | Mn    | Fe    | Cu    |
|---------|-------|---------------|-------|-------|-------|-------|-------|-------|
| A0572   | 1     | Fayalite      | 55.13 | 1.490 | 17.30 | -     | 26.09 | -     |
| A0577   | 2     | Fayalite      | 54.62 |       | 16.44 | -     | 28.94 | -     |
| A0581   | 3     | Fayalite      | 56.16 | 1.650 | 17.24 | 2.480 | 22.48 | -     |
| A0572   | 4     | Copper        | -     | -     | -     | -     | 7.360 | 92.64 |
| A0573   | 5     | Copper        | -     | -     | -     | -     | 7.010 | 92.99 |
| A0577   | 6     | Copper        | -     | -     | -     | -     |       | 100.0 |



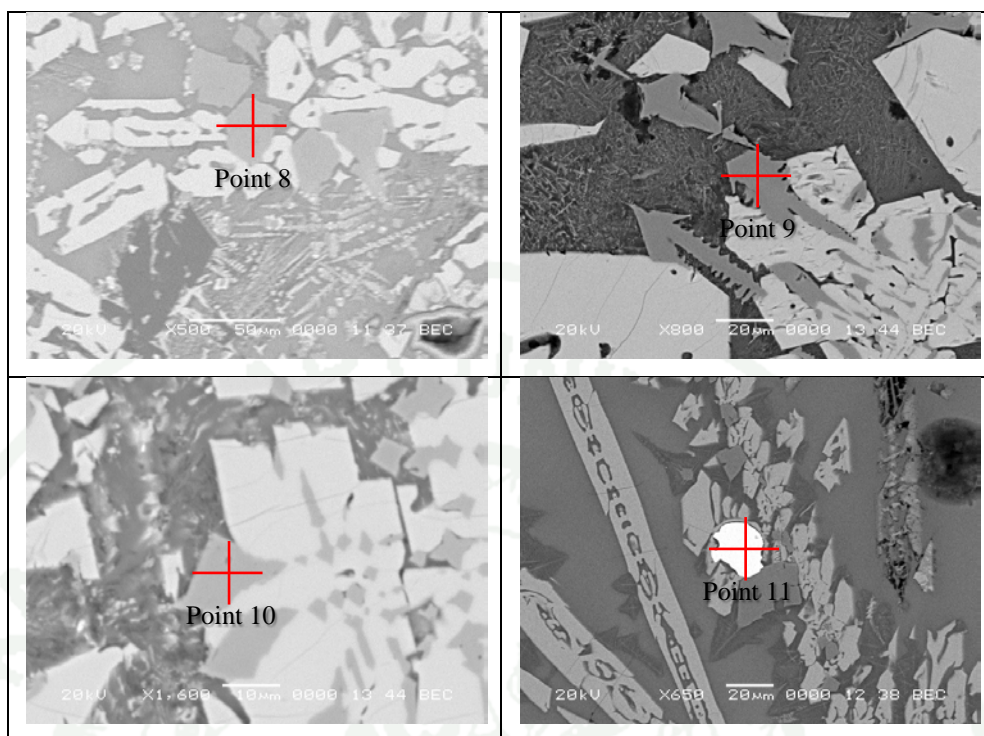
**Appendix Figure F2** SEM-EDS data of the phase composition of the slags from Khok Kroy Archaeological Site.

**Appendix Table F2** SEM-EDS data of the phase composition of the slags from Khok Kroy Archaeological Site (wt.%).

| Lab ID. | Point | Mineral/Metal | O     | Mg    | Al    | Si    | Ti    | V     | Cr    | Mn    | Fe    | Ni    |
|---------|-------|---------------|-------|-------|-------|-------|-------|-------|-------|-------|-------|-------|
| A0586   | 1     | Fayalite      | 54.95 | -     | -     | 16.69 | -     | -     | -     | -     | 28.36 | -     |
| A0588   | 2     | Fayalite      | 52.83 | -     | -     | 16.68 | -     | -     | -     | 3.330 | 27.16 | -     |
| A0590   | 3     | Fayalite      | 55.20 | -     | -     | 17.10 | -     | -     | -     | -     | 27.71 | -     |
| A0594   | 4     | Fayalite      | 56.69 | -     | -     | 18.16 | -     | -     | -     | 3.050 | 17.79 | -     |
| A0595   | 5     | Fayalite      | 55.31 | -     | 4.310 | 17.43 | -     | -     | -     | -     | 26.33 | -     |
| A0586   | 6     | Hercynite     | 52.10 | -     | 30.10 | 0.990 | -     | 0.980 | -     | -     | 15.82 | -     |
| A0588   | 7     | Hercynite     | 51.24 | -     | 31.58 | -     | 0.680 | -     | 0.550 | -     | 15.95 | -     |
| A0590   | 8     | Hercynite     | 52.32 | -     | 30.69 | -     | 0.590 | 0.620 | -     | -     | 15.78 | -     |
| A0594   | 9     | Hercynite     | 54.82 | 1.100 | 27.95 | -     | 0.420 | 0.870 | 1.100 | -     | 13.74 | -     |
| A0595   | 10    | Hercynite     | 51.57 | -     | 30.07 | 2.100 | -     | 1.020 | -     | -     | 15.25 | -     |
| A0588   | 11    | Iron          | -     | -     | -     | -     | -     | -     | -     | -     | 100.0 | -     |
| A0590   | 12    | Iron          | -     | -     | -     | -     | -     | -     | -     | -     | 100.0 | -     |
| A0594   | 13    | Iron          | -     | -     | -     | -     | -     | -     | -     | -     | 98.05 | 1.950 |
| A0595   | 14    | Iron          | -     | -     | -     | -     | -     | -     | -     | -     | 100.0 | -     |



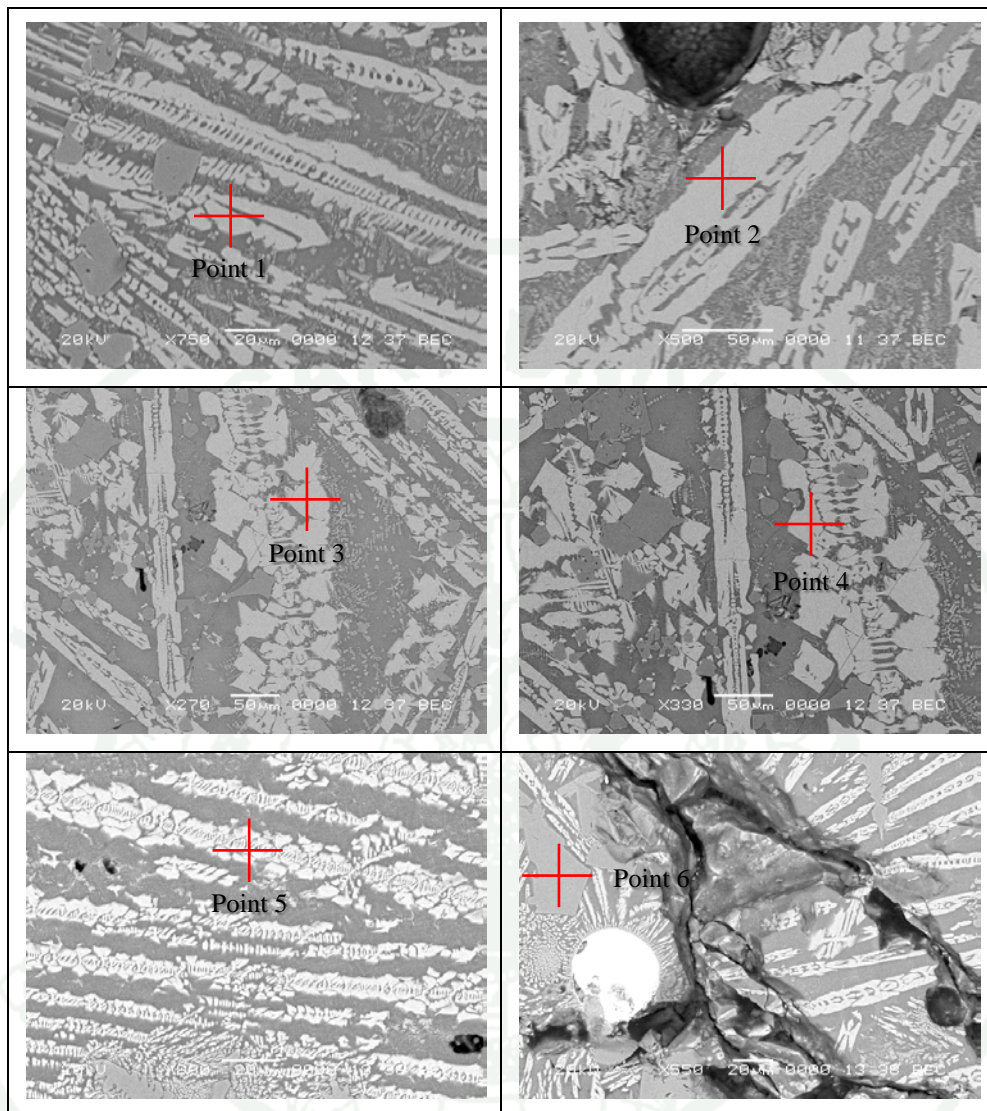
**Appendix Figure F3** SEM-EDS data of the phase composition of the slags from Ban Saitho 7 Archaeological Site.



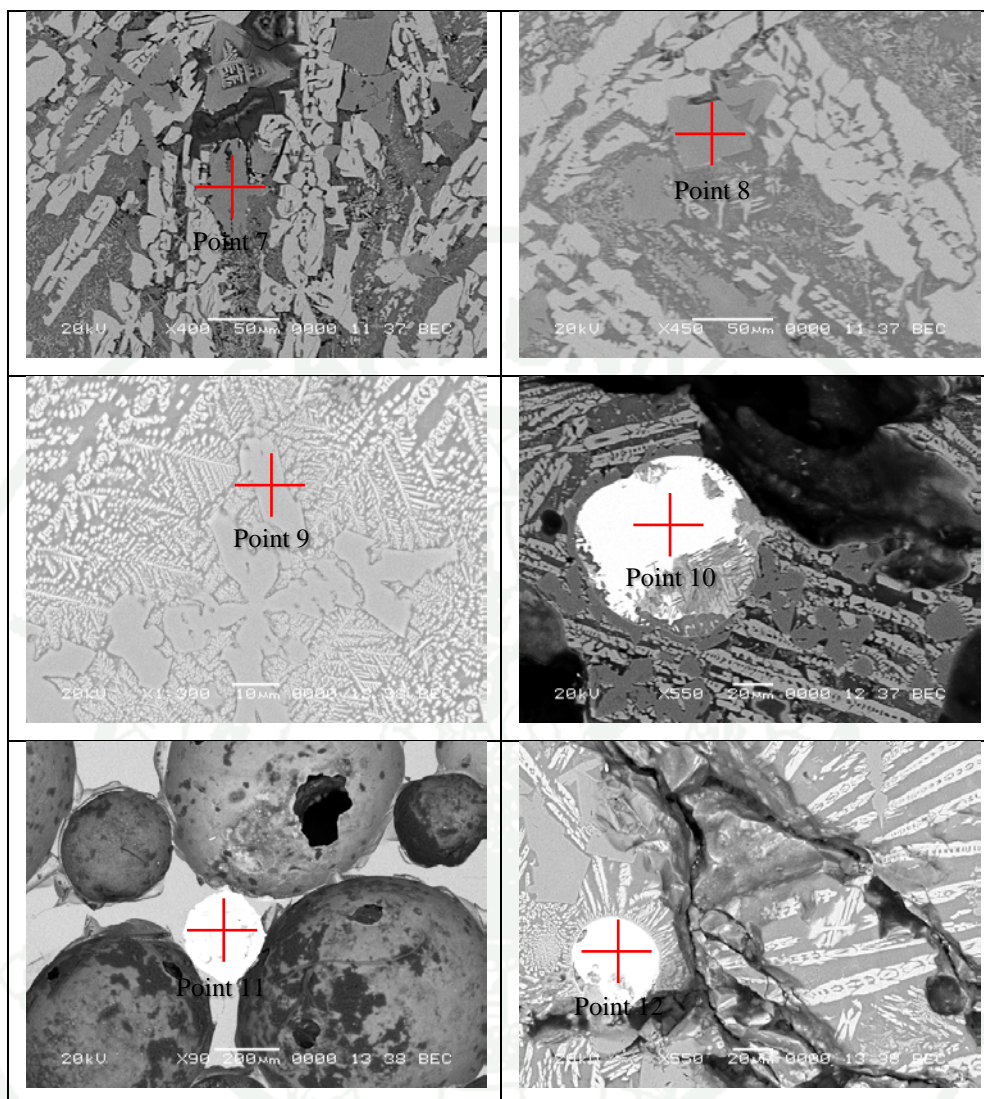
**Appendix Figure F3** (Continued).

**Appendix Table F3** SEM-EDS data of the phase composition of the slags from Ban Saitho 7 Archaeological Site (wt.%).

| Lab ID. | Point | Mineral/Metal | O     | Al    | Si    | Ti    | V     | Fe    |
|---------|-------|---------------|-------|-------|-------|-------|-------|-------|
| A0273   | 1     | Fayalite      | 55.46 | -     | 16.69 | -     | -     | 27.84 |
| A0281   | 2     | Fayalite      | 56.74 | -     | 16.05 | -     | -     | 27.21 |
| A0546   | 3     | Fayalite      | 53.94 | -     | 17.08 | -     | -     | 28.97 |
| A0546   | 4     | Fayalite      | 53.95 | -     | 17.61 | -     | -     | 28.44 |
| A0273   | 5     | Hercynite     | 52.06 | 31.03 | -     | -     | 1.610 | 15.30 |
| A0273   | 6     | Hercynite     | 51.35 | 31.35 | -     | -     | 1.410 | 15.89 |
| A0281   | 7     | Hercynite     | 52.97 | 28.21 | -     | 1.130 | 1.060 | 16.62 |
| A0281   | 8     | Hercynite     | 55.54 | 27.32 | -     | 0.730 | 0.560 | 15.85 |
| A0546   | 9     | Hercynite     | 52.93 | 29.15 | -     | 0.550 | -     | 17.37 |
| A0546   | 10    | Hercynite     | 53.42 | 29.30 | -     | 0.520 | -     | 16.75 |
| A0273   | 11    | Iron          | -     | -     | -     | -     | -     | 100.0 |



**Appendix Figure F4** SEM-EDS data of the phase composition of the slags from Ban Khao Din Tai Archaeological Site.

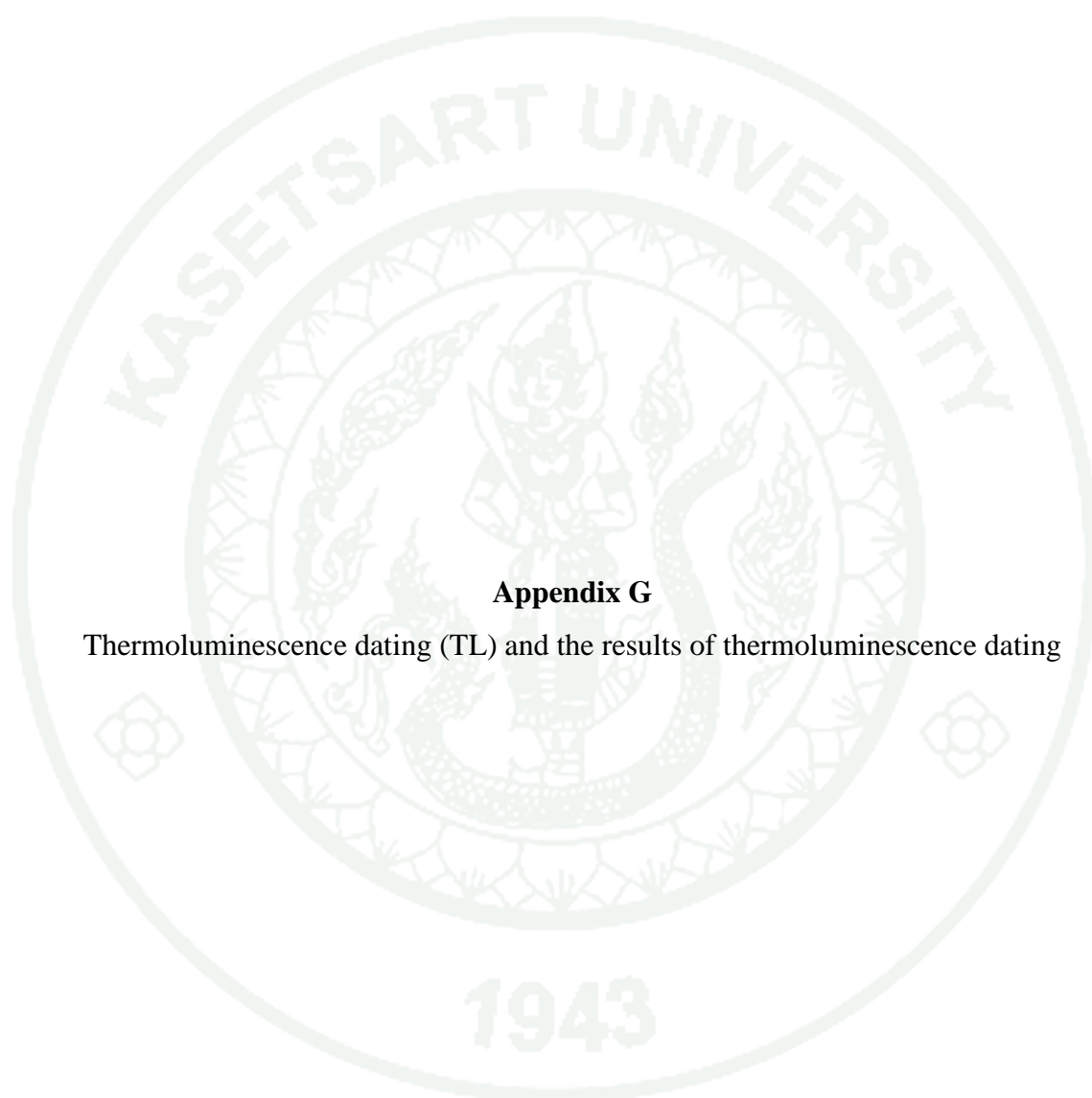


**Appendix Figure F4** (Continued).

1943

**Appendix Table F4** SEM-EDS data of the phase composition of the slags from Ban Khao Din Tai Archaeological Site (wt.%).

| Lab ID. | Point | Mineral/Metal | O     | Al    | Si    | Ti    | V     | Cr    | Fe    |
|---------|-------|---------------|-------|-------|-------|-------|-------|-------|-------|
| A0538   | 1     | Fayalite      | 52.46 | -     | 17.72 | -     | -     | -     | 29.82 |
| A0539   | 2     | Fayalite      | 52.93 | -     | 17.84 | -     | -     | -     | 29.23 |
| A0540   | 3     | Fayalite      | 55.34 | -     | 16.81 | -     | -     | -     | 27.85 |
| A0540   | 4     | Fayalite      | 54.19 | -     | 16.92 | -     | -     | -     | 28.89 |
| A0542   | 5     | Fayalite      | 58.83 | 1.760 | 16.21 | -     | -     | -     | 23.19 |
| A0538   | 6     | Hercynite     | 49.70 | 31.55 | -     | 0.670 | 0.720 | -     | 17.36 |
| A0539   | 7     | Hercynite     | 50.46 | 30.66 | -     | -     | 1.040 | 0.870 | 16.97 |
| A0539   | 8     | Hercynite     | 49.19 | 31.27 | -     | -     | 1.130 | 1.280 | 17.13 |
| A0542   | 9     | Hercynite     | 55.41 | 29.37 | -     | -     | 0.740 | -     | 14.48 |
| A0538   | 10    | Iron          | -     | -     | -     | -     | -     | -     | 100.0 |
| A0541   | 11    | Iron          | 58.01 | -     | -     | -     | -     | -     | 41.99 |
| A0542   | 12    | Iron          | -     | -     | -     | -     | -     | -     | 100.0 |



**Appendix G**

Thermoluminescence dating (TL) and the results of thermoluminescence dating

## Thermoluminescence dating (TL)

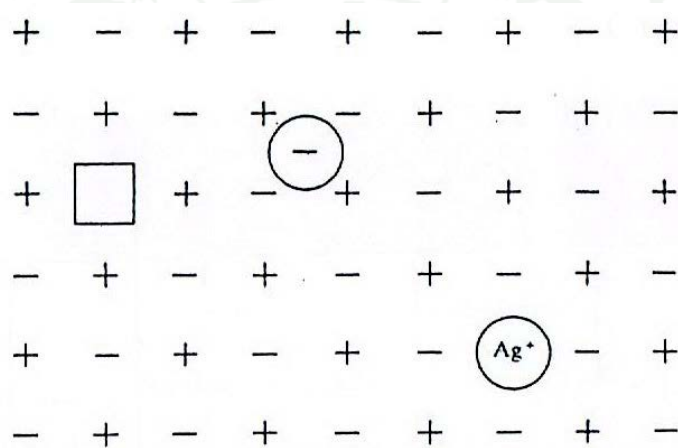
Thermoluminescence dating is the one of luminescence dating techniques to be developed and was originally applied to the dating of fired pottery or other forms of baked sediment. Since then, however, it has been used to date a wide range of media, including other fired materials, such as burnt flint artifacts, burnt stones and volcanic products, as well as unburnt samples, for example, cave speleothem carbonate, and sediments. Thermoluminescence is the thermally stimulated emission of light from an ionic crystal following the previous absorption of energy from ionizing radiation. The thermoluminescence process can be best understood in terms of the band theory of solid, as follows.

### 1. The thermoluminescence process

Ideally, an ionic crystal consists of a lattice of positive and negative ions arranged in patterns. However, there can be defects due to impurity atoms, rapid cooling from the molten state, and damage caused by nuclear radiation. There are many types of defect that can occur, of which three simple ones are shown in appendix figure G1. A defect acts as an electron trap that attracts an ionized electron that result from the action of nuclear radiation in detaching electrons from their parent nuclei. This ionizing effect of nuclear radiation, as opposed to the much less propable event of damage to the lattice, gives rise to the thermoluminescence.

Once in a trap an electron remains there until shaken out by the vibrations of the lattice. As the temperature is raised these vibrations get stronger, and the probability of eviction increases so rapidly that within quite a narrow temperature range the situation changes from the electrons being firmly trapped to being free to diffuse around the crystal. A variety of fates awaits a diffusing electron. It can be re-trapped and re-evicted; it can be trapped at different types of defect better able to shield it from the lattice vibrations, that is, a deeper trap; or it can recombine with ion from which an electron has previously been detached. This recombination can be of two types, that is, radiative or non-radiative. Ions or atoms at which radiative recombination occurs are called luminescence centers and the light emitted is the thermoluminescence.

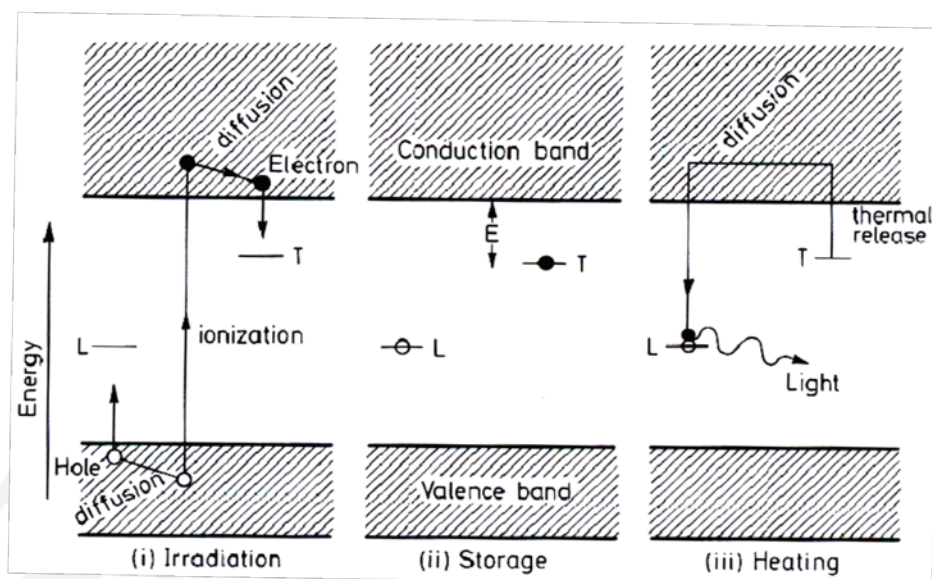
The basic process of the production of thermoluminescence is shown in appendix figure G2. A trap is characterized by the energy  $E$  that a trapped electron must acquire from lattice vibrations to escape to the conduction band (or valence band). Electrons in the conduction band can move freely in the crystal. Holes, which were removed from hole traps are free to move in the crystal, when they are excited to energy levels in the valence band. There is a characteristic temperature at which the thermal vibrations of the crystal lattice are sufficient to cause the release of trapped electrons. Some of the released electrons reach luminescence centers, which are filled with holes, and light is emitted in the recombination process (Aitken, 1985).



**Appendix Figure G1** A simple types of defect in the lattice structure of an ionic crystal: A negative-ion vacancy on the left, A negative-ion interstitial at the center, and substitution impurity center on the bottom right.

**Source:** Aitken (1985)

In summary, Naturally, There is ionization of electrons by nuclear radiation. In mineral crystals, this leads to ionization of the atoms in the host material and freed electrons may become trapped in structural defects or holes in the mineral crystal lattice. These electrons can be released by heating under controlled conditions, and where the trapped charges recombine at luminescence centers in the crystal, an emission of light occurs that is proportional in intensity to the number of trapped electrons.



**Appendix Figure G2** Thermoluminescence-process diagram showing energy-level related to three processes; (i) irradiation process, caused by crystal exposed to nuclear radiation, ionized electrons are trapped at hole (T); (ii) Storage stage in which electrons have been trapped, need hole deep enough for electrons (E) during geological time period of sample; and (iii) Heating process, at optimum level of temperature, electrons are released and re-combined at luminescence center (L), and then light (TL) is released.

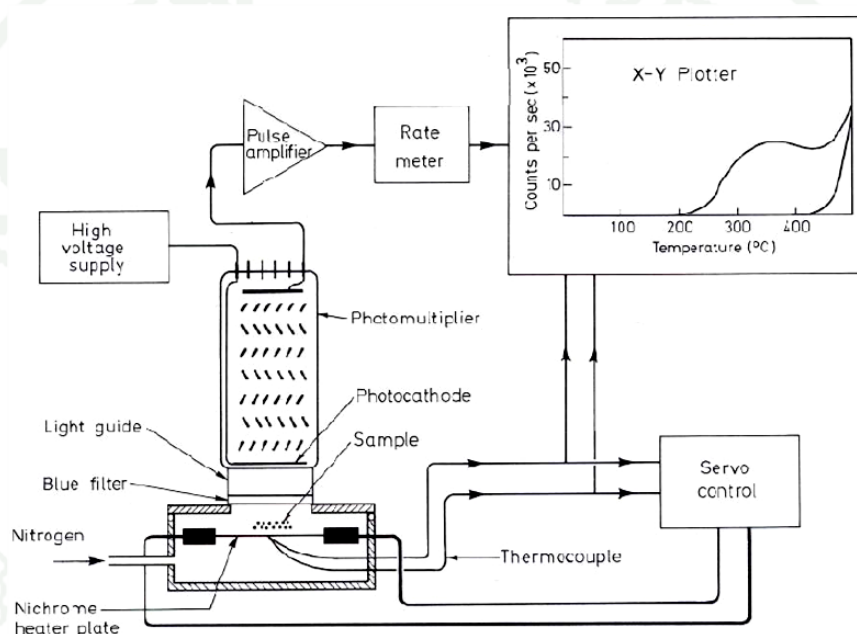
**Source:** Aitken (1985)

## 2. Thermoluminescence Measurements and Age Determination

TL measurements are carried out on a sample of mineral material, usually a separated quartz fraction. This is heated to temperatures around 400-500 °C or more, and as light is emitted from the process that previously discussed, the photons are converted to electric pulses using a photomultiplier tube (appendix figure G3).

Thereafter, the light emission (TL intensity) is then plotted against the heating temperature to produce a glow curve (appendix figure G4 A), in which the peaks are reflective of the thermal lifetimes of the various electron trap populations in

the sample. The natural TL signal is compared with the artificial signals (growth curve, see appendix figure G3 B) obtained from portions of the sample to which known doses of radiation have been administered from a calibrated laboratory radioisotope source. This allows an evaluation of the palaeodose (PD), which is a measure of the amount of radiation that would be needed to generate a TL signal equal to that which the sample has acquired subsequent to the most recent firing event or exposure to sunlight (Walker, 2005).



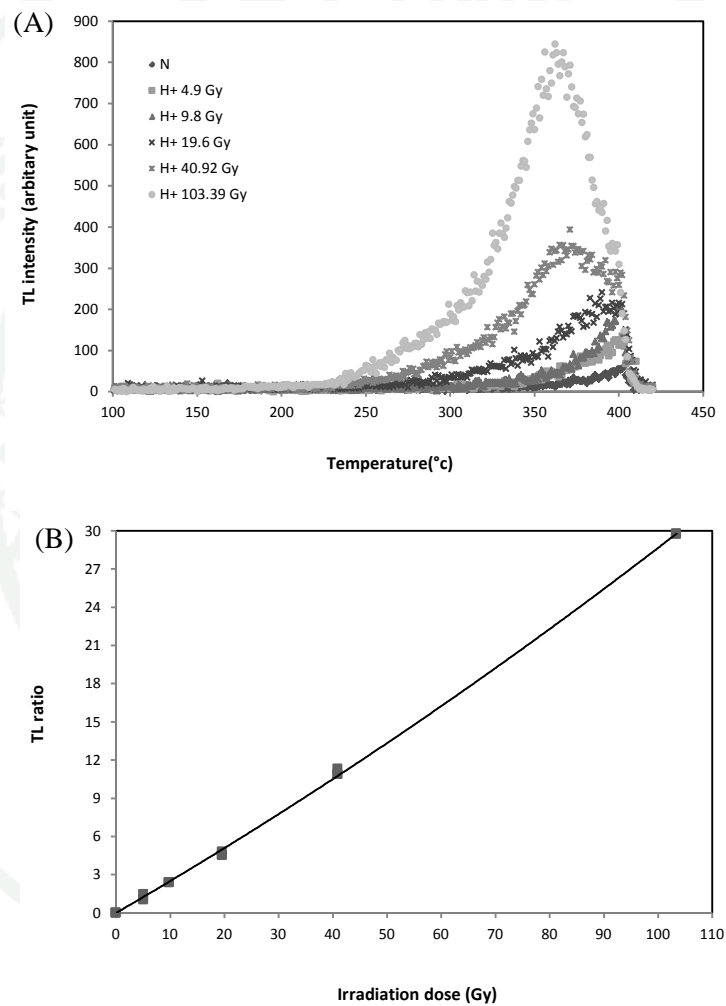
**Appendix Figure G3** Diagram of thermoluminescence instrument.

**Source:** Aitken (1985)

In order to arrive at an estimate of age, the environmental dose rate (annual dose) has to be determined. It is a measure of the radiation dose per unit of time absorbed by the mineral of interest. The dose rate is calculated from the contribution of cosmic radiation and an analysis of the radioactive elements in both the sample and its surroundings. These are determined using the measured concentrations of radioactive elements (uranium, thorium, potassium-40) within the sample and its surroundings, which are, in turn, converted into dose rates using standard conversion factors and formulae. Finally, TL age can be calculated from the the equation (1) (Aitken, 1985) as following:

$$\text{TL age} = \frac{\text{PD}}{\text{AD}} \quad (1)$$

Here, TL age in year  $\times 10^3$  unit, PD is the palaeodose in Grey unit and AD is the annual dose to which the crystal is exposed annually in mGrey per year unit



**Appendix Figure G4** (A) A TL glow curve (temperature versus TL signal intensity);  
(B) A TL growth curve.

**Appendix Table G1** The results of thermoluminescence dating of Smelting furnace fragment, potsherds and baked sediment samples.

| No. | LAB ID. | K2O (%) | U (ppm) | Th (ppm) | W.C. (%) | AD (mGy/a) | PD (Gy) | TL age (a) |
|-----|---------|---------|---------|----------|----------|------------|---------|------------|
| 1   | A 0548  | 1.892   | 3.769   | 16.64    | 10.71    | 3.955      | 5.692   | 1,439±115  |
| 2   | A 0549  | 4.642   | 6.022   | 21.28    | nil      | 7.298      | 7.335   | 1,005±80   |
| 3   | A 0550  | 2.588   | 5.256   | 17.17    | 9.524    | 4.978      | 6.063   | 1,218±97   |
| 4   | A 0551  | 4.350   | 8.200   | 25.15    | nil      | 7.863      | 9.940   | 1,264±100  |
| 5   | A 0552  | 1.296   | 6.288   | 13.10    | nil      | 3.778      | 4.723   | 1,250±100  |
| 6   | A 0554  | 0.248   | 2.913   | 5.537    | nil      | 1.451      | 0.900   | 620±50     |
| 7   | A 0555  | 3.992   | 5.081   | 14.14    | 1.042    | 5.953      | 3.923   | 659±53     |
| 8   | A 0556  | 8.292   | 10.14   | 21.40    | nil      | 11.55      | 7.770   | 672±54     |
| 9   | A 0557  | 9.200   | 10.63   | 25.45    | nil      | 12.67      | 8.050   | 635±51     |
| 10  | A 0558  | 1.928   | 4.504   | 10.06    | nil      | 3.672      | 2.519   | 686±55     |
| 11  | A 0338  | nil     | nil     | 9.046    | 2.994    | 0.777      | 0.916   | 1,179±71   |
| 12  | A 0339  | nil     | nil     | 7.878    | 2.536    | 0.690      | 0.819   | 1,186±142  |
| 13  | A 0340  | nil     | 4.509   | 7.243    | 1.480    | 1.740      | 2.045   | 1,176±202  |
| 14  | A 0341  | nil     | nil     | 6.530    | 0.370    | 0.589      | 0.708   | 1,202±180  |
| 15  | A 0272  | 5.003   | 6.075   | 27.71    | 2.890    | 8.045      | 9.557   | 1,188±119  |
| 16  | A 0277  | 4.636   | 4.968   | 23.99    | 3.623    | 7.175      | 8.075   | 1,126±135  |
| 17  | A 0282  | nil     | 0.774   | 6.490    | 1.010    | 0.774      | 0.819   | 1,058±85   |
| 18  | A 0335  | nil     | 0.167   | 8.568    | 2.564    | 0.782      | 0.886   | 1,133±168  |
| 19  | A 0336  | nil     | 0.256   | 7.948    | 0.935    | 0.757      | 0.860   | 1,135±76   |
| 20  | A 0337  | nil     | 0.311   | 6.801    | 2.830    | 0.685      | 0.761   | 1,111±192  |
| 21  | A 0607  | 1.989   | 4.459   | 12.90    | nil      | 3.929      | 4.320   | 1,099±88   |
| 22  | A 0605  | 0.686   | 2.725   | 7.933    | nil      | 1.974      | 2.300   | 1,165±93   |
| 23  | A 0606  | 0.565   | 11.49   | 51.44    | nil      | 7.287      | 8.980   | 1,232±99   |

## CURRICULUM VITAE

**NAME** : Miss Theeraporn Chuenpee

**BIRTH DATE** : March 15, 1986

**BIRTH PLACE** : Trat, Thailand

| <b>EDUCATION</b> | <b><u>YEAR</u></b> | <b><u>INSTITUTE</u></b> | <b><u>DEGREE/DIPLOMA</u></b> |
|------------------|--------------------|-------------------------|------------------------------|
|                  | 2009               | Kasetsart Univ.         | B.Sc. (General Science)      |

**POSITION/TITLE** : Research Assistance

**WORK PLACE** : Thermoluminescence Laboratory,  
Department of Earth Science, Faculty of  
Science, Kasetsart University.

**SCHOLARSHIP/AWARDS** : The Graduate Study Research Scholarship for  
International Publications